Iris Publishers

EFFICACIOUSLY TARGETING UNKNOWN ANOPHELINE ECO-GEOREFERENCEABLE ORTHOMOSIA CAPTURE POINTS EMPLOYING KRIGABLE PHOTOGRAMMETRIC RAYLEIGH OPTICAL DEPTHS AS A FUNCTION OF SUB-METER RESOLUTION SEMI-INFINITE ANISOTROPICALLY AZIMUTHALLY ASYMMETRIC SCATTERING SIGNATURE SPECTROSCOPIC FREQUENCIES UNDER DISPROPORTIONATE SOLAR EXOATMOSPHERIC IRRADIANCE CONDITIONS IN Q-DIMENSIONAL EUCLIDEAN SPACE IN A SEMI-AUTONOMOUS UNMANNED AIRCRAFT REAL-TIME SPECTROTEMPORAL OBJECT-BASED CLASSIFIER.

Efficaciously Targeting Unknown Anopheline Eco-Georeferenceable Orthomosiac Capture Points Employing Krigable Photogrammetric Rayleigh Optical Depths as a Function of Sub-Meter Resolution Semi-Infinite Anisotropically Azimuthally Asymmetric Scattering Signature Spectroscopic Frequencies Under Disproportionate Solar Exoatmospheric Irradiance Conditions in Q-Dimensional Euclidean Space in a Semi-Autonomous Unmanned Aircraft Real-Time Spectrotemporal Object-Based Classifier

Benjamin Jacob*

University of South Florida, Florida.

*Corresponding author

Benjamin Jacob, Research Assistant Professor, Department of Global Health, University of South Florida, Florida

Index

Abstracts

Trying to optimally identify, potential, unknown, un-geosampled, capture point, Aedes aegypti, seasonal, super beeder, larval, habitat, epi-entomological foci such as a county abatement discarded tire pile, with limited remote sensing tools [e.g., on foot with a Google Map TM Global Positioning Systems (GPS) tracker] is time consuming, costly and inefficient (e.g., many habitats may go undetected even in open, canopied, land cover). Waste tires pose a threat to human life as they are the perfect foci for Ae. aegypti, a mosquito that can spread chikungunya, Zika fever, Rift Valley fever, mayaro, Yellow fever and dengue, under the right temperature and precipitation conditions. The vector lays their eggs in containers with standing water, which later emerge as blood-feeding adult females that can transmit these viruses. Low-cost, ArcGIS and object-based, (e.g., ENVI), real-time technology is becoming available for small unmanned aerial vehicle (UAV) platforms. These technologies can be efficient in carrying out inspections of anomalous, reflectance, land use land cover (LULC) characteristics of potential, endemic, capture point, seasonal, super beeder, eco-georeferenceble, Ae. aegypti, larval/pupal habitat, county abatement foci. Here larval/pupal, habitat, LULC signatures were established of an Ae. aegypti, potential, seasonal, waste tire, county abatement, capture point in a semi-autonomous, unmanned, drone, aircraft dashboard, real-time, ArcGIS module. Incorporating silos of eco-georeferenceable, prolific, Ae. aegypti, larval/pupal habitat, seasonal, LULC, signature, capture point geolocations into a UAV, spectral library identified unknown super beeder foci (e, g., backyard with>12, larval/pupal habitats) in an epi-entomological, intervention, county abatement, study site. These sites were subsequently field verified ("ground truthed") by county abatement, district, vector, entomological, control officials who confirmed a 92.7 % success rate of the real-time captures (i.e., unknown tire sites). Unmixed, real-time, sub-meter resolution eco-endmember, interpolation techniques in a real time UAV, cartographic cyberenvironment can robustly map unfamiliar, potential, super breeder, capture point, Ae. aegypti, waste tire, larval habitats in an epi-entomological, intervention, county abatement, study site. We generated a mobile app for the DJI quadcopter for mission planning, which eluidatively defined any county abatement, LULC area of interest (e.g., urban commercial agro-pasturelands) by obtaining timely swaths and wayward capture points of super breeder, seasonal, Ae. aegypti, capture point, waste tires in real time. The UAV performed all the necessary system checks (e.g., battery levels, differential correction of GPS, camera storage, etc.), autonomously flew the mission with the proper photo overlapping and returned to home. The app uploaded the super breeder, LULC, capture point, UAV frequencies into multiple servers for immediate data processing during flight. A signature, drone app is useful for long-term, real-time, LULC, surveillance, monitoring and larval control of seasonal, super breeder, county abatement, Ae. aegypti, waste tire, larval habitats, since it is a quicker and more cost-effective option with high larval habitat detection rates of un-geosampled, unknown foci.

Keywords: Unmanned aerial vechile (UAV); Ae aegypti; capture point; kriging; signature; ENVI; ArcGIS

Introduction

Aedes aegypti is a known vector of several viruses including yellow fever virus, dengue virus chikungunya virus and Zika virus. This mosquito originated in Africa, but is now found in tropical, subtropical and temperate region throughout the world. In Europe, for example, local and imported cases are reported every year.

An observational, cross-sectional, population-based study in Barcelona, Spain was performed by Miller (2016) [1]. An analysis of the socio-demographic, epidemiological, clinical characteristics, and mosquito control activities of the zika cases detected between January 1st and December 2016 was carried out using a specific epidemiological survey disseminated by the Barcelona Public Health Agency. A total of 118 notifications of possible zika virus infections were received, and 44 corresponded to confirmed cases in Barcelona residents. Among these, the median age was 35 years and 57% were women. All cases were imported, 48% were Spanish-born and 52% foreign-born. Dominican Republic was the most visited country amongst foreign-born patients and Nicaragua amongst Spanish-born. The most frequent symptoms were exanthema, fever, and arthralgia. Among the 24 diagnosed women, 6 (25%) were pregnant. There was one case of microcephaly outside Barcelona city. Congenital zika syndrome is unique to fetuses and infants infected with zika virus before birth, and is described by the following five features:1)Severe microcephaly in which the skull is partially collapsed,2)Decreased brain tissue with a specific pattern of brain damage, including subcortical calcifications,3)Damage to the back of the eye, including macular scarring and focal pigmentary retinal mottling,4)Congenital contractures, such as clubfoot or arthrogryposis: and 5),Hypertonia restricting body movement soon after birth [https://www.cdc.gov/pregnancy/zika/testing-follow-up/zika-syndrome-birth-defects.html].

Entomological inspections were conducted at the homes of 19 cases (43.2% of the total) and in 34 (77.3%) public spaces. Vector activity was found in one case of the 44 confirmed cases, and 134 surveillance and vector control were carried out associated to imported zika cases. In all cases prevention measures were recommended to avoid mosquito bites on infected cases. The establishment of this mosquito in Europe raises concerns about autochthonous arbovirus transmission in other geographic locations.

The recent emergence of both dengue and zika viruses in the Americas increases the possibility that individuals may become infected by more than one *Ae. aegypti* -borne virus at a time. Recent clinical data support an increase in the frequency of coinfection in human patients (CDC 2015), raising the likelihood that mosquitoes could be exposed to multiple arboviruses during one feeding episode at the county abatement level. The impact of coinfection on the ability of relevant vector species to transmit any of these viruses (that is, their vector competence) has not been determined at the county abatement level. *Aedes* mosquitoes could transmit all combinations of these viruses simultaneously in a county abatement [2]. Importantly, infection, dissemination and transmission rates in *Aedes aegypti* mosquitoes may be amplified if affected by coinfection

October 10, 2016 the Center of Disease Control (CDC) issued guidance related to zika for people living in or traveling to Miami-Dade County, Florida, USA. They advised that pregnant women not travel to this area due to local transmission of zika virus [National Center for Emerging and Zoonotic Infectious Diseases (NCEZID) Division of Vector-Borne Diseases (DVBD)]. CDC designates areas for zika virus transmission prevention in the continental United States and Hawaii as red or yellow (www.cdc.org). Miami-Dade County was previously designated as a zika cautionary (yellow) area, but that designation was removed on June 2, 2017. This means that there are no longer any travel recommendations related to zika virus for Miami-Dade County, Florida. Although the level of risk of zika virus transmission after a yellow area is removed is not known, it is likely to be low. Further, sporadic cases may still occur due to re-emergence of immature, *Ae. aegypt,* from artificial water containers.

September 29th, 2016 a person in Miami-Dade County Florida caught a locally transmitted case of dengue fever. The case is the first in which a person caught dengue from a mosquito bite in 2016.Florida is not the only state to experience dengue. Hawaii had dengue outbreaks in 2001, 2011 and 2015, and Brownsville, Texas, had an outbreak in 2005. Of the *Aedes* species, the primary vector of the dengue virus is *Ae. aegypti.* however, *Aedes albopictus*, *Aedes polynesiensis*, and *Aedes scutellaris* - have a limited ability to serve as dengue vectors (https://www.nature.com/scitable/topicpage/dengue-transmission). For this reason, CDC recommends that people living in or traveling to warmer counties continue to protect themselves from mosquito-borne illnesses, including *Aedes* mosquitoes (www.cdc.gov) (Figure 1).
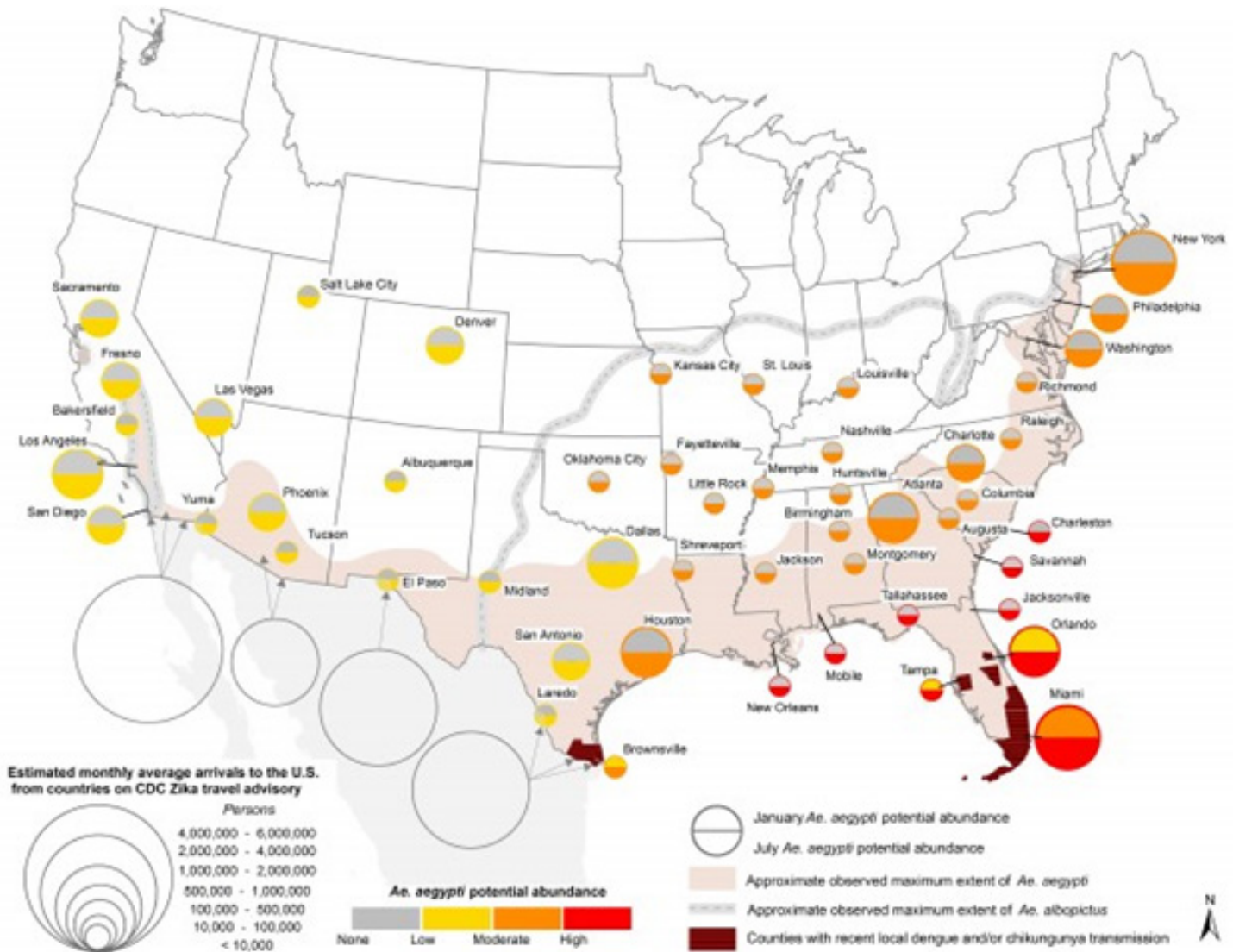
Figure 1: Map showing 1) Ae. aegypti potential abundance for Jan/July (colored circles), 2) approximate maximum known range of Ae. aegypti (shaded regions)), and 3) monthly average number arrivals to the U.S. by air and land from countries on the CDC Zika travel advisory.

Several different methods for control have been developed for prevention of Aedes, mosquito-related, infectious diseases [e.g., physical exclusion (nets, screens, etc.), pesticide application, biological control methods, sterile insect technique, and release of genetically modified mosquitoes [3] Unfortunately and for a variety of reasons, these approaches can be difficult to implement in many geolocations [4] Widespread insecticide resistance in disease-carrying, Aedes mosquito populations also poses a significant problem.

On an individual level, mosquito repellents are widely used to avoid Aedes disease exposure [5]. Behavioral responses of nine Aedes aegypti (L.) strains, six from recent field collections and three from the long-established laboratory colonies, were tested under laboratory-controlled conditions by using an excito-repellency test system Kongmee et al. 2004 Behavioral Responses of Aedes aegypti (Diptera: Culicidae) Exposed to Deltamethrin and Possible Implications for Disease Control of Medical Entomology) All nine strains showed significant behavioral escape responses when exposed to deltamethrin at the standard field dose ($0.02g/m^2$), regardless of background insecticide susceptibility status (susceptible or tolerant/resistant). Insecticide contact irritancy played a predominate role in overall female mosquito escape responses, whereas noncontact repellency was not observed at levels significantly different from paired noncontact control tests (P >0.01). Amongst the six field populations, the Jakarta (Indonesia) Toba (north Sumatra), and Bangkok female mosquitoes showed rapid exit (>78%) during 30 min of direct contact with insecticide-treated surfaces, whereas the other three strains demonstrated only moderate escape responses (32–56%) from the chambers. Moderate escape responses during direct insecticidal contact also were observed in the three laboratory test populations (44–60%). Higher percentage of mortality was observed from laboratory strains (8–33%) that failed to escape compared with nonescape females of field strains (2–16%), possibly a reflection of background deltamethrin susceptibility status. The authors concluded that contact

irritancy is a major behavioral response of *Ae. aegypti* when exposed directly to deltamethrin and that rapid flight escape from areas exposed to space sprays or surfaces treated with residual pyrethroids could have a significant impact on the effectiveness of adult mosquito control and disease transmission reduction measures.

Repellents, even though they can never guarantee complete protection, may lessen the chance of contracting vector-borne diseases [6]. The sense of smell is one of the most important senses that mosquitoes use for long range host seeking [7] dInsect olfaction has been extensively studied leading to the identification of the key proteins involved: odorant receptors, odorant receptor co-receptors, gustatory receptors, and odorant binding proteins [8].

There have been several studies that have shown an association between the use of personal protection products and a reduction in mosquito bites and disease incidence (Debboun and Strickman 2013). For example, permethrin-treated military clothing has shown to be effective in significantly reducing mosquito bites in the covered regions (Schreck and Kline 1989). Published data indicate that repellent efficacy and duration of protection vary considerably among products and among mosquito and tick species. Product efficacy and duration of protection against *Ae. aegypti* and other vector/nuisance mosquitoes are also markedly affected by ambient temperature, level of activity, amount of perspiration, exposure to water, abrasive removal, and other factors. In general, higher concentrations of active ingredient provide longer duration of protection, regardless of the active ingredient. Products with <10% active ingredient may offer only limited protection, often 1–2 hours. Products that offer sustained-release or controlled-release (microencapsulated) formulations, even with lower active ingredient concentrations, may provide longer protection times.

Application of the repellent DEET to ankles repellent soaps that contain DEET and permethrin have been shown to successfully reduce some vector arthropod infections Unfortunately, the CDC and Prevention article on "Protection against Mosquitoes, Ticks, & Other Arthropods" notes that "Studies suggest that concentrations of DEET and other off-the shelf repellants are approximately 50% hence, they do not offer a marked increase in protection time against Aedes mosquitoes; DEET efficacy tends to plateau at a concentration of approximately 50%"(www.cdc.gov).

Plant-based repellents have been proposed for generations in traditional practice as a personal protection measure against host-seeking mosquitoes. Knowledge on traditional repellent plants obtained through ethnobotanical studies may be a valuable resource for the development of new natural products which may be employable as preventionary devices against Aedes -oriented infections. Recently, commercial repellent products containing plant-based ingredients have gained increasing popularity amongst consumers, as these are commonly perceived as "safe" in comparison to long-established synthetic repellents although this is sometimes a misconception. To date insufficient studies have followed standard WHO Pesticide Evaluation Scheme guidelines for repellent testing. Unfortunately, there is a current need for further standardized studies in order to better evaluate plant repellent compounds for usage against *Ae. aegypti* infections and other vector/nuisanace arthropod species so as to develop new products that offer high repellency as well as good consumer safety.

Mosquito control is currently the optimal method for *Ae. aegypti* disease prevention. This primarily includes source reduction, pesticide spraying for larval control and "fogging" for adult control, or the use of mosquito traps like the lethal ovitrap. One way to reduce the vector control containers as a potential, larval, breeding site of Aedes by environmental management methods is to prevent or minimize infections associated with this vector mosquito.

The Aedes mosquitoes prefer to breed in areas of stagnant water, such as flower vases, uncovered barrels, buckets, and discarded tires [World Health Organization (WHO)]. Research has shown that certain chemicals emanating from bacteria in water containers stimulate the female mosquitoes to lay their eggs. They are particularly motivated to lay eggs in water containers that have the correct amounts of specific fatty acids associated with bacteria involved in the degradation of leaves and other organic matter in water. The chemicals associated with the microbial stew are far more stimulating to discerning female *Ae. aegypti* mosquitoes than plain or filtered water in which the bacteria once lived. Natural breeding habitats of *Ae. aegypti* in a county abatement region may be determined by conducting intensive seasonal, larval surveys. For example, [9] directed a rigrious larval survey in Trinidad. Puerto Rico, and the U.S. Virgin Islands. Twelve types of natural habitats were recorded: rock holes (9.7%), calabashes (2.4%), tree holes (19.5%), leaf axils (4.8%), bamboo joints (14.9%), papaya stumps (7.3%), coconut shells (4.8%), bromeliads (7.3%), ground pools (14.9%), coral rock holes (9.7%), crab holes (2.4%), and conch shells (7.3%), of which the coconut shell and calabash habitats were new to the Caribbean. The countries having the highest prevalence of natural habitats were Trinidad. Puerto Rico, and Jamaica, with 9 types (22.0%), 7 types (17.0%), and 6 types (14.6%), respectively. The distribution of natural habitats of *Ae. aegypti* in the Caribbean region was then discussed in relation to local vector control measures.

Refuse vehicle tires on undeveloped land plots near human dwellings may be a public health threat, as they can provide a suitable habitat for vector and nuisance mosquito (Diptera: Culicidae) population growth (Dinh 2015). Owing to resistibility and slow degradability that accounts for higher residence time, these materials qualify as potentially hazardous wastes as retention of water permits waste tires to form a congenial biotope for the breeding of different vector mosquitoes. This proposition was validated through the study on the porcelain and plastic household wastes as larval habitats of Dengue vectors (Aedes spp.) in rural and urban areas around Kolkata, India [10]. The wastes were characterized in terms of larval productivity, seasonal variation and a comparison between urban and rural, geoclassified, LULC, abatement

areas which was made using data of two subsequent years. The number of wastes positive as larval habitats and their productivity of Aedes spp. varied among the types of household wastes with reference to months and location. Multivariate analysis revealed significant differences in the larval productivity of the household wastes based on the materials, season, and urban–rural LULC context.

Results of a spatially filtered, autoregressions of, eco-georeferenced datasets of geosampled, eco-endmember, larval, habitat uncoalesced, orthogonal, oviposition, wavelength datasets of sub-meter, resolution, LULC signatures in an ArcGIS module may reveal multiple, unknown, seasonal, capture point, super breeder, iteratively interpolative covariates (e.g., independently, geosampled, county abatement, eco-georeferenced, capture points), weighted by structural properties such as species, foliar, densities, mass fractions etc.)[11]. A real-time, prognosticative, unmixed, grid-stratifiable LULC, signature, frequency, weighted, vulnerability, analyses employing autocorrelation functions rendered from spatial contiguity matrices in ArcGIS may indicate differences in abundance and distribution of *Ae. aegypti*, waste tire, larval habitats throughout, sub-county geoclassified, urban, residential and rural, agro-pastureland, eco-georeferenceable geolocations. The waste tires may be more productive in urban, abatement, LULC areas as compared to farmland sub-couty zip code agro-irriagted geolocation in an intervention, epi-entomological, study site, during pre-rain sample frames, for example, indicating a possible seasonal difference in endemicity of Ae, Egypt infections. A link between waste tires with Aedes productivity may be expected to increase the seasonal risk of dengue, zika and other epidemics if seasonal time increases such that the larval habitat foci becomes a super breeder whilst simultaneously waste tire generation is continued without appropriate measures to limit addition to a sub-county abatement environment.

Although the lifespan of an adult Ae. aegypti is two to four weeks depending on conditions, [Exposure to chikungunya virus and adult longevity in *Aedes aegypti (L.)* and Aedes albopictus (Skuse) Michael H. Reiskind, 1,2 Catherine J. Westbrook,1 and L. Philip Lounibos1], the eggs can be viable for over a year in a dry state,("overwintering") which can allow the mosquito to re-emerge after a cold winter or dry spell. The preference for biting humans is dependent on expression of the odorant receptor AeegOr4 [see McBride and Felix Baier and Aman B. Omondi and Sarabeth A. Spitzer and Joel Lutomiah and Rosemary C. Sang and Rickard Ignell and Leslie B. Vosshall}, booktitle={Nature}, 2014]. [12] investigated survival times of eggs under three humidity conditions (42%, 68%, 88% RH) among Aedes (Stegomyia) mosquitoes from temperate and tropical zones (5 species and 20 geographical strains). This subgenus tended to occupy small aquatic sites as larvae, where desiccation resistance of eggs is necessary during habitat drought (see Novak 1992). Interspecific comparison revealed that the egg survival time was correlated with egg volume and dryness of source locality, and probably with larval habitat. Further, *Ae. aegypti* was associated most with arid climate and human-disturbed habitats - its large eggs survived the longest periods at all humidities. The survival times for forest species eggs (A. riversi, A. galloisi, A. flavopictus) were variable at high humidities but at the lowest humidity were consistently shorter than for eggs of *Ae. aegypti*.

New research is looking into the use of a bacterium called Wolbachia as a method of biocontrol of Ae aegypti and other vector mosquitoes. Studies show that invasion of *Ae. aegypti* by the endosymbiotic bacteria allows mosquitoes to be resistant to certain arboviruses such as dengue fever and zika virus strains currently circulating. Mosquitoes carrying the endosymbiont bacterium Wolbachia have been deployed in field trials as a biological control intervention due to Wolbachia effects on reducing transmission of arboviruses [Using Wolbachia Releases to Estimate Aedes aegypti (Diptera: Culicidae) Population Size and Survival,]the authors performed mark, release and recapture (MRR) experiments using Wolbachia as an internal marker with daily collections with BG-Traps during the first two weeks of releases in Rio de Janeiro, Brazil. The MRR design allowed investigating two critical parameters to determine whether Wolbachia could successfully invade a field population: the probability of daily survival (PDS) of Wolbachia-infected *Ae. aegypti* females, and the wild population density during releases. Released females had a PDS of 0.82 and 0.89 in the first and second weeks, respectively, immediately after releases, which was well within the range of previous estimates of survivorship of wild mosquitoes in Rio de Janeiro. Abundance estimation of wild population varied up to 10-fold higher depending on the estimation method used (634–3,565 females on the average-difference model to 6,365–16,188 females). Wolbachia-released mosquitoes were lower than the density estimation of their wild counterparts, irrespectively of the model used. Individually screening mosquitoes for the presence of Wolbachia reduced uncertainty on abundance estimations due to fluctuation in capturing per week. However, *Ae. aegypti* fitness was unaffected by Wolbachia presence. Fitness costs in the vector may have been due to adaptive consequences of resistance. The continued use of chemical insecticides in the context of the National Program of Dengue Control in Brazil may have generated a high selective pressure on the natural populations of *Ae. aegypti*, leading to their resistance. Biological and reproductive performance of *Ae. aegypti* strains have revealed field population resistance to tempos, the main larvicide used for controlling mosquitoes [13].

To ensure sustainability of control efforts, *Ae. aegypti*, mosquito, control programs should strengthen their capacity to employ time series, remotely acquired, grid-stratifiable, sub-meter resolution, real-time, LULC signatures for decision-making with respect to evaluation of current, county abatement, vector reduction tactics. Employment of additional tools in conjunction with insecticide-treated nets (ITN)/Indoor Residual Spraying (IRS) approaches, case-detection and treatment strategies may regulate how much and what types of vector control and interdisciplinary input are required to achieve *Ae. aegypti* elimination at a sub-county abatement epi-entomological, intervention, study site. Similarly, there is a need for continued research to identify and evaluate new tools for vector control that can be integrated with existing biomedical strategies within county-level, abatement control programs for optimally remotely, targeting potential, eco-georeferenceable, super breeder, larval habitats of *Ae. aegypti* and other vector/nuisance mosquitoes. To achieve the ambitious goal of elimination of *Ae. aegypti* and

other vector/nuisance mosquitoes at the county abatement level, there must be complimentary indoor-based vector control interventions (such as bed nets and indoor spraying) with outdoor-based interventions such as real-time, supported drone maps.

Unmanned Aerial Vehicles (UAVs) (Remotely Piloted Airborne Systems) or RPASs (also known as drones or UASs (unmanned aerial systems) can capture landscape attributes which may be pertinent for remotely geolocating and robustly forecasting, unknown, potential, super breeder, eco-georeferenceable, aquatic, larval habitats of *Ae. aegypti*, in real time, in a sub-county abatement epi-entomological, intervention, study site, for implementing an Integrated Vector Management (IVM). Integrated Vector Management is a decision-making process for the management of vector populations, to reduce or interrupt transmission of vector-borne diseases; the strategy is based on the premise of integrating all available and effective measures, whether chemical, or biological. [14]. Salient attributes of UASs for implementing county abatement real-time IVMs for optimally, remotely, targeting, potential, super breeder, *Ae. aegypti*, seasonally declassifiable, waste tire, eco-dereferenceable, LULC, oviposition, signature sites and other vector /nuisance mosquitoes may include aggregating and interpolating sub-meter resolution, grid-ratifiable, unmixed, time series, spectral signatures. These wavelength markers may be extractable from hyper productive, seasonal, sparsely canopied, eco-dereferenceable, capture point, real-time, UAV imagery for distinguishing, positively autocorrelated, resampled geolocations of immature, high density, waste tire, larval habitats geospatially aggregated as clusters (i.e., IVM, vulnerability, county abatement, vulnerability, forecast map of tire piles). Many existing cartographic vector control interventions are known to be effective against multiple diseases. Numerous, seasonal, transitional, eco-georeferenced, capture point, larval habitat, cofactors (e.g., meteorological trends, LULC changeset.) may be examined for transmittance influences on potential, super breeder, eco-dereferenceable, seasonal foci which may help eco-cartographically optimally delineate unknown, potential, seasonal, super breeder, Ae aegypti, waste tire, larval habitats.

For any given, real-time, sensed, LULC material associated to an eco-dereferenceable, potential, seasonal, super breeder, county abatement, *Ae. aegypti*, larval habitat, waste tire, resampled, capture point the amount of solar radiation that is reflected will vary with wavelength in any real-time, UAV, dashboard, image analysis, software package (e.g., ArcGIS, ENVI). UAV per-pixel classifications, may improve, capture point, classification, models of signature frequencies (i.e., unmixed, water stagnant, intermittently canopied, eco-dereferenceable, RGB eco-endmembers) employing real-time, image, software applications of absorbed transmittance emissivity's which may then subsequently predict eco-dereferenceable, suitable, LULC geolocations of potential, unknown, seasonal, super breeder, waste tire, *Ae aegypti*, capture point foci. A per-parcel, sub-county abatement, signature, stochastic, iterative interpolator may address vector- and raster-mapping of an epi-entomological, intervention, study site by integrating unmixed, sub-meter resolution, sub-pixels (e.g., RGB eco-endmember photosynthetic and non-photosynthetic, shade canopy frequencies) within grid-ratifiable, reclassified, vector land parcels. Henceforth ancillary data may perform contextually enhanced UAV, spectral classifications on a per-parcel, real-time basis. In doing so, unknown, super breeder, eco-dereferenceable, waste tire, Ae aegypti, seasonal, foci friability may be diagnosable. If suffice capture point, attributed land parcel sub-pixels, may be prognosticated in a real-time, UAV eco-cartographic cyberenvironment (e.g., ArcMap 3-D Analyst).

Several deterministic, signature models have been developed in the literature to study the interactions of solar radiation within vegetation canopies of entomological, vector, arthropod, larval habitats in various sub-county abatement, geographic locations (henceforth geolocations) (e.g., hyper arid, arid, semi-arid), to understand how biodiversity responds to environmental degradation in fragile ecosystems for optimally, remotely targeting, eco-dereferenceable, seasonal, super breeder, foci. In these contributions, diversity and assemblage structure differed between seasons, amongst capture point geolocations and between protected LULC areas reclassified as tropical dry forest and adjacent communal lands suffering from desertification. Measured wavelength explanators of seasonal, hyper-larval productivity currently include canopy closure, vegetation height, percent cover of bare ground, leaf litter, and grasses amongst collected points in epi-entomological, intervention, sub-county, abatement, study sites. These models have adapted a system of simultaneous differential equations to investigate inhomogeneous, vegetation, LULC, canopy radiation. For example. Pinching [15]. Employed an ArcGIS deterministic model to distinguish, unmixed, directional, spectral reflectance of a capture point, LULC reclassified, vegetation, intermittently canopied paradigm. Meanwhile Conklin optimally mapped, discontinuous, LULC canopies employing uncoalesced, empirical datasets of near infra-red (NIR) and red, wavelength, interpolated, spectral signatures for remotely summarizing unobserved isoline convergence and soil radiance in Naegleria fowler sample sites. In both these research efforts the total proportion of spectral reflection absorbed by the canopy system changed as a function of solar zenith angle; the total global reflected spectral also changed. The solar zenith angle is the angle between the zenith and the center of the Sun's disc. The deterministic models simulated the apparent reflectance in multiple, moderate resolution, (Landsat at 28.5 m resolution) unmixed, LULC wavebands above the canopy, and this reflectance revealed varying solar zenith angles due to geometrical-radiation, signature interactions within the capture point, grid-stratified, (270mx 270m), canopied LULCs. Many epi-entomological, studies for identifying unfamiliar prolific foci do not distinguish between unmixed, LULC capture point, global and directional, interpolative, unmixed canopy, reflectance factors, (i.e., RGB sub-pixel, frequencies). This distinction may dictate the nature of the friability of eco-dereferenceable, sub-county abatement, capture point, canopy-vegetated, waste tire, Ae aegypti, larval habitat, unmixed, spectral, signature radiance for identifying, un-resampled, hyper productive, seasonal, breeding sites in a stochastic iterative interpolation. For example, vertical, spectral, real-time, UAV captured, reflectance covariates in an ArcGIS or object-based classifier (ENVI), may reveal definite, interpolative, signature trends that exist between global and directional, sub-meter resolution, LULC reflectance, seasonal leaf traits and this distinction may dictate the nature of of real-time, imaged, capture point, Ae aegypti, wavelength, alternativeness and interrogatability. Such tactics within a drone real-time platform may allow categorizing geo-Spectro temporal, resampled,

RGB frequencies seasonal time frame for optimally geolocating unknown, un-resampled, sub-county abatement, eco-dereferenceable, potential, super breeder foci. Understanding the vertical pattern of leaf traits across plant canopies provide critical information on plant physiology, ecosystem functioning and structure and vegetation response to climate change [16]. However, the impact of vertical canopy position on unmixed, leaf spectral properties and subsequently leaf traits across the entire spectrum for an eco-dereferenceable, sub-county abatement, potential, seasonal, super breeder, waste tire, Ae aegypti, larval habitat is poorly understood. Real-time, UAV, dashboard, optical properties may track variability in leaf traits across, a waste tire, Ae aegypti, eco-georeferenced, capture point, and generate a vertical canopy profile using Partial Least Square Discriminatory Analysis (PLS-DA) in a real-time, UAV dashboard, ArcGIS module. In so doing, leaf spectral measurements together with leaf traits (nitrogen, carbon, chlorophyll, equivalent water thickness and specific leaf area) may be studied at multiple, seasonal, vertical, canopy positions along the plant stem: lower, middle and upper. Observing, real-time, mappable UAV captured, foliar nitrogen (N), chlorophyll (Cab), carbon (C), and equivalent water thickness (EWT) may reveal, higher concentrations in the upper canopy leaves compared with lower shaded leaves in a potential, seasonal, eco-dereferenceable, hyper productive, *Ae. aegypti,* waste tire, capture point, larval habitat, sub-county abatement foci. Plants exhibit higher nutrient stoichiometry in the upper illuminated leaves that receive higher photon flux density compared to lower canopy shaded leaves [17].

Commercial platforms often focus on ease-of-use and broad coverage of image processing, software tasks (e.g., unmixing in homogeneously canopied, LULC, leaf structures) which may reveal distinctive, real-time, signature, frequency variations in absorption and reflection of solar radiation in eco-dereferenceable, potential, seasonal, county abatement, inhomogeneous, super breeder foci, plant canopy. A probabilistic, spectral, mixture ArcGIS model, may be developed that utilizes bundles of the field, spectral, reflectance, real-time, UAV measurements (e.g., eigen decomposed, waste tire, Ae aegypti, larval habitat, urban, residential, iteratively interpolative wavelengths) within a dashboard to estimate sub-pixel LULC cover of immature super breeder, habitat canopies, exposed to non-photosynthetic vegetation and soils in a sub-county abatement, epi-entomological, intervention, study site. The method may prove highly useful for Spectro temporally quantitating, declassifiable, grid-ratifiable, LULC, canopy cover fractions in eco-dereferenceable, seasonal, hyper productive, oviposition, sub-county abatement, waste tire geolocations (e.g., urban parklands), in real time. The information derived from this approach may allow real-time tracking seasonal canopy LULC transitions that influence immature productivity in seasonal, super breeder, sub-county abatement, Ae aegypti, waste tire, capture points, employing iteratively krig eable, uncoalesced, LULC signature, canopy cover, radiance, fractional data (i.e., sub-meter resolution, unmixed NIR frequencies) derived from UAV observations which may be highly and inversely correlated with field-based, capture point, canopy gap fractions. To minimize soil brightness influences from spectral vegetation indices involves conducting geographic transformations whereby the origin of reflectance spectra is plotted in NIR-red wavelength space for quantitating first-order soil-vegetation interactions and differential red and NIR flux extinction through vegetated canopies [18].

 Real-time, Aviagen spectroscopy may provide a cost-effective and practical means to monitor potential, seasonal, super breeder, Ae aegypti, waste tire, larval habitats in sub-county abatement ecosystems. Real-time, drone sensors may provide comprehensive, grid-stratfiable, real time, LULC, spectral, seasonal information that may provide a cost effective method to estimate foliar biochemistry, quantify plant biophysical properties, identify plant species and assess plant physiological status over space and time, in an epi-entomological, intervention, sub-county abatement, study site, eco-georeferenced, capture point for identifying irrigable, spectral, signatures of partially canopied, prolific, capture point, waste tire, Ae aegypti, larval habitats. Basically, two approaches (i.e., empirical (statistical) and physical models (radiative transfer models-RTM)) are often employed to link spectral signatures and field measured leaf traits (Jensen 2005). Empirical approaches may explore parametric and non-parametric statistical relationships between spectral data or feature attributes and leaf traits of a sub-county, abatement, resampled, potential, waste tire, Ae aegypti, prolific, seasonal, larval habitat, capture point. Real-time, UAV, biophysical, unmixed, LULC signature models on the other hand, may rigorously simulate light absorption and scattering inside capture point, vegetation canopies accounting for leaf traits composition, unmixed, canopy, structural properties and soil background based on radiation transfer theory for obesifying interrogatability (e.g., denoising real-time, regressed heteroskedastic frequencies) of eigen decomposed datasets of wavelength, RGB, sub-meter resolution, unmixed, spectral, waste tire, *Ae aegypti,* LULC signatures in a UAV dashboard ArcGIS module.

The physical basis of most solutions for many problems of radiation transfer in both nature studies and engineering applications is the notion of radiation transfer in an absorbing and scattering medium as some macroscopic process, which can be described by a phenomenological transfer theory and radiative transfer equation for quantitating spectral radiation intensity. It is of great importance that the problems, for which the radiation transfer theory can be applied, are quite numerous and contain the thermal radiation of various participating media (Jensen 2005). In the topic of the Radiation Area, remote senses employ the following main assumptions concerning a medium properties and radiative transfer:1)The radiation propagation is more rapid than any change of physical parameters, therefore the radiation intensity field is quasi-steady;2) The radiative properties on the medium do not depend directly on the radiation intensity, but they vary only with temperature;3) The wave polarization can be ignored in radiative transfer calculations;and4)the radiation scattering is not accompanied by any frequency variation .It may be of interest to remember the history of developing the radiation transfer theory including the analytical and computational methods. [19] The astrophysics, particularly the study of star photospheres, was the first branch of science which initiates the theoretical foundations and analytical methods of the radiation transfer theory in the beginning of the 20th century. One can read about it in classic books by Chandrasekhar (1960) and Sobole (1969).

Spectroscopic real-time UAV approaches for studying plant traits may reveal real-time spectra-trait relationships such as that mature, sunlit leaves at the top of canopy of a potential, seasonal, super breeder, waste tire, Ae aegypti, waste tire, larval habitat, county abatement, resampled, capture point, with information-content of the NIR bands. The implicit assumption currently is that variability in leaf traits content and leaf spectral properties within a waste tire, county abatement, resampled, Ae aegypti, potential, super breeder, larval habitat, eco-dereferenceable, capture point, and other vector arthropod species, discontinuous seasonal, LULC canopy are very small and consequently, top of canopy foliar samples are representative of the canopy. To this end, the vertical heterogeneity in leaf traits across the canopy in these vector arthropod breeding sites is often not accounted for in most predictive, risk modelling approaches. The distribution of leaf traits within vegetation canopies of seasonal, super breeder, waste tire, Ae aegypti, larval habitats may be complex and may vary across the canopy vertical profiles especially in resource constrained county abatement ecosystems]. [20] reconstructed the vertical pulse power distribution returned from a commercial small footprint discrete pulse airborne laser terrain mapper within a mixed forest landscape. By modifying a Beer-Lambert approach, the authors related the ratio of ground return power/total return power to the canopy gap fraction (P) as derived from digital hemispherical photography (DHP). The results were compared to the commonly cited ground-to-total returns ratio. Canopy gap LULC, fractionalized data were collected on five separate occasions from April to October of 2006 and analyzed using standard DHP procedures. Five airborne lidar datasets were collected during dry conditions coincident with DHP, and all acquisitions were performed using the same sensor and survey configuration. It was found that for the mixed wood environment studied, a lidar intensity-based power distribution ratio provides a higher correlation with DHP gap fraction ($r^2 = 0.92$) than does the often-used ground-to-total return ratio approach ($r^2 = 0.86$). Moreover, if the intensity power distribution ratio is modified to account for secondary return two-way pulse transmission losses within the canopy, the model required no calibration and provided a 1:1 estimate of the overhead (solar zenith) gap fraction.

The effects of off-nadir viewing and atmospheric constituents, coupled with the need to measure changing surface conditions, emphasize the need for multitemporal, real-time, reflected UAV, interpolative, signature, radiation measurements of potential, seasonal, super breeder, county abatement, eco-dereferenceable, Ae aegypti, waste tire, larval production to be estimated. Cartographic extraction of potential, super breeder, Ae aegypti, larval habitats from real-time, UAV imagery with the ENVI Feature Extraction Module (ENVI FX) for example, may geospatially classify spectral, and texture characteristics of unmixed, seasonal, leaf canopies of prolific, waste tire, breeding sites in real time. In doing so, the leaf properties that determine the radiation-interception, LULC signature, capture point, wavelength characteristics of eco-dereferenceable, discontinuous, plant canopies of waste tire, Ae aegypti, larval habitats may be directly linked to photosynthesis, stomatal resistance and evapotranspiration which may be inferred from the unmixed, real-time, UAV, RBG eco-endmember, frequencies (I.e, reflected solar energy).

Photosynthesis in terrestrial vegetation occurs in chloroplast organelles, which are largely contained within plant leaves [21]. The visible/near IR reflectance properties of leaves from several Culex returns and Culex pippin. habitat species were studied to determine whether county abatement, resampled, grid-stratified. reclassified, LULC, areas of high and low, larval abundance in an urban environment, based on fixed oviposition surveillance sites, corresponded to remotely sensed, signature, canopy data. (e.g., super breeder, immature habitat, canopy, chlorophyll content). Culex returns and Culex pippin are important vectors for arthropod borne viral infections affecting the health of humans, domestic and wild animals. They transmit diseases like West Nile fever, St. Louis encephalitis, Japanese encephalitis, Western equine encephalitis, and Rift Valley fever [CDC]. An LULC classification, based on Landsat-7 Enhanced Thematic Mapper Plus (ETM+) data acquired and Landsat-5 TM data, were compared to the abundance of Culex egg rafts in Urbana-Champaign, East-Central Illinois by Jaco et al. [22] The authors performed a maximum likelihood, unsupervised signature classification and generated three land cover classifications: urban residential, ago-pasturelands and water. Ground coordinates of the Culex surveillance sites were overlaid onto LULC maps with 10 m2 grid cells in ArcMap. The grid was stratified based on levels of drainage: 0 = poorly drained and 1 = well-drained. The most frequent LULC category was maintained urban. The egg raft rate was significantly higher in urban LULC habitats. Grid stratification of the urban land cover employing the Quick Bird visible and NIR data revealed that high-density canopy coverage was most frequently associated with high Culex abundance in the oviposition traps.

Furthermore, *Cx. restuans* showed a higher sensitivity to chlorophyll content with a reflectance near 710nm wavelength, than reflectance near 550nm of Cx. pipien, capture point, larval habitats which was associated with *Cx. restuans*. The NIR band was the least sensitivity to chlorophyll content which was located at 850nm. The use of Red (R)710nm as the sensitive band and R850 nm as the insensitive band, increased the correlation of the reflectance indices to chlorophyll content in both Culex species habitats. Amongst several reflectance indices tested, the ratio (R850-R710)/(R850-R680) performed best and was proposed by the authors as a new index for the estimation of chlorophyll content in potential, seasonal, super breeder, eco-georeferenced, Cx. pipiens and Cx. restuans, aquatic, larval habitats. This new index was sensitive to the effects of leaf scattering on reflectance and related strongly to the variation in reflectance caused by chlorophyll absorption in the immature, Cx. pipiens and Cx. restuans, larval habitat, county abatement, LULC, signature, capture points.

The main cause of scattering within canopy leaves is refractive-reflective scattering, which occurs as a consequence of the refractive-index differences between intercellular air spaces and hydrated cells and the irregular facets of the exteriors of cells [23,24]. As incident solar radiation enters the canopy leaf of a, real-time, UAV, imaged, potential, seasonal, super breeder, county abatement, geosamplde, waste tire, Ae aegypti, capture point, LULC region and penetrates downward, it would become increasingly scattered due to internal cellular, discon-

tinuously, canopied reflections. ENVI FX in a real-time, UAV dashboard, object-based classifier. may reveal unmixed, iteratively interpolative, inhomogeneous, canopied, attribute, feature descriptors (e.g., bidirectional single-scattering reflectance. leaf azimuth) of sub-meter resolution, vegetation-related, waste tire, capture point, LULC signatures, which may subsequently render air-cell, refractive-index differences and other interpolatable datasets. Hence such features as canopy architecture, leaf angle distribution, ground cover fraction, leaf morphology, vegetation spatial heterogeneity, and shadows of the capture point may be analyzed in real-time by the UAV platform Likewise, particle size distribution and canopy, surface-height variation (roughness) of the most important, in homogeneously canopied, LULC, waste tire, Ae aegypti, county abatement, capture point, signature, interpolative, epi-entomological factors influencing the scattering properties of the larval habitat may be quantitated in real time.

A decrease in UAV reflectance with increasing size of "roughness elements," with gridded, sub-meter resolution, LULC signature aggregates may contain many interaggregate spaces and shade-canopied surfaces in the real-time captured, potential, seasonal, super breeder, county abatement, geosampled, larval habitats. Model fitting methods may be employable in an object-based, UAV dashboard classifier. These real-time, signature models may categorize uncoalesced, inhomogenously canopied, LULC, Ae aegypti, capture point, eco-georeferenceable, geo-classfiable unmixed, sub-pixel, feature attributes in real-time to find inliers and outlier RGB frequencies for optimally predictively, describing geolocations of unfamiliar, prolific, waste tire foci in an epi-entomological, sub-county abatement, intervention, study site.

 For example, a well-known object-based classifier, is the random sample consensus (RANSAC) method. A comprehensive performance evaluation of the RANSAC family was performed by Choi et al. [25] The authors revealed an accuracy and robustness improvement for maximum likelihood estimation SAC (MLESAC). RANSAC may be employable in a real time, UAV, dashboard ENVI classifier for identifying potential, eco-georeferenceable, seasonal, super breeder, Ae aegypti, larval habitat, waste tire, iterative, interpolative, grid-stratifiable, LULC signatures for a county abatement, epi-entomological, intervention, study site. Further, these unmixed, sub-meters resolution, capture point, spectral signatures may identify unknown hyper productive, seasonal foci in a stochastic or deterministic iterative interpolator in a real-time, UAV, ArcGIS, frequency module when employed as a dependent/respose variable.

Another classical model fitting method class in a real-time ENVI classifer uses the Hough transform [26]. The purpose of the technique is to find imperfect instances of unmixed, geospatial, eco-georeferenceable, LULC signature objects within a certain class of shapes. This procedure is carried out in a parameter space, from which object candidates (e.g., potential seasonal, super breeder, waste tire, Ae aegypti, larval habitat, county abatement, eco-georeferenceable, capture points signatures) are obtained as local maxima in a so-called accumulator space that is explicitly constructed by the algorithm for computing the Hough transform. Although numerous, variants, rendered from progressive, probabilistic, Hough transforms are faster computationally. they are often employed as straight-line detectors and, thus, are preferred only for linear structure detection. Hence these transforms may not reveal inhomogeneously canopied, prolific capture point, unmixed, canopy, plant traits, (i.e. leaf chlorophyll content, water content leaf area index), geo-spectrotemrpoally extractable from a seasonal, super breeder, eco-geo-referenceable, waste tire, Ae aegypti, larval habitat, capture point geosampled in an epi-entomological, intervention, sub-county abatement, study site.

Optimally decomposable, non-linear, Ae aegypti, waste tire, potential, seasonal, super breeder foci, unmixed, RGB eco-endmembers may be modified in real time, at the landscape level, by optical-geometric algorithmic interactions in a UAV dashboard, whereby incident radiation is scattered in accordance with the three-dimensional (3-D) structure of a geo classified, county abatement LULC. Hence a real-time, UAV, ArcGIS vegetation canopy, landscape structural model may describe the 3-D arrangement of leaves within an eco-geoerferenced, potential, seasonal, super breeder, waste tire, county abatement, Ae aegypti, larval habitat which may include such attributes as canopy architecture, leaf angle distribution, ground cover fraction, leaf morphology, vegetation spatial heterogeneity, and shadows. Likewise, particle size distribution and surface-height variation (roughness) influencing the scattering properties of soils may be eco-cartographically identifiable in a real-time, UAV, ENVI platform. Canopy foliar traits—in particular, leaf chemistry—underpin functional biodiversity, which in turn may provide important information about ecological processes including biogeochemical cycles, biosphere–atmosphere carbon exchange, evolution, and community assembly. Object based classifiers (i.e., RANSAC grid methods) may aid the identification of eco-georeferenceable, seasonal, LULC signature objects having various non-homogeneous shapes (e.g., capture point, super breeder, waste tire, eco-georeferenecable, Ae aegypti, larval habitat, seasonal, canopy understory reflectance) while simultaneously quantitating unmixed, properties of plant canopies [e.g. incident Photosynthetically Active Radiation (PAR)]

Incident Photosynthetically Active Radiation (PAR) is an important parameter for terrestrial ecosystem, forecast-oriented, signature, vulnerability, sub-county abatement, signature models such as sub-meter resolution, LULC, waste tire, Ae aegypti, spectral, sub-pixel paradigms for remotely optimally, targeting potential, seasonal, super breeder, unknown foci. Presently, deriving PAR employing remotely sensed data is the only practical approach to meet the needs for large scale, real-time, epi-entomological, county abatement, signature modeling of real-time, UAV, imaged, partially canopied, waste tire, Ae aegypti, larval habitats. PAR is absorbed strongly within green leaves by the plant pigments present. Most of this absorption is due to chlorophyll a, chlorophyll b, and the carotenoids (Salisbury and Ross 1969). [27] The absorption of incident solar radiation by plant pigments and liquid water may be robustly, eco-cartographically described in a real-time, UAV, dashboard, ENVI platform. The usefulness of the currently available PAR products for aiding in optimally identifying unknown, county abatement, poten-

tial, seasonal, super breeder, eco-georeferenceable foci is constricted by their limited spatial and temporal resolution. [28]. The applicability of the existing algorithms for deriving PAR employing remotely sensed, unmixed, LULC signature data are limited by their requirements for external atmospheric information [29].

Fortunately, the relative proportion of the plant pigment, seasonal variation may be also determined in a real-time, UAV dashboard, ENVI module. In doing so, real-time, signature sub-meter resolution, grid-stratifiable, unmixed, decomposable, LULC canopy information (e.g., plant pigments present, projected green-leaf density) of seasonal, vegetation canopies of hyper productive, waste tire, eco-georeferenceable, Ae aegypti, larval habitat, capture points in an epi-entomological, county abatement, intervention study site may be eco-cartographically described, from unmixed real-time, iteratively interpolatable, geosampled, sub-pixel, LULC, signature datasets. Object-based UAV-PAR algorithms may differ from existing satellite algorithms in that the real time algorithms may derive signature surface properties and atmospheric optical properties employing time-series of at-sensor radiance without external atmospheric information. A new UAV PAR algorithm may be developed for sub-meter resolution, signature, visible band data in a real-time platform. The validity of the algorithm's underpinning operational iterative interpolativeness may be examined and associated errors (spatial multicollinearity, zero autocovariance) may be analyzed in light of their impact on PAR estimation accuracy for parsimoniously imaging, in homogeneously canopied, eco-georeferenceable, seasonal, potential, super breeder, waste tire, county abatement, Ae aegypti, larval habitat, capture point, LULC, unmixed signatures, in a drone real-time dashboard. In addition, the scaling of the real-time, derived instantaneous PAR to daily PAR may be addressed for a waste tire, capture point, sub-meter resolution, interpolative, LULC signature. The prognosticative, real time, UAV algorithm may be extended by inclusion of the bi-directional reflectance distribution function for optimally tabulating portioned, total LULC, surface reflectance wavelengths. In so doing, the real-time algorithm could exclude cloud-shadowed pixels when searching for iteratively interpolatable, potential, seasonal, super breeder, eco-georeferenceable, *Ae. aegypti*, waste tire, larval habitat, RGB frequencies in the UAV dashboard. In so doing, the topographic impact on PAR on a waste tire, capture point, discontinuously canopied, unmixed, parameter, frequency estimator (e.g., foliage height profile) may be also accessed and corrected in real-time for optimal signature interpolation for identifying unknown, seasonal, eco-georfeerenecable, *Ae. aegypti*, prolific, sub-county abatement foci Understanding the effect of vertical heterogeneity on leaf spectral properties in a seasonal, hyper productive county abatement, waste tire foci, may not only offer a promising path in canopy reflectance modeling using multi-layer, radiative transfer, drone models but also such data may have a strong implication on within-canopy sampling and leaf traits upscaling to canopy and subsequently landscape level of real-time LULC signals for identifying unknown prolific Ae aegypti foci.

A real-time, UAV platform may adjust flight campaigns over any willow eddy covariance flux LULC signature sites in an epi-entomological, intervention, county abatement, under different cloudiness levels and solar zenith angles employing varying real-time camera settings. The effects of solar zenith angle upon spectral data have been reported by Duggin [30]. Unfortunately, satellite-based imagery in optical domains cannot provide information on county abatement, land surface during periods of cloud cover. This issue is especially relevant for high latitudes county abatements where overcast days and low solar zenith angles are common. Hence, current remote sensing-based, LULC, canopy models of evapotranspiration or carbon assimilation are biased towards clear sky conditions, lacking important information on biophysical processes under cloudy, county abatement conditions. Real time, UAV, imagery has great potential to monitor and understand surface fluxes especially in discontinuously canopied, and other geoclassifiable, LULC, capture point, eco-georeferenceable, waste tire, potential, seasonal, super breeder, *Ae. aegypti* breeding sites under cloudy conditions. Although multispectral imagery acquired in cloudy, overcast conditions tends to present low brightness and dynamic ranges, and moderate noise levels, clouds should not have much effect on imaging prolific, seasonal, waste tire, eco-georeferenceable, Ae aegypti, immature foci unless an experimenter is flying through them. The FAA requires drones to be flown below 400 feet as well as 500 feet below clouds[(http://time.com/4658997/flydrones/).Radiance, reflectance, and vegetation indices may be validated within a real-time, UAV, aggregated, platform employing ENVI measurements and signal to noise metrics in an ArcGIS module employing, real time mapped eco-georeferenecable, cloudy county abatement geolocations of unknown, potential super breeder, eco-georeferenceable, waste tire, Ae aegypti, larval habitat, capture point foci. Employing a real-time, sub-meter resolution, unmixed, LULC signature, RGB eco-endmember frequencies as a dependent variable in a stochastic or deterministic, iterative interpolator may reveal, unknown, county abatement geolocations of seasonal, hyper productive, waste tire, Ae aegypti, capture points. Results may indicate that the spectral gains and camera settings can be tuned to allow higher signal to noise ratio for optimizing the UAV sensor sensitivity for optimally remotely targeting and predicting, intermittently clouded, unknown, potential, seasonal, super breeder, eco-georeferenceable, *Ae. aegypti*, waste, tire, county abatement, capture points. A real-time UAV platform may maximize the image radiometric resolution and prevent sensor saturation for each channel. In so doing, UAV dashboard image software may enable robust identification of unknown, seasonal, super breeder, LULC, *Ae. aegypti*, waste tire, capture points based on interpolated RGB frequency values for implementing, seasonal, larval control campaigns (IVM) in county abatement epi-entomological, intervention, study sites using optical cameras for low zenith angles and/or cloudy conditions.

Relatively large differentials may occur in spectral absorption by canopy layers in a potential, seasonal, super breeder, waste tire, LULC, county abatement, Ae aegypti larval habitat, capture point, especially in the photosynthetically active regions, as a function of solar zenith angle. In addition, the proportion of total global irradiance absorbed by individual layers in a in homogeneously canopied, prolific, sub-meter resolution, capture point signature may vary greatly seasonally as a function of solar zenith angle. Unmixed LULC, topological, spectral reflectance's from inhomogeneous, geo classified, grid-stratifiable, Ae aegypti, capture point, larval habitat, plant canopies at all sun angles may

tend to a minimum near nadir which may subsequently reveal increasing spectral reflectance with increasing off-nadir viewing for all azimuth directions for optimally mapping unknown, prolific, LULC larval habitats in a county abatement study site based on interpolated, unmixed, visible and NIR sub-meter resolution, waste tire signatures.

Initially, in Jacob et al. [31] a panchromatic, unmixed, grid-stratified, Quick Bird 0.61m, spatial resolution, eco-endmember, frequency, dataset of transmittance, LULC, spectral signatures of a district level, epi-entomological, riceland agro-ecosystem, intervention, study site in Gulu, Uganda was differentiated by visible and NIR wavelength, irradiance. Next, an object-based classification algorithm employed a divergence measure to match mixed pixels to the LULC, derivative spectra in ENVI. The spectrum of a selected pixel was calculated as a linear combination of the unmixed, eco-endmember, spectral frequencies weighted by the area coverage of each LULC within the pixel to determine if the scattering and absorption of electromagnetic radiation was dominated by a single, signature, capture point, RGB, sub-pixel component. A mosaicked signature dataset was employed to manage, display, serve, and distribute, raster, time series, intermittently canopied, YF virus, mosquito, vector, *Ae. aegypti*, oviposition, capture point, larval, habitat geolocations along the rice land, peripheral, forest-canopied, interface corridor. A new mosaicked dataset was created as an empty container in an ArcGIS module with default properties which was subsequently added to the raster dataset. Thereafter, the YF virus data was eco-cartographically illustratable as fractionalized abundances of non-pixelated, eco-endmember rice land, agro-village, non-homogeneous, LULC, geoclassifiable eco-zones (e.g., sparsely shaded, pre-flooded, densely canopied, post-harvesting paddies) within a supervised classification matrix. Non-normalized, seasonal, geometric, YF, case, distribution data was articulated from various Bayesian perspectives, thereafter. The models took inputs from table file in the sylvatic habitat geodatabase, which subsequently imput information of yearly population and YF cases from 1990 to 2012. Log-likelihood functions were also generated in PROC REG for each geosampled, YF virus, mosquito vector (i.e., *Ae. aegypti*), unmixed, eco-endmember, LULC-specified, visible and NIR, wavelength signature employing a joint log-likelihood function which was exponentially logarithmically quantitated in ENVI. Consequently, the epi-entomological, time series, model forecasts were positively correlated with a relative change in YF cases, where a regression line denoted a pseudo R2 of 0.93. To uncorrelated, noisy, oviposition, LULC, signature, wavelength residuals for deriving meaningful, unbiased, non-linear, regressable, interpolative, explanatory predictors in the YF model, a sequential iterative algorithm was employed in AUTOREG. A second-order, pertubation algorithm investigated the error and sensivity of the forecasts. Specified orthogonal matrices updated a subset of unmixed, RGB, eco-endmember, grid-stratifiable, synthetic functions and their spatial filtered renderings in SAS. A log-determinant Jacobian term eigendecomposed the LULC, epi-entomological, capture point, eco-georeferenceable, larval habitat data which ensured that the integral of the YF model's likelihood function equaled 1 when integrated over the densities of all unknown, signature, unmixed, frequency estimators. The model assumption that the post, unspecified, marginally monotone, semi-parametrically, supplemental, sub-meter resolution, wavelength, irradiance distributions were multivariate Gaussian was violated.

Hence, in Jacob et al. [31], generalized autoregressive moving average (GARMA) models were extended to autoregressive, integrated, moving average, (SARIMA) models in PROC ARIMA for optimally conducting, observation-driven, sub-pixel, RGB modelling of the non-Gaussian, non-stationary, YF-related, time series, unmixed, LULC signatures. A negative binomial model, with a non-homogeneous mean was compared to that of a Bayesian Gaussian fit. The posterior distributions appeared to be platykurtic [i.e., frequency distribution curve having a wide, rather flat distribution about the mode]. The logarithm of the posterior density was calculable for the endogenous, seasonal, geometric, explanatorial, unmixed, frequency, spectral regressors. Geospatial outliers were teased out in the residual plots. The normalized modes were validated employing a Monte Carlo simulation in PROC MCMC. The authors of Jacob et al. (2016) specified a likelihood function for the LULC signatures and a prior distribution for the larval habitat, YF, parameter estimators. The authors fitted hierarchical models, to specify hyperprior distributions, random effects and their prior distributions. PROC MCMC obtained samples from the corresponding posterior distributions, produced summary and diagnostic statistics, and saved the posterior samples in an output, LULC, signature, time series, unmixed dataset that was employed for further analysis. Data may be analyzed with any likelihood, prior, or hyperprior with PROC MCMC, as long as these functions can be programmed by using the SAS DATA step functions (www.sas.com).

Subsequently, in Jacob et al. [31], the unmixed, time series, YF, LULC, signature data was forecasted in C++ employing a stochastic-dynamic, random, weighted matrix. Homoscedastic residuals were cross-tabulated via various hierarchies of continuous and categorical, finite, seasonal, transitional, agro-irrigated, unmixed, eigen decomposable, LULC, signature, sub-meter resolution, eco-endmember frequencies. The YF signature interpolation model included, meteorological, eco-endmember values. The final model tabulation revealed prognosticated population growth and number of case occurrences to 2020 in C++ for the epi-entomological, intervention, study site. Furthermore, optimal, explicative, spectral, reflectance, geo-spectro temporal, endogenous descriptors of seasonal, hyper productive, sylvatic, eco-georeferenceable, Ae aegypti, newly transitioned, in homogeneously forest, canopied, to agro-irrigated, LULC abundance was eco-cartographically elucidated for implementing larval control strategies in the expanding agro-village, agro-irrigated, Ugandan, rice land, agr-irrigated complex due to anthropogenic pressure and for signature forecasting YF case distributions.

Eco-georeferenceable, potential, seasonal, super breeder, county abatement, waste tire, *Ae. aegypti*, larval habitat, county abatement, capture points may reveal that minimum spectral reflectance shifted slightly off-nadir in the forward-scattering direction in an iterative interpolative, sub-meter resolution, LULC, UAV real-time, captured, signature, unmixed RGB, eco-endmember, optimaizable dataset. Real-time,

fractionalized, UAV, reflectance synthesized from eco-georeferenceable, potential, seasonal, super breeder, waste tire, *Ae. aegypti*, larval habitat emittance may reveal the flux measured at off-nadir angles may be expressible relative to a fixed geoclassified, grid-stratifiable, LULC signature estimate (i.e., RGB eco-endmember frequency) in an ArcGIS module based on mapped county abatement, epi-entomological, intervention, study site geolocation on an imaginary sphere defined by the Instantaneous Field of View) (IFOV) at a radius, h (the height at nadir). While the defined cross-sectional area may be fixed, the associated LULC area or its signature projection onto the horizontal plane of the canopy surface may increase by a factor of cos(0v)-•. Reflected energy from a potential, seasonal, super breeder, eco-georeferenced, Ae aegypti, waste tire, larval habitat geosampled in a county abatement, epi-entomological, intervention, study site may be log-transformed as a function of O_v in a real-time UAV, platform object-based classifier for determining reflectance fraction from unknown, prolific, waste tire, breeding site canopies. The reflected, capture point, LULC signature, canopy fraction may be decomposable in the real-time dashboard by simple normalization of the canopy radiance measured at any O_v by a factor of cos (Or).In so doing the real-time, object-based classifier may standardize the drone sensed, waste tire, optimal, capture point, pixel size to that of the nadir view, hence, repressing the radiance on a standard surface area basis, rather than a fixed area on an imaginary sphere. In any O_v this is calculable as the ratio of the cos (0_v)-adjusted canopy radiance, LULC signature divided by the irradiance (determined in the same manner as for the capture point reflectance). The probability of gaps generally decreases as the off-nadir O_v increases.

Warner TA, et al. [32] investigated three simple normalization procedures for suppressing the eVects of solar heating and topography in daytime thermal data. The first method was the hyperspherical direction cosine (HSDC) transformation, which separated the pixel vector into an illumination/albedo component and a spectral component. The second method, a model correction, was based on the assumption that, once an elevation correction using the normal lapse rate had been applied, temperatures were proportional to the instantaneous solar heating as measured by the cosine of the solar illumination incidence angle. The third method was a statistic-empirical correction. These three normalization methods were applied to a test site in the Humboldt Range, Pershing County, Nevada, using Landsat Thematic Mapper data. It was found that geological patterns were much clearer in the normalized data than in the original temperature information. The HSDC correction brought out lithological signature differences which helped discriminate between iteratively, interpolatable, unknown, un-geosampled, gravels and spectrally similar sedimentary rocks with high classification accuracy. The model correction appeared to inadequately compensate for the cool temperatures found at high elevations. The rock contacts were relatively clear, and the classification. The statistic-empirical classification resulted in improved elevation correction.

The relative angles between leaf and light source and viewing directions may vary in a real-time UAV, dashboard ArcMap county abatement, waste tire, Ae aegypti, super breeder, capture point, LULC, frequency, signature model resulting in a complex pattern of reflected and transmitted radiation from a canopy so that reflectance can seasonally differ due to canopy geometry. Although vegetation indices formulated from a real-time UAV sensor may be developed to extract the plant signal only of a, waste tire, Ae aegypti, larval habitat, county abatement, potential, seasonal, super breeder foci, the soil background, moisture condition, solar zenith angle, view angle, as well as the atmosphere may alter the index values in complex ways. For example, nadir-viewed BRF values were 20% higher from a planophile wheat canopy than from an erectophile wheat canopy, although LAI and leaf optical properties were similar in Jackson and Pinter [33]. Lower reflectance from the erectophile canopy was attributed to scattering of radiation into the lower leaf layers by vertical leaves, whereas higher reflectance from the planophile canopy was attributed to greater reflection from horizontal leaves in the upper part of the canopy.

For sparse seasonal, canopy vegetated, larval habitat canopies, such as waste tire, Ae aegypti, potential, seasonal, super breeder, larval habitats geosampled in an epi-entomological, county abatement, intervention, study site, the anisotropic scattering properties of the soil surrounding the foci may be significantly influenced by the directional spectral reflectance of the capture point. In all, LULC, signature images of eco-georerenceable waste tire, capture point, inhomogeneous canopies, the spectral-reflectance distributions may tend to be azimuthally asymmetric. Solar radiative transfer processed through a real-time, UAV, ArcGIS module of atmosphere and plant canopy of an imaged, potential, seasonal, super breeder, waste tire, eco-georeferenced, Ae aegypti, larval habitat, may be modeled as a multiple-scattering problem through a layered medium of random scatterers. The radiative transfer equation may be thereafter solved by the discrete-ordinates finite-element method in the real-time, UAV, ENVI classifier.

The discrete-ordinates method has been classic in radiative transfer since Chandrasekhar introduced it in his book on radiative transfer. [34]. Although these original formulations were mainly concerned with astrophysical applications, they were also quickly applied to many meteorological problems employing various approximations such as the Eddington's approximation by Shettle & Weinman [35]. or the two-stream approximation by Samuelson [36], Liou [37] He performed a comprehensive evaluation of the discrete-ordinates method by comparing numerical results with those from other rigorous methods in applications to cloudy and hazy atmospheres. Although Liou [37] successfully demonstrated that high-accuracy results for the transmitted and reflected intensity and flux could be achieved with a fairly low-order discrete-ordinates method, this computational technique has not been found widespread in vector, entomological, remote sensing, research to date for determining unknown, geolocations of prolific capture point foci in a county abatement, epi-entomological, intervention study site. For solar and IR radiative transfer problems in the atmosphere, computations are usually performed with semiempirical methods for broad-based overview calculations and with the spherical harmonic's method for high-resolution detail analyses as developed by Dave [38].

Methods, like the doubling method, as studied by Wiscombe [39] and the method of successive orders of scattering, as described by Hansen & Travis [40] are also developed to a high degree of sophistication and computer effectiveness. However, computer codes based on these methods are mostly limited to 1-D slab models of the atmosphere.

In contrast, in the field of radiation shielding against neutron and gamma radiation and in reactor physics applications, the discrete-ordinates method has become the most widely employed computational technique for solution of the radiative transfer (here also called transport) equation. Efficient general purpose computer codes based on the discrete-ordinates method are available today to compute radiation distributions in 1-D, 2-D, and even 3-D geometries of vector entomological, seasonal, hyerproductive, eco-georeferenceable, breeding sute foci (e.g., real-time UAV geosampled, eco-georeferenceable, potential, super breeder, waste tire, Ae aegypti, larval habitats) in an epi-entomological, county abatement, intervention, study site. Some of these modern neutron transport codes have only recently been applied to atmospheric radiative transfer equation in ArcGIS modules. Demonstrating the value of these modern discrete-ordinates finite-element methods to a broad range of climatology and UAV, real-time, remote sensing, epi-entomological applications may distinguish noiseless, regressable covariates that may target unknown, potential, eco-georeferenceable, potential, super breeder, county abatement, waste tire, Ae aegypti, LULC, capture point foci. Analytic expressions may be derived that allow the calculation of scattering and absorption cross sections for any plant canopy layer from measurable unmixed, capture point, grid-stratifiable sub-meter resolution, LULC, signature parameters such as the leaf angle distribution, and individual leaf reflectance and or transmittance signature data. An expression for a canopy scattering phase function may be also rendered in real-time from the discrete-ordinates finite-element. Iteratively interpolated, unmixed, sub-meter resolution, signature, RGB, eco-endmember, frequency forecasts in a UAV dashboard, ArcGIS platform may reveal robust LULC, spectral, reflectance measurements directly above a un-geosampled, partially canopied, eco-georeferenceable, prolific, waste tire, *Ae. aegypti*, larval habitat, county abatement, capture points. A real-time, signature, frequency, sensitivity analysis with a coupled atmosphere/canopy, real-time, UAV model may temporally quantitate how waste tire spectral radiances are affected by increased atmospheric aerosols, by varying leaf area index, by anisotropic leaf scattering, or by non-Lambertian soil boundary conditions in a county abatement, epi-entomological, intervention, study site.

Nadir reflectance of vegetative canopies is a function of solar zenith angle (0s) and will vary with wavelength and soil substrate. Both factors must be considered before diurnal trends can be interpreted in an iteratively interpolative, real-time UAV, Ae aegypti, waste tire, larval habitat, signature, frequency model for remotely, optimally, targeting potential, seasonal, super breeder, eco-georeferenceable, county abatement, unknown, un-geosampled foci [41]. Soil surface reflectance is also non-Lambertian and is a function of wavelength, illumination and viewing directions, soil moisture content, particle size, organic matter content, soil mineralogy, and surface roughness[42] Hence, denoised, soil spectral, sub-meter resolution, LULC, signature, unmixed, RGB, eco-endmember frequency, iterative interpolative, radiance datasets in a real-time UAV platform may reveal a strong back scattering characteristic that may dominate observed reflectance distributions which may be quantizable by dashboard, ENVI, object-based classifiers [e.g., Spectral Angle Mapper(SAM)].In so doing, unbiased mapping variables may eb able to eco-cartographically delineate, infrequently seasonally, canopied, unknown, potential, super breeder, capture point waste tire, Ae aegpti, larval habitat, seasonal foci under lower solar zenith angles, in real time.

Spectral Angle Mapper is a physically-based spectral classification that uses an n-D angle to match pixels to reference spectra. The algorithm determines the spectral similarity between two spectra by calculating the angle between the spectra and treating them as vectors in a space with dimensionality equal to the number of bands. This technique, when employed on calibrated, unmixed, sub-meter resolution, grid-stratifiable, geoclassifiable, LULC signature, reflectance data (e.g., geosampled, county abatement potential, eco-georeferenecable, seasonal, super breeder, waste tire, Ae aegypti, larval habitat, capture points) may be relatively sensitive to illumination and albedo effects. Endmember spectra employed by SAM can come from ASCII files or spectral libraries, or may be extracted them directly from an image (as ROI average spectra) [http://www.harrisgeospatial.com/docs/] Hence, SAM could compare the angle between the unmixed, endmember spectrum of a potential, seasonal, super breeder, waste tire, Ae aegypti, larval habitat, vector and each neighboring capture point, LULC signature, pixel vector in n-D space. Smaller angles represent closer matches to the reference spectrum. Pixels further away than the specified maximum angle threshold in radians would not be classified. SAM classification of the eco-georeferenceable, waste tire, krig eable signature would assume LULC reflectance data only. In radiance data, the error is generally not significant because the origin is still near zero [43].

Measurements of solar reflected radiation from real-time UAVs include varying degrees of atmospheric influence. These measurements may employ unmixed, wavelength radiation to infer eigendecomposable, sub-meter resolution, signature, fractionalized LULC signature estimates (e.g, unmixed, canopy foliar density RGB eco-endmembers frequencies) which may in turn be employable in a real-time ArcGIS or ENVI platform to infer immature, capture point, signature counts (e.g., larval production of unknown, eco-georeferenceable, seasonal, super breeder, county abatement, Ae aegypti, waste tires) in specific, spectral, wavelength regions.

Real-time, UAV, geosampled, illumination coefficient, grid-stratifiable regressively optimizable estimates of primary production may involve the use of the 'greenness' indices. Hence various combinations of visible and NIR radiation may be employable to optimally remotely geolocate seasonal, waste tire, Ae aegypti, eco-georeferenceable, larval habitat, super breeder foci. The relative importance of aerosol scattering and absorption in specific. Canopied. wavelength regions may be vital to noiseless, iterative interpolation of unmixed, UAV geosampled, waste tire RGB eco-endmember frequencies in stochastic interpolators. These indices in a real-time, UAV dashboard may also extract geospa-

tial, eco-georeferenceble, LULC, signature, feature attributes such as, trees, for aiding in planning wayard markings for pre-drone, flight data collections for optimally conducting elucidative, epi-entomological, capture point investigations for optimally, remotely targeting unknown, eco-geo referenceable, seasonal, hyper productive, foci at an, sub-county abatement, intervention, study site. Flight commands require a GPS (to determine where drone is on earth during flight) and an Inertial Measurement Unit (IMU) to help the drone follow the flight plan in a controlled manner (https://www.digitaltrends drones/.com).

Assuming the eco-georeferenceable, prolific, waste tire, county abatement, geo sampled, *Ae. aegypti*, capture point. larval habitat surface has a Lambertian reflectance characteristic, its radiance would be proportional to the cosine of the angle between the solar vector and the surface normal vector in a real-time forecast, vulnerability, UAV, LULC, signature, RGB frequency model. Suppose an experimenter has a real-time, UAV captured, grid-stratified, LULC scene of an epi-entomological, county abatement, intervention, study site region with an eco-geo-referenced, geo sampled, potential, seasonal, super breeder, waste tire, Ae aegypti, larval habitat, consisting of two materials, discontinuously canopied, soil and vegetation, each having a certain within-class variance but no band-to-band correlation. The experimenter may generate reflectance images in the red and NIR spectral regions from random Gaussian distributions for each geo classified, gridded, LULC, signature class in each band. A real, topographic, 3-D, digital elevation model in the UA, ArcGIS module may thereafter be employed to distribute the soil and vegetation, LULC signature pixels equally across the scene.

The influence of terrain geometry on remote sensing measurements has been discussed in detail in Sjoberg & Horn [44] and Pinty et al. [45], including the possibility of reflectance by neighboring capture points (e.g., waste tire, eco-georeferenceable, LULC, Ae aegypti, larval habitat, capture points, spectral elements in county abatement terrain) into the IFOV at a pixel of interest (i.e., homogenous canopy LULC). The real-time, geosampled, UAV, capture point, LULC, signature image, spatial content may result from the product of two geo-Spectro temporally, decomposed, RGB, eco-endmember, wavelength varying terms, the reflectance and the terrain-dependent cosine factor (assuming the down-scattered term is small in the waste tire, Ae aegypti, real time, UAV spectral, forecast, geometric-optical, signature model). Either may be considered to spatially modulate the other. This relationship nay be useful in certain real-time, UAV, ENVI algorithms for image fusion which may unbiasedly allow iterative interpolation of an unmixed eco-georeferenceable dataset of prolific, seasonal, waste tire, Ae aegypti, county abatement, breeding site, LULC signatures for remotely, optimally targeting unknown, potential, seasonal, super breeder, sub-couty abatement foci.

To make the spatialized, waste tire, *Ae aegypti*, potential, seasonal, super breeder, eco-georeferenceable, capture point, LULC signature characteristics more realistic, a soil mask and a complementary vegetation mask may be created in the UAV ArcGIS module. Each drone mask may be filled with the simulated reflectance pixels from the respective, unmixed, sub-county abatement, capture point, LULC, signature classes, and the result may be multiplied by the topographic shaded relief image, to generate surface radiance, which may provide geolocations of unknown, seasonal, hyper productive, waste tires in a real-time stochastic or deterministic iterative interpolator. The in homogenously canopied, soil and vegetation LULC signature components may be composited into a two-band, simulated UAV, ArcGIS scene.

Viewing the NIR-red scattergram of the simulated, real-time, UAV images an experimenter may quantitate uncorrelated distributions in a potential, sub-county abatement, eco-georeferenced, seasonal, super breeder, waste tire, Ae aegypti, larval habitat, LULC signature, decomposed, RGB, eco-endmember frequency dataset. In so doing, strongly correlated capture points along lines passing through the scattergram origin, or zero reflectance may be detected in real-time. When this happens the incident radiation may be reduced by a cosine factor, scaled to the range [0,1] by saturating negative waste tire, frequency values at zero. This topographic modulation has long been recognized as an influence on spectral signatures in remote sensing data. Although no contribution in literature to date has been directed at reducing unmixed, LULC, signature, capture point topographic, reflection effects of discontinuously canopied, eco-georeferenceable, capture points extracted from multispectral, real-time, UAV imagery employing ArcGIS real-time, frequency models, this topographic modulation may decompose imaged, sub-county abatement, geosampled, potential, eco-georeferenceable, seasonal, super breeder, waste tire, Ae aegypti, larval habitat, grid-stratifiable, geoclassifiable, spectrometer data into its spectral constituents.

The real time UAV dashboard may describe the vertical profile of upward, diffuse, radiative flux and the attenuation of the flux, emitted from a potential, super breeder, waste tire, Ae aegypti, larval habitat, county abatement, eco-georeferenced, LULC, capture point, The real-time, UAV, object-based platform may define rescattering reflecting variation fractions of canopy photosynthesis and transpiration resistance of the capture point, which may be linearly dependent upon the one-way penetration of small radiative fluxes emitted from capture point, county abatement, LULCs in an upward direction following interception with canopy leaves in a real-time UAV platform. The platform may also define the fraction of the downward diffuse flux that is intercepted and scattered into the upward hemisphere from the capture point LULC that may be correlated to seasonal larval productivity (e.g., incident, signature, diffuse fluxes in the NIR with a potential, super breeder, waste tire, *Ae aegypti*, geo sampled, sub-county abatement, capture point).Contribution to the upward diffuse flux by the scattering of the direct incident flux intercepted at a specified threshold in a real-time, UAV dashboard, ArcGIS module of an iteratively interpolative, Ae aegypti, waste tire, larval habitat, LULC signature, in homogeneously canopied, sub-meter resolution, RGB signal may correspond to endoegneous descriptors of scattered diffuse flux which may be assigned to any number of wavelength directions. Nonetheless, a real-time UAV direct stream, unmixed,

signature dataset of, RGB eco-endmember frequencies in real time, may reveal unknown, eco-geo referenecable, geolocations of potential, super breeder, Ae aegypti, waste tire, larval habitat, seasonal, county abatement foci.

The inherent flexibility of ENVI FX would let experimenters (i.e., county abatement, vector entomologists, research collaborators) modify potential, super breeder, waste tire, larval habitat, Ae aegypti, capture point, LULC signature, RGB, eco-endmember, seasonal, hemispherically integrated reflectance at any stage of the unmixing process. Designed specifically for ArcGIS users and fully integrated with ESRI's ArcGIS® software, ENVI FX includes unique step-by-step workflows for previously complex image analysis tasks(www.harrisgeospatial.com). Such properties of object-based, real time, LULC signature, image analyses may allow experimenters to separate distinct, unmixed, larval habitat, vector arthropod, signature, cover types based on their response fluxes for a given real-time, UAV detected sub-meter resolution, partitioned wavelength. The response characteristics of a certain LULC, cover type, county abatement, agro-irrigated, pastureland, or urban residential, geosampled geolocations, for example, may be plotted against visible wavelength intervals or NIR, diffuse, attenuation coefficients extracted from interpolative, spectral signatures in a real-time, drone dashboard, object-based (ENVI) platform. This may be important for optimally, re-motely, targeting, potential, seasonal, super breeder, eco-georeferenceable, waste tire, LULC, Ae aegypti, capture points in a county abatement, epi-entomological, study site since suspended sediment (S) in the larval habitat may be easily confused with shallow (but clear) water, since these two phenomena appear very similar [46].

Water and vegetation, geo classified, grid-stratified LULCs may reflect somewhat similarly in the visible wavelengths but may be separable in the infrared (IR) in a seasonal, waste tire, county abatement, unmixed, LULC RGB, eco-endmember, sub-meter resolution, frequency UAV, real-time, signature model. The topography of the water surface (rough, smooth, LULC, floating materials, etc.) in an eco-geo referenceable, potential, seasonal, geo sampled, vector entomological, arthropod, waste tire, larval habitat can lead to complications for predictive interpre-tations of unknown, potential, super breeder, county abatement foci geolocations due to specular reflection and other influences on color and brightness emitted from the breeding sites [47]. Spectral response will vary for the same LULC target type (e.g., potential, super breeder, eco-geo referenceable, *Ae. aegypti*, capture point), and can vary with time (e.g. "green-ness" of canopy leaves in a waste tire,) and geolocation (e.g., county abatment, low socioeconomic, urban neighborhood). Knowing where and when to "look" spectrally and geospatially and understanding the factors which influence the frequency response of unmixed, LULC signature, transmittance, attribute emittance features of interest may be critical to correctly interpreting the interaction of electromagnetic radiation with the surface of potential, seasonal, eco-geo referenceable, super breeder, waste tire, county abatement, *Ae. aegypti*, larval habitat, capture points.

With correct knowledge of sub-meter resolution, LULC signature, decomposed spectral transmittance characteristics emitted from eco-geo referenceable, capture points in a county abatement, intervention, epi-entomological, study site, an experimenter may identify and map unfamiliar, eco-geo referenceable geolocations (e.g., unknown, seasonal, geo classified, LULC cover types of hyper productive, Ae aegypti, waste tire foci). For example, suppose an experimenter is provided a multi-spectral, RGB, sub-meter resolution, real-time, UAV, geo sampled image of an eco-georeferenced, county abatement, potential, super breeder, Ae aegypti, seasonal, larval habitat, waste tire, capture point. Even though he or she may be totally unfamiliar with the county abatement, gridded, LULC regions, they still may be able to identify the dominant cover types within the intervention epi-entomological, study site with a high degree of certainty by utilizing known knowledge about the unmixed spectral characteristics of certain surface materials (the red and NIR reflectance, capture point, catchment variability in substrate and leaf canopy reflectance for quantitating evapotranspiration) in a real-time UAV, ArcGIS geodatabase. For example, if longer wavelength,visible and near, IR radiation is absorbed more by stagnant, canopy water than shorter visible wavelengths in a potential, seasonal, super breeder, eco-geo referenceble, waste tire, county abatement, Ae aegypti, larval habitat, capture point, the spectral signature typically would look blue or blue-green due to stronger LULC reflectance at these shorter wavelengths, and darker if viewed at red or near IR wavelengths in a real-time, UAV dashboard classification. If there is suspended influx sediment (e.g., floating leaves, depositions or large brown algae on hanging vegetation) present in the upper layers of the water body, in the larval habitat, capture point, then this will allow better reflectivity and a brighter appear-ance of the water in a sub-meter resolution, waste tire, LULC signature, RGB, eco-endmember, waste tire image. The apparent color of the water will show a slight shift to longer wavelengths in the image which may accommodate scale effects of variability in climate, topography, soils and vegetation LULCs associated to a potential, sub-county abatement, seasonal, super breeder, waste tire, eco-geo referenceable, Ae aegypti, waste tire, larval habitat, seasonal, capture points.

Determining atmospheric and surface conditions consistent with the observed potential, seasonal, super breeder, waste tire, Ae aegypti, larval habitat, sub-meter resolution, LULC, capture point, unmixed, interpolative, signature radiances may aid in geolocating potential, sea-sonal, super breeder, eco-geo referenceable, capture point, LULC, *Ae aegypt*, larval habitats in an epi-entomological, county abatement, inter-vention, study site. In addition to determining accurate atmospheric temperature profiles even in the presence of cloud contamination, a UAV real-time platform may provide global estimates of land surface temperatures, and explanatory parameters related to cloud cover. Meanwhile, assessment of seasonal, unmixed, biophysical, soil properties through spectral decomposition techniques in a real-time, UAV dashboard, Arc-GIS module may spectro temporally quantitate topography of the LULC surface (e.g., rough, smooth, floating materials, etc.) of a potential, sea-sonal, super breeder, Ae aegypti, eco-geo referenceable, waste tire, larval habitat, geo sampled in a sub-county abatement, epi-entomological, intervention, study site. Soils of varying habitats tend to have reflection properties that increase approximately monotonically with wavelength [48,49]. Inferring canopy LULC, sub-meter resolution, grid stratifiable, unmixable, signature parameters through soil moisture and atmospher-

ic, frequency, model inversions in a real-time, UAV dashboard, ArcGIS module may allow optimal iterative interpolation of LULC signatures for identifying unknown, eco-geo referenceable, waste tire, Ae aegypti, county abatement, super breeder foci.

As described above, water is a relatively strong absorber of all wavelengths, particularly those longer than the red part of the visible spectrum. Therefore, as soils moisture content increases in a potential, seasonal, super breeder, Ae aegypti, county abatement, sub-meter resolution, grid-stratifiable, LULC, signature, capture point foci, the overall reflectance of that soil would tend to decrease. Soils rich in iron oxide reflect proportionally more of the red than other visible wavelengths and therefore appear red (rust colour) to the human eye [50]. Conversely, sandy soil surrounding a county abatement, larval habitat, capture point may tend to appear bright white in the imagery as visible wavelengths are more or less equally reflected, when slightly fewer blue wavelengths are reflected; this results in a yellow colour.

By analyzing a simple signature model of bidirectional reflectance for a canopy with azimuthally nonuniform leaf distributions in real-time, UAV image, unknown, forecasted, potential, seasonal, eco-geo referenceable, super breeder, LULC, geo classifiable, *Ae. aegypti*, capture point, may establish leaf inclinations employing a "Lambertian-viewing'" cone which may exist around the nadir (for a range of solar zenith angles). Lambertian reflectance is the property that defines an ideal "matte" or diffusely reflecting surface. An inversion procedure, based on a non-linear optimization technique in a real-time UAV platform may be employable to infer the intrinsic optical properties of the leaves of a field validated, seasonal, super breeder, eco-geo referenceable, county abetment, waste tire, Aedes foci, as well as information on the morphology of the capture point canopy, that is, on the geometrical arrangements of these scatters in geo-space. The model may then be employed to generate theoretical bidirectional reflectance's employing the unmixed signature values of the relevant LULC parameters retrieved from the inversion procedure in the drone dashboard. These real-time geos sampled, entomological, spectral values may compare favorably with the actual observations over the entire range of illumination and observation angle of known, potential, seasonal, super breeder, waste tire, eco-georeferenced, capture point, LULC signature foci. The decomposed values of the iterative interpolative parameters retrieved from the inversion procedure may thereafter be validated against actual independent, signature measurements interpreted by a real-time, UAV, cartographic platform for remotely optimally, identifying unknown, potential, seasonal, super breeder, Ae aegypti, waste tire, eco-georeferenced, larval habitats.

Complications in ecohydrological, LULC signature, sub-meter resolution, real-time, interpolative, UAV, iterative interpretations of eco-geo referenceable, unknown, potential, county abatement, foci (erroneous, RGB, eco-endmember un quantitated, wavelength scatterings) may be resolved remotely employing denoising algorithms in a real-time UAV dashboard. The received radiance of the drone sensor of a hyper productive, seasonal, waste tire, *Ae. aegypti*, larval habitat, county abatment, eco-geo referenceable, capture point may be degraded by atmospheric effects and instrumental (sensor) noises which include thermal (Johnson) noise, quantization noise, and shot (photon) noise [29]. Noise reduction is often considered as a preprocessing step for hyperspectral imagery. In the past decade, hyperspectral noise reduction techniques have evolved substantially from two-dimensional band wise techniques to three dimensional ones, and varieties of low-rank methods have been forwarded to improve the signal to noise ratio of the observed data. Despite all the developments and advances, there is a lack of a comprehensive overview of these techniques and their impact on imagery applications such as signature interpolation of an unmixed, Ae aegypti, capture point, orthogonally decomposed, geo classified, LULC, signature, RGB frequencies to identify potential, super breeder, breeding site, eco-geo referenecable, larval habitats. The denoising experiments have confirmed the advantages of the use of low-rank denoising techniques compared to the other denoising techniques in terms of signal to noise ratio and spectral angle distance. In the classification experiments, classification accuracies have improved when denoising techniques have been applied as a preprocessing step. Optimally quantitating noisy, discontinuously canopied, geo-spectro temporal, unmixed, signature grid-stratifiable potential, seasonal, super breeder, Ae aegypti, larval habitat, capture points would allow for a robust interpolation when identifying unknown, seasonal foci. The search for efficient image denoising methods for iteratively interpolative, sub-meter resolution, LULC signatures of vector entomological, arthropod, larval habitat, breeding site foic still is a valid challenge. In spite of the sophistication of the recently proposed methods, most denoising algorithms have not yet attained a desirable level of applicability.

We propose a generic recursive algorithm for improving image denoising methods for iteratively interpolating a real-time UAV imaged, waste tire, Ae aegypti, larval habitat, capture point LULC signature. Given the initial denoised, capture point, county abatement image, a real-time UAV dashboard ArcGIS may strengthen the RGB signal by adding a previous denoised image to the degraded input image in the platform, The dashboard could operate the denoising method on the strengthened, waste tire, Ae aegypti, larval habitat, grid-stratified image, while simultaneously subtracting the previous denoised image from the restored signal-strengthened, signature outcome (e.g., forecasted, unknown, prolific, waste tires). The convergence of this process may be studied for the denoising the real-time drone image with related algorithms. In the context of UAV, image denoising, interpretations, a real-time, unmixing algorithm may be applied in the UAV ENVI module for employing a technique for closing the gap between the local patch-modeling of the geo classified eco-geo referenced, capture point, LULC signature, waste tire, county abatement geolocations. This could lead to improved performance in the dashboard whence optimally, remotely, targeting prolific, un-geo sampled, unknown, eco-endmember foci. The object-based module may provide a graph-based interpretation of the method, where the recursive update effectively minimizes a penalty function in the larval habitat forecast, vulnerability model that aims to denoise the capture point, UAV, real-time image, while being regularized by a Laplacian graph.

In the mathematical field of graph theory, the Laplacian matrix, sometimes called discrete Laplacian, is a matrix representation of a graph [51]. The Laplacian matrix is a discrete analog of the Laplacian operator in multivariable calculus and serves a similar purpose by measuring

to what extent a graph differs at one vertex from its values at nearby vertices [52]. The Laplacian matrix arises in the analysis of random walks and electrical networks on graphs and in particular in the computation of resistance distances. The Laplacian also appears in the matrix tree theorem. The Laplacian matrix can be employed to find many useful properties of an unmixed, seasonal, super breeder, Ae aegypti, waste tire, LULC, sub-meter resolution, signature, RGB, capture point, frequency, ArcGIS graph. Together with Kirchhoff's theorem, it can be employed to calculate the number of spanning trees for a given capture point, LULC, signature graph.

A spanning tree of a grid graph was generated in ArcGIS by Jacob [53] for regressively optimally, forecasting seasonal, hyper productive, eco-geo referenceable, larval habitats of malaria mosquito, vector, An. arabiensis. A grid-based infrastructure was overlaid onto the UAV imaged dataset employing Grids and Graticules Wizard. in ArcGIS. It was a generalization of Cayley's formula which provided the number of spanning trees in the ArcGIS seasonal, super breeder, post tillering An. arabiensis larval habitat graph. In mathematics, Cayley's formula is a result in graph theory which is based on the principal that every positive integer n, is the number of trees on n labeled vertices. The formula equivalently counted the number of spanning trees of a complete, malaria, mosquito, capture point, graph with labeled vertices.

Initially in Jacob & Novak [47] a digitized, grid cell, geo-database in ArcGIS in a hand-held mobile device was employed to determine abundance of rice land Anopheles larvae in paddy and canal habitats in three, epi-entomological, intervention, study sites in the Mwea Rice scheme in Kenya. The authors determined the feasibility of using a Personal Digital Assistant (PDA) as a mobile Arc GIS, real-time, field data collection system by monitoring mapping and regressing digitized, sub-meter resolution, grid-stratified polygons of multiple, malaria, mosquito, Anopheline arabiensis s.s, aquatic, larval, habitat covariates using a spaaning tree, digitizable grid. The system employed Quick Bird raster imagery displayed on a Trimble Recon X 400 MHz Intel PXA255 Xscale CPU®. The mobile mapping platform was employed to identify specific geographical locations of treated and untreated seasonal An. arabiensis s.s. aquatic larval habitat, capture points in rice-village complexes in Kenya. As gridded data pertaining to eco-georeferenced, An. arabiensis s.s. larval habitats were entered, all treated and untreated rice paddies within a 2km buffer of the agro-village, riceland-complex, ento-epidemiological, study site were viewed and managed on the PDA.

In the spanning tree gridded regression models were able to generate real-time data on riceland larval habitats. The abundance of 1st instar larvae/dip collected in Rurumi and Kangichiri, agro-village, study sites was 0.99 and 1.95, respectively and significantly lower than 4.81 in the Kiuria study site ($F = 5.16$, df 2, 751, $p < 0.01$). Similarly, the abundance of 2nd instar larvae differed significantly among villages with that of 0.66 in the Rurumi study site being significantly lower than 1.09 or 2.11 in Kangichiri and Kiuria study sites, respectively ($F = 3.79$, df 2, 751, $p < 0.05$). The abundance of 3rd and 4th instar larvae as well as that of pupae did not differ significantly among villages ($F = 1.64$, 0.97 and 1.04, df 2, 75, $p > 0.05$).

In the Kangichiri study site, the difference in the abundance of pupae and 1st, 2nd and 3rd instar larvae collected in paddy and canal habitat, gridded, unmixed, data, feature attributes were not significant ($p > 0.05$) while that of 4th instar larvae was significantly higher in the paddy habitats than in the canals ($F = 5.19$, df 1, 179, $p < 0.05$) employing the. In the Kiuria study site, significantly higher abundance of 3rd instar larvae were collected in the gridded canals ($F = 4.68$, df 1, 179, $p < 0.05$) while the other immature stages did not differ significantly between canal and paddy habitats. In the Rurumi study site, paddy habitats had significantly higher abundance of 1st and 2nd instar larvae compared with the canals ($F = 5.60$ and 3.94, df 1, 188, $p < 0.05$) but the other immature stages did not vary significantly between paddy and canal habitats.

Kirchhoff's theorem relies on the notion of the Laplacian matrix of a graph that is equal to the difference between the graph's degree matrix (a diagonal matrix with vertex degrees on the diagonals) and its adjacency matrix (a (0,1)-matrix with 1's at places corresponding to entries where the vertices are adjacent and 0's otherwise). Hence for a given connected graph of a forecasted unknown, seasonal, super breeder, eco-geo referenceable, waste tire, Ae aegypti, larval habitat, capture points G may be found with n labeled LULC signature vertices, in a real-time, UAV dashboard ArcGIS module by letting $\lambda_1, \lambda_2, ..., \lambda_{n-1}$ be the non-zero, unmixed, RGB, frequency eigenvalues of its Laplacian matrix. Then the number of spanning trees of G would be good approximator of unknown, prolific, county abatement, capture point foci in the real-time signature interpolation. Equivalently the number of spanning trees would be equal to any cofactor of the Laplacian matrix of G in the real-time, UAV, dashboard, ArcGIS module.

A UAV, dashboard, ENVI module may also demonstrate several leading denoising methods (K-SVD, NLM, BM3D, and EPLL), for further denoising, real-time iteratively interpolative, LULC signature, waste tire, Ae aegypti, larval habitat, capture points unmixed RGB, eco-endmember frequencies geo sampled in a epi-entomological, county abatement, study site. As mentioned, one of the objectives of this paper was to define a general mathematical and experimental methodology to compare and classify classical image denoising algorithms, for optimally real-time UAV imaging a prolific, waste tire, eco-geo referenceable, *Ae. aegypti*, larval habitat. We also wanted to propose an algorithm (e.g., eigenfunction spectral decomposition) for addressing the preservation of the signature structures in a real-time captured, UAV, grid- stratifiable, image analyses based on unmixed, iteratively, interpolative, LULC signature, RGB Ae aegypti, waste tire, emitted frequencies for remotely identifying unknown seasonal, super breeder, county abatement foci. The mathematical analysis was based on the analysis of the "method noise", defined as the difference between a digital image and its denoised version. The NL-means algorithm is proven to be asymptotically optimal under a generic statistical image model see Jacob BG [54]. The denoising performance of all considered methods for optimally identifying unknown, iteratively, interpolated, seasonally prolific, LULC, Ae aegypti, larval habitat, frequency, signature capture points in an epi-entomological, county abatement, intervention, study site were compared in four ways; mathematical: asymptotic order of magnitude of the method noise under reg-

ularity assumptions; perceptual-mathematical: the algorithms artifacts and their explanation as a violation of the real-time, UAV, image, model assumptions and, quantitative experimental: by tables of distances of the denoised version to the original, real-time, kriged, county abatement, waste tire, potential, seasonal, super breeder, *Ae. aegypti*, larval habitat LULC signatures. Our assumption was that UAV sensed algorithms may spectrographically adjusting erroneous specular reflection and other influences on colour and brightness of soil and other LULCs in geo space in a real-time, capture point, unmixed, signature dataset. In so doing, the iteratively interpolated, RGB band frequencies we assumed would reveal specific geomorphological, LULCs of potential, seasonal, super breeder, waste tire, *Ae. aegypti*, larval habitats such as organic carbon and sand, silt, clay fractions and others immature habitat, geo sampled, LULC, signature sediments in an epi-entomological, intervention, county abatement, study site.

Individual spectral bands can explain a significant portion of the variability in soil moisture, moist soil color, dry soil color, organic carbon, sand, silt, and clay at a geo sampled, potential, seasonal, capture point [55]. Jacob and Novak [56] employed the unmixed, information content of reflectance spectra recovered from a sub-meter resolution real-time, satellite sensor of a potential, seasonal, super breeder, sylvatic, Ae aegypti, larval habitat, geo sampled in a rice agro-village complex in a epi-entomological, intervention, study site in Uganda which revealed high reflectance in all sub-meter resolution bands during specific, seasonal, sample frames. This of course was dependent on grid-stratifiable, iteratively interpolative, LULC signature factors such as the colour, constituents and especially the moisture content of the capture points detected in the image sensor.

In the first phase of our experiment, mosquito control experts and University of South Florida (USF) research collaborators, employed satellite, images, [i.e., Quick Bird visible and NIR data] and from Google Earth TM to map eco-georeferenced, mosquito, oviposition traps, and county abatement, mosquito reports from locals to identify a set of sub-meter resolution, unmixed, LULC capture point wavelengths that needed to be remotely inspected. In the second phase, the UAVs was autonomously navigated to eco-georeferenced, waste tire, capture points of super breeder, seasonal, *Ae. aegypti,* larval habitats where a signature of the radiance fluxes was generated in the drone dashboard. Finally, in the third phase of our proposed system we flew the quadcopter within localized, complex, county, abatement environments at very low altitudes to visually confirm and field verify the presence of prolific, seasonal, *Ae. aegypti,* waste tire, mosquito habitat, eco-geo referenceable, capture points on specific geo classifiable LULCs employing lognormally probabilistically kriged, unmixed, RGB, real-time, unmixed, iteratively interpolative, geo sampled, eco-endmember frequencies. Our assumption was analyzing forecast-oriented, vulnerability, signature interpolation maps derived from UAV real-time imaged, grid-stratfiable, Ae aegypti, larval habitat, waste tire, capture point unmixed, RGB, sub-meter resolution signatures. can optimally, identify unknown, prolific, seasonal foci. In doing so, county abatement, entomological, control personnel could make more informed decisions that increase efficiency, improve safety in real time and drive vector elimination by optimal identification of potential, seasonal, super breeder eco-geo referenceable, waste tire, sub-county abatement foci.

Marked, geo-spectro temporal, geo sampled, iteratively interpolated, unmixed, sub-meter resolution, LULC, signature variabilities (eco-geo referenceable, super breeder, seasonal, capture point, *Ae. aegypti*, waste tire, larval habitat, RGB, sub-pixel weights) may reveal county abatement mosquito infections of arboviruses based on geolocations of unknown super breeder, county abatement foci. However, in order to do so there would be a requirement to implement adaptive strategies for optimally quantitating field-sampling time frames, pool screening and LULC, signature data analyses in real-time. In particular, the distribution and aggregation patterns of immature Aedes mosquitoes can vary significantly seasonally in an epi-entomological, intervention, county abatement study site can statistically bias analyses of remotely, geo sampled, explanatory, field variables (e.g., heteroskedastic, eco-geo referenceable, LULC signature, iterative, unmixed, geo-spectro temporal, RGB, eco-endmember frequencies) in real time, generating possible misinterpretation of super breeder, un-sampled, unknown, larval habitat, surveillance, eco-geo referenceable, capture point geolocations.

A geometric regression real-time rectification of UAV imagery may improve the accuracy of eco-georeferenceable, super breeder, seasonal, capture point, *Ae. Aegypti*, waste tire, larval habitat signatures which may be evaluated quantitatively so experimenters can choose different UAV imaged, capture point, grid-stratifiable LULCs according to their accuracy requirements when extracting geographic information from satellite imagery. Geometric regression rectification accuracy was employed by Jacob [57] to measure the differences between the position of a entomological, eco-geographic capture point on sub-meter resolution, rectified, grid-stratified image and its real position, which was determined by the following formula: $mx = \sum i = 1N(XT - XR)i2NmY = \sum i = 1N(YT - YR)i2Nmp = mX2 + mY2$ where mX and mY were the accuracies of the rectified image in the X direction and the Y direction, respectively; mP was the planimetric accuracy of the rectified image; (XT, YT) and (XR, YR) were the true coordinates of the capture points and their coordinates on the rectified image, respectively; and N was the number of larval habitats used to evaluate the accuracy.

Jacob [11] employed spatial statistics and Quick Bird visible and NIR, multispectral, 4-band data for spatially rectifying a regressed seasonal, oviposition, RGB eco-endmember, frequency unmixed dataset of geoclassified, LULC, oviposition, trapping sites that were eco-cartographically related to malaria, mosquito, Anopheles arabinos ss, species occurrence, in an agro-irrigated, Riceland agro-ecosystem in central Kenya for implementing IVM. Quick Bird simultaneously collected up to 0.61m panchromatic and 2.88m 4 band multi-spectral data of the agro-village complex. The satellite imaged, eco-georeferenced, capture point, seasonal, larval habitat, LULC signature information came from, four multispectral bands in the visible to NIR range: Blue (450-520 nm), Green (520-600nm), Red (630-690 nm) and NIR (760-900nm). This

LULC spectral data revealed eco-georeferenceable, geolocations of multiple post-tillering, flooded and pre-harvesting, seasonally hyper productive, aquatic, larval habitat, signature, capture points. An unmixed, LULC, signature uncertainty, regression model was constructed from the geosampled, LULC, explanatory, oviposition, frequency, predictor variables. A non-homogenous, Poissonian, regression model with a gamma-distributed mean optimally decomposed the data into positive and negative, spatial filter, orthogonal eigenvectors. In probability theory and statistics, the gamma distribution is a two-parameter family of continuous probability distributions [58]. In linear algebra, an eigenvector or characteristic vector of a linear transformation, is a non-zero vector that only changes by a scalar factor when that linear transformation is applied to it. The probabilistic, regression, orthogonal, LULC, signature paradigm assumed the response variable Y (i.e., larval density of an eco-georerenceble, seasonal, super breeder, An. arabiensis, capture point, aquatic, larval habitat) had a Poisson distribution, and assumed the logarithm of its expected value could be modeled by a linear combination of fractionalized, parameterizable, geosampled, LULC, iteratively, interpolative, spectral explanators. Gamma process is one of the most popular stochastic process to model degradation of device in reliability theory [59].

Thereafter, in spectral unmixing algorithms Spectral Angle Mapper SAM in ENVI were employed to unmix the rice field, agro-village, aquatic larval, habitat, geosampled, sub-meter resolution, eco-georeferenced, LULC imagery of the potential, super breeder, signature, grid-stratified capture point, seasonal, An arabiensis larval habitat, RGB, eco-endmember foci. Subsequently, the authors eigen decomposed the super breeder, seasonal, LULC, capture point, image pixels extracted from the, aquatic, larval habitat geosampled, oviposition, frequency dataset for elucidatively forecasting, clustering tendencies in productive, An. arabiensis, seasonal, immature habitats at the epi-entomological, intervention, study site. Since regression models revealed that post-tillering habitats were the most abundant based on seasonal, larval productivity, individual, non-homogenous, spectral, reflectance transmittance from the Quick Bird visible and NIR pixels, of the rice cycle, super breeder, seasonal, eigen decomposed, an arabiensis, larval habitat, capture point, orthorectified, LULC polygons were then analyzed by employing a Li-Strahler geometric-optical model.

A signature, geometric-optical, reflectance, frequency model can be constructed which estimates the bidirectional reflectance distribution function (BRDF) of canopies by modeling four shadowing pattern components (i.e., illuminated crown, illuminated ground, shadowed crown, and shadowed ground). In Jacob [60]. the model represented the canopy as a group of discrete canopied LULC habitat geospatial objects (e.g., foliar densities) and then employed a deterministic ray tracing procedure to generate a 2-dimensional scene of shadow pattern, LULC, An. arabiensis, aquatic, larval habitat, unmixed, spectral signature, RGB, frequency components. The model provides the type of shadow fraction information used to calculate the reflectance of iteratively interpolative, LULC signatures when it was treated as an area-weighted sum of the shadow component capture point reflectance's. The model was designed to test the effect of canopy structure, An. arabiensis, larval habitat, endogenous parameters on the bidirectional reflectance of various grid-stratified LULCs at the intervention, Riceland, agro-irrigated, epi-entomological, intervention, study site. The model residuals easily adapted to accommodate different crown shapes, crown sizes, stem densities, and distributions of other discontinuously canopied, iteratively interpolative, geospatial, grid-stratifiable objects for optimally remotely targeting and identifying unknown prolific, eco-georeferenceable, An. arabiensis, aquatic, larval habitats.

A real-time, UAV, signature model may isolate and quantitate the effects of crown shape, canopy cover, of potential, super breeder, *Ae. aegypti*, waste tire, larval habitat along county abatement, canopy gaps based on the seasonal shadowing, LULC patterns, and the BRDF reflectance of a capture point. An unmixed, sub-meter resolution, grid-stratifiable, eco-georeferenceable, heuristically optimizable, BRDF dataset of statistically generated capture point, LULC, signature, sub-meter resolution, UAV, real-time scenes may reveal geolocations of iteratively interpolated, unknown, super breeder, county abatement, RGB eco-endmember foci. The illuminated crown component and the illuminated ground component have the greatest impact on reflectance values in the red and NIR region respectively. The red BRDF may be mainly influenced by the illuminated ground components of the capture point, which may prove to be signature sensitive to canopy cover, real-time, LULC pattern distribution, and canopy gaps [61]. The NIR, BRDF model affected by the illuminated crown component, may be sensitive to canopy cover, height distribution, and potential, seasonal, super breeder, larval, habitat shape. The sensitivity of the BRDF to canopy, LULC gaps may be investigated in more detail for an unmixed, potential, waste tire, super breeder, Ae aegypti, seasonal, stochastic or deterministic, real-time, UAV dashboard, iterative interpolator, where eco-georeferenceable reflectance may be the dependent variable measurements close to a sub-county abatement, hotspot geolocation. Forward scattering measurements may be found to be more sensitive to gap size and frequency in the waste tire model. The spatial effects of the RGB eco-endmember LULC features may be further evalued employing the capture point BRDF.

In Jacob [62] an ordinary, stochastic interpolator in ArcGIS employed the sub-meter resolution, sub-pixel, unmixed, seasonal, LULC signatures as individual, dependent/response BRDF explanatory, predictor, RGB, eco-endmember wavelength, variables were analyzed employing multiple, differential equations. The independent variables in these models were composed of irradiance from unmixed, non-continuous, RGB, sub-meter resolution, frequency, eco-endmember, capture point, explanatory, illuminative variables which were the geosampled, An. arabiensis, LULC signature, regress able covariates rendered from the productive larval habitats for optimally seasonally targeting unknown high density, breeding site foci, at the agro-village complex, eco-epidemiological, intervention, study site.

In Jacob [54] Eigen decomposable, BRDF sub-meter resolution, LULC, signature RGB, eco-endmember, unmixed frequencies of explanatory, eco-georeferenceable, unmixed, seasonal, capture points of super breeder, malaria mosquito vector, Anopheline funestus ss. larval habitat

were constructed in ArcGIS and object-based software. Eigenvector-based spatial filtering, as introduced by Griffith (b, 2004, 2008) is a linear regression solution to the spatial autocorrelation problem. Spatial autocorrelation is the correlation among values of a single variable strictly attributable to their relatively close locational positions on a two-dimensional (2-D) surface, introducing a deviation from the independent observation's assumption of classical statistics. The authors assumed that eigenfunction properties and approximations of selected incidence matrices may be employable in spatial analyses, interpolative, sub-meter resolution, grid-stratifiable, epi-entomological, unmixed, LULC, signature, RGB, eco-endmember, sub-meter resolution datasets [62]. A spatial filtering specification for the auto-logistic An. funestus models was constructed which provided spatial-filtering-based contributions from geographically weighted regression (GWR). A GWR is an n-by-n matrix with the same sequence of row and column location labels, whose entries indicate which pairs of locations are neighbors. This regression framework constructed a separate equation for every signature feature in the eco-georeferenced epi-entomological, LULC signature dataset. Incorporating the dependent and GWR explanatory variables of the geosampled, geoclassifiable, eco-georeferenecable, capture point, malaria, mosquito, LULC features revealed bandwidths of each target (i.e., hyper productive, immature, An funestus, larval habitat), capture point, signature, attribute feature. The GWR indirectly spatial filtered the eco-georeferenceable, An funestus, time series, geosampled, LULC signatures. In doing so, multiple, eco-georeferenceable, unknown, oviposition, seasonal, hyper productive, larval habitats were remotely, optimally prognosticated. A frequency, UAV module may be able to decompose and iteratively interpolate real-time, potential, seasonal, super breeder, Ae aegypti, waste tire, aquatic, larval, habitat data into autocorrelation eigenvectors by employing GWR, mapped, interaction terms in the geosampled epi-entomological, county abatement, intervention, study site signature dataset.

In Jacob [63] a geostatistical approach accounted for spatial autocorrelation in malaria, mosquito, aquatic habitats, (Anopheles gambiae sl) geosampled, in two urban towns in Kenya. Quick Bird 0.61m data, encompassing visible and the NIR bands, were selected to synthesize signature images of An. gambiae sl aquatic habitats in Kisumu and Malindi in Kenya. Field, time series, geosampled data of An. gambiae sl aquatic habitats were employed to determine which epi-entomological, LULC, signature covariates were associated with super breeder, larval habitat development in each town. A SAS/GIS® spatial database was employed to calculate univariate statistics, correlations and perform a Poissonian, regression, probabilistic analyses on the geosampled, A gambiae sl, eco-georeferenced, aquatic, larval habitat, prolific, capture points. Semi variograms and global autocorrelation statistics were generated in ArcGIS. The spatially dependent, probabilistic, models indicated the distribution of An. gambiae sl, aquatic habitats exhibited weak positive autocorrelation in both epi-entomological, intervention, study sites, with aquatic habitats of similar log-larval counts tending to cluster in geospacer. Individual anopheline habitats were further evaluated in terms of their covariations with spatial autocorrelation by regressing them on candidate spatial filter eigenvectors. This involved the decomposition of Moran's I statistic [i.e., an index of spatial autocorrelation], employing the computation of cross products of mean-adjusted values in ArcGIS that were geographic neighbors (i.e., potential seasonal, super breeder, eco-georeferenceable, habitat covariations), that ranged from roughly -1, to nearly 0 for negative, and nearly 0 to approximately 1 for positive, spatial autocorrelation, with an expected value of $-1/(n-1)$ for zero spatial autocorrelation (i.e., random geographic chaos).

In Jacob n denoted the number of areal units (i.e., eco-georeferenceable, An. gambiae sl potential, seasonal, super breeder foci) into orthogonal and uncorrelated map pattern components using a negative binomial regression. Bias-reduced, iteratively interpolative, unmixed, sub-meter resolution, grid-stratifiable, LULC, signature, UAV, real-time frequency, estimators of high quantiles, of heavy-tailed waste tire, Ae aegypti, larval habitat, potential seasonal, super breeder, eco-georeferenceable, county abatement, capture point, signature distributions may introduce a new estimator of the mean based on an infinite second moment in an epi-entomological, intervention, study site. In mathematics, the second moment method is a technique used in probability theory and analysis to show that a random variable has positive probability of being positive. More generally, the "moment method" consists of bounding the probability that a random variable fluctuates far from its mean, by using its moments [64].

Non-homogeneous gamma distributed means derived from negative binomial regression renderings may then purify the extracted LULC, Ae aegypti, capture point. signature RGB eco-endmember frequency covariates from over-Poisson variation due to extreme observations (i.e., noisy outliers) which has also shown in literature to adjust for second moment bias in eigenspace Novak RJ [65]. If is a square matrix and is an eigenvalue of, then the union of the zero vector in a geosampled, unmixed, frequency dataset of LULC waste tire, UAV, imaged *Ae. aegypti*, signature, larval habitat, orthogonal, synthetic eigenvectors corresponding to eigenvalues may be a subspace of in, a sub-meter resolution, RGB eco-endmember, iterative, interpolative, real-time model for remotely identifying unknown seasonal, super breeder, foci in an intervention, county abatement, epi-entomological, study site in the eigenspace of eigenvalues are a special set of scalars associated with a linear system of equations (i.e., a matrix equation) that are sometimes also known as characteristic roots, characteristic values Hoffman and Kunze [66]. The determination of the signature, decomposed, eigenvalues and eigenvectors of a system is extremely important in physics and engineering, where it is equivalent to matrix diagonalization and arises in such common applications as stability analysis, the physics of rotating bodies, and small oscillations of vibrating systems, to name only a few.

Asymptotic normality of proposed county abatement, real-time regress able, unmixed UAV constructed LULC, signatures of Ae aegypti, capture point, habitat, orthogonal, frequency, eigenvectors estimators may be hence established and validated in a simulation frequency, signature iterative interpolation for determining eco-georeferenceable, geolocations of potential, super breeder, waste tire, county abatement, seasonal, LULC, signature, eigenvector, sample sizes may be estimated. Moreover, an experimenter may compare, bias and mean squared error,

of an eigendecomposed, eco-georeferenced, seasonal, hyper productive, Ae aegypti, waste tire, larval habitat, capture point, LULC, signature, wavelength estimator, unmixed dataset with real-time, UAV parameters, to evaluate the accuracy of resulting confidence intervals for interpolated, RGB, eco-endmember frequencies for determining geolocations of unknown, county abatment foci. The procedure may be aided by synthetic, LULC, eigen-signatures representing time series projections of latent, spatial correlation representing geographic configurations of potential, super breeder, eco-georeferenceable, seasonal, grid-stratifiable, *Ae. aegypti*, larval habitat, county abatement, eco-georeferenceable geolocations. In Jacob et al. (2008) the Gaussian approximation spatial filter eigenvector, An. gambiae s.l. models accounted for approximately 13% to 32% pseudo-spatially, replicated, information in the uncoalesced signature, iteratively, interpolative, epi-entomological, time series, capture point, LULC, wavelength datasets.

Spatial filtering, epi-entomological, sub-meter resolution, potential, eco-georeferenceable, seasonal, super breeder, county abatement, geo-sampled, waste tire, Ae aegypti, grid-stratifiable LULCs may address apparent heterogeneity in seasonal behaviors of this vector arthropod by interacting orthogonal, synthetic, eigenvectors delineating real-time, unmixed, iteratively interpolative, LULC signatures and their RGB eco-endmember frequencies) (i.e., reflectance covariates). Spatially autoregressive, epi-entomological, larval habitat, signature, LULC forecast, vulnerability models rely on the assumption that responses of observational units are more likely to be influenced by nearby neighboring habitats (Jacob B, Griffith DA [63]. These paradigms commonly employ an n by n weight matrix (where n is the number of sample capture points (e.g., eco-georeferenced, potential, super breeder, Ae aegypti, waste tire, larval habitat, geosampled, county abatement, seasonal foci) to describe distance-decay spatial patterns, or any other pattern of decay. Spatial filtering addresses such spatial autocorrelation from a quasi-semi-parametric point of view for optimally regressing uncoalesced, geosampled, fractionalized, eco-georeferenceable, vector, arthropod-related, sub-meter resolution, LULC signatures Jacob B, Novak RJ [67,68]. Apart from the observed, capture point, grid-stratifiable, LULC, eco-georeferenecable, decomposed frequency, regressable covariates, the systematic component, spatial filtering techniques in a real time, UAV, ArcGIS platform may generate an unmixed, iterative, interpolative dataset of synthetic, explanatory potential, seasonal, super breeder, Ae aegypti, waste tire, larval, habitat, wavelength covariates which may ento-cartographically delineate spatial structures in eigenspace. More flexibility may be added to the epi-entomological, real-time model by Spectro temporally quantitating synthetic eigen-variables in real-time for considering the signature model's non-parametric components as systematic parts of a predictive LULC, sub-meter resolution, spatial, regression model for optimally remotely identifying unknown, potential, seasonal, super breeder, county abatement, waste tire, *Ae aegypti foci*.

In the context of unmixed, vector, epi-entomological, unmixed, sub-meter resolution, iteratively interpolative, LULC signature, RGB eco-endmember, spatial, time series, regression analysis, for optimally, remotely, targeting eco-georeferenceable, seasonal, super breeder, waste tire, Ae aegypti, larval habitat, county abatement, capture points, several methods may be employed in a UAV real-time dashboard to control for the statistical effects of spatial dependencies among geosampled, grid-stratifiable, breeding site, observations. Maximum likelihood or Bayesian approaches can account for spatial dependencies in a parametric framework, whereas recent spatial filtering approaches focus on nonparametrically removing spatial autocorrelation. In this paper we propose a real-time, semiparametric, spatial filtering approach in a real-time, UAV dashboard, ArcGIS module that allows experimenters to deal explicitly with spatially lagged, autoregressive, county abatement, time series, eco-georeferenceable, Ae aegypti, waste tire, LULC, signature, model estimators and their unmixed, autoregressive sub-meter resolution, RGB, eco-endmember frequencies. As in one non-parametric real-time, UAV, spatial filtering approach, a specific subset of eigenvectors from a transformed spatial link matrix was employed to capture dependencies among the disturbances of a spatial regression, Ae aegypti, geosampled, county abatment, LULC signature, sub-meter resolution, predictive, vulnerability model. Our assumption was that an optimal subset of proposed spatially filtered, Ae aegypti, orthogonal, frequency eigenvalues may intuitively identify unknown, potential, seasonal, county abatement, eco-georeferenceable, super breeder foci by employing an objective function in a real time, UAV, ArcGIS model for minimizing spatial autocorrelation in the frequency model fit.

In Jacob [54] multiple, An. arabiensis signature, sub-meter resolution, latent autocorrelation, LULC models were constructed in ArcGIS where a prevalence response variable was aggregated as counts over an unmixed, regressed dataset of eco-geographically, geoclassified, time series, geoclassified, grid-stratifiable, LULC, regional covariates sub-divided by administrative, grid-stratified, district boundaries in Uganda. Initially, univariate statistics were generated from district-level, geosampled, epi-entomological, LULC, capture point, frequency descriptors to determine spectral signatures associated to hyperendemic malarious regions at the epi-entomological, intervention, study site based on interpolated, monthly prevalence rates. Specific district level prevalence measures were forcasted employing autoregressive, RGB, eco-endmember, iteratively interpolative, frequency specifications of geosampled, unmixed, LULC, signature, data collections for optimally, predictively, remotely targeting, high, prevalence rates of eco-georeferenceable, district geolocations. Case data were employed as the dependent variable in a probabilistic, Poissonian, regression, model framework in PROC REG for optimally quantitating sub-pixel, LULC, signature datasets of uncoalesced, district-level, time series, sub-meter resolution, meteorological densities and other RGB, eco-endmembers, frequency distributions of health centers, vegetation indices etc. geosampled from 2006 to 2012 in Uganda.

Jacob B assumed that the number of unknown, eco-georeferenceable, seasonal, super breeder, capture point, larval habitats at the epi-entomological intervention, study site had a Poisson probability distribution. These were the un-geosampled, LULC, capture point, signature parameters to be estimated by the iterative algorithmic, procedure. The logarithm of the variable n was employed as an offset—that is, a

regression variable with a constant coefficient of 1 which subsequently delineated each, district level, geosampled, An. arabiensis s.s., capture point observation. A log-linear relationship between the mean and the regressor "Eucilidean distance to the nearest agro-village centroid from the seasonal, super breeder, seasonal, aquatic larval habitat capture point" and "Number of people living in a household" was specified by the log link function. The log link function ensured that the mean number of geosampled signature covariates in the fitted, spectral, RGB, eco-endmember, sub-meter resolution, LULC model was positive. The following statements invoked the GENMOD procedure to perform the analysis:

proc genmod data= An. arabiensis LULC, capture point;

class Distance to village, Number of people;

model c = dist/ people = poisson

link = log

offset = ln;

run;

The unmixed, epi-entomological, An. arabiensis larval habitat, predictors were specified as CLASS variables so that PROC GENMOD automatically generated the indicator variables associated with the parameterizable, unmixed, signature, LULC, grid-stratifiable, estimators "Eucilidean distance to the nearest agro-village centroid from the seasonal, super breeder, seasonal, aqatic larval habitat capture point" and "Number of people living in a household" explanatorily regressors. The MODEL statement specified c as the response variable. An intercept term was included by default. Thus, the model matrix (the matrix that had as its th row the transpose of the covariate vector for the seasonal, capture point, geoclassifiable, LULC observations) consisted of a column of 1s representing the intercept term of a super breeder foci, and columns of 0s derived from non-productive, seasonal, aquatic, larval habitat, eco-georeferenceable, indicator variables geosampled at the study site. That is, the model matrix was

$$x = \begin{bmatrix} 1 & 1 & 0 & 0 & 1 & 0 \\ 1 & 0 & 1 & 0 & 1 & 0 \\ 1 & 0 & 0 & 1 & 1 & 0 \\ 1 & 1 & 0 & 0 & 0 & 1 \\ 1 & 0 & 1 & 0 & 0 & 1 \\ 1 & 0 & 0 & 1 & 0 & 1 \end{bmatrix}$$

where the first column corresponded to the intercept, the next three columns corresponded to the variable "Euclidean distance to the nearest agro-village centroid from the seasonal, super breeder, eco-georeferenced, aquatic, larval, habitat, capture point" and the last two columns corresponded to the variable "Number of people living in a household." The response distribution was specified as Poissonian, and the link function was chosen to be log. That is, the Poissonian mean parameter μ was related to the linear predictor by $\log(\mu) = x_i^? \beta$ in the unmixed, LULC, signature, oviposition, epi-entomological, time series, sub-meter resolution, probabilistic, signature, forecast paradigm. The logarithm of n was specified as an offset LULC variable. This variable served to normalize the sub-meter resolution, grid-stratifiable, *An. arabiensis* capture point, district-level, fitted cell means on a per-capture point, seasonal, super breeder foci basis, since the total number of geosampled larval habitats, not immature individuals was employed as the dependent variable(s) in the PROC GENMOD default model output.

Results from a Poissonian and negative binomial (i.e., Possion random variable with a gamma distrusted mean) analyses revealed that the covariates were significant at a 95 percent confidence level but furnished no predictive capability in the An. arabienis, capture point, LULC signature, RGB eco-endmember, sub-meter resolution, forecast, vulnerability, Ugandan model. Inclusion of the uncoalesced, LULC signature variables denoted the time sequence and the district geolcation, spatial structure based on ArcGIS Thessian polygons which also failed to reveal meaningful, iterative, interpolative prognosticators. Hence, an Autoregressive Integrated Moving Average (ARIMA) model was constructed in ArcGIS which revealed a conspicious but not very prominent first-order, dependent dataset of outliers. Outliers are extreme observations [64] that can generate propogational uncertainties in unmixed, sub-meter resolution, LULC signature wavelength datasets [69,70]. A random effects term was then specified employing monthly, time series, LULC data. This specification included a district-specific, geoclassifiable, intercept term that was based on a random deviation from the overall intercept term which was based on a normalized, frequency, geoclassified, LULC distribution. In so doing, non-Gaussian signatures (i.e., heteroskedastic and/or multicolliner, exogenous, RGB eco-endmember regressors) were teased out (i.e., denoised) from the model frequency output. The random effect specification revealed a non-constant mean across the geosampled districts in the epi-entomological, intervention, study site. This random intercept represented the combined effect of all omitted, unmixed, LULC, signature covariates that caused districts to be more prone to malaria prevalence than other districts in Uganda. Further, inclusion of a random effect's specification assumed random heterogeneity in the district's propensity of malaria prevalence which persisted throughout the entire duration of the sample frame. This random effect term dispayed zero autocorrelation and failed to conform to a bell-shaped curve. The model's variance implied a substantial difference in prevalence of malaria across the geosampled districts at the study site. The estimated model contained considerable overdispersion (i.e., excess Poissonian variability): quasi-likelihood scale = 76.565. The following equation was then employed to forecast the expected value of the prevalence of malaria at the district-level: prevalence = exp [-3.1876 + (random effect) i].

Geomapping generalized eigenvalue frequency distributions for predicting prolific Aedes albopictus and Culex quinquefasciatus habitats based on spatiotemporal field-sampled count data Acta Tropica. 2:61-68] the shorthand X ~ gamma–Poisson (α, β) in PROC COUNTREG was regressively employed to optimally quantiate an uncoalesced geosampled dataset of time series, epi-entomological, signature eco-georeferenced, county abatement, sub-meter resolution, supre breeder, LULC, seasonal, Aedes albopictus, capture point, larval habitat, potential seasonal, random variables geosampled, in Birmingham, Alabama. Ae. albopictus is a competent vector of many viruses including dengue fever (CDC 2001) and Eastern equine encephalitis virus (Mitchell et al. 1992). The authors employed spatial statistics and Quick Bird visible and NIR, sub-meter resolution, grid-stratifiable, unmixed, LULC signature, RGB, eco-endmember, time series, frequency datasets for classifying the county abatement, oviposition, eco-georeferenceable, trapping sites that were related to Ae. albopictus occurrence, abundance and distribution. Ae. albopictus life cycle is closely associated with human habitats, and it breeds in containers with standing water, often tires or other containers. It is a daytime feeder and can be found in shady areas where it rests in shrubs near the ground. Ae. albopictus feeding peaks in the early morning and late afternoon; it is an opportunistic and aggressive biter with a wide host range including man, domestic and wild animals. The unmixed, geospatial, LULC, geospectral, Ae. albopictus, oviposition, capture point, immature habitat, signature, autoregressive, vulnerability, county abatement, sub-meter resolution, RGB eco-endmember frequencies were then employed to fit a Bayesian, hierarchical, Poissonian, probabilistic, regression model employing the RANDOM statement to over dispersed, count data in a PROC MCMC procedure.

PROC MCMC then employed a random walk Metropolis algorithm to parsimoniously obtain posterior samples for quantitating the unmixed, *Ae. albopictus*, oviposition, capture point, signature, interpolative LULC, signature, epi-entomological, data, feature attributes. In statistics and in statistical physics, the Metropolis–Hastings algorithm is a Markov chain Monte Carlo (MCMC) method for obtaining a sequence of random samples from a probability distribution which may be also used to approximate the distribution (e.g., to generate a histogram), or to compute an integral (such as an expected value) [71]. By default, PROC MCMC assumed that the larval habitat observations in the unmixed, county abatement, LULC, signature, frequency dataset were independent. The logarithm of the posterior density was calculated as follows: where was a vector of geosampled, epi-entomological, iteratively interpolative, unmixed, LULC signature, RGB eco-endmember frequencies. The term was the sum of the log of the prior densities specified in the PRIOR and HYPERPRIOR statements. The term was the log likelihood specified in the MODEL statement. The MODEL statement specified the log likelihood for a single geosampled, Ae. albopictus, oviposition, capture point, LULC observation in the decomposed, signature forecasted dataset.

The statements in PROC MCMC are in many ways like DATA step statements (www.sas.com). In Jacob [11] PROC MCMC evaluated every statement in the Ae. albopictus, capture point, county abatement, forecast-oriented, vulnerability, signature model. An order for each capture point, explanative, LULC, signature observation at the Birmingham, epi-entomological, county abatement, intervention, study site was devised based on seasonal, larval productivity. The procedure cumulatively added the log likelihood for each larval habitat observation. Statements between the BEGINNODATA and ENDNODATA statements were evaluated only at the first and the last habitat observations. At the last observation, the log of the prior and hyperprior distributions were added to the sum of the log likelihood to obtain the log of the posterior distribution.

With multiple PARMS statements (multiple blocks of parameters), PROC MCMC may update each block of real-time, UAV, geosampled, county abatement, *Ae. aegypti*, waste tire, potential, seasonal, super breeder, unmixed, LULC signature, iteratively interpolative, sub-meter resolution, RGB eco-endmember frequencies in a dashboard ArcGIS module while holding other signature constants. The procedure would step through all of the programming statements in the platform to calculate the log of the posterior distribution in real time, given the the proposed signature, larval habitat, reflectance values. In other words, the real-time, UAV, cartographic cyberenvironment would not calculate the conditional distribution explicitly for each block of uncoalesced, LULC, signature, grid-stratifiable, geoclassifiable, LULC signature decomposed parameters in a time series, county abatement, wavelength, *Ae. aegypti*, sub-meter resolution, forecast, vulnerability model for unbiasedly, identifying unknown, potential, seasonal, super breeder, eco-georeferenceable foci, instead the paradigm would employ the full joint distribution in the Metropolis step for every block update. If an experimenter wishes to quantitate real-time model dependent epi-entomological data—he or she may employ, $\log(f(y/\theta)) \neq \sum_i \log\log(f(y/\theta))$ in the PROC option. JOINTMODEL. PROC MCMC assumes that the input observations are independent and that the joint log likelihood is the sum of individual log-likelihood functions(www.sas.com). Hence an experimenter may specify the log likelihood of one potential, seasonal, super breeder, LULC, Ae aegypti, capture point, frequency, signature observation in the MODEL statement. In doing so, PROC MCMC could evaluate a function for each unknown, larval habitat wavelength observation from the geosampled, dataset of known unmixed breeding site covariates. If cumulatively summed capture point, epi-entomological, forecasted observations are not independent of each other, this summation would produce an incorrect log likelihood in an Ae aegypti, waste tire, signature model for optimally remotely identifying, unknown potenetial, seasonal, superbreeeder, eco-georeferenceable foci.

The RANDOM statement (available in SAS/STAT 9.3 and later), provides a convenient way to specify random effects with substantially improved performance (www.sas.edu). Overdispersion occurs when count data appear more dispersed than expected under a reference model. Overdispersion in a real-time, time series, geosampled, UAV, sub-meter resolution, grid-stratifiable, LULC signature, iteratively, explanatively inter palatable, eco-georeferenceable, capture point of a potential, seasonal, super breeder, Ae aegypti waste tire, larval habitat in an county abatment, epi-entomological, intervention, study site can be caused by positive correlation among, geosampled, RGB eco-endmember frequencies which could render an incorrect, distributional, larval, habitat specification or mis specified variance function.

The variance function is a smooth function which depicts the variance of a random quantity as a function of its mean [Glantz SA, Slinker BK (1990) Primer of Applied Regression and Analysis of Variance. McGraw-Hill Professional Publishing]. The variance function plays a large role in many settings of statistical epi-entomological, capture point, LULC signature, forecast, vulnerability, RGB, eco-endmember, frequency modeling for remotely, optimally targeting, seasonal, eco-georeferenceable, super beeder foci (see Jacob et al. 2011). It is a main ingredient in the generalized linear model framework and a tool used in non-parametric regression, semiparametric regression and functional, LULC signature, eco-endmember, data analysis. In parametric modeling, variance functions take on a parametric form and explicitly describe the relationship between the variance and the mean of a random quantity Glantz SA, Slinker BK (1990) Primer of Applied Regression and Analysis of Variance. McGraw-Hill Professional Publishing. In a non-parametric setting, the variance function is assumed to be a smooth function.

Random step functions on the plane generated from a UAV real-time signature vector arthropod, forecast, vulnerability model may be generated using Voronoi tessellations. Given a set P := {p1, ..., pn} of sites, a Voronoi Tessellation is a subdivision of the space into n cells, one for each site in P, with the property that a point q lies in the cell corresponding to a site pi if d(pi, q) < d(pj, q) for i distinct from j [Hazewinkle].The segments in a Voronoi Tessellation may correspond to potenial, eco-georeferenceable, LULC signature, random, seasonal, potential, Ae aegypti, larval habitat, capture point, RGB, eco-endmember, unmixed,frequency points. Smoothing between nearby intensity values may be applied by means of a Markov random field (MRF) prior in a Bayesian, larval habitat, county abatement, study site, epi-entomological, real-time, UAV, image analysis. The performance of the method may be illustrable in with both real and simulated geosampled, sub-meter resolution, LULC, grid-stratifiable, signature, iterative, interpolative, frequency datasets.

Proposing a flexible prior, sub-meter resolution, LULC, iterative, interpolative, potential, seasonal, super breeder, eco-georeferenceable, capture point, *Ae. aegypti*, larval habitat model in a UAV, real-time dashboard, may optimally render iteratively interpolative, unmixed, RGB, eco-endmember frequencies from real-time, binary, MRF defined on rectangular lattices and with maximal cliques defined from a template maximal clique in an ArcGIS module. The prior model may allow higher-order real-time interactions. The number of possible parameters for an MRF, *Ae. Aegypti*, larval habitat, LULC, capture point may allow identification of unknown, potential, seasonal, super breeder, capture points in a county abatement, signature model. To get a flexible model which may adapt to the structure of a particular, observed, LULC signature, sub-meter resolution, capture point image no absolute restrictions should be put on the parametrization. Instead an experimenter may define a parametric form for the MRF in a waste tire, Ae aegypti, larval habitat, grid-stratifiable, forecast, vulnerability, county abatement, signature, real-time model. In this paradigm the unmixed, inter palatable, signature, RGB, eco-endmember frequencies may remotely inter palatable potential, super breeder, waste tire, immature habitats in an epi-entomological, county abatement, intervention, study site for various transitional, seasonal, LULC configurations, while limiting the effective number of parameters by assigning apriori discrete probabilities for capture points where groups of parameter values are equal. To run such an algorithm in a real-time UAV dashboard we assumed we had to cope with the computationally intractable, normalizing constants of MRFs generated for the signature capture points.

Here we adopted a previously defined approximation for binary MRFs, but we also briefly discuss other alternatives. We demonstrate the flexibility of our prior formulation with simulated and real time acquired, unmixed, Ae aegypti, larval habitat, LULC signature datasets. Jacob [69,70] reveals how a SAS, Bayesian, hierarchical, Poissonian, regression modes may be effective in elucidative capturing time series overdispersion and providing a better fit in an oviposition, geoclassifiable, unmixed, LULC datasets of unmixed, sub-meter resolution, grid-stratifiable, stochastically regressable, unknown, foci, geometric explanators from known geosampled, capture point frequentistic covariates.

In this research effort, we assumed that hierarchical, county abatement, eco-georerenceable, waste tire, super beeder, seasonal, Ae aegypti, LULC capture point, sub-meter resolution, signature, regression model frequency estimators constructed from real-time UAV technology (i.e., uncoalesced, sub-meter resolution, RGB, seasonal, waste tire, super breeder, county abatement, geosampled wavelengths) is expressible in a Poissonian probabilistic paradigm. This model with a log link and a normal variance on the mean parameter we assumed could identify unknown, county abatement foci in a real-time dashboard ArcGIS module. More formally, we assumed that a real-time, UAV, geosampled, sub-meter resolution, real-time, hierarchical, waste tire, oviposition, capture point, eco-georerenecable, super breeder, county abatement, Ae aegypti, LULC signature, unmixed, RGB eco-endmember, regression model may be written as for, and in SAS PROC REG or PROC LOGISTICS for optimally determining geolocations of unknown, eco-georerenecable, super breeder, seasonal, county abatement larval habitats.

In Jacob et al. (2007) the gamma–Poisson, diagnostic, explanative, random variable X in the oviposition, county abatement, Ae. albopictus, endemic, transmission, forecast-oriented, vulnerability, SAS/GIS model had a probability mass function (PMF) $f(x) = \Gamma(x+\beta) \alpha x \Gamma(\beta)(1+\alpha) \beta + x x! \ x = 0,1, 2...$ for any $\alpha, \beta > 0$ (i.e., unmixed, eco-georeferenceable, LULC signature frequency, discrete, integer, explanatorial, diagnostic, seasonal, larval, density, count value). In probability theory and statistics, a PMF is a function that gives the probability that a discrete random variable is exactly equal to some value [72]. The PMF is often the primary means of defining a discrete probability distribution especially in an epi-entomological, geo-spectrotemrpoally optimizable, LULC, frequency, signature unmixed dataset of iteratively interrogatable (e.g., co-krigable), vector, arthropod, sub-meter resolution, RGB, eco-endmember frequencies, optimally derived from, geosampled, capture point county abatement LULC signatures whose functions exist for either scalar or multivariate random variables Jacob [11].

A gamma–Poissonian, discrete, real-time, UAV, eco-georeferenceable, geosampled, super breeder, seasonal, county abatement, Ae aegypti, sub-meter resolution, real-time imaged, waste tire, unmixed, LULC signature, randomized variable may be a Poissonian random variable with a

randomized, RGB eco-endmember parameter μ which may have the gamma distribution with parameters α and β. The cumulative distribution function (CDF) [i.e., a function whose value is the probability that a corresponding continuous random variable has a value less than or equal to the argument of the function] of X in a waste tire, eco-georeferenceable, UAV geosampled, unmixed, county abatement, LULC, signature. RGB, eco-end-member model may be optimally regressively quantizable in real-time, employing $F(x) = x \sum w = 0 \Gamma(W + \beta \alpha w \Gamma(\beta)(1+\alpha)\beta + WW! x = 0,1,2,.....$ Subsequently, the moment generating function of X may be quantized as $M(t) = E[etx] = (1+\alpha-\alpha et)-\beta-\infty < t < \infty$ in the drone dashboard ArcGIS. The characteristic function of X may be $\varphi(t) = E[eitX] = (1+\alpha-\alpha eit)-\beta-\infty < t < \infty$. In probability theory and statistics, the moment-generating function of a real-valued random variable is an alternative specification of its probability distribution {Bulmer, M.G., Principles of Statistics, Dover, 1979, pp. 75–79}. The population mean, variance, skewness, and kurtosis of X in a real-time, UAV geosampled, ArcGIS, oviposition, super beeder, seasonal, capture point, *Ae. aegypti*, sub-meter resolution, eco-endmember, signature, forecast, vulnerability model may be hence written as $E[X] = \alpha\beta V[X] = \alpha\beta + a2\beta E"X - \mu\sigma3 \# = 1+2\alpha p\alpha\beta(1+\alpha)E"X - \mu\sigma4 \# = 3\alpha2\beta + 6\alpha2 + 3\alpha\beta + 6\alpha + 1\alpha\beta(1+\alpha$ in the UAV dashboard which may be also usable to identify unknown, super breeder, seasonal, geolocations of interpolated. eco-georeferenecable foci and their respective, explanatory, LULC covariates for an epi-entomological, county abatement, intervention, study site.

Subsequently an autoregressive, eigen decomposition LULC, real-time, signature process in a sub-meter resolution, county abatement, super breeder, seasonal, *Ae. aegypti*, waste tire, forecast-oriented, endemic, RGB, cluster model, error term may be employable by experimenters to optimally derive the sample distribution of the Moran's statistic for determining latent residual, explanatory components (e.g., negatively autocorrelated LULC coefficients) in the geosampled, UAV, real-time, capture point, signature datasets. Recent additions made to explicitly include spatial information and revisualization spatial analytical tool, in ArcGIS include, the calculation of Moran's I and the eigenvector spatial filtering spatial statistical technique(www.esri.com).

In spatial statistics and spatial econometrics, spatial filtering is a general methodology supporting more robust findings in data analytic work and is based upon a posited linkage structure that ties together georeferenced data observations. Constructed mathematical operators are applied to decompose geographically structured noise from both trend and random noise in georeferenced data, enhancing analysis results with clearer and sounder statistical inference. In doing so, nearby/adjacent values (e.g., immature, geosampled, Ae aegypti, waste tire, interpolative seasonal, frequency, count data) are manipulated to help analyze attribute values at a given geolocation.(e.g., county abatement seasonally hyper productive foci) Spatial filtering mathematically manipulates data in order to correct for potential distortions introduced by such factors as arbitrary scale, resolution and/or zonation (i.e., surface partitioning) of epi-entomological, vector arthropod, LULC, signature data (Jacob et al. 2011). The primary idea is that some spatial, unmixed, proxy variables, RGB, eco-endmember frequencies extracted from a spatial relationship matrix are added as control variables to a model specification. The principal advantage of this methodology is that these control variables, may identify and isolate the stochastic spatial dependencies amongst Eco georeferenced, waste tire, Ae aegypti, seasonal, super beeder, larval habitat, capture point observations, allowing model building to proceed as if these observations were independent. Eigenvalues and eigenvectors of the sample covariance matrix are the basic statistics in spatial filters and their moments play a major role in the inferential process.

However, the exact distributions of time series, geosampled, unmixed frequency, LULC, signature datasets of seasonal, super breeder, larval habitat, capture point, real-time, extracted, eco-georeferenceable, *Ae. aegypti*, waste tire, LULC decomposed, time series, eigenvalues and eigenvectors of the sample covariance matrix remain unknown. In the literature various approximations have been obtained. Lawley 1956 [D.N. Lawley, Test of significance for the latent roots of covariance and correlation matrices, Biometrika 43 (1956) 128–136] obtained the first terms of a series expansion of a sample eigenvalue related to a simple population of eigenvalues. Hence, our assumption was that under the assumption of normality, approximated values for the mean, variance and covariance matrix extrapolated from eco-georeferenceable expansion series of oviposition, real-time, geo-Spectro temporal, unmixed, LULC signature, frequency, grid-stratifiable, datasets of sub-meter resolution, iteratively interpolative, RGB eco-endmember, super breeder, larval habitat, signatures constructed from real-time UAV geosampled, waste tire, capture points of potenetial, seasonal, super beeder, Ae aegypti breeding sites may reveal geolocations of unknown county abatement foci.

 The Global Moran's I tool in a UAV geosampled, drone dashboard ArcGIS may robustly measure non-zero, spatial autocorrelation in a geo-classifiable seasonal, unmixed, eco-georeferenceable dataset of sub-meter resolution, oviposition, county abatement, geolocations employing geosampled, LULC attributes and spectrally extractable, iteratively interpolative, RGB, eco-endmember values. The Spatial Autocorrelation Global Moran's I tool is an inferential statistic (www.esri.com), which means that the results of a real-time, ArcGIS, signature, frequency analysis of county abatement, waste tire, potential super breeder, real-time, unmixed interpolative, LULC signatures for remotely targeting unknown foci would always be interpretable within the context of its null hypothesis. For the Global Moran's I statistic, the null hypothesis states that the attribute being analyzed is randomly distributed among the features in a study area said another way, the spatial processes promoting the observed pattern of values is random chance [73,74]. The autocorrelation coefficients geosampled, in a sub-meter resolution, UAV imaged, wavelength, unmixed, frequency dataset, of optimizable, RGB, eco-endmember, decomposed, attribute features parsimoniously synthesized from an eco-georeferenceable, county abatement, super breeder, waste tire, capture point, seasonal, larval habitat, may then be quantitated in real time, employing semiparametric spatial filtering methods and autoregressive spatial regression models. Subsequently a real-time, drone dashboard ArcGIS may evaluate whether the seasonal, iteratively, interpolative. LULC signatures pattern expressed by known and unknown, waste tire, *Ae. aegypti*, super beeder foci in a county abatement, intervention, epi-entomological, study site is clustered, dispersed, or random.

The models may calculate the Moran's I Index value along with a z-score and p-value to evaluate the significance of that spatial index for optimally identifying un-geosampled, county abatement, *Ae. aegypti*, super beeder, LULC foci in a UAV real-time dashboard ArcGIS. Z score is a value that is used to indicate the distance of a certain number from the mean of a normally distributed dataset while P-values are numerical approximations of the area under the curve for a known distribution, limited by the test statis [75].

Real-time, sub-meter resolution, space time, LULC, orthogonal, eco-endmember functions may be robustly derivable from a, real-time ArcGIS eigen decomposition, spatial filter, orthogonal algorithm embedded in real-time drone dashboard. The simulation results may reveal specific spatial tessellations of a given geosampled, potential, super breeder, seasonal, waste tire, Ae aegypti, county abatment, capture point, employing a fixed set of unmixed, krig eable, sub-meter resolution, LULC, sub-pixel variables. UAV simulation studies may identify the effects of: (a) mis specified larval habitat structures, (b) improperly specified seasonal, geosampled, exogenous and/or endogenous sub-meter resolution, signatures and (c) mismatched capture point, RGB, eco-endmember frequency, data-generating processes. These, simulated, sub-meter resolution, super breeder, waste tire, eco-georeferenecable, Ae aegypti, larval habitat, unmixed, capture points may be aggregated in real-time in an epi-entomological, intervention county abatement, study site. An iterative, stochastic or deterministic, krige-based interpolator may determine eco-georeferenceble, county abatement geolocations of unknown potential, super breeder, seasonal, breeding site foci while semi-parametrically recovering the identically independently distributed inconspicuous propagational disturbances. The aim of semiparametric filtering is to use spatial proxy variables that can replace the misspecification terms in autoregressive models [75].

Unfortunately, under heteroscedasticity, that is, unequal variances of the rates due to different geosampled, waste tire, super breeder, seasonal, county abatement, vector arthropod, larval population sizes, for example, the moments of the test distribution of Moran's I under H0 may differ in the county abatment signature model output. Hence, UAV, sup-pixel, (i.e., Eco-endmember), real-time, simulation, of iteratively, interpolated signature results, may approximate the moments of Moran's I by means of incorporating gesampled, Ae aegypti, waste tire, larval habitat, seasonal, capture point population sizes into the covariance matrix. In so doing, rates may be obtained of a less biased test, for regressing an unmixed, time series, epi-entomological, eco-georeferenceable, oviposition sub-meter resolution, LULC, signature, unmixed, dataset of super breeder, seasonal, Ae aegypti, waste tire, larval habitat, capture points, RGB eco-endmember or any other county abatement geosampled vector/nuisance mosquito foci, uncoalesced, time series, spectral derivatives.

In this paper, we add a term to the series expansion obtained by Lawley [1956] and improve the approximations to their moments. Further, series expansions for the sub-meter resolution, frequency, capture point, signature, orthogonal eigenvectors and their moments were obtained from an unmixed LULC dataset of time series, epi-entomological, signature, sub-meter resolution, oviposition, Ae aegypti, RGB frequencies emitted from multiple artificial, county abatement, super breeder, seasonal, LULC, waste tire, larval habitat, capture points. The objective was to model the capture point, surrounding vegetation, LULC, habitat height, and canopy cover in a sub-meter resolution, gridded dataset. Our assumption was that seasonal, eco-georeferenceable, oviposition trap, real-time, UAV geosampled, waste tire, sub-meter resolution, field and satellite collection data, resolution unmixed, LULC data, and spatial regression techniques in a real-time ArcGIS and ENVI, dashboard platform could robustly, parsimoniously discriminate multiple, un-geosampled, seasonal, Ae aegypti, super breeder, signature, capture points in Hillsborough county. We assumed that the wide coverage of the sub-meter resolution, real-time, UAV sensor data could generate cost-effective realistic, sub-pixel, LULC signature estimates of the vegetation height and canopy cover in discontinuous, urban, and agro-pastureland, residential, shade- vegetated, in homogeneously canopied, LULC, grid-stratifiable, mapping products to be used in Hillsborough county abatement, for larval management and monitoring. In Jacob [76], several machine learning techniques were applied to an unmixed, interpolated, LULC, signature, interpolation task. Multiple signatures were evaluated and compared by employing statistical significance tests in ArcGIS and ENVI. All unmixed estimators rendered from the model were gauged for propogagtional, spectral, noise. Eigenvector ensemble methods in ArcGIS and ENVI performed significantly better than single- and multi-target, oviposition-related, regression trees [76].

Hence, real-time, geoclassifiable, RGB, eco-endmember, sub-meter resolution, waste tire, Ae aegypti, signature, frequency vulnerability, county abatement, unmixed, seasonal, sub-meter resolution, LULC, signature, vulnerability maps constructed in a real-time, UAV, ArcGIS/ENVI platform may be employable for identifying unknown, super breeder, capture point, eco-georeferenecable, county abatement foci. The ENVI module would unmix a UAV, real-time, captured waste tire, Ae aegypti image and then an iterative, stochastic or deterministic interpolator in ArcGIS could predictively risk map geolocations of ecogeoreferenced, potential, seasonal, super breeder, capture point, breeding sites. Furthermore, the real-time platform may quantitate propogagtional spectral noise (e.g., spatial heteroskedascity due to outliers) in an unmixed, Ae aegypti, oviposition, frequency dataset in real time for optimally monitoring managing and implementing ongoing county abatement control activities (e.g., IVM).

The prospect of regular assessments of insect defoliation employing remote sensing technologies has increased in recent years through advances in the understanding of the sub-meter resolution, spectral, uncoalesced, reflectance properties of vegetation and other LULC interpolative signatures. Several investigators have studied the relationship between canopy spectral reflectance and canopy vegetated characteristics employing algorithmic, time series, LULC, mapping databases of vector, entomological, larval habitat, capture points [77]. Spectral vegetation indices (VIs) calculated as linear combinations of NIR and VIS red reflectance was found to be well correlated with canopy cover, leaf area index (LAI), and absorbed photosynthetically active radiation (APAR) for agro-riverine tributaries where Similium damnsoum s.l., a black fly vector of onchocerciasis ("river blindness") commonly reside. Jacob et al. (2015) employed an eco-georeferenceable, geospatially unmixed,

5meter (m), Rapid Eye™, Red Edge, Normalized Difference Vegetation Index (NDVI), LULC signature of an eco-georeferenced, hyper productive, seasonal, larval habitat of S. damnosum s.l., to identify geolocations of unknown, seasonal, super breeder, capture point foci in a neighboring eco-entomological, intervention, agro-village, tributary, study site (Chutes Dienkoa) in Burkina Faso. NDVI is a simple graphical indicator that can be used to analyze remote sensing measurements, typically, but not necessarily, from a space platform, and assess whether the target being observed contains live green vegetation or not. In Jacob [76] an eco-georeferenced, seasonal, hyper productive, capture point, prolific, S. damnosum s.l. larval habitat was initially geosampled in an agro-irrigated, riverine village and overlaid onto the 5m resolution data of the study site. The Band Math function of ENVI 4.8TM was employed to calculate the Red Edge NDVI. The Rapid Eye Multispectral Imager (MSI) acquired the capture point, larval habitat, LULC, image datasets in five different spectral bands; each one with a geometric pixel resolution [or ground sampling distance, (GSD)] of 6.5m (at nadir), with the Red Edge band spectrally geolocated between the Red band and the NIR band without overlap. In a typical spectral response of green vegetation LULC, the Red Edge band covers the portion of the spectrum where reflectance drastically increases from the red portion towards the NIR plateau (https://resa.blackbridge.com/).

In Jacob [76], Fast Line-of-sight Atmospheric Analysis of Spectral Hypercubes (FLAASH®) removed the effects of multicasting in the eco-georeferenced, capture point, seasonally hyper productive, S. damnosum s.l. larval habitat, 5m resolution, LULC scene. The authors calculated the internal relative reflectance which normalized the image to a scene average spectrum. ENVI's Log Residuals Correction Tool removed the instrument gain, topographic effects, and albedo effects from the unmixed, reflectance, transmittance, signature, wavelength emissivity's. The instantaneous fraction of direct beam radiation intercepted by the larval habitat canopy was calculated and described as fPAR = 1 - exp (-k (LAI)/cosθs) where the extinction coefficient k was a function of leaf angle distribution. Subsequently the authors employed a successive progressive algorithm (SPA), a two-stream radiative atmospheric transfer analyses, a geometric-optical model and a BRDF in ArcGIS to unmix the S. damnosum s.l., geosampled, larval habitat, capture point, intermittently canopied, geo-spectro temporal, RGB, eco-endmember frequencies. The non-parametric, residually decomposed, sub-pixel, 5m resolution, LULC, signature, frequency estimators derived from the Rapid Eye data were then employed to construct a Boolean model. Thereafter, the imaged larval habitat and its ecohydrological, within-canopy pigments (e.g., chorophyll a zeathinins) were spectrally defined and a NDVI, Red Edge, LULC signature was subsequently decomposed in ENVI.

In Jacob et al. (2015) an autocorrelation uncertainty matrix in ArcGIS Statistical Analyst 10.3® was deconvolved into combinations of partially shade-canopied, RGB, eco-endmember frequencies. The epi-entomological, geoclassified, LULC, Rapid Eye, 5m, sensor data was divided by the exoatmospheric irradiance which aided in optimally quantitating propagational, band-specific biases. Subsequently, the eco-endmember, LULC, signature, eigendecomposed, RGB, eco-endmember frequencies with its multiple Top of the atmosphere (ToA) noise-adjusted coefficients were then probabilistically kriged in Geospatial Analyst of ArcGIS to identify unknown, un-geosampled, seasonal, S. damnosum s.l., eco-georefenceable, hyper productive, seasonal, larval habitat, geolocations along a northern Ugandan, agro-village, riverine, tributary ecosystem. Of the forecasted prolific, canopy-shaded, larval habitats rendered by the eco-entomological, LULC, signature, oviposition, capture point, interpolation model, 72.2% were found to contain S. damnosum s.l. larvae when field verified. The sensitivity of the test was 78.3 while the specifity was 100.

Seasonal, super breeder, eco-georeferenceable, capture point, geoclassifiable, LULC, grid-stratifiable, larval habitat, prolific, larval habitat, foci geolocations may influence arboviral infections (e.g., high Ae, aegypti biting rates on spontaneous afforestation ecosystems, or low income, partially shade-canopied, socio-demographic, urban residential or agro-pastureland LULCs) in an intervention, epi-entomological, county abatement, intervention, study site. Employing an optimizable, real-time, UAV geosampled, time series, unmixed, RGB, eco-endmeber frequency dataset of iteratively interrogatable, sub-meter resolution, eigen decomposable signatures geo-spectrotemrpoally extracted from a geosampled dataset of geoclassified, potential super breeder, seasonal, eco-georenecable, Ae aegypti, larval habitat, capture points may allow identifying unknown, seasonal, hyperendemic foci in such study sites within a real-time, stochastic krige map.

Deterministic methods are still widely employed for seasonal, vector arthropod, larval, habitat characterization and predictive risk modelling. The result of such methods is only one solution. It is clear that our knowledge about the sub surfaces for geolocating unknown, un-geosampled, seasonal, super breeder foci is uncertain. Since stochastic methods include uncertainty in their calculations and offer more than one solution sometimes, they are the best method to use. Jacob [60] shows testing of the (Ordinary Kriging) and stochastic, sequential, Gaussian simulations of waste tire, Ae aegypti, potential, seasonal, super breeder, capture point, eco-georeferenceable, eigendecomposed properties distribution. Multiple larval habitat realizations were obtained by the habitat simulation, which were sufficient for optimally defining unknown, prolific, eco-georenecable, An. arabiensis, larval habitat, capture point geolocations from an unmixed dataset of iteratively interpolated signatures. The results obtained were acceptable and LULC oviposition, breeding site areas with the highest uncertainties were clearly observed on the maps. High differences of frequency, immature, density count values in neighbouring habitat cells were visualizable in the weighted numerical simulation. For this reason, Ordinary kriging was employed for forecast modelling the An. arabeinsis capture point signatures. Smooth transitions between neighbouring cells eliminated the simulation duration problems. The Ordinary Kriging maps showed rice agriculture agro-irrigation channel transitional reservoirs of seasonally hyper productive. An. arabeinsis aquatic, larval habitat at the epi-entomological, intervention, study site.

Spatial filter algorithms may establish means, variances, distributional functions, and pairwise correlations for qualitatively determining eco-georeferenceable capture point, county abatement, sub-meter resolution, RGB, geosampled, frequency datasets synthesized from re-

al-time, UAV captured, LULC signatures to quantitatively determine seasonal, krigability of geosampled, predictor variables. Further, a spatial filter algorithm in a real-time, UAV, ArcGIS platform may optimally quantitate latent autocorrelation, propogagtional, erroneous, uncertainty coefficients in the mean response term of a sub-meter resolution, *Ae. aegypti*, capture point, forecast-oriented, epi-entomological, LULC, signature, risk model as a linear combination of various distinct, seasonal eco-georeferenceable, RGB, eco-endmember, vulnerability, map patterns which may be then iteratively interpolated to determine unknown, county abatement study site geolocations of potential, seasonal, super breeder, waste tire, Ae aegypti, larval habitat, capture points.

Unquantitable, latent autocorrelation, sub-meter resolution, grid-stratifiable, LULC, frequency estimators computated from an eco-geo-referenced, semiparametric, county abatement, LULC, waste tire, Ae aegypti, eco-endmember, prognosticative, signature model may be interpretable as propagational noise. Jacob [60] found that sub-pixel attributes that aggregated dissimiarily in geographic space (i.e., negative autocorrelation) was due to correlated redundant, (i.e, pseudo-replicated), grid-stratifiable LULC data in an. arabiensis, time series, malaria, mosquito, aquatic, larval habitat, capture point, forecast model eigenvector parameterizable estimators. A sub-meter resolution, epi-ento-mological, LULC, signature, interpolation model found that post-tillering, An. arabiensis, immature habitats were the most abundant based on seasonal, eco-georeferenceable, larval density, frequency counts. Subsequently an eigenvector specification in AUTOREG established the geolocations of the unknown, hyper productive, seasonal, foci. Hence an eigenfuntion decomposition, algorithm in a UAV, real-time, dashboard may conduct an unmixed, signature, frequency analyses on a dataset of gesampled, vulnerability, RGB eco-endmember frequencies which, may reveal geolocations of unknown, potential, eco-georeferenecable, super beeder, waste tire, larval habitats of, seasonal, *Ae. aegypti* capture points in a county abatement epi-entomological, intervention, study site. Unmixed denosing algorithmic, diagnostic outputs of eco-georeferenced, geosampled, eco-morphological, sub-meter resolution, grid-stratifiable, UAV, real-time imaged, LULC data, Poissioian and negative binomial regressions with non-homogenous, gamma distributed estimates and space-time synthetic eigenfunctions may geo-spectrotemrpoally robustly target, prolific, unknown, seasonal, larval, habitat, super breeder foci of Ae aegypti waste tires.

Statistically significant frequentistic and nonfrequentistic, residual quantification of environmental explanatorial, eco-georeferenceable, time series, unmixed, sub-meter resolution, real-time UAV captured, LULC signature covariates of arboviral, mosquito hyper productivity in waste tire habitats may be needed to limit the search criteria of the signature in a dashboard ArcGIS. This study aimed to develop an iteratively interpolative geo-spectral signature for detecting unknown, un-geosampled, waste tires conducive to mosquito propagation. After constructing various regression models, we found that the unmixed, real-time, UAV, geo-sampled, mosquito, frequency count, capture point data featured deviations from the assumptions of regression modeling (i.e., collinear and heteroskedastic, wavelength parameters) Thus, a negative binomial paradigm was utilized to appease the violations of regression analysis and to robustify the model's pseudo R2 value. The assumption was that the results of a frequency, real-time iterative interpolative, stochastic eigen-analyses, employing a spectral signature of an unmixed, hyper productive, county abatement, seasonal, eco-georeferenecd, potential, super breeder, waste tire, Ae aegypti, larval habitat, capture point may be created from multispectral UAV, band sensor data. The signature was then applied (i.e., interpolated) in Hillsborough County, FL to remotely determine the eco-geographical geo-locations of unknown, prolific, eco-georeferenceable, seasonal, waste tire habitats.

The underlying rationale for the real-time, eigenvector spatial filtering approach for eco-cartographically, optimally, forecasting, unknown, county abatement, eco-georeferenecable, geolocations of super breeder, seasonal, Ae aegypti, sub-meter resolution, LULC, waste tire, capture points is that the, extracted, frequency eigenvectors from a transformed spatial link matrix in a UAV real-time signature model may exhibit distinctive spatial patterns with autocorrelation levels. Further, these eigenvectors may be mutually orthogonal and uncorrelated in real-time in an unmixed, UAV, geosampled, time series, heuristically optimizable, wavelength dataset. A linear combination of a small subset of these real-time, larval habitats, frequency eigenvectors may be capable of: (a) capturing the hidden spatial pattern of a stochastic component in a county abatement, epi-entomological, sub-meter resolution LULC, signature, real-time, UAV model, and (b) filter this pattern from the covariance matrix of the vector arthropod, capture point, geosampled observations. We assumed that this subset of super breeder, seasonal, eco-georeferenceable, Ae aegypti, waste tire, larval habitat, eigendecomposed, synthetic, orthogonal eigenvectors may be a proxy either for those geospatially autocorrelated, unmixed, exogenous,prolific, capture point, LULC factors that have not been incorporated into a UAV, real-time model, or for an underlying spatial process that ties the capture point,LULC signatures together in geospace.

Furthermore, incorporation of all relevant (i.e., super breeder), seasonal, orthogonally eigendecomposable, eco-georeferenceable, larval habitat, orthogonal, frequency eigenvectors into a real-time, UAV gesampled, LULC signature, frequency model we assumed would leave the residual, RGB, capture point, unmixed, grid-stratifiable, decomposable components spatially uncorrelated. Consequently, standard, statistical, epi-entomological, forecast-oriented, sub-meter resolution, LULC, sub-pixel signature modeling and RGB eco-endmember, real-time estimation techniques as well as real-time UAV interpretations, we assumed would be robustly employable for optimally spatially filtering datasets of sub-meter resolution, waste tire, suprebreeder, county abatement, model frequencies in an ArcGIS dashboard. The key theoretical and practical strategies we assumed for employing an eigenvector, real-time, eigenfucntion eigendecomposition, filtering approach for UAV, targeting of unknown, eco-georeferenceable, seasonal, suprebreeder. Ae aegypti, waste tire, county abatement, larval habitats are that (a) capture point, orthogonal eigenvectors may constitute the potential candidates for specific regression models, and (b) determine selection strategy which may henceforth lead to uncorrelated residuals and a parsimonious set of eigenvalues for optimally remotely, targeting unknown, county abatment foci.

Here we propose, a UAV, geosampled, real-time. unmixed dataset of eco-georeferenceable, sub-meter resolution, orthogonal, spatial filter eigenvectors a real-time, semiparametric filtering, sub-meter resolution, LULC, time series signature collections for identifying, unknown, county abatement, eco-georefenecable, super breeder foci. Our assumption was that a robust geosampled subset of sub-meter resolution orthogonally spatially filtered, real-time.eigendecomposed frequency eigenevectors semiparamterically derived from sub-meter resolution, grid-stratifiable, unmixed, LULC signature, orthogonal, synthetic eigenvectors may be robustly iteratively interpolatable for targeting, unknown, un-geosampled, super breeder, Ae, aegypti, waste tire, seasonal, capture points in a epi-entomological, intervention, county abatement, study site.

To date, there have been no reported contribution in the literature on usage of eco-cartographic, real-time, UAV technology (i.e, real time dashboard ArcGIS, or ENVI platforms) to identify unknown, potential, seasonal, eco-georeferenceable, super breeder, Ae aegypti, larval habitat, waste tire, capture points on geoclassifiable, sub-meter resolution, grid-stratifiable, LULC data based on an stochastically or deterministically, iteratively interpolatable, capture point, RGB, eco-endmember, orthogonal, frequency eigenvectors or unmixed signatures for implementing IVM interventions in Hillsborough County, Florida. The aim of this study was to provide a proof of concept for the use of low-cost drones for real-time, LULC, signature, risk mapping unknown, potential, super breeder, seasonal, eco-georeferenceable, Ae aegypti, waste, tire, larval habitats for implementing IVM in county mosquito abatements throughout Florida. Drone, precision, sub-meter resolution, LULC, signature, seasonal, RGB, eco-endmember, real-time reference mapping the future potential occurrence, abundance and distribution of super breeder, waste tire, larval habitats of *Ae. aegypti*, at the county, abatement level, is an important step to determining the future eco-geography of vector/ nuisance mosquito, breeding site foci in Florida.

Furthermore, distance-based Moran's eigenvector maps, asymmetric eigenvector LULC maps, scalogram, RGB eco-endmember, sub-meter resolution, frequency variation partitioned, multivariate correlogram, multivariate regression trees, and two-way ANOVAs conceived in a real time ArcGIS drone dashboard may be employable to study space–time variability in waste tire, Ae aegypti, larval habitat datasets. This research has potential to be transferable to other important vector/ nuisance, county abatement, entomological arthropods, which may achieve higher solutions by quickly identifying the target(i.e., potential, seasonal super breeder foci) and then saving money by only deploying manpower to focused areas (e.g., eco-georeferenced, LULC, seasonal, potential super breeder, capture point, county abatement foci).

Materials and Methods

Study site

Hillsborough County was selected as the case study for this research (Figure 2). It is located in West Central Florida and is the fourth most populous county in Florida with 1,638,454 inhabitants (AFF 2015). The county has a total area of 3,280 square kilometers (km2), of which 640 km2 is water (U.S. Census 2011). Florida is low lying with part of Hillsborough County being at sea level. This humid subtropical climate region has two seasons. The hot, wet season receives around two thirds of the annual precipitation and runs from June through September.
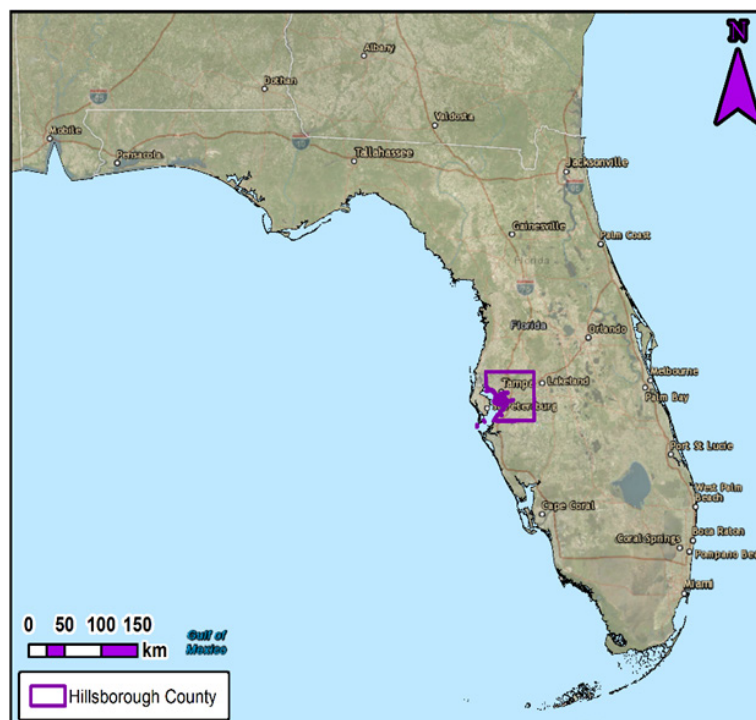

Figure 2: Site map of Hillsborough County, Florida.

1.1. Habitat mapping

Initially, base maps of the Hillsborough county abatement, intervention, study site were generated using the Quick Bird visible and NIR datasets and differentially corrected global positioning systems (GPS), reference, Hillsborough, county abatement ground coordinates of artificial, waste tire, capture point, LULCs. The GPS ground coordinates were acquired from a CSI max receiver which has a positional accuracy of ± .17. Using a local GPS broadcaster can compensate for ionospheric and ephemeris effects wcan improve horizontal accuracy significantly and can bring altitude error down in, entomological, vector arthropod, predictive, unmixed, LULC, signature, geo-Spectro temporal, distribution model [79].

Eco georeferenced, explanatory, capture point, LULC, feature attributes were entered into the VCMS™ relational database software product (Clarke Mosquito Control Products, Roselle, IL). The VCMS™ database supports a mobile field data acquisition component module, called Mobile VCMS™ that synchronizes field-geosampled data from industry standard Microsoft Windows Mobile™ devices and can support add-on GPS data collection [] http://store.elecdata.com/field_data_collection/vcms.aspx]. Mobile VCMS™ and its corresponding Field Bridge® middleware software component was used to support wireless synchronizing of the field, geosampled, seasonal, waste tire, capture point, potential super breeder, seasonal, *Ae. aegypti*, larval habitat data collected from the county abatement mosquito control personnel. The LULC data collected with the Mobile VCMS™ was then synchronized directly into a centralized VCMS™, relational, repository, LULC geo-database.

Thereafter, geocoded spatial display of the Spectro-temporal, geosampled, eco-georeferenced, LULC, super breeder, seasonal, larval habitat spectral data attributes was mapped employing the embedded VCMS™ GIS Interface Kit™ which was developed utilizing ESRI's Map Objects™ 2 technology. The VCMS™ database supported the export of all the geosampled, RGB, eco-endmember parameters using any combination of the time-series dependent, LULC, sub-meter resolution, remotely sensed, unmixed, wavelength estimators in order to further process and display specific, eco-georeferenceable, signature, data explanatorial, feature attributes in a real-time, drone dashboard ArcGIS 10.3® A visible and NIR, grid-stratfied, polygon layer outlining the county abatement, epi-entomological, study site, geoclassified, LULCs, imagery was generated in the image software.

Each LULC county abatement polygon was assigned a unique identifier. Field attribute tables were then linked to the polygons in ArcMap. The eco georeferenced, grid-stratified, polygons were employed to define the sampling frame, which was extended to include a 5 km buffer from the external boundary of intervention, ento-epidemiological, county abatement, study site. This allowed for multiple interactions enabling optimal, retrieval and transformation of the UAV geosampled LULC parameters efficiently, regardless of spatial dimensionality.

1.2. Drone

The drone surveys were carried out using a DJI Phantom 3 (DJI, http://www.dji.com) quadcopter system fitted with a DJI 4K Edition camera (Sony Exmor R Model IMX117: 7.81 mm CMOS sensor, 4000 × 3000 12 Megapixel) with an f/2.8 lens and a 94° field of view (Figure 3). It was used to capture RGB values of of potential habitat items (Figure 4).

Figure 3: A DJI Phantom 3.

Figure 4: Capturing spectral signatures, from potential artificial habitat containers.

Vegetation indices

The different modules in the UAV real-time, dashboard ENVI were employed to perform the NDVI calculations. The NDVI)is a simple graphical indicator that can be used to analyze remote sensing measurements, typically but not necessarily from a space platform, and assess whether the target being observed contains live green vegetation or not (Tucker 1991).The difference of the Red (R) and NIR bands was tabulated by dividing their sum, which in this research formed the functionally equivalent NDVI, over the canopy and gridded, terrestrial surfaces of the eco-georeferenced, LULC, vegetated, shade-canopied, capture point, *Ae. aegypti*, waste tire, super breeder, seasonal, larval habitats at the county abatement ento-epidemiological, study site. The NDVI was computed directly without any bias or assumptions regarding plant physiognomy, canopy cover class, soil type, or climatic conditions, within a range from -1.0 to 1.0 employing the 5m visible and NIR reflectances, (p), in the real-time, dashboard ENVI image software, employing the expression: . NDVI. differs from other NDVIs by employing bands along the red waveband, instead of the main absorption and reflectance peaks (http://www.satimagingcorp.com/satellite-sensors/other-satellite-sensors/rapideye/). The value of this index ranged from -1 to 1.

The following steps were employed in the real-time, drone dashboard ENVI in order to export the NDVI. From the Toolbox, the real-time dashboard selected Band Algebra > Spectral Indices. In the Spectral Index dialog, an object-based algorithm automatically chose an input, waste tire LULC, signature, eco-georeferenceable, capture point, RGB image. The super breeder, capture point, county abatement, *Ae. aegypti*, LULC images contained metadata which was then separated by wavelengths.

Figure 5 routine in the drone dashboard ENVI for separating eco-georeferenced, canopy shaded, waste tire Ae aegypti larval habitat NDVI pixels

e = ENVI ()

; Open an input file

File = Filepath ('_burkinafaso ', $

 Root_Dir=e.Root_Dir)

Raster = e. OpenRaster (File)

 ; Process a spatial subset

Subset = ENVISubsetRaster (Raster, Sub_Rect)

 ; Get the task from the catalog of ENVITasks

```
Task = ENVITask('QuerySpectralIndices')
 ; Define inputs
Task.INPUT_RASTER = Subset
 ; Run the task
Task.Execute
 ; Get the task from the catalog of ENVITasks
Task2 = ENVITask('SpectralIndices')
 ; Define LULC inputs
Task2.INPUT_RASTER = Subset
Task2.INDEX = Task.
 ; Run the task
Task2.Execute
 ; Get the field county data' data collection
DataColl = e. Ae aegypti LULC, waste tire data
 ; Add the output to the data collection
DataColl.Add, Task2.OUTPUT_RASTER
 ; Display the result
View1 = e. GetView ()
Layer1 = View1.CreateLayer(Task2.OUTPUT_RASTER)
 ; Print the available indices to the
; ENVI command line
Task.AVAILABLE_INDICES
Start the application
e = ENVI ()
 ; Open an input county file
File = Filepath (Hillsborough; Subdir=['data'], $
 Root_Dir=e.Root_Dir)
Raster = e. OpenRaster (File)
 ; Process a spatial subset
Subset = ENVISubsetRaster (Raster, Sub_Rect])
 ; Get the task from the catalog of ENVITasks
Task=ENVITask('SpectralIndices')
 ; Define LULC drone inputs
Task.INDEX = ['Normalized Difference Vegetation Index',]
Task.INPUT_RASTER = Subset
 ; Define outputs
Task.OUTPUT_RASTER_URI = e.
```

```
; Run the task
Task.Execute
 ; Get the drone LULC data Ae aegypti, habitat collection
DataColl = e. Data
 ; Add the output to the capture point LULC data collection
DataColl.Add, Task.Output_Raster
 ; Display the result
View1 = e. GetView ()
Layer1 = View1.CreateLayer(Task.Output_Raster)
```

We selected an output filename. In so doing, this enabled the Preview check box to see a preview of the settings in the real-time, drone, dashboard, ENVI, forecast vulnerability maps constructed for the ento-epidemiological, intervention, county abatement, study site. We clicked OK to process the eco-endmember, county abatement, drone geosampled, LULC data. The preview was calculated only on the area in the Image window. We selected the Display result option to display the output image when the processing was complete. In so doing, we were able to create potential, eco-georeferenceable, LULC, waste tire, Ae aegypti, super breeder, larval habitat, NDVI images that consisted of multiple indices (i.e., where each satellite band was a different index)

Figure 6 Refining the capture pint Ae aegypti larval habitat spectral index using the ENVI Spectral Indices Task API routine.

```
Start the application
e = ENVI ()
; Open an input file
File = Filepath (, Subdir=' Ae. aegypti LULC data'], $
 Root_Dir=e.Root_Dir)
Raster = e. OpenRaster (File)
 ; Process a spatial subset
Subset = ENVISubsetRaster (Raster, Sub_Rect= [600,200,799,399])
 ; Get the task from the catalog of ENVITasks
Task=ENVITask('SpectralIndices')
 ; Define inputs
Task.INDEX = ['Normalized Difference Vegetation Index',]
Task.INPUT_RASTER = Subset
 ; Define outputs
Task.OUTPUT_RASTER_URI = e.
 ; Run the task
Task.Execute
 ; Get the drone LULC data collection
DataColl = e. Data
 ; Add the output to the data collection
DataColl.Add, Task.Output_Raster
 ; Display the result
View1 = e. GetView ()
```

Layer1 = View1.CreateLayer(Task.Output_Raster)

The sub-meter resolution, grid-stratified, county abatement, *Ae. aegypti*, capture point, larval habitat, eco-georeferenced, waste tire, LULC image was then segmented in the UAV geosampled, real-time, ArcGIS with a multi-resolution algorithm employing a fine scale parameter and 4 different weights (from 0 to 100) which were assigned to the spectral bands to evaluate its influence in the segmentation and classification process. Each weight generated a segmented, NDVI, capture point, LULC image in the real-time, drone dashboard, ENVI, image software.

Explanatorial, spectral, immature habitat, capture point, uncoalesced, time series, real-time, LULC, signature data, feature attributes related to information, sub-pixel surface geometry and texture were calculated for each county abatement, image segment which was performed employing ENVI classifiers. The LULC dataset included field data to select 'classes (e.g., Dense vegetation, Sparse vegetation, Bare land, and Water). A decision tree approach was then applied to the samples in the drone dashboard to select the attributes that provided the best separation among the classes within the scenes (see Table 1). A decision tree is a decision support tool that uses a tree-like graph or model of decisions and their possible consequences, including chance event outcomes, resource costs, and utility. It is one way to display an algorithm that only contains conditional control statements [80].

Table 1: An accuracy assessment comparing in canopy LULC different weights assigned to the spectral bands of a superbeeder, tire Ae aegypti. capture point.

Accuracy Measure %	No near inra -red	Only Red	W=1	W=10	W=20	W=50	W=100
Overall Accuracy	93.91	84.77	95.78	95.32	87.67	91.84	86.91
Kappa	85.96	73.57	88.32	87.65	76.78	87.95	85.88
Dense Vegetation	97.78	97.89	91.54	97.17	95.44	95.09	95.21
Sparse vegetation	87.89	76.63	86.87	87.81	66.42	71.29	68.66
Bare land	82.55	72.18	81.57	84.78	58.8	86.75	78.89
Water	100	100	100	100	100	100	100

1.3. Spatial hydrological model

The latest version of PCI Geomatics Orthoengine® software was then employed in the drone dashboard ArcGIS to generate a Digital Elevation Model (DEM) from the geosampled, capture point, super breeder, seasonal, *Ae. aegypti,* sub-meter resolution, LULC signatures and their respective, RGB, eco-endmember, larval, habitat data (Figure 7) in the real-time. A DEM is a raster representation of a continuous surface, usually referencing the surface of the earth. The accuracy of the eco-georeferenced, geosampled, explanative, time series, LULC data was determined primarily by the resolution (i.e., the distance between the grid-stratifiable, capture point, count abatement, geolocations). Other factors affecting accuracy of DEMs are data type (integer or floating point) and the actual sampling of the surface when creating the original DEM.
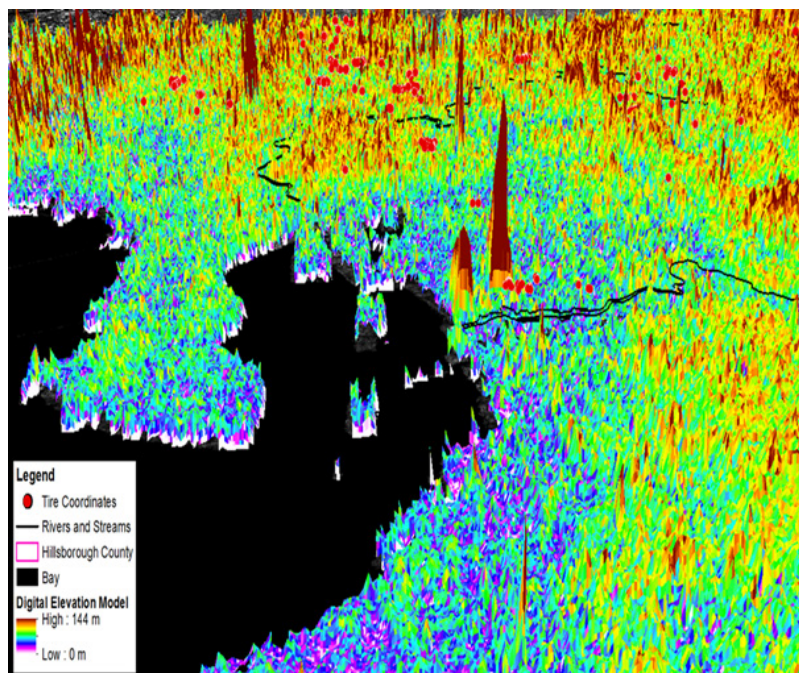

Figure 7: 3-Dimentional Digital Elevation Model (DEM) with georeferenced waste tire capture points overlaid.

Figure 7. 3-Dimentional Digital Elevation Model (DEM) with georeferenced waste tire capture points overlaid.

1.4. The Successive Projection Algorithm (SPA)

A SPA in the real-time, drone dashboard, ENVI classifier was employed to generate sub-meter, resolution, LULC signatures from an unmixed frequency, dataset of RGB partially canopied, super breeder, *Ae. aegypti,* waste tire, larval habitat, NDVI, eco-endmembers. P (i, j) denoted the spectrum for the spectrally extracted capture point pixels using the image coordinates (i, j), as the foundation of the unmixing algorithm. The signatures were defined by $\bar{p}_{(i,j)} = \sum_{k=1}^{m} f_{(i,j)k} \bar{e} + \bar{\varepsilon}_{(i,j)}$ and

$f_{(i,j)k} \geq 0, k = 1, \ldots, m, \sum_{k=1}^{m} f_{(i,j)k} = 1$ where m was the number of the eco-georeferenceable, county abatement, shade-canopied, larval habitat, grid-stratfiiable, LULCs $\bar{e}_k$ was the kth canopied LULC eco-endmember, $\bar{\varepsilon}_{(i,j)}$ was the approximation error term (i.e., residual), and f (i j) k, was the fractional abundance for the kth, super breeder, county abatement, capture point, representative, immature, habitat pixel (i, j).

The error term in $\bar{p}_{(i,j)} = \sum_{k=1}^{m} f_{(i,j)k} \bar{e} + \bar{\varepsilon}_{(i,j)}$ omputed the possible linear mixtures from and $f_{(i,j)k} \geq 0, k = 1, \ldots, m, \sum_{k=1}^{m} f_{(i,j)k} = 1$ which $\bar{p}_{(i,j)} = \sum_{k=1}^{m} f_{(i,j)k} \bar{e} + \bar{\varepsilon}_{(i,j)}$ formed a simplex Cm in the drone dashboard, defined by m vertices which corresponded to the NDVI, orthogonally, eigendecomposable, LULC, frequency, signature, larval, habitat RGB, sub-meter resolution, eco-endmembers, $\bar{e}_1, \bar{e}_2, \ldots, \bar{e}_m$ According to Jacob et al.2013 [Jacob BG, Novak RJ, Toe LD, Sanfo M, Griffith DA, Lakwo TL, et al. (2013) Validation of a Remote Sensing Model to Identify Simulium damnosum s.l. Breeding Sites in Sub-Saharan Africa. PLoS Negl Trop Dis], the volume of the simplex Cm for a seasonal, super breeder, capture point, sub-meter resolution, vector arthropod,larval habitat can be calculated from the equation $V(C_m) = \frac{1}{(m-1)!} \left| \det(WW^T) \right|^{\frac{1}{2}}$ where $W = [\bar{e}_2 - \bar{e}_1, \bar{e}_3 - \bar{e}_1, \ldots, \bar{e}_n - \bar{e}_1]$ is the volume of the simplex defined by m grid-stratifiable, geoclassifiable, LULC, immature habitat, RGB eco-endmembers, when det(·) denotes the determinant of an unmixed matrix representing the operation of an absolute value. Once the eco-georeferenced, waste tire, super breeder, capture point, LULC, *Ae. aegypti,* larval habitat, county abatement, NDVI, estimates $\bar{e}_1, \bar{e}_2, \ldots \bar{e}_m$ were determined, their fractional abundance, RGB ento-endmembers were estimated in the real-time ENVI image software through the least square's method initially, which was equivalent to a projection on the simplex in the real-time drone dashboard.

A mathematical procedure for finding the best-fitting curve was provided by a given set of sub-meter resolution, LULC, seasonal, super breeder, *Ae. aegypti,* unmixed, capture point wavelengths in the real-time drone dashboard ArcGIS by minimizing the sum of the squares of the offsets (i.e., the sub-meter resolution, grid-stratifiable, larval habitat. county abatement, foci, regression residuals) of the points from the curve. The sum of the squares of the offsets were then employed to quantitate and iteratively, interpolative, unmixed, spectral, LULC datsets of capture points instead of the offset signature absolute values as this procedure allowed the residuals to be treated as continuous differentiable quantities. However, our assumption was that because squares of the offsets were employable to determine unknown, eco-georeferenceable, LULC covariates, outlying larval habitat, county abatement, capture points could have a disproportionate effect on the fit of the geosampled, real-time, drone imaged, larval habiytat geosampled variables.

In practice, the vertical offsets from a line (polynomial, surface, hyperplane, etc.) are almost always minimized instead of the perpendicular offsets (see Kenney JF [81]). Hence, we perceived that this fitting would provide a real-time, function for a UAV geosampled, county abatement, geo-spectro temporal, RGB, eco-endmember, sub-meter resolution, seasonal, waste tire, *Ae. aegypti,* larval habitat, capture point, LULC signature for optimally regressively and eco-cartographically detecting unknown, super breeder, foci estimates. Uncertainties of the seasonal, super breeder, independent, wavelength explanators were featured along the x and y axes in this. As such, a much simpler analytic form for fitting the super breeder, seasonal, capture point, LULC, signature geosampled, waste tire, *Ae. aegypti* parameters was obtained since the fit in the real-time models was based on perpendicular offsets.

The residuals of the best-fit line for a set of geosampled, artificial, eco-georeferenceable, seasonal, *Ae. aegypti*, waste tire, county abatement, larval habitats employing unsquared perpendicular distances of the geosampled, potential, super breeder $R_{\perp} = \sum_{i=1}^{n} d_{\gamma}$ capture points (x_γ, y_γ) was given by in the real-time, UAV dashboard ArcGIS module. Since the perpendicular Euclidean distance from a line y= a+bx to a county abatment, capture point was given by $d_{\gamma} = \frac{|y_\gamma - (a + bx_\gamma)|}{\sqrt{a + b^2}}$

where the function to be minimized was $R_{\perp} = \sum_{i=1}^{n} \frac{|y_\gamma - (a + bx_\gamma)|}{\sqrt{a + b^2}}$

Unfortunately, because the waste tire, larval habitat, sub-meter resolution, grid-stratfiiable, LULC, signature absolute, decomposed, value function did not have continuous derivatives, minimizing was not amenable to any analytic solution. However, when the the square of the perpendicular distances $R_{\perp} = \sum_{i=1}^{n} \frac{[y_\gamma - (a + bx_\gamma)]^2}{\sqrt{1 + b^2}}$ [Equation 2.1] was minimized, the county abatement, vector epi-entomological, RGB eco-endmember, county abatement, larval habitat risk models were solved in closed form. $R_{\perp}^2$ was a minimum when $\frac{\partial R_{\perp}^2}{\partial_a} = \frac{2}{1 + b^2} \sum_{i=1}^{n} [y_\gamma - (a + bx_\gamma)](-1) = 0$ The former rendered in the signature habitat, real-time model $a = \frac{\sum_{\gamma=1}^{n} y_\gamma - b \sum_{\gamma=1}^{n} x_\gamma}{n} = \bar{y} - bx,$ and the latter

$\frac{\partial R_{\perp}^2}{\partial_a} = \frac{2}{1 + b^2} \sum_{i=1}^{n} [y_\gamma - (a + bx_\gamma)](-x_\gamma) + \sum_{i=1}^{n} \frac{[y_\gamma - (a + bx_\gamma)](-1)(2b)}{(1 + b^2)^2} = 0$ But $[y - (a + bx)]^2 = y^2 - 2(a + bx)y + (a + bx)^2 = y^2 - 2ay - 2bxy + a^2 + 2abx + b^2 x^2$ so (2.1) became $(1 + b^2) \left(\sum_{i=1}^{n} x_\gamma y_\gamma - a \sum_{i=1}^{n} x_\gamma - b \sum_{i=1}^{n} x_\gamma^2 \right) + b \left(\sum_{i=1}^{n} y_\gamma^2 - 2a \sum_{i=1}^{n} y_\gamma - 2b \sum_{i=1}^{n} x_\gamma y_\gamma + a^2 \sum_{i=1}^{n} 1 + 2ab \sum_{i=1}^{n} x_\gamma + b^2 \sum_{i=1}^{n} x_\gamma^2 \right)$

in the optimized, waste tire, Ae aegypti, capture point, county abatement, sub-meter resolution, residual UAV dataset when

$$-b\sum_{i=1}^{n}x_{\gamma}^2+(1-b^2)\sum_{i=1}^{n}x_{\gamma}y_{\gamma}+b\sum_{i=1}^{n}y_{\gamma}^2+\frac{1}{n}(b^2-1)\left(\sum_{i=1}^{n}y_{\gamma}-b\sum_{i=1}^{n}x_{\gamma}\right)\sum_{i=1}^{n}x_{\gamma}-\frac{2}{n}\left(\sum_{i=1}^{n}y_{\gamma}-b\sum_{i=1}^{n}x_{\gamma}\sum_{i=1}^{n}x_{\gamma}\right)b\sum_{i=1}^{n}y_{\gamma}+\frac{b}{n}\left(\sum_{i=1}^{n}y_{\gamma}-b\sum_{i=1}^{n}x_{\gamma}\right)^2=0$$

After a fair bit of algebra, the model of the least square fitting in the real-time, UAV geosampled, LULC, signature, optimizable dataset was

$$b^2+\frac{\left[\sum_{i=1}^{n}y_{\gamma}^2-\sum_{i=1}^{n}x_{\gamma}^2+\frac{1}{n}\left[\left(\sum_{i=1}^{n}x_{\gamma}^2\right)^2-\left(\left(\sum_{i=1}^{n}y_{\gamma}^2\right)^2\right)\right]\right]}{\frac{1}{n}\sum_{i=1}^{n}x_{\gamma}\sum_{i=1}^{n}y_{\gamma}-\sum_{i=1}^{n}x_{\gamma}y_{\gamma}}b-1=0$$

Subsequently the sub-meter resolution, county abatement, Ae aegypti, predictive, risk models were defined by $\frac{1}{2}\frac{\left[\sum_{i=1}^{n}y_{\gamma}^2-\frac{1}{n}\left(\sum_{i=1}^{n}y\right)^2\right]-\left[\sum_{i=1}^{n}x_{\gamma}^2-\frac{1}{n}\left(\sum_{i=1}^{n}x\right)^2\right]}{\frac{1}{n}\sum_{i=1}^{n}x_{\gamma}\sum_{i=1}^{n}y_{\gamma}-\sum_{i=1}^{n}x_{\gamma}y_{\gamma}}=\frac{1}{2}\frac{\left(\sum_{i=1}^{n}y_{\gamma}^2-n\overline{y}^2\right)-\left(\sum_{i=1}^{n}x_{\gamma}^2-n\overline{x}^2\right)}{n\overline{xy}-x_{\gamma}y_{\gamma}}$ when the quadratic formula rendered $b=-B\pm\sqrt{B^2+1}$ with a which was found using ($\diamond$). Note there existed unwieldy forms of the best-fit LULC, signature RGB, ec-oendmember, regressable parameters in the formulation. In addition, minimizing $R_{\perp}^2$ for a second- or higher-order polynomial lead to the signature, Ae aegypti, capture point, polynomial equations having higher order. The fitting technique was easily generalizable from a best-fit line to a best-fit, super breeder, seasonal, county abatement, *Ae. aegypti,* larval habitat, sub-meter resolution, geoclassified, grid-stratifiable, LULC, signature polynomial whence sums of vertical distances of the capture points were used in the real-time, geosampled, geospectral paradigm. In any case, for a reasonable number of noisy, 3-D, epi-entomological, real-time, LULC, data points, the difference between vertical and perpendicular fits wers quite small in the eco-endmember model outputs.

For fitting eco-georeferenceable, geolocation, county abatement, RGB, super breeder, seasonal, waste tire, sub-meter resolution, LULC, Ae aegypti, capture point, parameters, least squares fitting was applied iteratively to a form of the function until convergence was achieved in the real-time, UAV geosampled, signature models. It is often possible to linearize a nonlinear function in an unmixed, epi-entomological, sub-meter resolution, vulnerability. LULC signature, forecast-oriented, model for determining fit of sub-meter resolution, geo-spectro temporally extracted, RGB eco-endmembers without resorting to probabilistic Bayesian matrices (Jacob [76]). This approach does commonly violate the implicit assumption that the distribution of errors is normal, but often still gives acceptable results using normal equations, (i.e., a pseudoinverse). We assumed that if propagational uncertainties (e.g., error ellipses) are quantitable for the eco-georeferenceable, LULC, sub-meter resolution, capture point, larval habitat, unmixed, RGB eco-endmembers, the iteratively interpolative, geo-spectro temporal predictors could be weighted differently. We further assumed that the model renderings from such eco-morphological, explicative regressors could reveal eco-georeferenecable, county abatement, un-geosampled, geolocations of seasonal, super breeder, waste tire, *Ae. aegypti,* super breeder foci and their LULC estimates efficiently in a real-time, stochastic equation.

Here, the vertical least squares fitting proceeded by finding the sum of the squares of the vertical deviations R^2 for the real-time, UAV, geo-sampled, county abatement, unmixed, oviposition LULC, frequency dataset of n sub-meter resolution, waste tire, super breeder, Ae aegypti, capture points $R^2=\sum\left[y_{\gamma}-f(x_{\gamma},a_1,a_2,.....a_n)\right]^2$ from a function f. Note that this procedure did not minimize the actual deviations from the line (which w as measured perpendicular to the given function). In addition, although the unsquared sum of distances might have seemed more appropriate to minimize, the geosampled, *Ae. aegypti,* capture point, signature, LULC covariates, we employed the absolute value realizations derived from discontinuous, geoclassified, grid-stratifiable, RGB, eco-endmember frequencies which could not be treated analytically. The square deviations from each county abatement, geosampled LULC, capture point was therefore summed, and the resulting residual was then minimized to find the optimal, unbiased, fit line. This procedure resulted in outlying points being given disproportionately large weighting in the real-time drone dashboard ArcGIS.

The condition for R^2 to be a minimum in the LULC, capture point, waste tire, super breeder, *Ae. aegypti,* sub-meter resolution, real-time, UAV geosampled, LULC signature, RGB, eco-endmember, risk model was $\frac{\partial(R^2)}{\partial a}=0$ for $i=1....,n.$. For a robust linear fit, $R^2(a,b)=\sum_{i=1}^{n}\left[y_{\gamma}-(a+bx_{\gamma})\right]^2$ $\frac{\partial(R^2)}{\partial a}=-2\sum_{i=1}^{n}\left[y_{\gamma}-(a+bx_{\gamma})\right]=0$ $f(a,b)=a+bx$ so, and $\frac{\partial(R^2)}{\partial a}=-2\sum_{i=1}^{n}\left[y_{\gamma}-(a+bx_{\gamma})\right]x_{\gamma}=0$ This led to the least squre equations $na+b\sum_{i=1}^{n}x_{\gamma}\sum_{i=1}^{n}y_{\gamma}$ and $a\sum_{i=1}^{n}x_{\gamma}+b\sum_{i=1}^{n}x_{\gamma}^2\sum_{i=1}^{n}x_{\gamma}y_{\gamma}$ In the matrix form, the seasonal, super breeder, *Ae. aegypti,* LULC, signature, RGB, eco-endmember, sub-meter resolution, wavelength, real-time model was written as $\begin{bmatrix}n\sum_{i=1}^{n}x_{\gamma}\\\sum_{i=1}^{n}\sum_{i=1}^{n}x_{\gamma}^2\end{bmatrix}\begin{bmatrix}a\\b\end{bmatrix}=\begin{bmatrix}\sum_{i=1}^{n}y_{\gamma}\\\sum_{i=1}^{n}x_{\gamma}y_{\gamma}\end{bmatrix}$, so $\begin{bmatrix}a\\b\end{bmatrix}=\begin{bmatrix}n\sum_{i=1}^{n}x_{\gamma}\\\sum_{i=1}^{n}\sum_{i=1}^{n}x_{\gamma}^2\end{bmatrix}^{-1}\begin{bmatrix}\sum_{i=1}^{n}y_{\gamma}\\\sum_{i=1}^{n}x_{\gamma}y_{\gamma}\end{bmatrix}$ in the UAV, dashboard, real-time ArcGIS.

A 2x 2 matrix inverse was generated in the real-time, drone dashboard, which was written as $\begin{bmatrix}a\\b\end{bmatrix}=\frac{1}{n\sum_{i=1}^{n}x_{\gamma}^2-\left(\sum_{i=1}^{n}x_{\gamma}\right)^2}\begin{bmatrix}\sum_{i=1}^{n}y_{\gamma}\sum_{i=1}^{n}x_{\gamma}^2-\sum_{i=1}^{n}x_{\gamma}\sum_{i=1}^{n}y_{\gamma}x_{\gamma}\\n\sum_{i=1}^{n}y_{\gamma}x_{\gamma}-n\sum_{i=1}^{n}x_{\gamma}\sum_{i=1}^{n}y_{\gamma}\end{bmatrix}$,

Hence $a=0\frac{\sum_{i=1}^{n}y_{\gamma}\sum_{i=1}^{n}x_{\gamma}^2-\sum_{i=1}^{n}x_{\gamma}\sum_{i=1}^{n}x_{\gamma}y_{\gamma}}{n\sum_{i=1}^{n}x_{\gamma}^2-\left(\sum_{i=1}^{n}x_{\gamma}\right)^2}=\frac{\overline{y}\sum_{i=1}^{n}x_{\gamma}^2-\sum_{i=1}^{n}x_{\gamma}y_{\gamma}}{\sum_{i=1}^{n}x_{\gamma}^2-n\overline{x}^2}$

Hence $b=\frac{n\sum_{i=1}^{n}x_{\gamma}y_{\gamma}-\sum_{i=1}^{n}x_{\gamma}\sum_{i=1}^{n}y_{\gamma}}{n\sum_{i=1}^{n}x_{\gamma}^2-\left(\sum_{i=1}^{n}x_{\gamma}\right)^2}=\frac{\left(\sum_{i=1}^{n}x_{\gamma}y_{\gamma}\right)-n\overline{xy}}{\sum_{i=1}^{n}x_{\gamma}^2-n\overline{x}^2}$ The, ento-epidemiological, seasonal, capture point, eco-georefereneceable, LULC, waste tire, Ae aegypti, signature, wavelength model was then rewritten in a simpler form in the real-time dashboard by defining the RGB, eco-endmember, predictive, sums of squares as $ss_{xx}=\sum_{i=1}^{n}\left(x_{\gamma}-\overline{x}\right)^2=\left(\sum_{i=1}^{n}x_{\gamma}^2\right)-n\overline{x}^2$, $ss_{yy}=\sum_{i=1}^{n}\left(y_{\gamma}-\overline{y}\right)^2=\left(\sum_{i=1}^{n}y_{\gamma}^2\right)-n\overline{y}^2$, $ss_{xy}=\sum_{i=1}^{n}\left(x_{\gamma}-\overline{x}\right)\left(y_{\gamma}-\overline{y}\right)=\left(\sum_{i=1}^{n}x_{\gamma}y_{\gamma}\right)-n\overline{xy}$. The county abatement, capture point,real-time, LULC, signature models were also written as $\alpha_a^2=\frac{ss_{xx}}{n}\alpha_y^2=\frac{ss_{yy}}{n}$ and $cov(x,y)=\frac{ss_{xy}}{n}$ Here, $cov(x,y)$ was the covariance and α_x^2 and α_y^2 were variances. Note that the LULC quantities $\sum_{i=1}^{n}x_{\gamma}y_{\gamma}$ and $\sum_{i=1}^{n}x_{\gamma}^2$ were interpreted as the dot products i.e. $\sum_{i=1}^{n}x_{\gamma}^2=X,X\sum_{i=1}^{n}x_{\gamma}y_{\gamma}=X,Y$

In mathematics, the dot product or scalar product is an algebraic operation that takes two equal-length sequences of numbers (usually coordinate vectors) and returns a single number [82]. In Euclidean geometry, the dot product of the Cartesian coordinates of two vectors is widely used and often called inner product (or rarely projection product) [83] Algebraically, the dot product is the sum of the products of the

corresponding entries of the two sequences of numbers. Geometrically, it is the product of the Euclidean magnitudes of the two vectors and the cosine of the angle between them. We noted that these definitions were equivalent when defining the seasonal, eco-georerenceable, gesampled, sub-meter resolution, waste tire, super breeder, Ae aegypti, larval habitat, RGB, capture point, county abatement, LULC signature, coordinates. In modern geometry, Euclidean spaces are often defined by using vector spaces [Griffth 2003]. In this case, the dot product was employed for defining lengths (i.e., the length of a eco-georferenceable, waste tire, seasonal, super breeder, Ae aegypti capture point), whilst vector was defined as the square root of the dot product of the vector by itself) and angles (i.e., the cosine of the angle of two vectors of the county abatement, geoclassified, sub-mter resolution, LULC, larval habitat polygon);and, the quotient of their dot product by the product of their lengths.

In terms of the sums of squares, the regression coefficient b for the county abatement, geoclassified, grid-stratfiied, LULC, sub-meter resolution, signature, Ae aegypti, capture point, super breeder, risk-related, least square models was given by $b = \frac{\text{cov}(x,y)}{\alpha_x^2} = \frac{ss_{xy}}{ss_{xx}}$, whence a was given in terms of b employing ($\diamond$). The overall quality of the fit was then parameterized in terms of a correlation coefficient, in the real-time, UAV dashboard which was defined by $r^2 = \frac{ss_{xy}^2}{ss_{xx}ss_{yy}}$, in the *Ae. aegypti* model output which unbiasedly rendered the proportion of which was accounted for by the model estimation. The larval habitat, LULC signature, RGB, eco-endmember estimators for the variance was $e_\gamma \; s^2 = \sum_{i=1}^{n} \frac{e_i^2}{n-2}$ Then s was given by $s = \sqrt{\frac{ss_{yy} - bss_{yy}}{n-2}} = \sqrt{\frac{ss_{yy} - \frac{ss_{xy}^2}{ss_{xx}}}{n-2}}$.

The standard errors for a and b were optimally quantitatable employing $s\sqrt{\frac{1}{n} + \frac{\bar{x}^2}{ss_{xx}}}$ in the real-time ArcGIS drone dashboard. The regression covariates from the Ae aegypti model was then exported to an ENVI module. ENVI analytics was executed from within the ArcGIS environment and results were accessed directly from ArcMap

1.5. Radiative transfer model

We then focused on the radiation field of the atmosphere and capture point, waste tire, LULC canopy as a single coupled medium. We constructed real-time, radiative transfer models in the drone dashboard, real-time, ENVI image software which was separately described because of the different attenuating properties in the county abatement, geosampled dataset. Radiation processes in remotely geoclassified, LULC vegetated canopies can be analyzed using methods based on the equation of radiative transfer or by computer simulations. These artificial, RGB, eco-endmember, LULC, *Ae. aegypti,* signature, waste tire, equation-based, frequency models described inhomogeneous vegetation canopies (e.g., grassland, dense, broadleaf vegetation LULC) at the Hillsborough, county abatement, eco-entomological, intervention, study site.

Wang and Leuning (1998) developed a comprehensive two-leaf approach with the canopy described by variables and parameters that represented the bulk properties of all sunlit or shaded leaves, employing a radiation model to estimate the total amount of radiation in visible, NIR and thermal bands. Conductances of the stomata and leaf boundary layer were also integrated over all the sunlit and shaded leaves separately. They compared the fluxes of CO2, water vapor, and sensible heat as predicted by their two-leaf model with those of a multilayered model and found no significant differences in their predictions. The two-leaf model has recently been refined to further improve the agreement in the predicted fluxes between the two-leaf model and a multilayered, canopy, frequency model. Jacob et al. [84] showed that the fluxes predicted by the two-leaf model with Goudriaan and van Larr's radiation are very similar (relative differences <5%) to those by the two-leaf model employing the two-stream approximation. The authors derived the eco-physiological, eco-geomorphological, unmixed LULC signature properties for both sunlit and shaded leaves but considered sunlit and shaded leaves separately. in a spatial filter analyses and a Bayesian matrix for deriving qualitative Gaussian process probabilistic inferences from an epi-entomological, ecological, regressed dataset of noisy georeferenced riverine-based larval habitats of Similium damsnous a black fly vector of onchocerciasis. The authros intention was to simulate optimally unbiased, seasonal, endemic, transmission-oriented, explanatory, covariate coefficients based on spatial aggregations of productive habitats within a riverine, agro-village tributary, study site by introducing a latent variable within a non-linear autoregressive equation in ArcGIS. Autocorrelation scatterplots revealed that the Moran's coefficient was 0.067, while the Gearys ratio was 0.891 in the forecasts. Improvement of fit of a WinBUGS hierarchical Bayesian model revealed that the adjusted covariate Presence of hanging vegetation was statistically important to prolific sampled habitats.

Here, our assumption was that a radiative transfer, drone geosampled, waste tire, sub-meter resolution, LULC, *Ae. aegypti,* county abatement, eco-georeferenecable, signature model could link measurable, canopy structure, unmixed, RGB, eco-endmembers of a super breeder, county abatement foci in real-time, to seasonal, eco-geomorphological 3-D Bayesian, covariates s (e.g., soft substrate, parameters). Models of discontinuous canopies are complex models which describe the canopy structure at different scales (leaf, conifer needle, shoot, branch, tree crown, forest stand) and analyze radiative structure in such structures [85].

We assumed that the geosampled, UAV, simulation, LULC models constructed in a seasonal, suprebreeder, waste tire, *Ae. aegypti,* larval habitat, capture point, LULC, vegetation canopy paradigm would use real-time, computer graphics methods in ArcMap to simulate scene radiance in the dashboard. Geostatistical Analyst tools may be used is that for simulating landscapes ((Gu W [86]) and varying geospatial, seasonal, objects (e.g., contamination of canopied water, by a pollutant in a county abatement, potential, seasonal, super breeder, Ae aegypti, larval habitat, waste tire). Exhaustive studies are expensive and time consuming, so the breeding site phenomenon is usually characterized by taking samples at different epi-entomological, inrervention, study site geolocations We assumed real-time UAV geostatistics may be used to produce

ArcGIS predictions for un-geosampled, prolific, waste tire, county abatement eco-georferenecd, geolocations. Geostatistical Analyst offers tools to help a UAV explore the sample larval habitat data as well as several different interpolation methods jn the dashboard.

Interpolation methods produce only one value for every location in the study area. This value may not provide all the information needed to make good decisions. Drone2Map for ArcGIS streamlines the creation of professional imagery products from drone-captured still imagery for visualization and analysis in ArcGIS. https://www.esri.com/en-us/arcgis/products/drone2 map/overview Additionally, the interpolated surfaces are usually smoother (less variable) than the real phenomenon.

We assumed also that real time, UAV simulation techniques could generate multiple seasonal, interpolated surfaces of the Hillsborough, intervention,county abatement, epi-entomological, study site employing an unmixed, RGB, eco-endmember LULC signature of an eco-georeferenced,potential, seasonal, super breeder, waste tire, Ae aegypti, larval habitat as a dependent variable in a krige model.In so doing, we assumed we could replicate the spatial and spectral, eigendecomposed, capture point inhomogeneous, sub-meter resolution, grid-stratifiable, LULC signature, characteristics found in the sample data. When all the simulated, county abatement, potential, eco-georeferenceable, capture point, LULC signatures were assembled into the UAV dashboard ArcGIS module, we assumed then that the real-time geosampled interpolated maps would provide a distribution of eco-georeferenced, waste tire, capture point, prognosticated, GPS coordinates with larval values for each hyper productive, potential, breeding site geolocation in the study area. We understood that the basis for a larval control habitat intervention (UAV real-time IVM) would require geo-spectro temporal, eco-endmember, frequency, risk analyses and other estimations (uncertainty quantiation), in order to attain prcise data (geolocations of unknown, prolific foci) in real-time.

The UAV collected images to seamless orthorectified, geospatially, accurate, LULC products (DEMs, orthomosaics, 3D point clouds) The dashboard provided, fully automated image-stitching, feathering, light and color balancing for each imaged, potential, super breeder, capture point, Ae aegypti waste tire, seasonal, larval habitat within a geoclassified LULC at the Hillsborough county abatement, ento-epidemiological, intervention, study site. The real-time, object-based, ENVI classifier supported entry of the capture point, ground control points (GCPs) for high geolocation accuracy signature acquisition.

The coupled mediums geo-spectro temporally illustrated the frequency, decomposed, sub-meter resolution, *Ae. aegypti*, larval habitat, capture point, orthogonal, sub-pixel, LULC signature on various equations in which optical depth replaced the regressable, geometric altitude values in the drone dashboard real-time ENVI module. The top of atmosphere (ToA) was set to -r = 0 while the bottom was set to Ta, and the total optical depth to Tt. The optical depth of the eco-georeferenced, geosampled, capture point, larval habitat, LULC county abatement, discontinuous, canopy signatures was calculated employing Tt—Ta, which was tabulated employing Leaf area Index (LAI). This index was calculated employing $P = P_{max}\left(1 - e^{-cLAI}\right)$ in the the drone dashboard, real-time ArcGIS where Pmax designated the maximum primary production and designated a growth coefficient. This inverse exponential function then generated primary production functions for the county abatement, sub-meter resolution, LULC, waste tire, super breeder, Ae aegypti, larval habitat, eco-georeferenceable, geosampled, capture points.

LAI is definable as the projected area of leaves over a unit of land ($m^2\ m^{-2}$), so one unit of LAI is equivalent to 10,000 m2 of leaf area per hectare. Sometimes LAI is expressed based on all leaf surfaces. For broadleaf trees, the total is twice the projected area; for needle-leaf trees the conversion is between 2.4 and 2.6 and only rarely pi (π), because leaves are seldom perfect cylinders. These indices have been found to be well correlated with various vegetation LULC parameters including green leaf area, biomass, percent green cover, productivity, and photosynthetic activity of various inhomogeneously canopied, epi-entomological, seasonal, capture point, super breeder, vector arthropod, larval habitat, oviposition, frequency, density counts (Jacob [57],[62]).

(Table 2): The radiative transfer equation predictor covariate coefficients in the decomposition of the radiation field of the eco-georeferenced waste tire, capture point, *Ae. aegypti* larval hábitat, LULC signatures

F^0 extraterrestrial solar radiance

$F(\bullet)$ Fresnel reflectance function

$f(\Omega',\Omega)$ BRDF of soil

$gl(\Omega)$ distribution function of the leaf normal orientation

$\Gamma(\Omega',\Omega)$ area scattering transfer function of canopy

H height of canopy in meters

i^0 extraterrestrial solar net flux incident on the top of atmosphere

$I^0(\tau,\Omega)$ unscattered solar radiance

$I^M(\tau,\Omega)$ single scattering radiance

$I^M(\tau,\Omega)$ multiple scattering radiance

$J^M(\tau,\Omega)$ source function of radiative transfer

k leaf dimension parameter

λ wavelength

LAD leaf angle distribution

LAI leaf area index

μ_0 cosine of solar zenith angle

η leaf wax refractive index

N total Lumber of layers of the coupled medium split for multiple scattering calculation, each of thickness $\Delta\tau$

$\Omega(\mu,\phi)$ solid angle consisting of cosine of zenith angle μ and azimuth angle ϕ

$P(\Omega,\Omega)$ phase function of atmosphere

ϕ_0 solar azimuth angle

Rl leaf reflectance

$R^{s(\Omega,\Omega)}$ bidireccional reflectance factor of soil surface

R_s reflectance of Lambertian surface

τ optical depth of medium

τ_α atmospheric optical depth

$\tau_{\alpha e}$ aerosol optical depth

τ_Γ molecular optical depth

τ_t total optical depth of the coupled atmosphere-canopy medium

t_l leaf transmittance

$u_l(z)$ leaf area density

ω single scattering albedo

Next, in order to optimally geo-spectro temporally characterize the shade-vegetated, intermittently canopied, super breeder, waste tire, county abatement, eco-georeferenceable, LULC, capture point, *Ae. aegypti,* larval habitat, seasonal, hotspot phenomenon effectively and obtain stable solutions of within-canopy multiple scattering, we decomposed the extracted RGB eco-endmembers into three parts; unscattered radiance $I^0(\tau,\Omega)$ single scattering radiance $I^1(\tau,\Omega)$, and multiple scattering radiance $I^M(\tau,\Omega) = I^0(\tau,\Omega) + I^1(\tau,\Omega) + I^M(\tau,\Omega)$. A simple scheme was then represented by $I^0(\tau,\Omega)$ which was denoted by 1, in the county abatement, sub-meter resolution, LULC, wavelength, signature model which was not scattered by the atmosphere, but was reflected directly by the within canopy, surface, unmixed, attribute features of the waste tire, *Ae. aegypti,* geo-classified, county abatement. capture points. In the real-time, drone dashboard, ENVI, image software, $I^1(\tau,\Omega)$ represented the various uncoalesced, NDVI and RGB eco-endmember, irradiance values, either scattered once by the atmosphere, denoted by 2, or once by the within shade-canopied, LULC, structural, spectral, weight frequency variables which was denoted by 3. $I^M(\tau,\Omega)$ was the most complicated, capture point, geoclassifiable, LULC, signature component, which included all other real-time, UAV imaged, larval habitat, intermittently cano-pied, eco-georeferenceable, waste tire, RGB, unmixed, spectral components in the radiation field of the coupled medium. Unscattered sunlight radiances $I^0(\tau,\Omega)$ were then algorithmically characterized by the following radiative transfer equation in the real-time, drone dashboard, ENVI, object-based classification. with corresponding LULC, boundary conditions When T< Ta occured in the capture points, the radiative transfer model rendered: $\begin{cases} -\mu\frac{\partial I^0(\tau,\Omega)}{\partial\tau}+I^0(\tau,\Omega)=0 \\ I^0(0,\Omega)=\delta(\Omega,\Omega_0)\mu_0\mu<0 \end{cases}$ where τ_α^{bot} and τ_c^{top} where the optical depths at the bottom of the atmosphere and the ToA of the super breed-er, county abatement, seasonal, larval, habitat geoclassified, infrequently canopied, LULCs respectively. Here different notations from the re-al-time, drone imager was used to indicate the physical meaning of the capture point, canopy boundary, LULC conditions. The model provided the upper boundary condition, which meant only parallel sunlight illuminated the atmosphere at the eco-georeferenced, top of the capture point, super breeder, seasonal, *Ae. aegypti,* larval habitat, partially, shaded canopy in the direction Ω_0 but when $\tau > \tau_\alpha$, the residuals were expressed in the following equations: Jointly solving the above equations with these boundary conditions in the real-time, drone dashboard, ENVI classification rendered: $\left\{ -\mu\frac{\partial I^0(\tau,\Omega)}{\partial\tau}+h(\tau,\Omega)G(\Omega)I^0(\tau,\Omega)=0 \right.$ The unmixed, seasonal, RGB, eco-endmember, eco-georeferenceable, super breeder,

LULC, *Ae. aegypti,* capture point, signatures were subsequently expressed as $I_{u2}{}^0(\tau,\Omega)$ which represented the upwelling sunlight radiance within the geosampled, shade-vegetated, waste tire, county abatement, capture point, super breeder foci. In the ENVI real-time model output vegetated LULC, canopy signatures plus the function was equivalent to $\varepsilon(\tau,\Omega)$. The solar zenith angle and the wavelength, the minima of the downwelling and the upwelling radiance, geometricsignature distributions were measured close to the zenith and to the nadir. This tabulation occurred in the real-time drone dashboard workflow. Automated tools were opened in the ArcToolbox® and the results were pushed directly to ArcMap which were accesseable via ArcOnline in realtime.

We modified the extinction coefficients emitted from the grid-stratifiable, partially. Canopied, RGB eco-endmembers. We then incorporated the extracted, real-time, unmixed, within-canopy, LULC, signature radiance including the floating, hanging and surrounding dead vegetation, geospectral uncoalesced waste tire, components (e.g., spectral, texture, and inhomogenously canopied, phonological, epi-entomological, predictor variables of potential, county abatement, super breeder, capture points):

$$\varepsilon(\tau,\Omega)=\frac{1}{\pi}\int_\tau^\cdot h(t,\Omega)G(\Omega)dt$$
$$=G(\Omega)\frac{\tau}{\mu}$$

where t0 was optimally defined as $t_0 = \exp\left[-\frac{\Delta(\Omega,\Omega)\tau}{KH}\right] - \exp\left[-\frac{\Delta(\Omega,\Omega)\tau}{KH}\right]$ The, LULC, signature, *Ae. aegypti,* signature, waste tire, capture point, larval habitat, sub-meter resolution, super breeder models revealed that for single scattering RGB, eco-endmember, radiances, unscattered sunlight b**é**came the scattering source, and the boundary conditions for any potential, super breeder, waste tire, county abatement, capture point geosampled at the epi-entomological, intervention, study site.These conditions were then determined based on the fact that no incident single scattering radiances originated from above ToA or below the bottom of thecapture point,gridded canopy. In the real-time, drone dashboard, ENVI image, RGB classification, whence T<Ta occurred, the capture point, eco georeferenced, super breeder, LULC, county abatement, regressable, signature residuals rendered:

$$\begin{cases}-\mu\dfrac{\partial I^0(\tau,\Omega)}{\partial\tau}+I'(\tau,\Omega)=\\ I^1(0,\Omega)=0\,\mu<0\\ I^1(\tau_a^{bot},\Omega)\,\mu>0\end{cases}$$

Additionally, when T >T was employed in the decomposition, in the real-time, drone dashboard, ENVI, Feature Extraction Module (ENVI FX), the sub-meter resolution, LULC, *Ae. aegypti,* waste tire, larval hábitat, eco-endmember, signature model rendered:

$$\begin{cases}-\mu\dfrac{\partial I^0(\tau,\Omega)}{\partial\tau}+h(\tau,\Omega)G(\Omega)I^0(\tau,\Omega)\\ I'(\tau_c^{sup},\Omega)=I^1(\tau_c^{bot},\Omega)\,\mu<0\\ I'(\tau_0,\Omega)=0\,\mu>0\end{cases}$$

$$i_0'$$

where i_0' was the incident solar net flux arriving at the top of the eco-georeferenced, capture point, breeding site, canopied foci? $i_0' = i_0\exp(-\tau_a/\mu_0)$ In the downward direction $\mu<0$ was easily derived. When T < Ta, the unmixed, eco-endmember, sub-meter resolution, unmixed, RGB, eco-endmember, larval habitat, Hillsborough county, epi-entomological, study site, signature, frequency model in the real-time, UAV, dashboard, ENVI module resolved noisy LULC, real-time geosampled parameters employing:

$$\begin{cases}-\mu\dfrac{\partial I^0(\tau,\Omega)}{\partial\tau}+I'(\tau,\Omega)=0\\ I^0(0,\Omega)=\delta\\ \exp(-\tau_a/\mu_0)\Omega=\Omega_0\end{cases}$$

Unmixed, eco-endmember, signature, iteratively interpolative, wavelength uncertainty of an epi-entomological, potential, unknown, eco-georeferencecable, seasonal, super breeder, vector arthropod, larval habitat, waste tire, LULC, sub-meter resolution, grid—stratifiable, capture point may be defined as a parameterizable estimator that optimally geo-spectro temporally characterizes the dispersion of RGB frequency values that could reasonably be attributable to the inhomogeneously canopied,measures (Jacob [76]) Eco-epidemiological Capture Point Morphometrics by Geo-spectro temporally Iteratively Stochastically Interpolating Metrizable Sub-Mixel Mean Solar Exoatmospheric Quantum Scalar Irradiance Wavelength Periodicities where θi is a Zenith Angle and Diatomically Etiolated Xanthophylls with Azimutually Isotropic Sources of Chloroplastic Carotenoid Zeaxanthins Stoichiometerically Extracted from a RapidEye™ Red Edge Normalized Difference Vegetation Index Reference Biosignature: A Case Study in Burkina Faso and Uganda (Journal of Geophysics and Remote sensing 2015 5(1):. 12-103. The standard uncertainty, u (to which we will refer simply as uncertainty), we assumed should be expressed in terms of the standard deviation of the discontinuouslt canopied, eco-georeferenecable, unmixed, LULC signature, eigendecomposed, frequency values in a real-time UAV analysis of the county abatement collected data (the so-called type A evaluation) or through an adequate, alternative mean (type B evaluation). All the numerical quantities calculated from uncertain measurements turned out to be also uncertain quantities in the signature, waste tire, Ae aegypti, waste tire, real-time, forecast, vulnerability, county abatement, models and therefore should have associated uncertainty prognosticative, unmixed values (combined standardizable, LULC iteratively interpolative, uncoalesced, geo-spectro temporal RGB, eco-endmember, frequency uncertainties,), calculated through uncertainty propagation formulaes in the real-time UAV dashboard ArcGIS modules . That being the case, we assumed we would beable to express the uncertainty associated with each single raw larval habitat unknow, predicted data value to be used in the data analysis task. This implied that there should not be only one data table to be explored, but rather two tables: the usual raw waste tire, *Ae aegypti*, larval habitat data table and another one with the associated geometric optical uncertainties. Therefore, with this added knowledge at our disposal, we would then assume we wuld be able to integrate the unxed LULC signature datasets into thr real-time UAV, frequency, RGB data analysis tasks. There is already a trend towards this explicit consideration of measurement uncertainties. Namely, Wentzell [87] developed the so-called maximum likelihood principal component analysis (MLPCA), which estimates a PCA model in an optimal maximum likelihood sense when data are affected by measurement errors exhibiting a known complex structure, such as cross-correlations along sample or variable dimensions.

Subsequently, $\tau_\alpha < \tau < \tau_t$ in the, real-time, LULC, signature, eco-endmember frequency, model residuals were solved employing the equation:

$$\left\{ \frac{i_0'(\Omega_o \to \Omega)}{\pi G(\Omega)\mu_0 - G(\Omega)\mu} + t_{1\triangle}I^1(\tau_t,\Omega) \right. \text{ where t1 was defined by the equations}$$

$t_1 = \exp\left[G(\Omega_0)\frac{(\tau,\tau_\alpha)}{\mu_0} \right] - \exp - G(\Omega)\frac{(\tau,\tau_\alpha)}{\mu}$ and which was employed to quantitate the single scattering, partially shaded, county abatement, super breeder, seasonal, eco-georeferenceable, larval habitat, waste tire, capture point, canopy radiances emerging from the atmosphere without scattering in the LULC discontinuous gaps.

In the upward direction (p > 0), the capture point, RGB, eco-endmember, LULC, signature, eco-endmember solutions in the real-time drone model were a little more complicated because of the hotspot effect in which i was determined by where t_2 was: $t_2 = \exp\left[-\frac{\tau}{\mu_0} \right] - \exp\left[\frac{\tau}{\mu} - \left(\frac{1}{\mu_0} + \frac{1}{\mu} \right) \right]\tau\alpha$ and the second integration at Ta < T < Tt. This equation was geo-spectro temporally obtained by means of an alternative unmixed, dataset of explicative, time series, unmixed, LULC signature, discrete, integer values and frequency ranges, which was solved in real-time employing .The radiance $I^1(\tau_t,\Omega)$ at Ta < T <Tt derived for the geoclassified, sub-meter resolution, LULC, capture point, RGB wavelengths was then numerically evaluated without further assumptions. An explicit approximation to $I^1(\tau_t,\Omega)$ was optimally derived and used for inversion in the, LULC, signature decomposition in the real-time drone, object-based classification. It was noted that canopied LULC, reflectance measurements in the NIR regions took advantage of known absorption features of the LULC (e.g., water content) based on the penetration depth of light in the NIR region to make integrated capture point, signature, frequency counts (Figure 7).

3-D point cloud feature extractione were available in the UAV dashboard ENVI module. Feature identification which were performed on an entire gridded eco-georeferenced, LULC sigature, capture point, waste tire, larval habitat, unmixed dataset of a super breeder, capture point, county abatement, seasonal, *Ae aegypti*, foci which was deribed from a cloud scene. User-defined subsets of the eco-georeferenced, sub-meter resolution, county abatement, epi-entomological, intervention, study site scene with accurate LULC signature information was generated in the dashboard in real-time.

1.6. Object-oriented classification

Before applying spectral index to the capture point, Ae aegypti, waste tire, capture point,LULC imagery,raw pixel values [i.e., Digial Numbers (DN)], the county, abatement, remotely sensed, grid-stratifiable, real-time, retrived, drone geosampled, Hillsborough county, epi-entomological, intervention, study site, county abatement, decomposed data was converted into physically meaningful units which was subsequently calibrated. Noisy, frequency, RGB, eco-endmember, LULC signature variables were corrected. The eco-georeferenecd, super breeder, seasonal, capture point, *Ae. aegypti,* waste tire, larval habitat, signature, LULC products were delivered in an integer format which were rescaled to the ToA reflectance employing unmixed, radiometric, rescaling coefficients provided in the product metadata file (MTL file) in the real-time, UAV, dashboard, ENVI classification algorithms (e.g., Spectral Angle Mapper).

The following equation was employed to convert the capture point, geosampled, county abatement, LULC signature, *Ae. aegypti,* immature habitat, DN values to ToA reflectance in the UAV, geosampled, eco-georeferenced, real-time, LULC data: ρλ′=MρQcal+Aρ where: ρλ′ = ToA planetary reflectance, without correction for solar angle. Note that ρλ′ did not contain a correction for the sun angle in the ENVI module. Hence, we employed Mρ = Band-specific multiplicative as a rescaling factor in the real-time,county abatement LULC metadata(REFLECTANCE_MULT_BAND_x), when x was the band number), where Aρ = Band-specific was the additive rescaling factor originating from the *Ae. aegypti,* capture point, waste tire, metadata (REFLECTANCE_ADD_BAND_x), where x was the band number. Qcal quantized and calibrated the standardized, eco-georeferenceable, artificial, waste tire, *Ae.aegypti,* LULC signature, capture point, larval habitat,sub-meter resolution, sub-pixel values employing the DN and ToA reflectance with a correction for the sun angle i.e., ρλ=ρλ′ cos(θsz) =ρλ′ sin(θse) where: ρλ = ToA planetary reflectance and θse was the Local sun elevation angle. The scene center sun elevation angle in degrees was provided in the metadata (SUN_ELEVATION) which rendered θsz = Local solar zenith angle and θsz = 90° - θse for the potential, super breeder, seasonal, county abatement, eco-georeferenced, waste tire, *Ae aegypti,* capture points geosampled in the Hillsborough county study site.

The ENVI software easily converted the geometric, seasonal, super breeder, eco-georeferenecable, *Ae aegypti*, capture point, LULC, signature, RGB eco-endmember, grid-stratifiable, sub-meter resolution, waveband data to ToA reflectance values. A file was opened that ended with "_MTL.TXT"in the drone dasboard. From the ENVI main menu bar, "Open Image File" was selected. The real-time, ENVI modules automatically opened the capture point, waste tire, super breeder, seasonal, eco-georeferenced, *Ae aegypti,* larval habitat, LULC images using multiple files. For creating a reflectance data file from the ENVI main menu bar, the Basic Tools, Preprocessing and Calibration Utilities was employed. The optical data file and the ENVI Calibration dialog opened all the capture point, time series, explanatory, eco-georeferenceable, parameterizable estimators. By clicking the reflectance radio button in the dashboard, object-based, classifier, an eco-endmember, output file name (i.e., *Ae. aegypti* waste tire, capture point) was entered. The real-time, RGB eco-endmember values of the county abatement, larval habitat, LULC signatures ranged from 0.0 to 1.0 which was stored in floating point data format in the dashboard.

The DN values converted radiance, seasonally prolific, eco-georeferenced, waste tire, *Ae. aegypti,* larval habitat, to seasonal, LULC values in ENVI. Thereafter, these radiance values were converted to RGB specified, capture point, larval habitat, reflectance values. The formula to

convert DN to radiance values was based on gain and bias within where: Lλ was the radiance estimate and DN was the grid cell value. It was noted that DN gain was the gain value for a specific band and bias was the deviated value for any specific, geoclassified, geosampled, LULC, *Ae. aegypti,* capture point, wavelength, reflectance band. The ENVI formula in Band Math was 0.05518 * (B1) + 1.2378 which was calculated employing an eco-georeferenceable, county abatement, artificial, super breeder, seasonal, LULC, larval habitat, county abatement, capture point, with a scene specific gain value of 0.05518 and an offset value of 1.2378 for each sub-meter resolution, waste tire, LULC signature. In the Band Pairing dialog B1 was matched with the appropriate optical band. The formula employed in the classification process was as follows: where:Lλ was the grid cell value as radiance, QCAL was the DN, LMIN was the spectral radiance scales to QCALMIN, LMAXλ was the spectral radiance scales to QCALMAX, QCALMIN was the minimum sub-meter resolution, LULC, signature, capture point, values and QCALMAX was the maximum quantitable radiance to ToA reflectance, larval habitat, pixel value(i.e.,255)

The formula was employed to optimally quantitate multiple illumination, viewing angle, reflectance variables, emitted from the capture point, LULC, *Ae. aegypti* -related, super breeder, seasonal, sub-meter resolution, unmixed datatset of RGB, eco-endmember, geosampled county abatement, explanatory, canopied, frequency, covariate coefficients. In the formula ρλ was the unitless plantary reflectance; L was the waste tire, larval habitat, spectral radiance; d was the Earth-Sun distance in astronomical units; ESUNλ was the mean solar exoatmospheric irradiances and θs was solar zenith angle. Solar exoatmospheric irradiance and Rayleigh optical thickness within pass band of the real-time drone sensor were then calculated for the capture point, LULC, signature, geometric, time series RGB, eco-endmember, inhomogeneously canopied optical prognosticators.

Incident solar radiation at the Earth's surface is the result of a complex interaction of energy between the atmosphere and the surface, This physically-based solar radiation formulations was modeled employing interaction over topographic and plant canopies of the county abatment, potential super breeder, geo-spectro temporal, geosampled, eco-georeferenceable, Ae aegypti, waste tire,larval habitat, capture points based on range of spatial and temporal scales. We summarized the solar radiation, wavelength, capture point, county abatement, frequency LULC signature models within both real-time ArcGIS and the object based, UAVdashboard, image processing systems. An overview of the effects of topography and the plant canopies on solar radiation real-time realizations rendered from the solar radiation models was provided in the real-time dashboard. We considered issues of design, including error propagation in the unmixed signatures. For calculating the solar exoatmospheric irradiance and Rayleigh optical thickness within the super breeder, seasonal, inhomogeously canopied, LULC, *Ae. aegypti,* larval habitat, reference sub-meter resolution, RGB eco-endmember signatures, modern Rayleigh scattering calculations were employed within the real-time, drone dashboard, ENVI Opticalscape. which generated real-time, Digital Surface Models (DSMs) and orthorectified images from the UAV imaged, canopy, capture point, data.

Opticalscape, UAV processed, multiple stereo, Hillsborough county abatement, LULC images and created, orthorectified mosaicked capture point, Ae aegypti, larval habitat signature, iteratable, interpolative images while correcting for sensor orientation. Spectral data on solar radiation, Rayleigh scattering, ozone absorption and absorption were critically evaluated.

Employing ENVI image and data analytic capabilities within the real-time UAV environment enabled the use of a drone app to access ENVI analytics. The uncoalesced signature, sub-meter resolution wavebands were transformed to minimize the depth-dependent variance in the reflectance, waste tire, *Ae. aegypti,* capture point signal. Deploying ENVI analytics through our real time platform successfully helped data migrate to a drone cloud.

We visualized and exported elevation profile data with a Pix4D Cloud. We created an elevation profile in Pix4D Cloud in the real-time UAV dashboard. The on Pix4D Cloud uploaded a georeferenced digital surface waste tire, *Ae. aegypti,* capture point, LULc signature, RGB eco-endmember frequency, model which processed on a Drones and photogrammetry software are empowering organizations to transition to smart asset management. [http://futureaerial.com/future-drone-cloud/] Drone-real-time mapping helped to create and maintain up-to-date, epi-entomological, capture point, waste tire, frequency, eco-georeferenecable, signature, UAV databases of the Hillsborough county study site.

Rayleigh optical thickness may be remotely quantifiable using dry atmosphere for a given relative optical air mass or solar elevation angle in a radiative transfer model [Tyler AN [88]]. Hence we assumed the results from the radiative transfer geosampled, real-time, UAV, frequency, signature model may be comparable to the corresponding unmixed, LULC, sub-meter resolution gesampled, county abatementAe aegypti, super breeder, seasonal, waste tire, larval habitat, capture point, iteratively, interpolative, RGB, eco-endmember,unmixed dataset.We assumed that this process was calculable with multiple parameterization formulae in a real-time drone dashboard.

The DN values converted radiance, seasonally prolific, eco-georeferenced, waste tire, *Ae. aegypti,* larval habitat, to seasonal, LULC values in ENVI. Thereafter, these radiance values were converted to RGB specified, capture point, larval habitat, reflectance values. The formula to convert DN to radiance values was based on gain and bias within where: Lλ was the radiance estimate and DN was the grid cell value. It was noted that DN gain was the gain value for a specific band and bias was the deviated value for any specific, reclassified, geosampled, LULC, *Ae. aegypti,* capture point, wavelength, reflectance band. The ENVI formula in Band Math was 0.05518 * (B1) + 1.2378 which was calculated employing an eco-georeferenceable, county abatement, artificial, super breeder, seasonal, LULC, larval habitat, county abatement, capture point, with a scene specific gain value of 0.05518 and an offset value of 1.2378 for each sub-meter resolution, waste tire, LULC signature. In the Band Pairing dialog B1 was matched with the appropriate optical band. The formula employed in the classification process was as follows:

$L_\lambda = \left(\left(LMAX_\lambda - LMIN_\lambda \right) / \left(QCALMAX - QCALMAX \right) \right) * \left(QCAL - QCALMIN \right)$ where: Lλ was the grid cell value as radiance, QCAL was the DN, LMIN was the spectral radiance scales to QCALMIN, LMAXλ was the spectral radiance scales to QCALMAX, QCALMIN was the minimum sub-meter resolution, LULC, signature, capture point, values and QCALMAX was the maximum quantitable radiance to ToA reflectance, larval habitat, pixel value(i.e.,255).

The formula $p_\lambda = \pi^* L_\lambda * d^2 / ESUN_\lambda * \cos\theta_s$ was employed to optimally quantitate multiple illumination, viewing angle, reflectance variables, emitted from the capture point, LULC, *Ae. aegypti* -related, super breeder, seasonal, sub-meter resolution, unmixed datatset of RGB, eco-endmember, geosampled county abatement, explanatory, canopied, frequency, covariate coefficients. In the formula ρλ was the unitless plantary reflectance; L was the waste tire, larval habitat, spectral radiance; d was the Earth-Sun distance in astronomical units; ESUNλ was the mean solar exoatmospheric irradiances and θs was solar zenith angle. Solar exoatmospheric irradiance and Rayleigh optical thickness within pass band of the real-time drone sensor were then calculated for the capture point, LULC, signature, geometric, time series RGB, eco-endmember, inhomogeneously canopied optical prognosticators.

Incident solar radiation at the Earth's surface is the result of a complex interaction of energy between the atmosphere and the surface, This physically-based solar radiation formulations was modeled employing interaction over topographic and plant canopies of the county abatment, potential super breeder, geo-spectro temporal, geosampled, eco-georferenceable, Ae aegypti, waste tire, larval habitat, capture points based on range of spatial and temporal scales. We summarized the solar radiation, wavelength, capture point, county abatement, frequency LULC signature models within both real-time ArcGIS and the object based, UAVdashboard, image processing systems. An overview of the effects of topography and the plant canopies on solar radiation real-time realizations rendered from the solar radiation models was provided in the real-time dashboard. We considered issues of design, including error propagation in the unmixed signatures. For calculating the solar exoatmospheric irradiance and Rayleigh optical thickness within the super breeder, seasonal, inhomogeously canopied, LULC, *Ae. aegypti,* larval habitat, reference sub-meter resolution, RGB eco-endmember signatures, modern Rayleigh scattering calculations were employed within the real-time, drone dashboard, ENVI Opticalscape. which generated real-time, Digital Surface Models (DSMs) and orthorectified images from the UAV imaged, canopy, capture point, data.

Opticalscape, UAV processed, multiple stereo, Hillsborough county abatement, LULC images and created, orthorectified mosaicked capture point, Ae aegypti, larval habitat signature, iteratable, interpolative images while correcting for sensor orientation. Spectral data on solar radiation, Rayleigh scattering, ozone absorption and absorption were critically evaluated.

Employing ENVI image and data analytic capabilities within the real-time UAV environment enabled the use of a drone app to access ENVI analytics. The uncoalesced signature, sub-meter resolution wavebands were transformed to minimize the depth-dependent variance in the reflectance, waste tire, *Ae. aegypti,* capture point signal. Deploying ENVI analytics through our real time platform successfully helped data migrate to a drone cloud.

We visualized and exported elevation profile data with a Pix4D Cloud. We created an elevation profile in Pix4D Cloud in the real-time UAV dashboard. The on Pix4D Cloud uploaded a georeferenced digital surface waste tire, *Ae. aegypti,* capture point, LULc signature, RGB eco-endmember frequency, model which processed on a Drones and photogrammetry software are empowering organizations to transition to smart asset management. [http://futureaerial.com/future-drone-cloud/] Drone-real-time mapping helped to create and maintain up-to-date, epi-entomological, capture point, waste tire, frequency, eco-georeferenceable, signature, UAV databases of the Hillsborough county study site.

Rayleigh optical thickness may be remotely quantifiable using dry atmosphere for a given relative optical air mass or solar elevation angle in a radiative transfer model [Tyler AN [88]. Hence, we assumed the results from the radiative transfer geosampled, real-time, UAV, frequency, signature model may be comparable to the corresponding unmixed, LULC, sub-meter resolution gesampled, county abatementAe aegypti, super breeder, seasonal, waste tire, larval habitat, capture point, iteratively, interpolative, RGB, eco-endmember, unmixed dataset. We assumed that this process was calculable with multiple parameterization formulae in a real-time drone dashboard.

We employed tht Penndorf method [89] for calculating Rayleigh optical thickness of the intermittent canopy of the eco-georeferenced, super breeder, seasonal LULC, Ae aegypti, waste tire, larval habitat, capture points. In Penndorf's paper, the refractive index is calculated using the equation of Edlén: $(n-1)\times10^8 = 6432.8 + \frac{2949810}{146-\lambda^{-2}} + \frac{25540}{41-\lambda^{-2}}$ where ns is the refractive index and λ is the wavelength in micrometers. We assumed that by quantitating an empirical relationship in a real-time, eco-entomological, vulnerability, object-oriented, LULC, sub-meter resolution, signature, frequency model, we would be able to optimally identify eco-georeferenceble, unknown, geolocations of seasonal, super breeder, *Ae. aegypti,* larval, habitat, county abatement foci by optimally fitting the best available experimental, signature, time series, RGB eco-endmember frequency dataset which was not dependent on the composition of air, particularly CO_2 and water vapor of the capture point.

Rayleigh scattering coefficient employing the equation: in the real-time, UAV dashboard ArcGIS where σ was the scattering cross section; Ns was LULC density; the term (6 + 3ρ)/(6 − 7ρ) was the depolarization term, (i.e, the King factor); and ρ was the depolarization factor or depolarization ratio, which was described as the effect of the anisotropy in the entomological, real-time UAV, geosampled, unmixed, LULC, wavelength dataset. Anisotropy is the property of being directionally dependent, which implies different properties in different directions,

as opposed to isotropy which can be defined as a difference, when measured along different axes, (absorbance, refractive index, conductivity, tensile strength, etc.). The Rayleigh-scattering optical depth is used to measure the overall attenuation of incoming direct solar irradiance along the vertical atmospheric path due to the scattering effects produced by air molecules. This quantity is dimensionless since it is given by the integral of the volume Rayleigh-scattering coefficient along the vertical path of the atmosphere, including all the molecular-scattering effects produced by the Rayleigh component consisting of the molecular scattering that occurs "without change of frequency" and the Raman component "as the Raman-scattered photons have come from the incident beam, just as the unshifted photons have" [90].

Here, we assumed that the Rayleigh optical depth could be defined by an appropriate term comprising both Rayleigh scattering and vibrational Raman scattering effects, in an unmixed, waste tire, LULC signature, RGB eco-endmember, Ae aegypti, iterative, interpolative, forecast, vulnerability model for optimally remotely targeting potential, eco-georeferenceable, seasonal, super breeder, waste tire, larval habitat in a real-time UAV dashbiard where the Rayleigh-scattering component consisted of rotational Raman lines and the central Cabannes line; the latter being composed of the Brillouin doublet and the central Gross or Landau–Placzek in the dashboard. A simple modification was proposed in which the effect of dispersion of the county abatement, epi-entomological, study site, capture point, eco-georeferenced, potential, seasonal, super breeder, waste tire, Ae aegypti, larval habitat radiance was included by defining βshs=1/(ρvhs2), in the breeding site, foci model where vhs was found from the experimentally measured Brillouin shift. Brillouin scattering (BLS) may be defined as inelastic scattering of light in a physical medium by thermally excited unmixed endmembers Schowengerdt RA [90]. We proved gridded, LULC, signature parameters for the description of Rayleigh scattering in air and for the detailed rotational Raman scattering component for scattering by O2 and N2 are presented for the wavelength range 200–1000 nm. These unmixed, sub-pixels, LULC, signature parameters enabled more accurate optical, frequency, geometric calculations to be made of bulk molecular scattering in the real-time platform of the eco-georwferenced, potential, seasonal, super breeder, capture point.

A real-time, unmixing formula in the UAV dashboard was employed for calculating the iteratively interpolatable, eco-georeferenceable, shade-canopied, super breeder, seasonal, county abatement, waste tire, Ae aegypti, larval habitat, capture point, LULC reflectance where (r) was tv Eo stz EdLs Lp d+-=qpr (cos (). In this equation Lp denoted path radiance, d-earth to sun distance in astronomical units, Eo –band pass exoatmospheric irradiance, Ed - down welling spectral irradiance from the atmosphere, tv – atmospheric transmittance along the path from the geosampled, eco-georeferenceable, county abatement, LULC Ae.aegypti, capture points, to the sub-meter resolution, UAV real-time, image sensor, and tz – atmospheric transmittance along the path from the sun to ground. The transmittance terms were then calculated employing the equations: tv= exp (-t secq v) and tz = exp (-t secq s). Here vq and sq were respectively, the zenith angles of the sun and sensor. The parameter t was the total optical thickness of the atmosphere, which included the unmixed, signature, RGB eco-endmember frequency, acquisition in the drone dashboard, ENVI, real-time, classification algorithms. Out of these, the capture point, LULC, signature, canopy illumination contribution of the larvl habitat canopied, RGB eco-endmember frequencies was calculated which depended strongly on the uncoalesced, waste tire, super breeder, eco-georeferenecable, *Ae. aegypti,* larval habitat, iteratively interpolative, reflectance wavelengths which were estimated from r = exp (-0.1188* h - 0.00116* h2) {0.00859 *l-4 (1 + 0.0013*l-2 + 0.00013*l-4)} where h was the height of, canopy, shade-vegetated, eco-endmember, geosampled, county abatement, LULC surfaces above sea level.

The solar zenith angle of the eco-georeferenced, grid-stratfiable, LULC, county abatement, unmixed signature, capture points was then calculated employing the Solar Position Calculator in the real-time, drone dashboard. The solar zenith angle is the angle measured from directly overhead to the geometric centre of the sun's disc, as described using a horizontal coordinate system. The horizontal coordinate system is a celestial coordinate system that employs the observer's local horizon as the fundamental plane. It is expressed in terms of altitude (or elevation) angle and azimuth. The solar elevation angle is the altitude of the sun, the angle between the horizon and the center of the sun's disc [29,91].

In the real-time, UAV platform, ENVI image classification, we re-wrote θs for the solar zenith angle for the eco-georeferenceable, sub-meter resolution, unmixed, waste tire, capture point, *Ae. aegypti,* LULC, signature, frequency, model estimators. In so doing, the solar elevation angle αs = 90° – θs was optimally rendered for the larval habitat, discontinuous, LULC signatures. Subsequently, ENVI's Radiometric Calibration tool calibrated the real-time, UAV, geosampled, potential, super breeder, county abatement, eco-georeferenceable, seasonal, *Ae. aegypti,* larval habitat, LULC imagery from radiance and ToA reflectance. An atmospheric correction tool Fast Line-of-sight Atmospheric Analysis of Spectral Hypercubes (FLAASH®) then removed the noisy, RGB, eco-endmember effects of the capture points. In so doing, robust, surface reflectance of the geosampled, capture point, temporal data was obtained. FLAASH automatically scales reflectance data by 10,000 to produce integer data, which consumes less disk space (www.ittvis.com/portals). Other tools in ENVI such as Dark Subtraction, Empirical Line Correction, Flat Field Correction, and Internal IAR Reflectance Correction also aided in correcting propagational, non-normal, radiometric, LULC, signature, deviant effects for preparing the multispectral, sub-meter resolution, capture point, super breeder, seasonal, eco-georeferenceable, *Ae. aegypti,* geo-spectro temporal, geosampled, signature waveband, data for generating iteratively quantitative, interpolative, spectrally unmixed, RGB, eco-endmember, signature indices.

Once an optimizable, geo-spectro temporal, sub-meter resolution, RGB, eco-endmember, unmixed frequency dataset of iteratively interpolative, explanatorial, field-operationizable, eco-georeferenecable, time series, LULC, signature, covariates was constructed, ENVI® spectral tools were employed to analyze the real-time, UAV dashboard, LULC images of the eco-georeferenced, waste tire, capture point, super breeder, seasonal, county abatement, *Ae. aegypti* immature habitats by red and NIR band wavelengths. We input the data into ENVI® technology em-

ploying the GeoTIFF format. ENVI supports Input File functions including GeoTIFF, NITF and Tile Product (.til) (www.ittvis.com/portals). In ENVI a spectrum plot, known as a z-profile, of the pixel under the cursor was run through all bands of the real-time, UAV captured, *Ae. aegypti,* capture point, LULC images. The basic workflow involved importing the decomposed real-time, signature frequency data collected at the ento-epidemiological, county abatement, study site from the eco-georeferenced, field-operationizable, geosampled, intermittently canopied, super breeder, *Ae. aegypti,* larval habitat, seasonal, capture point, LULC signature, UAV geosampled data into a spectral library. A spectral library was employed in the eco-endmember collection workflow to perform a supervised classification, based on the reflectance values of each unmixed, capture point, LULC, image attribute and the waste tire. signature, capture point, eco-georeferenced, RGB, uncoalesced, eco-endmember frequency. Binary Encoding, SAM, SID and Spectral Feature Fitting were employed to rank and match any unknown spectrum to the materials in the UAV spectral library.

The sub-meter resolution, LULC, imaged, capture point, RGB eco-endmembers of the eco-georeferenced, waste tire, potential, super breeder, county abatement, *Ae. aegypti,* larval habitat, reference LULC signatures and its associated shade-vegetated, partially canopied, unmixed attributes were then extracted from the real-time, UAV dashboard, ENVI spectral library. Several derivative signature decomposed spectra corresponding to the different backgrounds in the geosampled, larval habitat (i.e., rippled, water, pixel components) county abatement scenes had to be included, since multiple scatterings between floating leaves in the habitat, for example, and a bright soil background increased the NIR reflectance of each UAV generated product in the real-time, object-based classifier. Leaf cells have evolved to scatter (i.e., reflect and transmit) solar radiation in the NIR spectral region [92].

After the calibration of the spectrally dependent, explanatorial, waste tire, capture point, eco-georeferenceable, partially shade-canopied, *Ae. aegypti,* larval habitat, unmixed, LULC coefficients, we determined if the county abatement images could be converted to match spectral contents within the real-time ENVI library. Analogously, the reference, capture point, decomposed, LULC signatures and RGB, eco-endmember, derivative spectra in the library were transformed into larval habitat, geosampled, real-time acquired images. We employed a random selection of the capture point LULC pixels to assess the classification accuracy. Each image class representative, larval habitat, county abatement, capture point pixel was then selected and compared to a reference, RGB, training dataset. During the segmentation procedure, image objects were generated based on several adjustable criteria of homogeneity such as color, shape, and texture.

Data pre-processing involved converting DN to radiance atmospheric correction employing FLAASHTM, and co-registration techniques in the real-time UAV dashboard. FLAASHTM generated multiple waste tire, capture point, eco-georeferenceable, county abatement, LULC signature, sub-meter resolution, frequency models which was stored in the gmd file in the dashboard, ENVI, image, software. The *Ae. aegypti,* larval habitat, waste tire, gridded image, DN to at-sensor radiance was computed at-sensor reflectance for normalizing the solar elevation angle. The equation employed was as follows: $\rho_{BandN} = \frac{(L_{BandN} * Gain_{BandN} + Bias_{BandN}) * D^2}{E_{BandN} * (\cos(90 - \theta) * \pi / 180)}$ where, BandN = Reflectance for Band NLbandN = Digital Number for Band N D = Normalized Earth-Sun DistanceEbandN = Solar Irradiance for Band N. Most eco-georferenceable, sub-meter resolution, seasonal, vector arthropod, capture point, geoclassifiable, grid-stratifiable, LULC, immature, habitat surfaces are not perpendicular to the Sun, and the energy they receive depends on their solar elevation angle (Jacob et al. 2011). The maximum solar elevation is 90° for the overhead Sun. (www.britannica.com/ /solar-elevation-angle). Selected random, capture point, image, sub-meter resolution, gridded, LULC pixels from the thematic map were compared to the reference, uncoalesced, RGB, eco-endmember, frequencies in the drone dashboard. The estimated accuracy for the spectrally extractable, LULC signature, RGB, specified, eco-endmember data was then calculatedemploying where, x was the number of correctly identified capture point pixels, n was the total number of pixels in the geosampled, unmixed, eco-georeferenced dataset, θ was map accuracy while (1-α) was the confidence limit.

1.7. Inverted geometric-optical model

Overhead multi- and hyperspectral imaging has enabled a variety of quantitative remote sensing techniques, such as the determination of the abundance and health of vegetation LULC through the NDVI [Jensen 2005]. In addition, anomaly and target detection have been made possible by advanced matched filter algorithms. Here, the optically geometrically, real-time, derived capture point, LULC surface, waste tire, Ae aegypti, county abatement, eco-georeferenceble, signature reflectance from which the iterative interpolative techniques relied upon was directional, and, as such, was dependent upon the incident solar and receiving detector angles. We assumed that quantitatively augmenting the bidirectional reflectance distribution function (BRDF) may compensate for any misspecified, anisotropic reflectance of an optimally krigable, eco-georeferenecable, geosampled, sub-meter resolution, real-time, UAV captured, super breeder, seasonal, LULC, county abatement, *Ae. aegypti,* waste tire, larval habitat.

We employed the Li-Strahler geometric-optical model in the drone dashboard ArcGIS module based on the assumption that the remotely quantitative, real-time, BRDF synthesized from the eco-georeferenced, super breeder, seasonal, capture point, *Ae. aegypti,* structural, sub-meter resolution, RGB eco-endmembers could parsimoniously illustrate partially, vegetated, canopy-shaded, eco-georeferenceable, real-time geosampled super breeder, seasonal, LULC, variables from an NDVI, UAV risk map. The Li-Strahler geometric-optical model [61] is based on the assumption that the BRDF is a purely geometric phenomenon resulting from a scene of discrete, 3-D, LULC, geospatial objects being illuminated and viewed from different positions in the hemisphere. The unmixing technique in this algorithm has been previously described in Jacob et al. [2015]. Briefly, the BRDF for an eco-georeferenced, super breeder, waste tire, LULC, sub-meter resolution, seasonal, county abatement, *Ae. ae-*

gypti, capture point, seasonal foci signature was defined in the real-time drone dashboard by $f_r(\omega_i, \omega_r) = \frac{dL_r(\omega_i)}{dE_i(\omega_i)}$ where L was the radiance, E was the irradiance, and θi was the angle made between ωi and the potential, hyper productive, oviposition, eco-georeferenced, LULC site and its associated unmixed, topological, seasonal, LULC vegetation, reflectance emissivity's. Because the BRDF is a 4-D function that defines how light is reflected at an opaque surface (Jensen 1983), the function in the real-time, drone dashboard, county abatement, *Ae. aegypti,* ArcGIS, frequency models took an incoming light direction, ωi, and outgoing direction, ωo, which were defined in the eco-endmember, capture point, signatures. The eco-georeferenced habitat and its neighboring canopy, LULC vegetation n was mapped in real time. The ratio of reflected, capture point, larval habitat, RGB radiance exiting along ωo returned to the irradiance incident from direction ωi. Each direction ω was itself parameterized by azimuth angle φ and zenith angle θ, therefore, the BRDF was 4-D. The BRDF had units sr−1, with steradians (sr) being a unit of solid angle.

We also optimally quantitated Lambertian reflection in the sub-meter resolution, LULC signature, partially shade-canopied, seasonal, county abatement, *Ae. aegypti,* RGB eco-endmember, capture point, waste tires. In computer graphics, Lambertian reflection is often used as a model for diffuse reflection [McCree KJ (1981) Photosynthetically active radiation. Encyclopedia of Plant Physiology 12: 41-55]. This technique caused all closed, signature, *Ae. aegypti*, capture point, RGB, UAV, real-time, grid-stratified, LULC polygons (such as a triangle within a 3D mesh), to reflect light equally in all directions. We assumed that the waste tire, LULC, larval habitat, capture point canopy changed the way it reflects light if it is tilted away from its initial normal vector, since the area would be illuminated by a smaller fraction of the incident radiation. Hence, the reflection of the county abatement, LULC, grid-stratefied, capture point, polygons was calculated by taking the dot product of the surface's normal vector, and a normalized light-direction vector, L, pointing from the surface to the light source in the real-time, drone dashboard. This number was then multiplied by the color of the eco-georeferenceable, geoclassified, capture point, LULC surface and the intensity of the light of the canopy surface: where was the intensity of the diffusely reflected light (i.e., larval habitat surface brightness), was the color and was the intensity of the light in the ENVI, image software. Because $L.N = |N||L|\cos\alpha = \cos\alpha$, where was the angle between the direction of the two vectors in the sub-meter resolution, Ae aegypti, LULC, sub-meter resolution, RGB, eco-endmember, super breeder, capture point, seasonal model, the illumination intensity was the highest when the vector pointed in the same direction as the light vector (i.e., $\cos(0) = 1$ When the surface is perpendicular to the direction of the light, the normal vector is perpendicular to the light vector (i.e., $\cos(\frac{\pi}{2}) = 0$, the surface runs parallel with the direction of the light) [85].

The inverted, sub-meter resolution, geometrical, *Ae. aegypti,* LULC signature, sub-meter resolution, RGB, eco-endmember, real-time, frequency model was then employed to retrieve specific uncoalesced, geospectral, waste tire, intermittently canopied, explanatorily, reflectance, (e.g., stochastically co-krigable), time series, super breeder, seasonal eco-georeferenceable, coefficient estimates. The RGB reflectance associated with the eco-georeferenced, LULC super breeder, seasonal, capture points were treated as an area-weighted sum of four fixed reflectance components: sunlit canopy, sunlit background, shaded canopy, and shaded background in real-time. In the geoclassified, shade-vegetated, LULC, partially canopied, waste tire, capture point, *Ae. aegypti,* larval habitat, RGB, eco-endmember, signature model, these four components were simplified to three: sunlit canopy–C, sunlit background–G and shadow–T. The eco-endmember, unmixed, spectrally, grid-stratifiable, county abatement, sub-meter resolution, UAV imaged, LULC components were optimally derived using G, C, T components' classes which were estimated by the the real-time imagery in ENVI®.

For inverting the seasonal, super breeder, eco-georeferenceable, waste tire, capture point, sub-meter resolution, *Ae. aegypti,* LULC, capture point, real-time, UAV model, parts of the three spectral components were represented by (Kg) which we calculated employing:

$$K_g = e^{-\pi - M\left[\sec(\theta_1) + \sec(\theta_1) - 0\right]}$$

where, I q u q were the zenith angles of illumination and viewing. In the real-time, RGB, eco-endmember, capture point LULC, drone analyses, O was the average of the overlap function between illumination and viewing shadows of the imager, sub-pixel, decomposed signatures and the larval habitat's associated canopy floating and hanging, dead vegetation, geoclassifiable components as projected onto the background. j was the difference in azimuth angle between illumination and viewing in each signature, sub-pixel, real-time, RGB, model frequency, parameter estimator.

Boolean models were then generated in the ENVI platform. The equation was employed where k was expressed as and where $\overline{0}(\theta_1, \theta_2, \phi)$ was the average of the overlap function $0(\theta_1, \theta_2, \phi, h)$ between illumination and viewing shadows of the county abatement, geosampled, potential seasonal, eco-georeferenceable, super breeder, *Ae. aegypti,* waste tire, capture point, larval habitats and their associated, iteratively interpolative, sub-pixel, grid-stratifiable, discontinuously canopied, LULC, derivative, unmixed, feature attributes. The Boolean model for a random subset of the plane or higher dimensions, analogously is a common tractable model in stochastic geometry [Schowengerdt RA (2007) Optical radiation models in Remote Sensing: models and methods for image processing, 45-88. Amsterdam. Academic Press]. Canopy structure was described in the real time, frequency dashboard with arrays of asymmetric crown envelopes, adaptable to various LULC geometries (height at crown insertion and at the greatest width of the crown, crown radii in four orthogonal directions, and shape coefficients of vertical crown profiles). Unlike previous models, this canopy model can simulate the high level of asymmetry in crown shape and displacement typical of natural and semi-natural forests (Huete AR [18]). Within an individual crown, the vertical distribution of leaf area density (LAD) was modelled using the Beta or Weibull equationin the real time UAV platform.

The effect of the spatial pattern of canopy, capture point leaf area was considered by simulating random, regular or clumped distributions. Parameters related to the super breeder, seasonal, county abatement, capture point waste tire, canopy architecture (vertical and spatial distribution of the leaf area, angular distribution of the leaf normal) were treated as species-specific, so that mixed LULCs could be optimally eco-cartographically represented in the real-time, UAV dashboard, ENVI image software. Light penetration was modelled by the 'turbid medium hypothesis'; that is, by computing the beam path length and the LAD within single crowns with a high angular resolution (0.05–5 deg). Diffuse fluxes generated by reflection and transmission of intercepted radiation were simulated by the Adding method in ENVI, based on the capture point, leaf scattering, larval habitat coefficients. Employing the UAV frequency model, the distribution of radiation intensity and derivateive capture point, spectra beneath heterogeneous, LULC canopies were analyzed in time and space at sub-meter resolution. The object-oriented approach did not impose any limit to the number of capture points in an experimental gridded plot. was the difference in azimuth angle between viewing and illumination positions of the real-time, UAV imaged, county abatement, epi-entomological, intervention, study site, larval habitat, capture point, geo-spatial, eco-georeferenced, LULC objects associated to the super breeder, grid-stratifiable, seasonal, *Ae. aegypti* foci. To simplify the equation, the overlap function was approximated by the overlap area and center positions of the ellipses. This approximation is justified when solar zenith and viewing zenith angles are not too large [see Baret F [92]]. In the case of long ellipsoidal shadows i.e., ij, the capture point, larval habitat, sub-meter resolution, county abatement, gridded images, however, this approximation could have overestimated the width of the super breeder, seasonal, Ae .aegypti, immature, habitat, county abatement, capture point, eco-georeferenceble, LULC hotspots in the azimuthal direction and by so doing, underestimated the width of the hotspot. To improve the accuracy and preserve the proper hotspot, another signature approximation was developed in the real-time, drone dashboard ArcGIS as follows; First, the overlap function was determined in the principal plane. W and were employed as the elliptical, illuminative, LULC, signature, capture point, RGB, eco-endmembers and then the viewing shadows were aligned in the same direction. The overlap area was approximated by an ellipse with one axis equal to the overlap length and the other equal to the capture point, *Ae. aegypti,* super breeder, seasonal, larval habitat width encompassing the hanging, floating and dead vegetation, geospectral, explanatorily, capture point, LULC, waste tire, sub-pixel, decomposed, signature components which was yielded by $0\left(\theta_1, \theta_v, \phi\right) = \dfrac{1}{2}\left[\sec\theta_1' + \sec\theta_v' - \dfrac{h}{2}\right]$

Our real-time, Boolean, LULC signature, vulnerability analyses optimally represented the decomposed, capture point, potential, super breeder, seasonal, waste tire, *Ae. aegypti,* larval habitat, shade-vegetated, partially canopied, RGB eco-endmembers as a vector in the county abatement models. Vector space is an algebraic model for representing text documents and any objects, in general as vectors of identifiers, such as, for example, index terms [Jensen 2005]. Each I dimension corresponded to a separated, sub-meter resolution, RGB eco-endmember (e.g., floating shaded LULC vegetation). A final LULC, signature was generated (Figure 8)
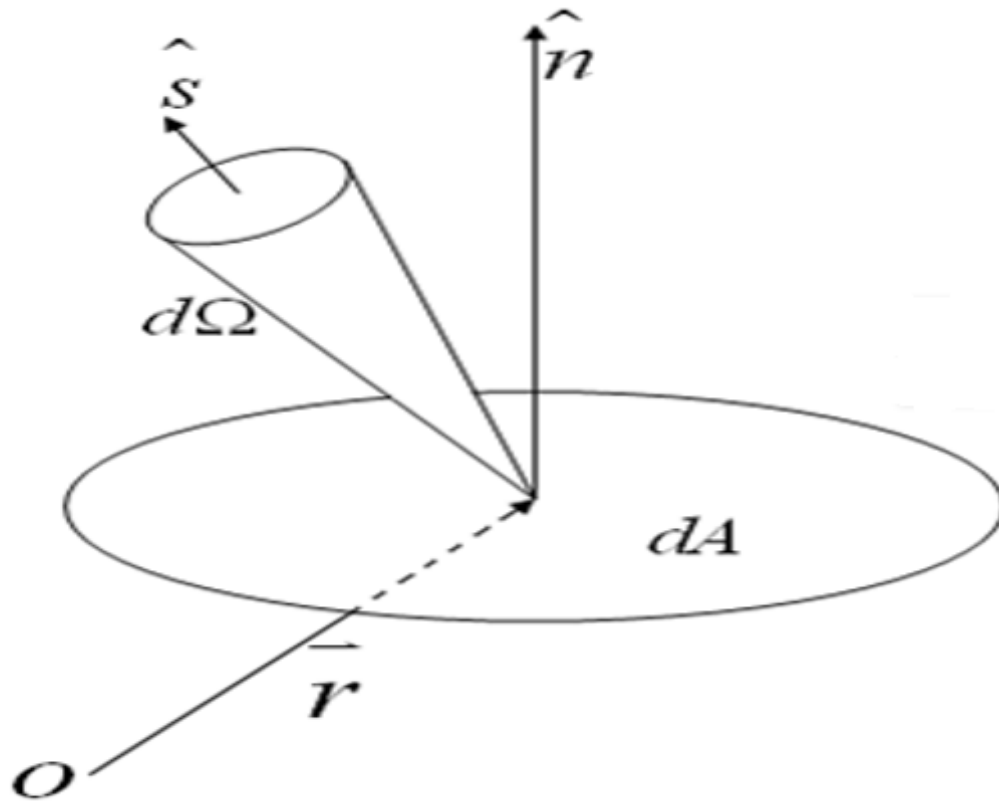

Figure 8: The Ae aegypti habitat LULC signature discontinuous canopy energy flux as calculated by in the real-time drone dashboard in UAV diffusion equation.

Interpolation analyses

Waveband, LULC, signature, unmixed, explanatorial, eco-georeferenced, predictors were generated from the eco-georeferenced, RGB eco-endmember, capture point, geosampled datasets of waste tire, artificial, potenetial super breeder, county abatement, *Ae. aegypti,* larval habitats employing an Ordinary kriged-based equation in the real-time, UAV, frequency dashboard ArcGIS. We stochastically, iteratively, interpolated the signature, LULC capture point values over the real-time, drone geosampled, sub-meter resolution images of the county abatement study site. The algorithms for our interpolation have already been described in Jacob [76]. Briefly, the dependent variable was the spectrally illuminated, eco-georeferenced, LULC signature estimates generated from the unmixed, capture point, *Ae. aegypti,* capture point, RGB, emissitives which was transformed to fulfill the diagnostic normality test prior to performing the kriging in the drone, real-time ArcGIS. The kriged-based algorithm was employed to generate county, abatement, predictive, larval habitat, LULC, risk maps. In order to parsimoniously interpolate the value $Z(x0)$, the decomposed, eco-georeferenced, *Ae. aegypti,* waste tire, larval habitat, RGB, spectral values $Z(x)$ and the capture point's associated partially, shade-vegetated, canopied, LULC components x0was used where zi = Z (xi), i = 1...,.In the epi-entomological, geo-spectro temporal, geosampled, probabilistic drone paradigm, n represented forecastable, eco-georeferenceable, prolific, unknown, immature, habitat geolocations, x1, xn.

Ordinary kriging was computed as an unbiased, grid-stratifiable, waste tire, potential super breeder, seasonal, larval habitat, capture point, sub-meter resolution, LULC, signature estimator, [i.e., Ž(xo) of Z(x0)], based on the, geosampled, real-time drone captured, krige model, parameterizable, frequency estimators. The dependence in the model was quantitated by a variogram γ (x, y) and by the expectation μ(x) = E[Z(x)] and the covariance function (x, y) of the random field. The super breeder, seasonal, LULC signature, waste tire, Ae aegypti, geosampled, iteratively interpolative, parameter estimator was given by a linear combination of the algorithm: employing the decomposed, partially shade-canopied, capture point, county abatement, RGB, datasets where zi = Z(xi) with their respective eco-endmember, capture point weights wi (xo), i = 1,...,n were chosen such that the variance in the autoregressive, eco-endmember, wavelength model was optimally tabulated by

$$-b\sum_{i=1}^{n}x_{\gamma}^{2}+(1-b^{2})\sum_{i=1}^{n}x_{\gamma}y_{\gamma}+b\sum_{i=1}^{n}y_{\gamma}^{2}+\frac{1}{n}(b^{2}-1)\left(\sum_{i=1}^{n}y_{\gamma}-b\sum_{i=1}^{n}x_{\gamma}\right)\sum_{i=1}^{n}x_{\gamma}\sum_{i=1}^{n}x_{\gamma}-\frac{2}{n}\left(\sum_{i=1}^{n}y_{\gamma}-b\sum_{i=1}^{n}x_{\gamma}\sum_{i=1}^{n}x_{\gamma}\right)b\sum_{i=1}^{n}y_{\gamma}+\frac{b}{n}\left(\sum_{i=1}^{n}y_{\gamma}-b\sum_{i=1}^{n}x_{\gamma}\right)^{2}=0$$

A Voronoi diagram was constructed along with the geosampled, explanatorial, eco-georeferenceable, *Ae. aegypti,* larval habitat, super breeder, seasonal, capture points as the center of the decomposed, signature polygons employing the Weighted Voronoi Diagram Extension in the real-time drone dashboard ArcGIS. This model was constructed for spatially rectifying geosptially erroneous eco-epidemiological, county abatement, study site, eco-georeferenecable, LULC variables. Using the Generate tab in ArcGIS Spatial Analyst, in the drone dashboard, a weighted Voronoi diagram was generated in in real-time, from the forecasted unknown, waste tire, LULC capture point RGB sub-meter resolution eco-endmember features.

The Voronoi Diagram was generated in the UAV real-time dashboard, whereby, a forecasted, unknown, potential, super breeder, seasonal, Ae aegypti, waste tire, larval habitat, was associated with pi (i.e., spectral grid-stratifiable, RGB, unmixed eco-endmembers) in each real-time, LULC, signature, UAV, geosampled, sub-meter resolution model using $P = \{p_1, ..., p_n\}$ where $2 \le n \le \infty$ and $x_i \ne x_j$ for $i \ne j$, i, $j \in$ I$_n$. The gridded, county abatement, LULC region was given by V(p$_i$) = {x: || x - x_i|| ≤ || x - x_j || for $j \ne i$, $i \in$I$_n$} which was the Ordinary Voronoi polygon associated with *p.* The set given by V = {V(pi), ..., V(pn)} was the planar Ordinary Voronoi diagram generated by P. A planar ordinary Voronoi, waste tire, super breeder, seasonal, eco-georeferenceable, *Ae. aegypti,* capture point, real-time, LULC diagram was then defined with half planes as follows where P = {pi, ..., pn} R2, where 2 ≤ n ≤ ∞ and xi ≠ xj for i ≠ j, i, j In. We called the region which was the ordinary Voronoi polygonised boundaries in each seasonal, super breeder, *Ae. aegypti,* larval habitat, real-time UAV, geosampled, county abatement, LULC signature, RGB, sub-meter resolution, eco-endmember, frequency model associated with pi and set V(P) = {V(p1), ..., V(pn)}. The planar Ordinary Voronoi diagram was then generated by P. A raster image showing normal Euclidean distances and adjusted Euclidean distances was then created in real-time as well as a Voronoi polygon shapefile. The unmixed, capture point, potential, super breeder, seasonal, *Ae. aegypti* larval habitat, shade-canopied, eco-georeferenced, iteratively interpolated, signature frequency, signature, data, feature attributes were then transferred to Voronoi polygons automatically by appending the geo-spatialized, LULC, signature attributes of one layer to another in the drone dashboard, real-time ArcGIS.

1. Results

We employed a Worldview 2, (4 band imagery), real-time, NDVI, eco-endmember, detection analysis in the drone dashboard ArcGIS module. Our proposed technique was to evaluate NDVI signatures on geosampled LULC for identifying. potential, super breeder, seasonal, *Ae. aegypti,* eco-georeferenceable, capture points in Hillsborough county and then subsequently run a Random Classification in the real-time, UAV dashboard. We followed the guidance outlined in the Digital Globe Radiometric Use of Quick Bird Imagery document, a to make the county, abatement imagery, comparable based on signatures between eco-georeferenced, waste tire, capture points on specific geoclassified LULCs. Our workflow included converting DN to ToA spectral radiance employing the drone dashboard, ArcGIS raster calculator. We then ran the NDVI and the waste tire, capture point, *Ae. aegypti,* larval habitat, sub-meter resolution, geo-classifications employing the appropriate ToA band-average, LULC, reflectance layers. From the Digital Globe technical document, the radiometric balancing for multiple scenes was outlined for converting to ToA band-average reflectance for the real time, UAV imaged eco-georeferenced, potential, seasonal, superbrewery, waste tire, county abatement, larval habitat, foci.

Barren LULC areas in the ento-epidemiological, county abatement, intervention, study site was designated a value of 0.1 or less, and dense vegetation LULC was closer to a +1. Here the NDVI was computed by transforming raw, UAV, geosampled, real-time, captures of *Ae. aegypti,* larval habitat, LULC signatures into a new image using object-based algorithms (i.e., SID, SAM). This variable was calculated as the ratio of the difference between NIR and red reflectance bands divided by their sum i.e., NDVI=(ρ_NIR-ρ_RED)/ (ρ_NIR xρ_RED) These two bands were employed for optimally quantitating the capture point, waste tire, eco-georeferenceable, *Ae. aegypti,* larval habitat, LULC, geo-spectral, frequency measures due to their ability to reflect the green dense vegetation and the chlorophyll in the green vegetation LULCs where pNIR was the NIR radiation wavelength and pRED was the red wavelength.

The real-time, Band Math function of ENVI 4.8TM in the real time, drone dashboard was then employed to calculate the unmixed, NDVI, sub-meter resolution, iteratively interpolative, capture point, RGB eco-endmembers. Before applying the spectral index to the larval habitat imagery, raw pixel values, (DNs) were converted into physically meaningful units to differentiate absorption reflectance, capture point, derivative, LULC spectra of a real-time, UAV imaged Ae aegypti, waste tire, county abatement, prolific foci. Linear regression was employed to equate unmixed, waveband, capture point, LULC, grid-stratified data to DN. The model also quantized larval, habitat, capture point, reflectance values which in the sub-meter resolution, RGB, real-time, eco-endmember, frequency, risk analysis was equivalent to removing the solar irradiance and the atmospheric path radiance in the real-time, UAV dashboard. A radiometric calibration tool subsequently calibrated the spaceborne sensor data to radiance and ToA reflectance.

Additionally, Fast Line-of-sight Atmospheric Analysis of Spectral Hypercubes (FLAASH®) removed the effects of scattering in the county abatement, real-time, UAV imaged, larval habitat, capture point, LULC scene. We calculated the internal relative reflectance which normalized the image to a scene average spectrum. ENVI's Log Residuals Correction Tool removed the instrument gain, topographic LULC and albedo effects from the eco-georeferenced, super breeder, seasonal, capture point, *Ae. aegypti,* waste tire, larval habitat, unmixed, RGB, wavelength emissitivities. The instantaneous fraction of direct beam radiation intercepted by the habitat canopies was calculated and described mathematically as fPAR = 1 - exp (-k (LAI)/cosθs) where the extinction coefficient k was a function of leaf angle distribution.

We employed a SPA, a two stream, radiative, atmospheric, transfer analyses, a geometric-optical model and a BDRF to unmix the super breeder, seasonal, larval habitat, shade-vegetated, partially canopied, RGB eco-endmembers, in the real-time, UAV dashboard ArcGIS module. The non-parametric, residually decomposed, sub-pixel, parameter estimators derived from the LULC signature, capture point, larval habitat, ento-epidemiological, time series, signature data were then used to construct a Boolean real-time model. Therefater, the imaged, capture point, eco-georeferenced, *Ae. aegypti,* county abatement, capture point, super breeder, LULC foci and its geospatially associated, within-canopy, pigments were defined and multiple, larval habitat, county abatement, super breeder signatures were decomposed in ENVI.

An autocorrelation matrix was deconvolved into linear combinations of the unmixed, capture point, waste tire, *Ae. aegypti,* LULC endmembers. Subsequently, the NDVI signature, decomposed, explanatorial, canopy eco-endmembers with its multiple ToA noise-adjusted coefficients were adjusted in Geospatial Analyst of ArcGIS 10.3® embedded in the real-time, drone dashboard to identify unknown, un-geosampled, prolific, eco-georeferenceable, waste tire, super breeder, seasonal, *Ae. aegypti,* larval habitats in the county abatement, epi-entomological, study site.

Residual explanatory, diagnostic estimates from the 3-D, time series, NDVI, *Ae. aegypti,* capture point, waste tire signatures were evaluated in a spatial error (SE) model in the real-time, UAV dashboard, real-time, ArcGIS module. An autoregressive LULC, immature habitat model was constructed that employed a seasonal, potential, eco-georeferenceable, super breeder, capture point, inhomogenously canopied, sub-pixel, larval habitat, geosampled, eco-endmember, unmixed wavelength RGB variable, Y, as a function of nearby immature habitat Y, pixel values [i.e., an autoregressive response (AR) or spatial linear (SL) specification] and/or the residuals of Y as a function of nearby Y residuals [i.e., an AR or SE specification]. Distance between the geosampled, capture point, county abatement, waste tire, larval habitats was defined in terms of an n-by-n geographic weights matrix, C, whose cij values were 1 if the geosampled, LULC, super breeder, *Ae. aegypti* breeding site foci count abatement, eco-georeferenced, geolocations i and j were deemed nearby, and 0 otherwise. Adjusting this matrix by dividing each row entry by its row sum, with the row sums given by C1, converted this matrix to matrix W in the real-time, UAV eigen decomposition eigenfunction, spatial filter, orthogonal algorithm in the real time UAV ArcGIS module.

The n-by-1 vector x = [x1 ⋯ xn] T contained measurements of a quantitative, 3-D drone geosampled, real-time, NDVI, capture point, seasonal, eco-georeferenceable, super breeder, *Ae. aegypti,* regress able, partially shade-canopied, unmixed dataset of LULC variables for n spatial units and n-by-n spatial weighting matrix W. The formulation for the Moran's index of spatial autocorrelation in the UAV dashboard ArcGIS was $I(X) = \frac{n \sum_{(2)} W_{ij} (X_i - \bar{X})(X_j - \bar{X})}{\sum_{(2)} W_{ij} \sum_{i=1}^{n} (X_i - \bar{X})^2}$ where with i ≠ j. The values wij were defined as RGB eco-endmember, LULC, signature, frequency weights which were stored in the symmetrical matrix W [i.e., (wij = wji)] that had a null diagonal (wii = 0). The matrix was initially generalized to an asymmetrical matrix W. Matrix W can be generalized by a non-symmetric matrix W* by using W = (W* + W*T)/2 [Griffth 2003]. Moran's I was rewritten using matrix notation: where H = (I - 11T/n) was an orthogonal projector verifying that H = H2, (i.e., H was independent) in the real-time, UAV dashboard, entomological, larval, habitat, real-time, ArcGIS, signature model. Features of matrix W for analyzing a geosampled, seasonal, eco-georeferenceable, sub-meter resolution, larval dataset of unmixed, capture point, time series, sub-meter resolution, LULC signatures of the county abatement, super breeder habitats included that it expressed each observed RGB, eco-endmember, non-frequenctistic value, yi, as a function of the average of the breeding site foci geolocation i's with nearby larval/pupal counts, which allowed a single spatial autoregressive parameter, ρ, to have a maximum value of 1.

A real-time, spatially autoregressive (SAR), epi-entomological, sub-meter resolution, RGB eco-endmember, capture point, LULC, forecast, vulnerability, model specification was employed in the UAV dashboard, ArcGIS module to describe the, variance, uncertainty estimates in the waste tire, Ae aegypti, county abatement, frequency, signature model. A spatial filter (SF) model specification in the dashboard was also employed to describe geoclassifiable, Gaussian, capture point, eco-georeferenceable, county abatement, iteratively interpolative, random, un-mixed, grid-stratified, LULC, signature variables. The resulting SAR model specification took on the following form: (3.1) where μ was the sca-lar conditional mean of Y, and ε was an n-by-1 error vector whose elements were statistically independent normalized, random variates. The spatial covariance matrix for equation (3.1), employing the geosampled, time series, capture point, orthogonally decomposed, LULC, signature, *Ae. aegypti,* larval habitat, sub-meter resolution, RGB, eco-endmember covariates employing E [(Y - μl)' (Y - μl)] = Σ = [(I - ρ W')(I - ρ W)]-1σ2, where E (●) denoted the calculus of expectations, I was the n-by-n identity matrix denoting the real-time, covariance matrix, transpose oper-ation, and σ2 was the error variance in the UAV dashboard, ArcGIS, signature, frequency, forecast, vulnerability model.

When a mixture of positive and negative spatial autocorrelation is present in an entomological, vector arthropod, larval habitat, capture point, county abatement, LULC, signature, super breeder, seasonal, eco-georeferenceable, sub-meter resolution, RGB eco-endmember, risk model, a more explicit representation of both effects may lead to a more accurate interpretation of empirical results. Alternately, the excluded values may be set to zero in the model, although if this is done then the mean and variance must be adjusted in order that the regression model output reveal county abatement, ecogeoreferenceable, geolocations of unknown, potential, seasonal, super breeder, waste tire, Ae aegypti, larval habitat, capture points.

Here, the geospatially autocorrelated, waste tire, super breeder, eco-georeferenecd, real-time, capture points geosampled at the Hillsbor-ough County, eco-epidemiological, intervention, study site was decomposed into stochastic signala and multiple, white noise, LULC, signature, unmixed components. A real-time, vulnerability, forecast map of the stochastic, sub-meter resolution, RGB signals appeared in the UAV dash-board AUTOREG which exhibited spatial patterns based on the spatial filtering procedure. Propagational misspecifications often occur in remotely sensed, vector, epi-entomological, geoclassified, LULC signature, eco-endmember, prognosticative, RGB eco-endmember frequency, vulnerability models due to unquantitable, multiscattering, spatial trend, surface irradiance (see Jacob [67, 84]) which may reval zero autocor-relation (i.e., random chaos) in sampled datasets.

Gaining a better understanding of signature frequency, unmixed, UAV, real-time, data to determine eco-georeferenceble, grid-stratifiable geolocations of unknown, potential, seasonal, super breeder, waste tire, Ae aegypti, larval habitat, and a deeper meaning of spatial statistical, entomological, vector, arthropod prognosticative, time series, vulnerability, model results gleaned from eco-georeferenced, unmixed, capture point, LULC signature data requires a more complete knowledge of RGB eco-endmember properties and the underlying geometry of a potential seasonal, hyper productive, county abatment foci. [11, 68]. Here we addressed these two topics by further investigating important, iteratable interplative, geometric features of the decomposed, real-time UAV data. The importance of this work was expressed in the dashboard employ-ing representations of geographic space. Three conclusions were obtained here. One was sub-meter resolution LULC signature, UAV captured, wavelength, orthogonal, frequency eigenvectors associated with the three largest capture point eigenvalues rendered from a binary, real-time, geographic weights matrix had interpolatable interpretations(i.e., forecastable, noiseless, RGB signature qualities) Secondly, the eigenvalues of the weights matrix provide understanding of the sampling distribution in potential, seasonal, super breeder, waste tire, larval habitats geo-sampled in the Hillsborough county abatement, intervention, epi-entomological, study site, geographic landscape. Finally, the issue of spatial autocorrelation in LULC signature, uncoalesced wavelength RGB eco-endmember, capture point, larval habitat components was gleanable from urban census tract data (www.planhillsborough.org/demographic-economic-data/) and the square tessellations of remotely sensed data (www.planhillsborough.org/gis-maps-data-files/of the county abatement study site on line.

The white noise, waste tire, *Ae. aegypti* laval habitat, potential, eco-georeferenceable, seasonal, superbreeeder, residuals were spatially uncorrelated, that is, they did not exhibit any distinctive, spatial, LULC pattern. Orthogonality synthesized from the real-time, UAV, geosampled, autoregressive, Ae aegypti, waste tire, larval, habitat real-time, eigen decomposition models allowed for precise interpretation of the geosam-pled, sub-meter resolution, capture point, seasonal, county abatement, super breeder, foci stochastic signals which subsequently allowed for robust representation of the spatial and apatial inconspicuous dependencies within the covariance matrix in the UAV dashboard. Here, two different geospatial, autoregressive, sub-meter resolution, grid-stratefiable, LULC, capture point, iteratively interpolative, geosampled, RGB, eco-endmember parameters appeared in the spatial covariance matrix. A waste tire, capture point, Ae.aegypti, larval habitat, unmixed, signa-ture frequency specification, was generated for the SAR model specification, in the real-time, UAV dashboard, ArcGIS module which became: (3.2) where the diagonal matrix of the frequency, autoregressive, unmixed, sub-pixel, orthogonal, LULC, signature components <ρ >diag, con-tained two geosampled parameters: ρ+for those county abatement, capture point, waste tire, immature habitats displaying positive spatial dependency, and ρ. for those habitats displaying negative spatial dependency. For example, by letting σ2 = 1 and employing a 2-by-2 regular square tessellation: for the vector, enabled positing a positive relationship between the capture point, LULC, potential, super breeder, seasonal, county abatement, signature, *Ae. aegypti,* larval habitat, frequency covariates in the UAV dashboard real-time, ArcGIS mod-ule. In the model, y1 and y2 revealed a negative relationship between covariates, while y3 and y4, had no relationship. This covariance speci-fication yielded: and where I+ was a binary (0-1), explanatorial, time series, county abatement, geosampled, wavelength, signature, indicator variable which denoted those LULC, frequency, *Ae. aegypti,* RGB, specified, eco-endmember, capture point, county abatement, larval, habitat

covariates displaying positive spatial dependency, and I- was a binary 0-1 indicator variable denoting the geosampled eco-georferenecable, county abatement, capture points displaying negative spatial dependency, using I+ + I- = 1. Expressing the preceding 2-by-2 example in terms of equation (3.3) yielded:

$$\begin{bmatrix} y_1 \\ y_2 \\ y_3 \\ y_4 \end{bmatrix} = \mu \begin{bmatrix} 1 & 0 & 0 & 0 \\ 0 & 1 & 0 & 0 \\ 0 & 0 & 1 & 0 \\ 0 & 0 & 0 & 1 \end{bmatrix} - \rho_+ \begin{bmatrix} 1 & 0 & 0 & 0 \\ 0 & 1 & 0 & 0 \\ 0 & 0 & 0 & 0 \\ 0 & 0 & 0 & 0 \end{bmatrix} - \rho_- \begin{bmatrix} 0 & 0 & 0 & 0 \\ 0 & 0 & 0 & 0 \\ 0 & 0 & 1 & 0 \\ 0 & 0 & 0 & 1 \end{bmatrix} \begin{bmatrix} 1 \\ 1 \\ 1 \\ 1 \end{bmatrix} + \rho_+ \begin{bmatrix} 1 & 0 & 0 & 0 \\ 0 & 1 & 0 & 0 \\ 0 & 0 & 0 & 0 \\ 0 & 0 & 0 & 0 \end{bmatrix} + \rho_- \begin{bmatrix} 0 & 0 & 0 & 0 \\ 0 & 0 & 0 & 0 \\ 0 & 0 & 1 & 0 \\ 0 & 0 & 0 & 1 \end{bmatrix} \begin{bmatrix} 0 & \frac{1}{2} & \frac{1}{2} & 0 \\ \frac{1}{2} & 0 & 0 & \frac{1}{2} \\ \frac{1}{2} & 0 & 0 & \frac{1}{2} \\ 0 & \frac{1}{2} & \frac{1}{2} & 0 \end{bmatrix} \begin{bmatrix} y_1 \\ y_2 \\ y_3 \\ y_4 \end{bmatrix} + \begin{bmatrix} \varepsilon 1 \\ \varepsilon 2 \\ \varepsilon 3 \\ \varepsilon 4 \end{bmatrix}$$

In the real-time, capture point, sub-meter resolution, grid-stratified, LULC, super breeder, eco-georeferenced, *Ae. aegypti,* waste tire, county abatement, larval habitat, capture points either ρ+ = 0 (and hence I+ = 0 and I- = I) or ρ- = 0 (and hence I- = 0 and I+ = I). As such, equation (3.3) reduced into equation (3.1). These regressed, unmixed, waste tire, eco-georeferenceable, super breeder, seasonal, capture point, LULC signature, spectral, indicator variables generated a signature classification that was parsimoniously constructed in accordance with the quadrants of the corresponding Moran scatterplot in the real-time UAV platform.

The Moran scatter plot is a useful visual tool for exploratory analysis, as it enables assessing how similar an observed value is to its neighboring observations. Its horizontal axis is based on the values of the observations and is also known as the response axis. Here, the vertical Y axis of the eco-georferenced, waste tire, capture point was based on the waste tire, *Ae. aegypti,* seasonal, breeding site, potential, super breeder, foci weighted average, or spatial lag of the corresponding UAV–geosampled, county abatement, real-time specified, LULC signature, unmixed, RGB frequency observations on the horizontal X axis.

The Moran scatter plot in the real-time, ArcGIS, UAV dashboard provided a visual representation of spatial associations in the neighborhood around each eco-georeferenced, super breeder, capture point, LULC observation. The county abatement observations were represented by their standardized signature, RGB eco-endmember frequency values. For each geosampled, potential, county abatement, super breeder, Ae aegypti, seasonal, county abatement foci, the VARIOGRAM procedure in the real-time, UAV, ArcGIS platform computed the weighted average, which was the weighted mean value of its neighbors (i.e., seasonal immature, eco-georeferenceable habitats) Then, the centered weighted average was geo-spectro temporally plotted against the standardized, unmixed, iteratively interpolative, county abatement, geosampled, grid-stratifiable, LULC, signature observations. As a result, the potential, seasonal, super breeder *Ae. aegypti,* larval habitat, waste tire, scatter plot was centered on the coordinates (0,0), in the real-time UAV ArcGIS module and Eucildean distances in the plot were expressed in deviations from the origin (0,0).

Depending on their position on the plot, the Moran plot, data points expressed the levels of spatial association of each potential super breeder, county abatement, waste tire, capture point, eco-georeferenceable, *Ae. aegypti,* larval habitat, unmixed, LULC signature observation with its neighboring ones. Conceptually, these characteristics differentiated the Moran plot from the semivariogram in the real-time, UAV dashboard, ArcGIS module. The latter was used to depict spatial, grid-stratifiable, a eco-georeferenceable ssociations between the forecasted capture point, prolific, unknown, larval habitats across the whole county abatement, epi-entomological, study site domain as a continuous function of a distance metric (e.g., Euclidean distances, between, known county abatement super breeder, eco-georeferenced, waste tire, capture points).

The capture point, LULC, explanatorial, signature, data points on the Moran scatter plot occurred in four quadrants which were defined by the horizontal line y=0 and the vertical line .Points in the upper right (or high-high) and lower left (or low-low) quadrants indicated positive spatial association of the geosampled, iteratively interpolative, unmixed, county abatement, sub-meter resolution, geoclassified, UAV extracted, real-time, LULC, signature RGB eco-endmemebr frequencies that were higher and lower than the sample mean, respectively. The lower right (or high-low) and upper left (or low-high) quadrants included waste tire habitat observations that exhibited negative spatial association; that is, these observed values carried little similarity to their neighboring ones.

We employed binary, row-averaged, LULC weights for the creation of the waste tire, county abatement, super breeder, eco-georeferenceable, Ae aegypti, capture point, larval habitat, real-time, Moran scatter plots in the UAV real-time platform. The autocorrelation statistics was equivalent to the regression slope of the Moran scatter plot. That is, we specified PLOTS=MORAN(ROWAVG=ON) in the PROC VARIOGRAM statement and AUTOCORR (WEIGHTS=BINARY(ROWAVERAGING)) in the COMPUTE statement in the UAV real-time platform. In so doing, the regression line slope of the capture point, eco-georeferenceable, LULC, signature specified, sub-meter resolution, county abatement, scatter plot was the Moran's coefficient shown in the real-time, UAV, ArcGIS, waevlength module. The Moran scatter plot provided a detailed exploratory view of the positive autocorrelation behavior of the individual geosampled, super breeder, county abatement, capture point, potetaial, super breeder, waste tire, seasonal, Ae aegypti, sub-meter resolution, unmixed, eco-georeferenceable, LULC, signature observations. This detailed view revealed outliers ("cold spots") with respect to the regression line slope of the Moran scatter plot in the real-time, drone dashboard ArcGIS.

Negative autocorrelation coefficients may be eco-cartographically, geo-spectro temporally delineated as dissimilar aggregations of image sub-pixel radiance which may be eco-geographically defined as a "cold spot" (Jacob [67]). Extreme observations ('negative autocorrelation') may also be classified as propagation, non-Gaussian noise. A big problem in county abatement pi-entomological, vector arthropod inversti-

gations for determining unknown geolocations of prolific larval habiats seasonal, eco-feorferenceable foci is that the error distribution is usually not truly Gaussian (see Jacob B [67]). Violations of normality create problems for determining whether unmixed, entomological, vector arthropod, larval habitat, model coefficients are significantly different from zero and for calculating confidence intervals for forecasts (e.g., geo-locations of unknown, potential, seasonal, super breeder, eco-georeferenceble, waste tire, Ae aegypti, county abatement, larval habitats). Some-times the error distribution in an epi-entomological, forecast, vulnerability, spectral eco-endmember, unmixed, frequency model, diagnostic output may be "skewed" by the presence of a few large outliers (i.e., extreme observations) which may be eco-cartographically delineated as spatially non-conforming, non-clustering, seasonal, potential, eco-georeferenecable, county abatement foci, capture points. Since parameter estimation in our county abatement, forecast, vulnerability, real-time UAV captured, LULC signature, iterative, interpolative, unmixed, RGB, eco-endmember, wavelength model was based on the minimization of squared error, we assumed a few extreme eco-georeferenceable, waste tire, larval habitat observations may have exerted enough disproportionate influence on the eco-georeferenced, potential. seasonal, waste tire, breeding site, super breeder, decomposed, capture point, estimates. Calculation of confidence intervals and various significance tests for coeffi-cients are all based on the assumptions of normally distributed errors [Glantz SA, Slinker BK (1990) Primer of Applied Regression and Analysis of Variance. McGraw-Hill Professional Publishing]. Hence we assumed that if the error distribution in the eco-georeferenceable, forecast, vul-nerability, UAV imaged, grid-stratified, real-time, geoclassified, waste tire, Ae aegypti, larval habitat, capture point signature model frequency estimators was significantly non-normal, confidence intervals may be too wide or too narrow for optimally prognosticating potential, seasonal, super beeder, county abatement, eco-georeferenceable foci Glantz SA [72].

Technically, the normal distribution assumption is not necessary in an epi-entomological, eco-georeferenceable, time series, LULC unmixed, vector arthropod, iterative, interpolative, signature, RGB eco-endmember, frequency, probabilistic paradigms for detecting unknown pporlific foci in an intervention, epi-entomological, county abatement study site. If an experimenter is willing to assume the frequency, real-time, UAV, dashboard model equation is correct then the only necessity would be to remotely estimate its coefficients and generate predictions (e.g., covariates of known foci) in such a way as to minimize mean squared error. The formulas for estimating such eco-georeferenceable, pote-netial, hyper productive, county abatement, larval habitats (e.g., potential seasonal, hyper productive, Ae aegypti, waste tire, capture points) coefficients would require no more than that offered by a simple ANOVA analysis. Currently however, experimenters are interested in making inferences about real-time, frequency, county abatement, signature vulnerability models for optimally remotely estimating the probability that a given forecast error will exceed some threshold in a direction, in which case distributional assumptions would be important in such models. A significant violation of the normal distribution assumption is often a "red flag" indicating that there is some other problem with the model assumptions and/or that there are a few unusual data points that should be studied closely and/or that a better model is still required [Glantz SA [72]].

Among the best test for normally distributed errors is a normal probability plot or normal quantile plot of the residuals [93]. These are plots of the fractiles of error distribution versus the fractiles of a normal distribution having the same mean and variance. If a seasonally fore-casted, Ae aegypti, waste tire, seasonal, potential super breeder, eco-georeferenceable, breeding site county abatement, larval habitat, distribu-tion is normal, the points on such a plot should fall close to the diagonal reference line. A bow-shaped pattern of deviations from the diagonal would indicate that the residuals in a real-time UAV ArcGIS module have excessive skewness (i.e., they are not symmetrically distributed, with too many large errors in one direction). An S-shaped pattern of deviations would indicate that the prognosticated, grid-stratifiable, LULC sig-nature, RGB, eco-endmember, unknown potential, seasonal, county abatement, super breeder, foci model explanators have excessive kurtosis (i.e., there are either too many or two few large errors in both directions). Such a regression deviation problem may be revealed in real-time in a UAV dashboard, cyberenvironment.

As noted by Jacob [76] extreme, county abatement, epi-entomological, grid-stratifiable, time series, dependent LULC, signature, unmixed, sub-meter resolution, RGB eco-endmember, frequency observations can indicate the presence of local stationarities: they can suggest potential problems with the autocorrelation signature weights matrix; or they may hint at characteristics of the spatial structure that might be present at a finer scale in a grid-stratifiable, frequency, county abatement, forecast, vulnerability, real-time UAV, LULC signature, RGB frequency, vulner-ability, county abatement model. Outliers may function as leverage points that affect the Moran's coefficient value.

We specified a neighborhood size with the LAGDISTANCE= option in the COMPUTE statement in the real-time, UAV ArcGIS module. The waste tire, *Ae. aegypti,* larval habitat, seasonal, super breeder, time series, LULC signature, sub-meter resolution, unmixed, RGB, eco-endmem-ber frequencies were represented by their standardized values; therefore, only no missing observations were shown in the plot. For each one of those, the VARIOGRAM, procedure computed, the weighted average was the weighted mean, geosampled, LULC, signature, unmixed, frequency, coefficient value of its neighbors. Subsequently, the centered weighted average was plotted against the standardized, RGB, eco-endmember, wavelength observations. As a result, the scatter plot was centered on the coordinates (), and distances in the plot which were expressed in deviations from the origin () in the real-time, drone dashboard, ArcGIS module.

Depending on their position on the plot, the eco-georeferenced, Moran's coefficient plotted, capture points expressed the level of spatial association of each potential, eco-georeferenceable, county abatement, super breeder, *Ae. aegypti,* larval, habitat, waste tire, LULC, signature, eco-endmember frequency observation with its neighboring ones. Conceptually, these signatures, characteristics differentiated the Moran plot

from the semi variogram. The latter is typically used in geostatistics to depict spatial associations across the whole domain as a continuous function of a distance metric.

We found that the geospatial zed eco-georeferenced, LULC signature, super breeder, capture point, waste tire, seasonal, *Ae. aegypti,* larval habitat, geoclassified, capture points on the Moran scatter plot occurred in any of the four quadrants which was definable by the horizontal line and the vertical line. The real-time, UAV geosampled, epi-entomological, county abatement, LULC signature, capture points in the upper right (or high-high) and lower left (or low-low) quadrants indicated positive spatial association which were higher and lower than the sample mean, respectively. The lower right (or high-low) and upper left (or low-high) quadrants included county abatement, eco-georeferenceable, immature habitat, seasonal observations that exhibited negative spatial association; that is, these observed, waste tire, Ae aegypti, larval habitat values carried little similarity to their neighboring, grid-stratifiable, capture points.

Binary, row-averaged, super breeder, eco-georeferenceable, seasonal, waste tire, *Ae. aegypti,* larval habitat, potential super breeder, seasonal, county abatement, geoclassifiable, LULC, eco-georferenceable, geosampled, seasonal, frequency weights were employed for the creation of the Moran scatter plot and the autocorrelation statistics, (i.e., the Moran's coefficient) in the real-time, UAV, dashboard, ArcGIS module. The model residuals were equivalent to the regression slope of the Moran scatter plot. That is, when we specified PLOTS=MORAN(ROWAVG=ON) in the PROC VARIOGRAM statement and AUTOCORR(WEIGHTS=BINARY(ROWAVERAGING)in the COMPUTE statement, in the real-time, UAV dashboard ArcGIS module, then the regression line slope of the Moran scatter plot was the Moran's coefficient. In this sense, the Moran's coefficient possessed a global character, whereas the Moran scatter plot provided a more detailed exploratory view of the autocorrelation behavior of individual, geosampled, county abatement, potential, super breeder, seasonal, LULC, Ae aegypti, waste tire, larval habitat, unmixed, iteratively interpolative, geo-spectro temporal, RGB signature, eco-endmember, capture point, frequencies.

This detailed view revealed county abatement, real-time, oviposition, eco-georeferenceable, seasonal, capture point, signatures and RGB eco-endmember outliers with respect to the regression line slope of the Moran scatter plot. Outliers, if present, can function as leverage points that affect the Moran's coefficient value. Such extremes, we assumed, could indicate the presence of local stationarities: they could have also suggested potential problems with the quantized, residual capture point, autocorrelation regressed, unmixed, LULC waste tire, signature coefficients rendered from the eco-georeferenced, prolific, Ae aegypti, waste tire, weights matrix in the real-time, UAV dashboard, ArcGIS platform.

The degree of spatial autocorrelation amongst the various, Ae. aegyti, waste tire, potential, super breeder, LULC, capture points varied in the UAV dashboard ArcGIS, eigenvector, frequneyc, image analyses. This autocorrelation could have orginated from missing exogeneous, real-time, LULC, signature factors that may have exhibited distinct, capture point, time series, spatial patterns and tied those RGB residuals in geospace. Underlying spatial, larval habitat, unmixing processes from spatial exchange mechanisms amongst unmixed, eco-georeferenceable, signature decomposed, datasets of LULC seasonal, county abatement, sub-meter resolution, RGB eco-endmember, frequencies at the county abatement, epi-entomological, intervention, study site level can provide a mapping technique to view inapproporiate spatial aggregations of potential, super breeder, eco-georeferenced, capture points(Jacob [76]) .Here we generated latent autocorrelation frequency coefficients from the prolific, waste tire, eco-georeferenced, *Ae. aegypti* forecast, vulnerability, county abatement real-time model parameter estimator dataset. The presence of spatial autocorrelation violates the ordinarily stated assumption of stochastic independence amongst frequency observations, on which statistical inference from most classical statistical models is based. Thus, our assumption was that ignoring spatial autocorrelation in a UAV dashboard, LULC signature, geoclassified, sub-meter resolution, Ae aegypti, waste tire, county abatement, eco-endmember real-time, model may have led to biased standard errors and/or biased, RGB, frequency, non-parameterizable estimatators, as well as artificially inflated degrees of freedom.

In a spatial filter model specification, if positive and negative spatial autocorrelation processes counterbalance each other in a mixture, the sum of the two spatial autocorrelation parameters--(ρ+ + ρ.) will be close to 0 which may be determined using a Jacobian matrix. In vector calculus, the Jacobian matrix is the matrix of all first-order partial derivatives of a vector-valued function. When the matrix is a square matrix, both the matrix and its determinant are referred to as the Jacobian in literature [e.g., Jacob [67]].

In the county abatement, waste tire, capture point, LULC, sub-meter resolution, real-time, signature, RGB unmixed frequency real –time UAV model, Jacobian estimation was implemented by utilizing the difference able grid-stratifiable, seasonal, super breeder, eco-georeferenceable, capture point, *Ae. aegypti,* larval habitat, real-time geosampled, indicator, variables (I+ - γ I-), for estimating ρ+ and γ with maximum likelihood techniques in the datasets and setting. The calculation of the elements of the Jacobian matrix in the real-time, ArcGIS module required the values of the eigen decomposed, RGB, eco-endmember, wavelength, derivative spectra of the model function to become the input LULC signature valued, waste tire, *Ae. aegypti,* county abatement, eco-georeferenceable, capture point. Numerical differentiations techniques were employed in the geosampled, immature, habitat, geosampled signature, decomposed data to approximate the derivative employing forward differences formulae: $J_{ij} = \frac{T_i(P_k + h_j ej)}{h_j}$ where j was the unit vector in the direction and represented the known, geosampled, super breeder, county abatement, seasonal, larval count, eco-georeferenced, LULC, foci, explanatorial, orthogonally eigen decomposed UAV, real-time, geosampled, wavelength values. Decreasing the step size () can reduce the truncation error.

The Jacobian generalized the gradient of a scalar valued function of the geosampled, eco-georeferenced, county abatement, unmixed, iteratively interpolative, time series, LULC frequency, capture point, eigen decomposed, signature variables. A more complex, waste tire, Ae aegypti,

larval habitat, sub-meter resolution, RGB, eco-endmember, capture point, LULC specification was then posited in the UAV, dashboard, ArcGIS module by generalizing the grid-stratifiable, real-time, RGB, eco-endmember, geoclassifiable, indicator explanators. We employed F: Rn → Rm as a function from Euclidean n-space to Euclidean m-space which was generated employing the tabulated, distances between the, potential, seasonal, super breeder, county abatement, larval habitat, geosampled, unmixed, eco-georeferenced covariates. Such a function was given in the drone county abatement, LULC signature model by m capture point, waste tire, larval habitat, covariates (i.e., component functions), y1(x1, xn), ym (x1, xn). The partial derivatives of all these functions were organized in an m-by-n matrix, by the dashboard, real- time Jacobian matrix J of F, which was as follows: This matrix was denoted by JF (x1,..., xn) and $\frac{\partial(y_1,...,y_m)}{\partial(x_1,...,x_n)}$ in the UAV platform. The i th row (i = 1,..., m) of this matrix was the gradient of the ith component function yi:(i.e., ∇ yi). In the, ArcGIS, vulnerability, real-time, capture point signature frequency analyses, p was a geosampled, sub-meter, resolution, unmixed, waveband, Ae.aegypti, capture point, eco-geoeferenecable, RGB, frequency, orthogonal, spatially filtered, orthogonal estimator in Rn (i.e., capture point,seasonal, larval/pupal, frequency, discrete, density, integer count) and F was differentiable at p; its derivative was given by JF(p). The model described by JF(p)) was the unbiased, linear approximation of F near the eco-georeferenced, forecasted, unknown, capture point, waste tire, grid-stratifiable, LULC, county abatement, super breeder, geolocation foci p, in the sense that: $F(x) = F(p)$ (3.4).

The spatial structuring of the sub-meter resolution, eco-georeferenced, unmixed, LULC, signature, capture point, *Ae. aegypti,* larval habitat, super breeder, foci were achieved by employing an unmixed, linear combination of a subset of the county abatement, RGB eco-endmember, LULC eigenvectors rendered from a modified geographic weights matrix in the real-time, UAV dashboard ArcGIS modeule employing (I - 11'/n) C (I - 11'/n) that appeared in the numerator of the Moran's Coefficient (MC). Spatial autocorrelation can be indexed with a MC, a product moment correlation coefficient (Griffith 2003). A frequency subset of unmixed, sub-meter resolution, super breeder, seasonal, LULC, capture point, orthogonal eigenvectors were then selected with a stepwise regression procedure in the real-time, UAV, dashboard. Because (I - 11'/n) C (I - 11'/n) = E Λ E', [3.5] where E is an n-by-n matrix of eigenvectors and Λ is an n-by-n diagonal matrix of the corresponding eigenvalues, the resulting eco-georefenceable, geo-spectro temporal, super breeder, capture point, sub-meter resolution, *Ae. aegypti,* larval habitat, RGB eco-endmember, real-time, vunerability, capture point, wavelength, model output, LULC, signature specification was given by: (3.5) where µ was the scalar mean of Y, Ek was an n-by-k matrix containing the subset of k <<n eigenvectors selected with a stepwise regression technique, and β was a k-by-1 vector of unmixed, regression coefficients in the real-time, UAV dashboard, ArcGIS module.

A number of the geoclassifiable, eco-georeferenceable, larval habitat, capture point, potential, super breeder, *Ae. aegypti,* real-time, UAV imaged, model, orthogonal eigenvectors were extracted from (I - 11'/n) C (I - 11'/n), which were found to be geo-spectro temporally affiliated with eco-geographic, super breeder, seasonal, eco-georeferenecable, LULC patterns and the RGB unmixed, spectral covariates, geosampled at the ento-epidemiological, county abatement, intervention, study site. These synthetic eigenvalues portraying a negligible degree of non-zero spatial autocorrelation. Consequently, only k of the n eigenvectors was of interest for generating a candidate set for a stepwise regression procedure in the real-time, dashboard ArcGIS module. Candidate eigenvector represents a level of LULC, spatial autocorrelation which can account for the redundant information (i.e., pseudo replicated data) in eco-georeferenecable, seasonal, vector, entomological, hyper productive capture point, seasonal, county abatement, vulnerability, signature, map patterns.

The preceding orthogonal, LULC eigenvector properties resulted in and for equation (3.3). Expressing equation (3.3) in terms of the preceding 2-by-2 in the real-time, UAV, dashboard ArcGIS yielded

Of note the 2-by-2 square tessellation rendered repeated eigenvalues.

$$\begin{bmatrix} y_1 \\ y_2 \\ y_3 \\ y_4 \end{bmatrix} = \begin{bmatrix} 1 \\ 2 \\ 3 \\ 4 \end{bmatrix} + \begin{bmatrix} 0.5 & -0.69048 & 0.15240 \\ -0.5 & 0.15240 & 0.69048 \\ -0.5 & -0.15240 & -0.69048 \\ 0.5 & 0.69048 & -0.15240 \end{bmatrix} \begin{bmatrix} \beta_1 \\ \beta_2 \\ \beta_3 \end{bmatrix} + \begin{bmatrix} \varepsilon1 \\ \varepsilon2 \\ \varepsilon3 \\ \varepsilon4 \end{bmatrix}, and \, \beta = \begin{bmatrix} 0.5 & -0.69048 & 0.15240 \\ -0.5 & 0.15240 & 0.69048 \\ -0.5 & -0.15240 & -0.69048 \\ 0.5 & 0.69048 & -0.15240 \end{bmatrix} \begin{bmatrix} y_1 \\ y_2 \\ y_3 \\ y_4 \end{bmatrix}$$

To identify geoclassifiable, eco-georeferenceable, LULC signature, seasonal, clusters of potential, super breeder, waste tire, capture point, county abatement, *Ae. aegypti,* larval habitats, Thiessen polygon surface partitionings were generated in the drone dashboard, ArcGIS to construct robust, neighbor matrices, which also were employed in the RGB eco-endmember, frequency, spatial autocorrelation, real-time, vulnerability analysis for predicting unknown, county abatement, prolific, breeding site foci. Entries in matrix were 1, if two eco-georeferenceable, geosampled, potential, super breeder, larval habitat, county abatement, *Ae. aegypti,* signature, capture points, shared a common Thiessen polygon boundary and 0, otherwise. Next, the linkage structure for each capture point, grid-stratifiable, LULC, geoclassifiable, unmixed, eco-georeferenceable, signature attribute feature was edited to remove unlikely seasonal, capture point, super breeder, larval habitats sharing a common Thiessen polygon boundary. Attention was restricted to those capture point, county abatement, seasonal, LULC signature, map patterns associated with at least a minimum level of spatial autocorrelation, which, for implementation purposes, was defined by |MCj/MCmax| > 0.25, where MCj denoted the jth value and MCmax, the maximum value of MC. This threshold value allowed two candidate sets of, eigendecomposed, LULC signature, UAV, real time imaged, orthogonal, larval habitat, *Ae. aegypti,* RGB eco-endmember, capture point, frequency, super breeder, eco-georeferenceable, seasonal, waste tire, spatial filter, orthogonal eigenvectors to be considered for substantial, positive and substantial, negative, spatial autocorrelation respectively. These statistics indicated that the detected, negative, spatial autocorrelation in the county abatement, *Ae. aegypti,* LULC, eco-endmember, sub-meter resolution, larval habitat, signature, frequency dataset may be considered to be statistically significant, based upon a randomization perspective. Of note, is that the ratio of the PRESS (i.e., predicted error sum of squares) statistic to the sum of squared errors from the MC scatterplot trend line was 1.21 which was well within two standard deviations of the average, standard, prediction, error value (roughly 1.13) for any immature, seasonal, eco-georeferenceable, county abatement, regressed, vector entomological, arthropod, capture point, geosampled at an epi-entomological, intervention, study site.

One approach to dealing with spatial autocorrelation in the eco-endmember, county abatement, LULC, sub-meter resolution, vector entomological, time series regression analysis involved filtering, which in this investigation sought to transform a spatially dependent, capture point, mapping signature variable into an independent variable by removing the spatial dependence embedded in it. Here the original eco-geo-referenceable, geoclassified, LULC, signature, capture point, county abatement, waste tire, super breeder, Ae aegypti, eco-endmember, RGB attribute variables were partitioned into two synthetic variables: a filtered nonspatial variable and a residual spatial variable. Haining (1991) shows that the temporal-type filtering approach is equivalent to a spatial autocorrelation adjustment for the case of bivariate correlation. He employed one of the family of autoregressive models, the simultaneous (SAR), of the generalizable form discussed in Anselin (1988) and Griffith (1988) to implement his version of spatial filtering. In essence, these real-time, UAV, geosampled, sub-meter resolution LULC signature, Realtime epi-entomological, forecast, vulnerability, county abatement models did not depend on one or more spatial structural matrices that removed (filtered) spatial autocorrelation from he, capture point, eco-endmember data from which model RGB parameters were estimated: (e.g., from equation (1.3), $(I- \rho W)-1Y = \mu Y \ 1 + \varepsilon \ Y$ for teasing out non-zero, latent, autocorrelation coefficients in the geosampled, signature datasets. The filtering devices were constructed from, real time RGB eco-endmembers weights which were used to capture the covariation amongst multiple, county abatement, signature values in the UAV real-time dashboard ArcGIS module, of one or more random, potential super breeder, waste tire, Ae aegypti, seasonal, larval habitat.

Because count data were being analyzed, a spatial filter model LULC specification was employed in the real-time, UAV dashboard, eigenfunction eigen decomposition, orthogonal, spatial filter algorithm in the ArcGIS module. The model specification was written as: and where μi was the expected, predicted, seasonal, mean, immature count for a potential, forecasted, unknown, super breeder, capture point, eco-geo-referenceable, county abatement, *Ae. aegypti,* waste tire, larval, habitat geolocation i, μ was an n-by-1 vector of expected larval/pupal counts, LN denoted the natural logarithm (i.e., the generalized linear model link function), α was an intercept term, and η was the negative binomial dispersion parameter. This real-time, UAV dashboard derived, log-linear equation had no error term; rather, estimation was executed assuming a negative binomial random variable.

Several eco-georeferenceable seasonal, potential, super breeder, Ae aegypti, LULC, capture point, sub-meter resolution, RGB eco-endmember, larval habitat, capture point, frequency, unmixed signature, estimators were proposed for the negative binomial dispersion parameter in the real-time UAV dashboard ArcGIS module. The proposed orthogonal spatial filter estimators were combinations of appropriate wavelength weights in the real-time dashboard. Subsequently, the biases and efficiencies of the proposed, geosampled, capture point, LULC simulated, frequency signature estimators with those of the method of moments estimators and the quasi- maximum likelihood estimate (QMLE).

Jacob[67], employed a QMLE (, also known as a pseudo-likelihood estimate or a composite likelihood estimate) to estimate a parameter θ in a vector arthropod [i.e., Similium damnsoum s.l., a black-fly vector of onchocerciasis in a sub-meter resolution, LULC signature, stochastic, iterative interpolator, risk model that was formed by maximizing a function that was related to the logarithm of the likelihood function, but was not equal to it. In contrast the maximum likelihood estimator of the capture point, super breeder, eco-georeferenceable, county abatement, sub-meter resolution, LULC signature, uncoalesced, capture point, *Ae. aegypti,* vulnerability, forecast model maximized the actual log-likelihood function for the epi-entomological, seasonal county abatement, UAV, geosampled, real-time, signatures. The function was maximized to form a QMLE that was a simplified form of the actual log-likelihood function. Simplified functions were employed to quantitate the log-likelihood function of a misspecified, unmixed dataset of LULC signature, RGB, eco-endmember frequencies in real time. The effects of heteroskedasticity (i.e., uncommon variance) common in regression, vector, epi-entomological, time series, grid-stratifiable, optimally forecastable, LULC, sub-meter resolution, signatures Jacob BG, et al. [11].

may be removed by removing any parameter from a UAV real-time signature wavelength model that mischaracterize dependencies. Here, removal of the non-homoskedastic, frequency, capture point, larval habitat, regressors in the real-time, geo-spectro temporal, super breeder, county abatement, waste tire, Ae aegypti, sub-meter, resolution, signature paradigms rendered a more robust outcome (e.g., real-time dataset of geolocations of seasonal, super breeder, eco-georeferenced, capture points).

Conceptually, our orthogonal, spatial filter, LULC eigenvector, capture point, classification method was based on a linear, sub-meter resolution, time series, LULC, signature, vector arthropod RGB, immature habitat, capture point, functions in its most general form of minimum (asymptotic) variance unbiased estimation. The so-called quasi-score (QS) estimating function was adapted in the real-time, UAV, dashboard, ArcGIS module for generating robust renderings from the capture point, super breeder, county abatement, *Ae. aegypti,* forecast-oriented, geo-spectro temporal, RGB eco-endmember, LULC signature, vulnerability, real-time, model by employing a set of appropriately chosen summary statistics. The derivation of the QS is part of the general approach of quasi-likelihood (QL) estimation, which subsumes standard parameter estimation methods such as, for example, ML or (weighted) least square LS. Here, the QL estimator for the signature, sub-meter resolution, seasonal, super breeder, LULC, UAV, geosampled, county abatement, Ae. aegypti, capture points were derived from the solution to the QS equation.

As a common starting point the QS can be seen as a gradient specification similar to the score vector in ML theory . If a likelihood is available, both functions coincide and the score function from ML is an optimal estimating function in the sense of QL in an epi-entomological, real-time, RGB, prognosticative, sub-meter resolution, LULC signature, vector entomological, iterative, interpolative model (Jacob [76]). Except

in some rare cases, when expectations, derivatives thereof and variances of the statistics are known at least numerically, any kind of criterion function derived including the QL approach, would lack a closed-form expression and hence could only be computed slowly with substantial random error either due to the inherent simulation variance or erroneous evaluation of the involved statistics such as in an eco-entomological. forecast-oriented, LULC, sub-meter resolution, county abatement, spectral signature, spatial filter, RGB, eco-endmember, real-time, UAV, Arc-GIS, probabilistic paradigm in fact, nothing is said about a QL function in theory which could be employed as an objective function for minimization in order to derive an estimate of the true model parameter in such models.

Therefore, our idea was to treat such a signature LULC function as a black box objective function and to transform the general parameter estimation problem into a simulation-based UAV geosamplde, real-time signature, optimization setting with an expensive objective function for optimally determining krigable geolocations of unknown, seasonal, super breeder, eco-georeferenceable, waste tire, *Ae aegypti*, larval habitat, capture points in Hillsborough county. For this kind of optimization problem, it was assumed that derivative information was either not available or computationally prohibitive such that gradient-based or Newton-type methods were not directly applicable in the capture point, real-time, super breeder, Ae aegypti, larval habitat, geo-spectro temporal, frequency, LULC signature, sub-meter resolution RGB model.

In calculus, Newton's method is an iterative method for finding the roots of a differentiable function f (i.e. solutions to the equation f(x)=0). In optimization, Newton's method is applied to the derivative f ′ of a twice-differentiable function f to find the roots of the derivative (solutions to f ′(x)=0), also known as the stationary points off. [94].

We quantitated the capture point, eco-georeferenced, real-time, waste tire, super breeder, seasonal, *Ae. aegypti,* larval habitat, orthogonal, eigenfunctions as rendered from a spatial weighting matrix in the real-time UAV, dashboard ArcGIS. The upper and lower bounds for a spatial matrix generated using Morans indices (I) was given by λmax (n/1TW1) and λmin (n/1TW1) where λmax and λmin which were the extreme eigenvalues of Ω = HWH. Hence, the capture point, eco-georeferenceable, *Ae. aegypti,* larval habitat, RGB signature, LULC, frequency eigenvectors of Ω were vectors with unit norm maximizing Moran's I. The eigenvalues of this matrix were equal to Moran's I coefficients of spatial autocorrelation post-multiplied by a constant. Eigenvectors associated with high positive (or negative) eigenvalues have high positive (or negative) autocorrelation (e.g., six analytical maps for west nile virus). The eigenvectors associated with eigenvalues with extremely small absolute values corresponded to low spatial autocorrelation and werenot suitable for defining spatial structures in the waste tire, *Ae. aegypti,* capture point, eigen decomposed, eco-endmember, real-time, LULC, signature, vulnerability, county abatment, forecast-oriented, frequency analyses .

The diagonalization of the spatial weighting matrix generated from the field and remote gesampled, previously unknown, Ae aegypti, seasonal, eco-georeferenceable, super breeder, county abatement, aquatic, larval habitat, signature, covariate coefficients in the real-time, UAV dashboard ArcGIS module, consisted of finding the normalized vectors ui, stored as columns in the matrix U = [u1 ⋯ un], satisfying:

where Λ = diag (λ1 ⋯ λ n), $u_i^T u_i = \|u_i\|^2 = 1$ and $u_i^T u_i = 0$ for i ≠ j. Note that double centering of Ω implied that the larval habitat orthogonal, real-time frequency orthogonal eigenvectors ui generated from the epi-entomological, geosampled, *Ae. aegypti,* capture point, super breeder, seasonal, larval habitat, RGB, sub-meter resolution, LULC unmixed, signature covariates were centered and at least one eigenvalue was equal to zero. Introducing these eigenvectors in the original formulation of Moran's index lead to: $I(x)=\frac{n}{1^T W1}\frac{X^t HWHX}{X^T HX}=\frac{n}{1^T W1}\frac{X^T U \wedge UX}{X^T HX}$ (3.6). Considering the centered vector z = Hx and using the properties of idempotence of H, equation (3.6) was equivalent to Subsequently we quantitated the latent, autocorrelation, correlation, coefficient, effect specification of the geosampled, eco-georeferenced, *Ae. aegypti,* capture point, larval habitat, sub-meter resolution, LULC signature RGB, frequency covariates. As the eigenvectors ui and the vector z were centered, equation (3.7) was rewritten: $\frac{n}{1^T W1}\sum_{i=1}^{n}\lambda_i \cos r^2(u_i,z)$ (3.8) in the real-time, drone, dashboard ArcGIS module.

In the waste tire, *Ae. aegypti,* LULC, real-time, UAV dashboard, ArcGIS, the capture point, eco-endmember, RGB wavelength estimators, r was also the number of null eigenvalues of Ω. These orthogonal, frequency eigenvalues and corresponding eigenvectors were removed from Λ and U respectively. Equation 3.8 was then strictly equivalent to: $I(x)=\frac{n}{1^T W1}\sum_{i=1}^{n}\lambda_i \cos r^2(u_i,z)$ (3.9). Moreover, it was demonstrated that Moran's index for a given eco-georeferenceable, capture point, LULC super breeder, seasonal, Ae, aegypti, waste tire, county abatement, orthogonal, RGB eigenvector ui was equal to I(ui) = (n/1TW1) λ i so the equation was rewritten in the real-time UAV ArcGIS module as $I(x)=\sum_{i=1}^{n}I(u_i)\cos r^2(u_i,z).$ The term cor2 (ui, z) represented the part of the variance of z that was explained by ui in the immature, habitat county abatement model: z = β i ui+ ei. This quantity was equal to By definition, the capture point, eigenvectors ui were orthogonal, and therefore, the geosampled, LULC, regression coefficients of the linear models z = β i ui+ei were those of the multiple regression, county abatement, signature, sub-meter resolution RGB model; z = Uβ + ε = β iui + ⋯ + β n-r un-r + εin the real-time, drone, dashboard ArcGIS module.

The distribution of the error residuals in the autocovariance, waste tire, *Ae. aegypti,* RGB, eco-endmember, sub-meter resolution, LULC, real-time signature, covariance matrix was rendered in the UAV dashboard ArcGIS module. The maximum value of I was obtained by all of the variation of z, as explained by the eigenvector u1, which corresponded to the highest eigenvalue λ1 in the capture point, LULC, spatial autocorrelation, diagnostiuc, regression, error matrix. In the real-time dashboard, cor2 (ui, z) = 1 (and cor2 (ui, z) = 0 for i ≠ 1) and the maximum value of I, was deduced for Equation (3.9), which was equal to Imax = λ1(n/1TW1). The minimum value of I in the error matrix was obtained as all the variation of z was explained by the eigenvector un-r corresponding to the lowest eigenvalue λn-r generated in the Ae aegypti, super breeder, county abatement, real-time, larval habitat, capture point, LULC, signature model. This minimum value was equal to Imin = λn-r (n/1TW1). If the ento-ecological, geosampled, county abatement, geo-spectro temporal, sub-meter resolution, real-time, eco-endmember, LULC, signature,

explanatory, eco-georeferenceable, predictor variable was not spatialized, the part of the variance explained by each eigenvector was equal, on average, to cor2 (ui, z) = 1/n-1. Because the field and remote, geosampled, capture point, LULC, *Ae. aegypti,* waste tire, super breeder, seasonal, habitat and it's RGB variables in z were randomly permuted, it was assumed that we would obtain this result. Further, the set of n! random permutations, revealed that $E_R(I) = \frac{n}{1^T W 1(n-1)} \sum_{i=1}^{n} \lambda_i = \frac{n}{1^T W 1(n-1)} trace(\Omega)$ in the entomological, county abatement, LULC model, explanatory, real-time, diagnostic signature ouput. It was easily demonstrated that $trace(\Omega) = -\frac{1^T W 1}{n}$ and it followed that $E_R(I) = -\frac{1}{n-1}$ in the waste tire, *Ae. aegypti,* capture point, oviposition, LULC, eco-endmember, model specifications.

A SPA was built for unmixing the sub-meter resolution, 3-D, *Ae. aegypti* larval, habitat, LULC signatures capture point, RGB, eco-endmember employing convex geometry and orthogonal projection in the real-time, UAV dashboard ArcGIS module. The extraction included separating canopied, sub-pixel, field-operationizable, image eco-endmembers from the decomposed LULC, sub-meter resolution, RGB signatures without having to reduce the sampled data dimensionality. The SPA was built by a convex geometry search algorithm in the real-time, UAV dashboard, ArcGIS module by including a constraint on the spatial adjacency of the candidate, *Ae. aegypti,* capture point, eco-endmember larval habitat, unmixed, LULC, signature variables with its associated explanatorial, eco-georeferenceble, sub-pixel, RGB, capture point, reflectance components. The SPA reduced the susceptibility for searching for outliers. The algorithm described how a vertex was identified based on its spectral uniqueness in the simplex. The drone real-time algorithm measured the vector Euclidean norm and the distance of the NDVI, larval, habitat, derivative spectra to the subspace which was defined by selected RGB eco-endmembers. A meaningful eco-endmember for this vertex was the multiple, candidate, LULC reflectance that were spectrally distinct (e.g., those that were geolocated at or near one of the corners of the simplex) of a potential eco-georefernced, waste tire, *Ae. aegypti,* larval habitat, county abatement, geosampled, capture point, super breeder foci.

The convex geometry SPA provided information on the convergence of the algorithm in the real-time, UAV, dashboard ArcGIS. This property was employed in the SPA algorithm to determine the main step in the larval habitat, eco-endmember, waste tire, *Ae. aegypti,* LULC signature, pixel decomposition for identification of the NDVI spectral heterogeneity at the vertices of the simplex. For the given geosampled, eco-endmember, eco-georeferenecable, larval habitat, capture point, *Ae. aegypti,* super breeder, LULC signature unmixed point in the simplex, a point with maximum distance was geolocated at the vertex of the simplex.

Based on the SPA algorithmic output, the affine transformation (i.e., orthogonal projection) of the simplex generated was also a simplex in the real-time, UAV, dashboard ArcGIS module. This output revealed that the partially canopied, eigende composed, NDVI and LULC, signature RGB eco-endmember frequencies were located in the vertices of the new simplex after the transformation. This transformation allowed the usage of orthogonal subspace projections as the core mechanism for parsimoniously conducting the decomposition, RGB, extraction exercise in the real-time UAV dashboard. A vector with maximum Euclidean norm (i.e., magnitude) was generated at the vertices of the simplex in the ArcGIS real-time module. In linear algebra, functional analysis and related areas of mathematics, a norm is a function which assigns a positive length or size to all vectors in a vector space, other than the zero vector. A semi-norm was then allowed to assign zero length to some non-zero vectors. We employed 3-D Euclidean space R2 equipped with the Euclidean norm in the drone dashboard for analyzing the initially eigende composed, *Ae. aegypti,* larval habitat, LULC signature, sub-mter resolution, RGB wavelength eco-endmembers. Euclidean space is a particular metric space that enables the investigation of topological properties such as compactness [95]. An inner product space is a generalization of a Euclidean space. Both inner product spaces and metric spaces of the larval habitat, capture point, sub-pixel, eco-endmember, waste tire, potential, super breeder county abatement, vulnerability real-time model was explored within a functional analysis. Elements in this vector space are usually drawn as arrows in a 2-dimensional cartesian coordinate system starting at the origin (0,0) [96].

By including a constraint on the geo-spatialized, Euclidean subspace adjacency of the shaded, explanatorily, spectrally decomposed, vegetated, canopy-related, *Ae. aegypti,* LULC, larval habitat, capture point sub-pixel, RGB, dataset and their individual reflectance, eco-endmember, spectral values, the SPA algorithm captured the contiguous 31 cm-pixel VI in the red, IR and NIR bands, employing advanced data pre-processing applications in the real-time UAV dashboard ArcGIS. The eco-georeferenced, shade-canopied, LULC, capture point, grid-stratifiable, RGB wavelength data was able to describe the change of the simplex volume ratio between successive iterations during the eco-endmember extraction process. Further, the algorithm reduced the susceptibility to outlier 31 cm pixel, spectro temporally-oriented, erroneous, resdiualized covariate coefficients which allowed for optimizing the unmixed canopy, eco-endmember, RGB spectra and eco-geographically geo-classify them based on their actual reflection attributes.

Although, the NDVI, sub-meter resolution, unmixed, spectral, RGB, signature, eco-endmember, decomposed values were parsimoniously extracted from the real-time UAV, capture point LULC image, the final county abatement, larval, habitat dataset did not include any treatment of diffuse irradiance and canopy multiple scattering and leaf specularity. This simulation required the selection of individual wavelength information for each unmixed, geosampled, geoclassified, canopied, LULC shade-vegetated, photosynthetic, unmixed, feature attribute which we assumed was calculable by a radiative transfer equation in the real-time, UAV dashboard ArcGIS platform. An analytical was optimally derived for the eco-endmember, real-time, vector, arthropod, epi-entomological, real-time immature habitat model employing the inclination angle density function which here was $g(\alpha) = \frac{2\chi^3 \sin \alpha}{\lambda \left(\cos^2 \alpha + \chi^2 \sin^2 \alpha \right)^2}$ where α was the leaf inclination angle, X was the ratio of vertical to horizontal projections of canopy elements, and A was a normalized ellipse area, approximated by λ=χ+1.774(χ+1.182)−0.733.

We employed a 3-D, radiative, transfer model to decompose the LULC, signature, *Ae. aegypti,* larval habitat, sub-meter resolution, county abatement, RGB signatures. The process of solar radiative transfer at the land surface is important to energy, water, and carbon balance, espe-

cially for vegetated LULC areas [Van der Meer F (1999) Iterative spectral unmixing (ISU). International Journal of Remote Sensing 20: 3431-3436]. We employed a two-stream model to consider the capture point, larval habitat's canopy plant functional types within a grid cell in the real-time, UAV, dashboard ArcGIS module to determine independence of the vegetated LULCs and their horizontal non-homogeneous tendencies. The model revealed an increase of canopy absorption within sparse vegetation LULC than with multilayered canopied LULCs geosampled at the capture point geolocations with a large sun zenith angle θsun which may have been due to increases of the ground and sky shadows and of the optical path length. This phenomenon may have been also due to shadow overlapping LULCs between the eco-georeferenced, shaded, larval habitat, canopy layers.

A differential equation describing radiance [i.e., $L(\bar{r},s,t)$] of the intermittently canopied, LULC, county abatement capture points was also generated in the real-time UAV dashboard ArcGIS module. The signature, frequency capture point, signature, county abatement models were based on conservation of energy. Briefly, this theory states that a beam of light loses energy through divergence and extinction (including both absorption and scattering away from the beam) and gains energy from light sources in the medium and scattering directed towards the beam [97]. Coherence, polarization and non-linearity in the eco-georeferenced, unmixed, waste tire, Ae aegypti, LULC signature, sub-meter resolution, RGB, eco-endmember, UAV, real-time model was neglected. Optical properties such as refractive index, absorption coefficient μa, scattering coefficient μs, and scattering anisotropy were taken as time-invariant in the real-time dashboard ArcGIS module.

An ecogeoreferenceable, shade-vegetated, LULC signature, canopy-related, RGB sub-meter resolution, regression equation was then written from the irradiance, unmixed, time series, sub-meter resolution, 3-D, NDVI datasets. The geosampled, county abatement capture points were then tabulated employing in the dashboard where was the relative refractive index, μt μa+μs was the extinction coefficient $P(s',s)$, was the phase function, representing the probability of canopy light with propagation direction being scattered into solid angle around . In most cases, the phase function depends only on the angle between the scattered and incident directions, i.e. $P(s',s) = P(s'.s)$ [55]. The scattering anisotropy of the potential, seasonal, super breeder, larval habitat, LULC, eco-georeferenceable, signature, *Ae. aegypti,* sub-meter resolution, capture point, was then expressed as $g = \int (s'.s) P(s',s)$ and in the real-time UAV, dashboard, ArcGIS module.

In diffusion theory, radiance is taken to be largely isotropic, so only the isotropic and first-order anisotropic terms are used. Here we defined the the geosampled, shade-canopied, potential, super breeder, waste tire, county abatement, eco-georeferenceable, *Ae. aegypti,* larval habitat, capture point, partially shaded, canopy radiance employing in the real-time, UAV dashboard ArcGIS model where n, m were the expansion coefficients. Radiance was expressed with 4 terms; one for n = 0 (the isotropic term) and 3 terms for n = 1 (the anisotropic terms). Using properties of spherical harmonics and the definitions of fluence rate [$\Phi(\bar{r},t)$ and unmixed, partially shade-canopied, capture point, Ae aegypti, potential, super breeder, seasonal, county abatement, geosampled LULC densities $\bar{J}(\bar{r},t)$], the isotropic and anisotropic terms were respectively expressed as follows: $\frac{\Phi(\bar{r},t)}{4\pi}$ and Hence, we approximated the capture point, LULC, potential super breeder, eco-georeferenceable, *Ae. aegypti,* larval habitat canopy radiance as $L(\bar{r},s,t)\frac{1}{4\pi}\Phi(\bar{r},t)+\frac{3}{4\pi}\bar{j}(\bar{r},t)$ in the UAV, dashboard, ArcGIS, county abatement, frequency, signature real-time model.

Substituting the above expression for the county abatement, prolific, ecogeoreferenceable, capture point, LULC signature radiance, the geosampled, shade-canopied, prolific, seasonal, Ae aegypti, larval habitat, forecasting, ento-epidemiological, risk model rendered regressable orthogonal eigenevctor prognosticators that were respectively rewritten in scalar and vector forms in the real-time, drone dashboard ArcGIS model. The scattering term integrated over the complete solid angle. For the vector form, the photosynthetic, LULC, capture point, signature reflectance covariates were multiplied by direction before evaluation. The forecasts rendered revealed two outcomes: The diffusion approximation reduced scattering absorption coefficients in the real-time, ArcGIS, eco-georeferenced, capture point, inhomogeneously canopied, county abatement, geosampled LULC, potential super breeder foci, drone model, regression dataset especially those having a minimum layer thickness.

Using the second assumption of diffusion theory, we noted that the fractional change in canopy LULC density $\bar{J}(\bar{r},t)$ over one transport mean free path in the geosampled capture point, potential, seasonal, super breeder, Ae aegypti, waste tire, larval habitat signatures was negligible. The vector representation of the diffusion theory reduces to Fick's law $\bar{J}(\bar{r},t)=\frac{-\Delta\Phi(\bar{r},t)}{3(\mu_a+\mu_s')}$ [98] which we employed to define optimally regressable, unmixed, wavelength, canopied LULC densities (e.g., foliar density flux) in terms of the gradient of fluence rate. Substituting Fick's law into the scalar representation of the operationalizable, geosampled, capture point, eco-georeferenceable, waste tire, Ae aegypti, larval habitat, potential, super breeder, county abatement, frequency datasets with the unmixed, UAV estimates rendered the diffusion equation . The model revealed $D=\frac{1}{3(\mu_a+\mu_s')}$ which was the diffusion coefficient and $\mu's=(1-g)$ μs which was the scattering coefficient in the real-time, epi-entomological, sub-meter resolution, signature, ArcGIS models. A stochastic, radiative, transfer equation for discontinuous vegetation was constructed in real-time in the drone dashboard ArcGIS for measuring differences in flux in homogeneous and non-homogeneous, LULC, canopied, capture point, eco-georeferenceable, county abatement geolocations (Figure 8).

Notably, there was no explicit dependence on the scattering coefficient in the diffusion equation in the real-time, UAV dashboard, ArcGIS, signature models. Instead, only the reduced frequency scattering coefficient appeared in the expression for. Diffusion in the the real-time, geosampled, LULC signatures retrieved in the drone dashboard revealed seasonal, county abatement, partially canopy-shaded, potential, super breeder, eco-georeferenced, Ae aegypti. larval habitat, unmixed, frequency, signature model estimators which were unaffected by spatial

heteroskedascity if the anisotropy of the scattering medium was changed while the reduced scattering coefficient remained constant. Spatial heteroskedascity or negative autocorrealtion may render mispecified model outcomes (e.g., non-specific forecasted, prolific, seasonal, capture points). For quantiating various configurations of LULC boundaries (e.g. layers of canopy and light sources), the diffusion equation in the real-time, drone dashboard, ArcGIS, mapped the LULC boundary conditions in real-time of the capture points for optimally eco-cartographically defining the source term as the situation demanded in the UAV dashboard model output.

A solution to the diffusion equation for the simple case of a short-pulsed point source in an infinite homogeneous medium was then computated from the eco-georeferenced, potantial, super breeder, county abatment, LULC signature, capture points in the real-time, drone dashboard ArcGIS, signature, model output. The source term in the diffusion equation became when was the position at which fluence rate was measured in the real-time image softawre, and was the position of the source (unmixed, capture point, 31 cm resolution, LULC, unmixed, reflectance values). The pulse peaked at time. The diffusion equation was solved for fluence rate which yielded. $L(\vec{r},s,t)\frac{1}{4\pi}\Phi(\vec{r},t)+\frac{3}{4\pi}\vec{j}(\vec{r},t)$

The term $\exp\left[-\mu_\alpha c(t-t')\right]$ in the potential, super breeder, waste tire, Ae, aegypti, larval habitat county abatment, foci represented the exponential decay in the geosampled, fluence rate due to absorption in accordance with Beer's law (see Appendix 1). The other terms in the real-time, UAV dashboard ArcGIS module were included from the broadening of the RGB eco-endmember, real-time frequencies due to scattering of the sub-meter resolution, shade-canopied, potential, seasonal, super breeder, waste tire, eco-georeferenceble, Ae aegypti, larval habitat, capture point, LULC, county abatement, frequency signatures. Given the equation 3.8, an arbitrary source was characterized in the real-time, epi-entomological, oviposition, real-time models as a superposition of short-pulsed point sources in the drone dashboard, image, software module. Taking time variation out of the geosampled, real-time diffusion equation rendered the following: We noted that $\mu_{\text{eff}} = \sqrt{\frac{\mu_a}{D}}$ was the effective attenuation coefficient in the model which was based on the rate of spatial decay in fluence in the epi-entomological, sub-meter resolution, prognosticative, county abatement, eco-georeferenceable, capture point, LULC, signatures, of potential, county abatement, super breeder foci.

Consideration of the eco-georeferenced, county abatement, larval habitat, shade-canopy, boundary conditions permitted use of the equation 3.9 in the real-time, geosampled, drone dashboard, ArcGIS model to remotely optimally characterize light propagation in the discontinuous, capture point, canopied, LULC signatures. To begin to address a boundary, one can consider what happens when photons in the medium reach a boundary (i.e. a surface) [99, 100]. The uncoalesced, capture point, LULC, canopy radiance at the boundary was determined in the real-time, UAV dashboard Arc GIS module. The medium was equal to the direction-integrated, potential, super breeder, county abatement, waste tire, unmixed radiance at the boundary which was based on directed out of the medium, regressively quantitatable co-factors (, larval habitat, soil substrate reflection) multiplied by total capture point, Ae aegypti,LULC signature, polygon reflectance where was normal to and pointing away from the boundary. The diffusion approximation in the UAV dashboard ArcGIS module subsequently rendered an expression for radiance in terms of fluence rate and current density.

The steps in representing a pencil beam incident on a semi-infinite anisotropically scattering medium as isotropic, in the UAV dashbard, required that a capture point, LULC signature source in the real-time ArcGIS, epi-entomological, county abatement, prognosticative, waset tire, Ae aegypti, frequency model generate $L(\vec{r},s,t)\frac{1}{4\pi}\Phi(\vec{r},t)+\frac{3}{4\pi}\vec{j}(\vec{r},t)$ where $R_\theta = \int 2\sin\theta\cos\theta$ In so doing, was computatble. Substituting Fick's law then renderd an exact Euclidean distance from the eco-georeferenced, county abatement, predicted, immature, habitat canopy boundaries when z=0 and when . Solutions to the equation of radiative transfer. equation included in the real-time, epi-entomological, drone dashboard, ArcGIS models. The differences were essentially due to the various the emission and absorption coefficients.

A decrease of canopy, LULC absorption occured in densely vegetated, partially shaded, eco-georeferenced, larval habitat, geosampled, potential seasonal super breeder, county abatement, capture point, geolocations with small θsun. For a one-layer canopy, these decreases may have been due to crown shape effects that enhanced the transmission through the canopy edge of the capture point. For the multilayer canopy portion of the eco-georeferenced, potenbetial, seasonal, super breeder, waste tire, county abatement, larval habitats, aside from the shape effects, endemic transmission may have been increased by the decreased ground shadow due to the shadow overlapping between layers. Ground absorption usually changes with opposite sign as that of the canopy absorption. Somewhat lower albedos are found over most vegetated LULC areas throughout the year [101,102]. The real-time 3D, epi-entomological, capture point, signature, prognosticative, sub-mter resolution LULC model quantitated the unmixed, interpolative, signature affects based on the fraction of sunlit canopy leaves and their corresponding absorption values in the geosampled, shade-canopied, waste tire, Ae aegypti, county abatement, potential super breeder, capture point, eco-georeferenced, forecasted, larval, habitat unmixed dataset.

The Pareto frontier, P(Y), was formally described in the real-time, UAV geosampled, time series datasets by considering a system with function $f: R^m \rightarrow R^n$, where X was a compact set of feasible decisions in the metric space R^n, and Y was the feasible set of criterion vectors in R^n, such that $f: R^m \rightarrow R^n$. This equation was constructed employing the photosynthetic, waste tire, capture point, eco-georeenecable, county abatement, larval habitat, synthesized geo-spectro temporal UAV geosampled, covariates. Assumptions were determined of the preferred directions of known, unmixed, sub-meter resolution, LULC, signature, capture point criteria values. A geosampled potential super breeder, county abatement, capture point forumation [i.e., $y'' \in R^m$] was determined which was then written as $y''\gamma y'$ in the real-time, drone dashboard, ArcGIS model. The Pareto frontier for the geosampled, geo-spectro temporal, county abatement, Ae aegypti, larval habitats was then $P(Y) = \left\{ y' \in Y; \{y'' \in Y\} \notin 0 \right\}$.

In the UAV, ArcGIS epi-entomological, real-time model the shape of the hotspot function of the eco-georefenceble, geosampled, Ae aegypti, larval habitat, capture point, eco-georenecable, iterative, interpolative, LULC signatures was found to be based on the viewing and illumination positions in the real time, geosampled model, which were diverged due to the shape and height of the spheroids. The equation was helpful to understand how the shape of the geosampled, larval habitat, frequency, capture points, and geospectrally/geospatially associated floating, hanging and dead vegetation, shade-canopied, LULC signature components governed the shape of overlap functions at a potential, county abatment, eco-georeferenceable, super breeder foci. The exact overlap function on the principal cone was also captured using the hybrid of the real-time drone geosampled, vulnerability, forecast model which revealed unmixed, bidirectional reflectance values over specific grid-stratifiable, potentially eigendecomposable, sub-meter resolution, RGB eco-endmember, uncoalesced, capture point, data feature, signature attributes.

In the drone model the viewing zenith was the viewing direction which had a different azimuth than the illumination position. Rather than computing the overlap of ellipses rendered from the decomposed, LULC signature, RGB eco-endmembers at arbitrary inclinations, a linear function was instead employed which optimally quantitated the diminution of the overlaps rendered from the model residuals using azimuth angles. The hotspot in the geosampled, shade-canopied, discontinuous, capture point, LULC, larval habitat canopy was then geolocated.

The shape of the hotspot capture point, LULC functions was found to be based on the viewing and illumination positions in the 3-D, larval habitat, LULC, discontinuous 3-D, canopy reflectance model outputs which commonly diverged due to the shape and height of the signature spheroids. The equation $K_g = e^{-\lambda R^2 \left[\sec\theta_i' + \sec\theta_v' - \overline{O}(\theta_i,\theta_v,\phi)\right]}$ was helpful to understand how the shape of the decomposed, RGB, eco-endmember, canopy-shaded, larval, habitat, potential super breeder, eco-georeferenceable, capture point, Ae aegypti, unmixed seasonal, LULC signature components governed the shape of the overlap functions. Since it is important to have an exact solution for overlap function (Schowengerdt RA (2007) Optical radiation models in Remote Sensing: models and methods for image processing, 45-88. Amsterdam). on the principal plane $O(\theta_i,\theta_v,\phi) = (t - \sin t \cos t)(\sec\theta_i' + \sec\theta_v')/\pi$ was employed where $\cos t = \dfrac{h|\tan\theta_i' - \tan\theta_v'\cos\phi|}{b(\sec\theta_i' + \sec\theta_v')}$ in the models as in Liu [103].

Exact overlap function on the principal cone was obtained for the real-time drone dashboard, ArcGIS epi-entomological, vulnerability, forecast, sub-meter resolution, LULC, signature eco-endmember model where $\theta_v' = \theta_i'$ and ϕ varied from 0 to 2π. The hybrid of geometric opticality for the county abatement, real-time, capture point, frequency signatures was then tabulated for optimally quantitating bidirectional reflectance of the decomposed, potential super breeder, larval habitat, 3-D, partially canopied, RGB eco-endmember, geo-spectral, LULC values.

The unmixed, sub-meter resolution, eco-georeferenceable, capture point, RGB, eco-endmembers modelled the viewing zenith in the Ae aegypti, waste tire, frequency model which was θ_v, but the viewing direction had a different azimuth than the illumination position. Rather than computing the overlap of ellipses rendered from the eco-georeferenced, capture point, larval habitat, canopy floating, hanging and dead vegetation-related, LULC signature, temporally dependent, RGB eco-endmember components at arbitrary inclinations and Euclidean distances directly in the real-time drone dashboard ArcGIS models, a linear function was instead fit to the paradigm outputs for quantitative diminution of the overlaps generated employing azimuth angles $\Phi = \dfrac{4R}{h(\tan\theta_v + \tan\theta_i)}$. was then approximated by the azimuthal cut-off of the hotspot as determined by the 3-D, Ae aegypti, waste tire, larval habitat, RGB eco-endmember, real-time, capure point, county abatement, LULC, signature, UAV, real-time, ArcGIS, frequency models. Linearly iteratively, interpolatable, epi-entomological forecasts were employed for defining ϕ between 0 and Φ or π in the capture point models. For the case $\Phi < \pi$, we assigned $O(\theta_i,\theta_v,\phi) = O(\theta_i,\theta_v,\phi = \pi)$ for all ϕ between Φ and π. Though by employing signature approximations we were able to robustly quantitate any small errors in overlapping shade-canopied LULC areas in the county abatement, real-time, forecast, vulnerability models. The output from the equation $O(\theta_i,\theta_v,\phi) = \dfrac{1}{2}\left[\sec\theta_i' + \sec\theta_v' - \dfrac{h}{b}|\tan\theta_i' - \tan\theta_v'\cos\phi|\right]$ was subsequently employed to determine if the model optimally quantitated azimuthal width effectively for adequately tabulating the potential seasonal, super breeder, eco-georefenceble, Ae aegypti, waste tire, larval habitat, shaded-canopy, geoclassifiable, eco-cartographic, LULC, "hotspot" effect as determined by the R/h ratio in the drone dashboard ArcGIS. The outward width of hotspot on the principal plane in the models were quantifiable by ratio; and, the inward width was determinable the unmixing algorithms in the cartographic, real-time, UAV image software.

Exact contribution of sunlit, geosampled, partially canopied, capture point, waste tire, *Ae. aegypti,* potential super breeder, eco-georeferencable, larval habitat, gridded surface, illuminative, predictor variables and their shading effects were then determined in the real-time, ArcGIS, predictive, vulnerability models. In this research, the effect of sunlit canopy on the bidirectional reflectance was spectrally quantized employing the second term in equation $R(i,v) = K_g G + \dfrac{C}{A}\iint_{A_c} \dfrac{\langle i,s\rangle \langle v,s\rangle}{\cos\theta_i \cos\theta_v} d$ [3.3]. This variation depended on both the density and angular distribution of in the equation [3.3]. We assumed that each eco-georeferenceable, UAV, real-time, potential, super breeder, geoclassifiable, LULC, Ae aegypti, waste tire, capture point, immature habitat, geospatial object in a sub-meter resolution, signature scene geosampled at the Hillsborough county ento-epidemiological, intervention, study site could be modeled as a sphere without mutual illumination shading between elements. As such, a second term for quantitating the decomposed, capture point, RGB, eco-endmembers from the LULC signature frequencies was approximated by $K_c C = \dfrac{1}{2}(1 + \langle i,v\rangle)\left(1 - e^{-\lambda R^2 \sec\theta_v}\right)C$ in the real-time, ArcGIS, epi-entomological, county abatement, signature models In this expression, the first term was the illuminated proportion of the area of a single sphere viewed at position at eco-georeferenced, county abatment, LULC sites which was also were illuminatable at position. This was weighted by the second term in the county abatement signature models which was the proportion of the LULC area of spheres visible from zenith angle θ_v. Since both terms varied smoothly between zero and one, this contribution to the hotspot was quite flat. In the case of a spheroid, we simply replaced $\langle i,v\rangle$ by $\langle i',v'\rangle$ where. $\langle i',v'\rangle = \cos\theta_i'\cos\theta_v' + \sin\theta_i'\sin\theta_v'\cos\phi$

The first term in the unmixed frequency signature equation $K_c C = \frac{1}{2}\left(1 + \langle i, v \rangle\right)\left(1 - e^{-\pi R'^2 \sec \theta_i}\right) C$ ignored the problem of mutual shading in the LULC, *Ae. aegypti,* larval habitat, capture point, canopy floating, hanging and dead vegetation sub-meter resolution, RGB, eco-endmember, signature components in the drone model. We handled this problem in the real time, dashboard, ArcGIS module by employing multiple integration, in which the mutual shadowing of the capture point, grid-stratifiable, LULC, county abatement, unmixed canopies and other associated wihin-canopy, larval habitat objects were treated in the same way as the mutual shading of the leaves. Our objective was to derive a simple approximation in the real-time geo-spectro temporal, UAV, geosampled, signature, forecast paradigm to describe the effect of the unmixed, sub-meter resolution, RGB, eco-endmember, iteratively, interpolative, LULC reflectance as emitted from the capture point, county abatement, potential super breeder, canopy-shaded, larval habitat, based on collections of geosampled, individual, discrete, surface values (i.e., fractionalized, floating vegetation, RGB components) for rendering robust, model forecasts (e.g., precise seasonal, geolocations of unknown, seasonally prolific, eco-georeferenecable, waste tire, county abatement, capture point, larval habitat foci). To carry this out, we developed an approach that applied one-stage geometric optics to optimally quantitate the relationship betweeen the unmixed, RGB, eco-endmember, sub-mter resolution, derivative, reflectance spectra of the geoclassified, canopied, topological, LULC components that was mutually shaded in the illumination direction and the unmixed, eco-georeferenceable explanatorial parts mutually shaded in the view direction. Quantification of the mutual shadowing, capture point, waste tire, larval habitat, explanatorial, unmixed, proportional frequencies generated from the decomposed, geosampled, potential super breeder, county abatement, larval habitat, capture point, LULC canopies and its associated unmixed, floating, dead and hanging vegetation, RGB, eco-endmember components revealed no collinearity. Real time simulation of the partially canopied, frequency, capture points was simplified employing an ArcGIS nadir-viewed cone, signature, real-time model in the drone dashboard. We noted that mutual shadowing of illumination did not change the ratio $K_c / (1 - K_g)$ in the model outputs. In the capture point, larval habitat, reflectance, forecasting, county abatement, vector arthropod, vulnerability models, this ratio was itself denoted Kc which was employable for synthesizing A_c / A. This value parsimoniously quantitated consistency with Kg in the LULC signature, orthogonal, real-time, paradigm derivatives but only where the mutual shadowing in illumination and viewing directions in the prognostications (i.e., geolocations of unknown, potential, seasonal, super breeder, county abatement, eco-georeferenceable foci) was deemed independent (i.e., A_c / A) for consistency with Kg. in the real-time, drone dashboard, ArcGIS, Ae aegypti, waste tire, frequency, capture point models.

We then considered the proportion of the eco-georeferenceable, larval habitat geoclassifiable, real-time, LULC sigature canopies which was mutually shadowed by employing unmixed, canopy vegetation, RGB eco-endmember, frequency dataset components as model regressors. In the direction of illumination, there was some capture point, photosynthetic, spectral, reflectance,LULC components which had an area (e.g., $\pi R^2 \sec \theta_i'$) only in specific areas of the iteratively interpolative, 3-D, time series, NDVI signature, county abatement, potential super breeder, seasonal, geosampled data. For example, the total projected area of the immersed, sub-meter resolution, RGB eco-endmember, LULC vegetation components was $\pi R^2 \sec \theta_i'$, if there was no mutual shadowing in the real-time drone dashboard ArcGIS, frequency models.

If there was mutual shadowing in any, county abatement, sub-mter resolution, NDVI eco-endmember signature, the net projected area in the larval habitat, capture point, geoclassifiable, LULC canopy was $1 - e^{-\pi R^2 \sec \theta_i'}$. The difference indicated the total mutual shadowing of the entire LULC, canopy cover. The quantity Mi was the mutual derived canopy shadowing proportion in the illumination direction which was calculatable as $M_i = 1 - \frac{1 - e^{-\pi R^2 \sec \theta_i'}}{\pi R^2 \sec \theta_i'}$. The product revealed the degree of mutual canopy LULC shadowing in the illumination direction in the capture point, county abatement, sub-meter resolution, unmixed, signature, frequency dataset. Next, a spheroid was determined in real-time in the UAV dashboard, ArcGIS, epi-entomological models which on average, had a proportion Mi of the potential, seasonal, eco-georeferenceable, larval habitat, super breeder, Ae aegypti, waste tire, canopied, signature, LULC surface area in the county abatement, epi-entomological, intervention, study site that was not sunlit. This part of the immature habitat canopies was concentrated at the lower part of the spheroid. We then generated multiple risk maps drawn based on the capture point, habitat, shaded, seasonal, canopy boundaries and LULC surface types for the spheroid in the 3-D, ArcGIS real-time UAV dashboard signature frequency models with the area comprising Mi located below it in the unmixed invariant dataset.

The concept of canopy spectral invariants expresses the observation that simple algebraic combinations of leaf and canopy spectral reflectance which may become wavelength independent and determine two canopy structure specific variables – the recollision and escape probabilities. In this research these, potential, super breeder, eco-georeferenceable, sub-meter resolution, UAV, real-time geosampled, LULC, Ae aegypti, waste tire, unmixed RGB signature variables specified an accurate relationship between the spectral response of a vegetation canopy LULC to incident solar radiation at the leaf and the canopy scale. They were sensitive to important structural features of the eco-georefereceable, capture point, larval habitat, county abatement, canopy such as forest cover, tree density, LAI, crown geometry, forest type and stand age. Our assumption was that linking to eigenvalues and eigenvectors of the 3-D radiative transfer equation in the real-time ArcGIS, epi-entomological, forecast, vulnerability,capture point, LULC signature models we would be able to defined Mv as the mutual shadowing proportion of the floating, hanging and dead vegetation-related sub-pixel, eco-endmember, explanatorial, unmixed components in the view direction as $M_v = 1 - \frac{1 - e^{-\pi R^2 \sec \theta_v'}}{\pi R^2 \sec \theta_v'}$.

The viewing shadows were concentrated at the lower part of the spheroid so the Mv boundary was definable in the real-time ArcGIS, epi-entomological, frequecy models. The proportion of sunlit in the geosampled, UAV, real-time, sensor captured, LULC data corresponded to the area above both M1and Mv canopy boundaries in the county abatement, oviposition, data collection which was dependent on both zenith

and azimuth differences between the illumination and view directions in the signature models. At the hotspot, Mi and Mv t boundaries overlapped and the real-time, geosampled, LULC data revealed no mutual shadowing of the geosampled, larval habitat, vegetation-related, RGB, sub-meter resolution, canopy-shaded, eco-endmember frequencies. Interestingly, when the view zenith angle was larger than the illumination zenith angle, in the real-time, ArcGIS, real-time, UAV geosampled, epi-entomological, county abatement, model Mv was greater than Mi and little, or no mutually-shaded, larval habitat, canopy LULC, signature area was visible, based on the azimuth differences between the imaged capture point objects. Thus, the signatures were able to quantitate mutual-shading LULC effects of the partially canopied, floating, hanging and dead vegetation, decomposed, unmixed, RGB spectral components of the capture point, potential, super breeder, eco-georeferenceable, Ae aegypti, waste tire, county abatement, larval habitat foci.

The F-Ratio of nonnadir-viewed, canopy-based spheroids were the spectro temporally quantitated employing the decomposed, submeter resolution, drone, real-time, geosampled, capture point, unmixed, LULC signatures. First, we considered a single spheroid in the Ae aegypti, larval habitat, canopy sub-pixel, unmixed, RGB, eco-endmember uncoalesced datasets. For the spheroidal case, it is necessary to show whether the f-Ratio is still independent of density, as in the case of the nadir-viewing cones [104]. From the view direction, the spheroid had a projected area $\Gamma_v = \pi R^2 \sec\theta'_v$; however, only the portion $\frac{1}{2}(1 + \langle i', v' \rangle)$ of the larval habitat canopy cover was sunlit in the real-time, geosampled, drone dashboard, ArcGIS, models. Similarly, the illumination shadow on the ground occupied the canopied, LULC, habitat area (i.e., $\pi R^2 \sec\theta'_i$). The compound area of viewed larval habitat, canopy, floating, hanging and dead vegetation, capture point, RGB, eco-endmember, sub-pixel, unmixed signature components plus illumination shadow projected onto the background was $\Gamma = \pi R^2 [\sec\theta'_i + \sec\theta'_v - O(\theta'_i, \theta'_v, \phi)]$. We defined the f- ratio for the spheroidal and its eco-georferenceable, spectro temporally associated explanatory, LULC, signature, coefficients in the real-time ArcGIS model as $F = \frac{\Gamma_c}{\Gamma} = \frac{\frac{1}{2}(1 + \langle i', v' \rangle)\sec\theta'_v}{\sec\theta'_i + \sec\theta'_v - O(\theta'_i, \theta'_v, \phi)}$, where was the sunlit area of the capture point, waste tire, potential super breeder, Ae aegypti, county abatement, capture point, shade-canopied, floating, hanging and dead vegetation, RGB eco-endmember components. The corresponding ratio $f = \frac{K_c}{1 - K_g}$ for the signature selection was then defined for the decomposed signature, NDVI, sub-pixel emissivities in the real-time, drone dashboard, imaging, softare module.

In the waste tire, county abatement, eco-georeferenced, forecast, vulnerability model, n represented the canopy shadowed, LULC, fractionalized, signature, time series, sub-meter resolution, parameterizable, frequency estimators generated from the unmixed, drone geosampled, RGB, eco-endmember eco-georeferenced, 3-D, Ae aegypti, waste tire, potential seasonal, capture point, larval habitat decomposed, NDVI, suprebreeder, sub-pixel datasets. If there was no mutual shadowing, the epi-entomological, county abatement vulnerability model rendered $f = F$. As n increased, however, mutual canopy, LULC shadowing occurred and, as such $K_g = e^{-k R^2 [\sec\theta'_i + \sec\theta'_v - O(\theta_i, \theta_v, \phi)]}$, was required to refine the real-time, drone dashboard, ArcGIS, model output. We noted that the mutual canopy shadowing, frequency LULC proportion M was definable as $M = 1 - \frac{1 - K_g}{A\Gamma}$, which was the fraction of total shadowing cast from the floating, hanging and dead vegetation, eco-endmember, signature frequency components that fell onto the capture point, larval habitat LULC canopy cover instead of the background. The sunlit and viewed shaded, canopy-related, unmixed, capture point, geo-spectro temporal, explanatory, topological, feature attributes were then reduced by hiding either from viewing or from illumination.

The f-Ratio with mutual LULC, larval habitat canopy shadowing was $f = \frac{n\Gamma_c - \sum\Delta_{A_c}}{A(1 - K_g)}, = F\frac{1 - \sum\Delta_{A_c}/(n\Gamma_c)}{1 - M}$ $\quad f = \frac{n\Gamma_c - \sum\Delta_{A_c}}{A(1 - K_g)}, = F\frac{1 - \sum\Delta_{A_c}/(n\Gamma_c)}{1 - M}$ where $\sum\Delta_{A_c}$ was the total decrement from $n\Gamma_c$ to A_c (i.e., the background-projected area of viewed, sunlit, capture point surface) in the real-time drone geosampled ArcGIS, epi-entomological, capture point, larval habitat models. $\sum\Delta_{A_c}$ was expressed employing three terms: a decrement due to mutual canopy shading in the view direction plus a decrement due to mutual canopy shading in the sun direction, minus those elements shaded in both directions employing $\sum\Delta_{A_c} = n\Gamma_v (P_v M_v + P_i M_i - P_o)$, where Pv was the conditional probability that the geosampled capture point, county abatement, eco-georeferenceable, potential, super breeder, Ae aegypti, waste tire, larval habitat faced the sun given that it was mutually shaded from view. Here Pi was the probability that the floating, hanging and dead vegetation, LULC, unmixed, RGB eco-endmember surface elements faced the drone viewer given that it was mutually canopy shaded from illumination. Both Pi and Pv were average proportions of the canopy-related, gridded, drone projected, LULC, county abatement, geosampled areas in the view direction.

Po, the third term in the, eco-georeferenecable, potential, super breeder, county abatement, Ae aegypti, waste tire, larval habitat, real-time model, was the overlapped part of the first two geosampled terms, in the oviposition LULC datat set which was expressed as a fraction of. Po, which also contained three parts derived from the real time, drone imaged, 31m resolution, canopy-related, capture point, real time geosampled, larval habitat surface elements (i.e., floating, hanging and dead vegetation LULCs). This collection contributed to remote quantification of the canopy hotspot for the county abatement capture points due to the spatial correlation of the shadows. Since the probabilities of being hidden in multiple directions were not independent, we were able to substitute $\sum\Delta_{A_c} = n\Gamma_v (P_v M_v + P_i M_i - P_o)$ into $f = \frac{n\Gamma_c - \sum\Delta_{A_c}}{A(1 - K_g)}, = F\frac{1 - \sum\Delta_{A_c}/(n\Gamma_c)}{1 - M}$ in the real-time models which yielded a single expression for $f = F\frac{1 - \Gamma_v(P_v M_v + P_i M_i - P_o)/\Gamma_c}{1 - M}$ in the drone dashboard ArcGIS vulnerability paradigm. We then modelled, Pv, Pi and Po. We employed all illumination or viewing canopy shadows incorporating Mior Mv where the 3-D, NDVI reflected, unmixed, canopied, LULC boundaries respectively. In the real-time, drone geosampled, county abatment models, Pv, Pi and Po, were employed to visualize the Mv and Mi boundaries. Since, viewing and illumination, discontinuous, canopy-related shadows fell strictly below Mv and Mi boundaries, Pv, the conditional probability that at surface element (potential super breeder, *Ae. aegypti,* waste tire, seasonal foci) facing the sun given the mutually shadowed LULC areas, was the ratio of the illuminated portion of the real-time, drone projected sub-meter resolution, surface below the Mv boundary in the dashboard ArcGIS model.

Correspondingly, Pi was the conditional probability that the explanatorial, operationizable, geosampled, county abatement, geo-spectro temporally geosampled, potential super breeder, seasonal, larval habitat, unmixed, LULC, signature, frequency components directly faced the real-time drone viewer and was mutually partially, canopy-shaded from illumination. The ratio of the viewed portion of the projected, 3-D, NDVI eco-cartographically delineated, shade-canopied, larval habitat, capture point, geoclassifiable, LULC areas below the Mi boundary. Note, that Mi was the proportion of mutually-shaded, NDVI, delineated, capture point, intermittently canopied, LULC, surface projected to the direction of illumination, but $P_i M_i \Gamma_v$ was the area of this fraction of the geosampled, immature, capture point, canopied, LULC surfaces with floating hanging and dead vegetation-related, sub-pixel, RGB components projected to viewing direction. Proper quantitation of this portion of the eco-georeferenced, county abatement, capture point, larval habitat, potential suprebreeder, geosampled canopy and its associated LULC attributes involved some projection change in the drone dashboard. We used Po as the forecast signature, iterative interpolative, real-time variable representing all the overlapping LULC areas (i.e., o), in the drone swaths which was represented as a fraction of Γ_v in the epi-entomological, LULC signature, Ae aegypti, waste tire, potential, super breeder, eco-georeferenceable, capture points.

We then considered the case in the principal plane. For simplicity, we assumed that all shadows from the capture point, sub-meter resolution, LULC, county abatement, waste tire, eco-georeferenceable, seasonal, larval habitat, floating, hanging and dead RGB eco-endmember, vegetated, capture point components fell below the boundaries Mv and Mi, which were the traces of planes intersecting the spheroid at its center in the drone dashboard, ArcGIS, real-time model. The angle between the planes of the Mi and the illumination boundary $\theta_{M_i} = \cos^{-1}(1 - 2M_i)$ was in the epi-entomological 3-D model. We defined θ_{M_v} similarly. At the county abatement larval habitat hotspot, the Mi and Mv boundaries coincided when $P_v = P_i = 1$, $P_o = M_v = M$ and $f = F = 1$ we then assumed that the viewing zenith angle in the drone epi-entomological, real-time habitat signature model increased to $\theta_v > \theta_i$. In usual cases when mutual shadowing of an eco-entomological-related, seasonal geosampled, potential, prolific, (i.e., super breeder), larval habitat is to be considered, the Mv boundary is higher than the Mi boundary (see Li X, Strahler AH [105].

In the real-time drone sensor's view, Pv was the ratio of the sub-meter resolution, Ae aegypti, larval habitat's surface LULC area between M_v boundary and the illumination boundary to the whole area under the Mv boundary. That is while $P_v = \frac{M_v \Gamma_v - (\Gamma_v - \Gamma_c)}{M_v \Gamma_v}$ Pi was one, and Po cancelled the Mi term. Then, the equation become $f = F \frac{1 - P_v M_v \Gamma_v / \Gamma_c}{1 - M} = F \frac{(1 - M_v) \Gamma_v}{(1 - M) \Gamma_c} = \frac{1 - e^{-2\Gamma_v}}{(1 - K_g)}$. This result suggested that when the viewing direction in the principal plane deviated from (θv >θi) in the drone real-time geosampled, epi-entomological, paradigm the f-ratio changed in the capture point, Hillsborough county, abatment, epi-entomoloigcal, intervention, study site, larval habitat, canopy reflectance forecasts (i.e., geolocations of unknown potential, super breeder foci). We realized that when θv moved inward on the principal plane but had not reached nadir, the Mi was higher than Mv : hence $P_v = 1$, $P_o = M_v$ and $P_i = \frac{1 - \cos(\theta_{M_i} - \theta_v' + \theta_v' \cos\phi)}{1 - \cos\theta_{M_i}}$ after θv passed the nadir, the Mvboundary went to the opposite side of the spheroid from Mi. In this case, the NDVI, sub-pixel, RGB eco-endmember, unmixed, spectral, sub-meter resolution LULC, county abatement, geosampled data revealed the horizontal projection of the larval habitat canopies and its floating, hanging and dead vegetation, LULC, temporally, decomposed components at $\phi = \pi/2$. We then used Pi just as in Strahler and Jupp Bidirectional reflectance modeling of forest canopies using boolean models and geometric optics. Proceedings, International Geosciences and Remote Sensing Symposium: IGARSS9O, Washington DC) with equal to π where Pv was the fraction of Mv over the illumination boundary, i.e.,

$$P_v = \begin{cases} \dfrac{1 - \cos(\theta_{M_v} - \theta_v' + \theta_v' \cos\theta)}{1 - \cos\theta_{M_v}}, & (\theta_{M_v} - \theta_v' + \theta_v' \cos\theta) \geq 0 \\ 0, & (\theta_{M_v} - \theta_v' + \theta_v' \cos\theta) < 0 \end{cases}$$

Note when θ_v was between the explanatorial, eco-georeferenceable, geosampled, waste tire, Ae aegypti, larval habitat hotspot and nadir, Pv was always 1 and a discontinuity of Pv appeared at the nadir. This discontinuity arose from the assumption that all the county abtament, capture points, larval habitat, unmixed, sub-meter resolution, drone geosampled, LULC, shadow components fell under the M_v boundary. Additionally, the M_v at $\theta_v = 0$ was the physical intersection of the canopy, LULC boundaries between the potential super breeder, eco-georeferenceable, LULC, signature, capture point, larval habitat, floating, dead and the hanging immersed, RGB, eco-endmember components, which did not change with viewing geometry: thus, PvMv was still continuous at nadir, and equal to Po. In other words, the wastetire, prolific seasonal, eco-georeferenced, *Ae. aegypti,* capture point, larval habitat, canopy formula had a very large viewing zenith, so that $\theta_{M_v} - \theta_i' + \theta_v' \cos\phi) > 0$ in the real-time, drone dashboard, 3-D, epi-entomological, forecast, signature, capture point, UAV real-time, model.

The decomposed, eco-endmember, sub-meter resolution, LULC signature, interpolation model revealed that when M_i and M_v were independent in $\sum \Delta_{A_c} / (n\Gamma_c) = M$, $\frac{f - \frac{n\Gamma_c - \sum \Delta_{A_c}}{A(1 - K_s)}}{-F \frac{1 - \sum \Delta_{A_c} / (n\Gamma_c)}{1 - M}}$, $\frac{f - \frac{n\Gamma_c - \sum \Delta_{A_c}}{A(1 - K_s)}}{-F \frac{1 - \sum \Delta_{A_c} / (n\Gamma_c)}{1 - M}}$. If all spatial objects are at the same height, the situation will be very close to the "uniform height case" – mutual, time series, fractionalized, canopy-related shadows will always fall on the lower part of the objects and the object top-viewing effect will be strong [Rahman AF, Gamon JA, Fuentes DA, Roberts DA, Prentiss D (2001) Modeling spatially distributed ecosystem flux of boreal forests using hyperspectral indices from AVIRIS imagery. Journal of Geophysical Research 106: 33579-33591.]. However, we assumed that when sub-meter resolution, real-time, LULC, geoclassifiable, canopy heights are distributed over a wide range of iteratively interpolative, eco-cartographically specified, RGB, eco-endmembers, the top layer of the canopy will play a more important role in determining the BRDF of the canopy than the lower layer. Therefore, when the larval habitat, canopy, structural height in the decomposed, 3-D NDVI signature was spectrally quantitated by their distribution wavelength estimates, the BRDF was apparent in the, drone dashboard, ArcGIS real time forecast-oriented signature, interpolation, county abatement, vulnerability model estimation.

The BRDF was determined by the size, shape, and height of the geosampled, potential, super breeder, seasonal, capture point, Ae aegypti, waste tire, geosampled, larval habitat, LULC canopy and the floating, hanging and dead vegetation, unmixed, sub-meter resolution, RGB,

sub-pixel components in the top layer. Restrictions need to be exercised when quantitation of a single canopied top layer is conducted, especially when employing varying ranges of frequency distributions of height retrived from unmixed, geosampled, explanatorial, geosampled, larval habitat, shade-canopied, physical elements in a sub-meter resolution LULC signature and its sampled attributes (Jacob [76]).

To share the weighting between the geosampled, 31m resolution, eco-georeferenceable, potential, seasonal, super breeder, *Ae. aegypti,* waste tire, county abatement, foci a real-time, drone geosampled, parameterizable, LULC signature, optimizable estimator [i.e., $\beta = \left(1 - \frac{h_2 - h_1}{4b}\right)^2$] was employed, when the model output revealed $(h_2 - h_1) \le 4b$. When $(h_2 - h_1) > b$, β is forced to be zero there is a requirements to redefine the layers [Gao BC, Goetz AFH (1995) Retrieval of equivalent water thickness and information related to biochemical components of vegetation canopies from AVIRIS data. Remote Sensing of Environment 52: 155-162]. By so doing, both Pv and Pi were optimally calculated in the real-time, drone dashboard, ArcGIS, 3-D, epi-entomological sub-meter resolution, LULC, iterative interpolative, forecast-oriented, vulnerability, county abatement, signature, model as a weighted sum of corresponding terms $P = \beta P_1 + (1 - \beta) P_2$, where P_1 and P_2 were the spectral, time series, propagational, uncertainty probabilities associated with the uncoalesced spatial dimensions of the geosampled immature habitat gridded canopy. If LULC signature is employed to determine eco-georeferenecable, geolocations of unknown, super breeder, seasonal, vector entomological, capture points) erroneous geo-spectro temporality in unmixed frequencies must be quantitated in order to generate iteratable interpolative, robust, forecast, vulnerabilty maps remotely targeting un-geosampled county abatement hyper productive, foci (Jacob [76]).

$$
\left|
\begin{aligned}
&-\mu \frac{\partial I^M(\tau, \Omega)}{\partial \tau} + I^M(\tau, \Omega) = \\
&\frac{\omega}{4\pi} \int_{4\pi} p(\Omega' \to \Omega) I^M(\tau, \Omega') d\Omega' \\
&+ Q_1(\tau, \Omega) \qquad \tau \le \tau_\alpha \\
&-\mu \frac{\partial I^M(\tau, \Omega)}{\partial \tau} + G(\Omega) I^M(\tau, \Omega) = \\
&\frac{1}{\pi} \int_{4\pi} \Gamma(\Omega' \to \Omega) I^M(\tau, \Omega') d\Omega' \\
&+ Q_2(\tau, \Omega) \qquad \tau_\alpha < \tau < \tau_t
\end{aligned}
\right.
$$

The space of the LULC canopy realizations from the real-time, county abatement, LULC model was generated in the drone dashboard by randomly drawing each radiative transfer equation input waste tire, county abatement, potential super breeder, eco-georeferenceable, unmixed, prognosticative, signature and RGB, decomposed, eco-endmember geosampled datasets within distribution laws. The radiative transfer equations and their boundary conditions were given by:

$$
\left|
\begin{aligned}
&-\mu \frac{\partial I^M(\tau, \Omega)}{\partial \tau} + I^M(\tau, \Omega) = \\
&\frac{\omega}{4\pi} \int_{4\pi} p(\Omega' \to \Omega) I^M(\tau, \Omega') d\Omega' \\
&+ Q_1(\tau, \Omega) \qquad \tau \le \tau_\alpha \\
&-\mu \frac{\partial I^M(\tau, \Omega)}{\partial \tau} + G(\Omega) I^M(\tau, \Omega) = \\
&\frac{1}{\pi} \int_{4\pi} \Gamma(\Omega' \to \Omega) I^M(\tau, \Omega') d\Omega' \\
&+ Q_2(\tau, \Omega) \qquad \tau_\alpha < \tau < \tau_t
\end{aligned}
\right.
\qquad \text{Where} \quad
\left|
\begin{aligned}
&Q_1(\tau, \Omega) = \frac{\omega}{4\pi} \int_{2\pi^+} p(\Omega' \to \Omega) \\
&\cdot I^0(\tau, \Omega') d\Omega + \frac{\omega}{4\pi} \int_{4\pi} p(\Omega' \to \Omega) \\
&\cdot I^1(\tau, \Omega') d\Omega' \qquad \tau \le \tau_\alpha \\
&Q_2(\tau, \Omega) = \frac{1}{\pi} \int_{2\pi^+} \Gamma(\Omega' \to \Omega) \\
&\cdot I^0(\tau, \Omega') d\Omega' + \frac{\omega}{\pi} \int_{4\pi} \Gamma(\Omega' \to \Omega) \\
&I^1(\tau, \Omega') d\Omega' \qquad \tau_\alpha < \tau < \tau_t
\end{aligned}
\right.
$$

in the real-time, 3-D, drone geosampled, model, notice that the correction function was not used in the second equation in [3.2], since no hotspot effect was taken into account in the multiple scattering calculations. It was obvious that no closed solution could be optiamlly derived for the eco-georeferenceable, waste tire, capture point, potential super breeder, LULC, Ae aegypti, forecast-oriented, sub-meter resolution, county abatement, real-time, RGB eco-endmember, signature model.

The geo-spectro temporal, drone geosampled capture point, unmixed, real-time, input LULC, signature variables were assumed initially independent as no information was available about their possible covariance in the dashboard ArcGIS 3-D, predictive, vulnerability, county abatment, epi-entomological forecast model. The distribution law of each within a partially canopied, capture point, potential super breeder,eco-georeferenced, Ae aegypti, larval habitat, geosampled, decomposed, grid-stratified, LULC, signature variable at the intervention, county abatement, study site was selected so that the density of probability was set to be proportional to the sensitivity of the shade reflectance of the eco-georeferenced, capture point, potential, super breeder, county abatement foci considered. This customizaton allowed qualitatively quantitating sample, LULC, canopy domains where the reflectance was more sensitive to the spectrally-dependent, NDVI, reflectance, covariate coefficients. We achieved this by applying transformations for each decomposed, larval habitat, capture point, canopy-related, signature, sub-pixel, explanatorial, variable where the sensitivity of the reflectance was a constant transformed variable. The transformations were selected employing a trial and error process which was applied in the real-time, UAV dashboard directly for quantitating the geo-spatiotemporal red and NIR nadir observations. Then, uniform random drawing was completed over the transformed LULC dataset of unmixed, sub-meter resolution, potential, eco-georefereneceable, waste tire, super breeder, Ae aegypti, larval habitat, eco-endmember, frequency signature variables.

In the explanatorial, geometric-optical, county abatement, frequency signature paradigm, the bidirectional reflectance was modelled as a purely phenomenon that resulted as scenes of discrete, 3-D geo-spatial, capture point, waste tire, potential, super breeder, eco-georeference-able larval habitat, LULC objects (i.e., hanging and floating vegetation, sub-pixel, RGb eco-endmember frequency components) of the geosampled, capture point, canopy which was viewed from different positions in the hemisphere. The resulting scene was broken down into their canopy fractions specifically sunlit and shadowed, background and scene brightness. Illumination direction was calculated by a linear combination of the capture point, LULC, canopy fractions and their respective radiance estimates. The shape of the 31cm, remotely derived, canopied hanging, dead and floating vegetated, eco-endmember, LULC patterns of the diffuse, ripple, water components of the larval habitats were among the driving vulnerability regressors in the county abatement, frequency models. These capture point, Ae aegypti, LULC, canopy spectral

sub-pixel waste tire, emissivities conditioned the mixture of sunlit and shaded objects and background data that was observed from multiple viewing directions thereby quantitating all directions of illumination emitted from the capture points. This mixture, in turn, controlled the brightness in the LULC images. Corrections of the effects from varying sun sensor target canopy geometries in the multitemporal decomposed datasets were described by the BRDF. Measuring the spread of the corrected results from the desired equal reflectance line provided a measure of the accuracy of our method. After correction, the root mean square (RMS) reflectance errors were approximately 0.01 in the visible and 0.02 in the NIR in the real-time UAV dashboard, 3-D, ArcGIS, epi-entomological, forecast-oriented, LULC real-time, capture point, signature model.

An expression for additional azimuthual variation was also derived from the geometric-optical, capture point, LULC, forecast model. This azimuthual variation differed fundamentally in canopy radiance for each unmixed, capture point, 3-D, NDVI, sub-meter resolution, RGB eco-endmember, signature variable. It was observed that all non-zero polar angles were most evident in the larval habitat canopy when vertical and nearly opaque components of the county abatement, eco-georeferenceable, capture point and its floating, dead and hanging vegetation, signature, LULC components were illuminated and viewed along polar sun angles. For quantitating the variation of the directional reflectance of the canopy LULC cover with azimuthual view angle, shade-related, explanatorial parameters were quantified when the illuminated area of the real-time, drone imaged, sub-meter resolution, discontinuously canopied, capture point, larval habitat (i.e., eco-georeferenced areas that was affected by the sun at large angles from the zenith) was remotely identified.

This study characterized the geometric patterns of the first derivative reflectance LULC signature sub-meter resolution, capture point spectra in the real-time, UAV, geosampled, county abatement, data region of the, geosampled, waste tire, eco-georeferenced, potential super breeder, Ae aegypti, county, larval habitat. The ratio of the wavelength area was less than 729 nm compared to the entire unmixed, immature habitat, unmixed spectrum which was negatively correlated with canopy chorophyll LULC count. This finding allowed the construction of a new parameter, defined by symmetry from the real-time drone geosampled, LULC signature, county abatement, epi-entomological, sub-mter resolut6ion model.

Compared to the commonly used LULC signature parameters (i.e IR canopy edges), NIR was a better predictor of low chorophyll content in the larval habitat canopy. This NIR wavelength was easily calculable employing the reflectance of canopied, waste tire, potential, eco-georeferenceable, super breeder, Ae aegypti, waste tire, capture point, LULC canopy-shaded boundary wavebands at 675 and 755 nm and reflectance of Red wavelength at 718 nm Compared to the common landscape parameters,NIR may be a better operationizable predictor of, discontinuously canopied, geo-spatiotemporal, geosampled prolific Ae aegypti, waste tire, larval habitats in a county abatement, intervention, epi-entomological, study site.

Here, the NIR band was employed to exactly estimate the chlorophyll content of leaves over the canopied LULC of the geosampled, Ae aegypti, larval habitat, waste tire, capture point which was easily calculated using the reflectance of NIR boundary wavebands at 675 and 755 nm (R675 and R755) and reflectance of NIR center wavelength at 734nm. The close relationships between the simulated NIR and larval habitat, geoclassifiable, chorophyll count indicated a high feasibility of forecasting the phosynthetic pigment with simulated NIR from the unmixed, sub-meter resolution, LULC data to determine unknown, seasonal, hyper productive foci.

The red-NIR transition zone of unmixed, LULC vegetation, reflectance spectrum marked the boundary between absorption by chlorophyll in the red visible region and scattering due to leaf internal structure in the NIR region in the larval habitat, prolific, capture point. The distance between two large sun angles A and B were then employed as representative canopy explanatorily, geospectral, discontinuously canopied, LULC, *Ae. aegypti,* vegetated, larval habitat, reflectance capture points which were quantized by $\det \begin{vmatrix} 0 & d(AB)^2 & d(AC)^2 & 1 \\ d(AB)^2 & 0 & d(BC)^2 & 1 \\ d(AC)^2 & d(BC)^2 & 0 & 1 \\ 1 & 1 & 1 & 0 \end{vmatrix}$. Another highly symmetrical form of the reflected, larval habitat, canopied eco-georeferenced, capture points $(4\Delta)^2 = \begin{bmatrix} a^2 & b^2 & c^2 \end{bmatrix} \begin{bmatrix} -1 & 1 & 1 \\ 1 & -1 & 1 \\ 1 & 1 & -1 \end{bmatrix} \begin{bmatrix} a^2 \\ b^2 \\ c^2 \end{bmatrix}$

was then given by

For, $j = 3$ the content of the 3-simplex (i.e., volume of the general tetrahedron) was then given by the determinant $288V^2 = \begin{vmatrix} 0 & 1 & 1 & 1 & 1 \\ 1 & 0 & d_{12}^2 & d_{13}^2 & d_{14}^2 \\ 1 & d_{21}^2 & 0 & d_{23}^2 & d_{24}^2 \\ 1 & d_{31}^2 & d_{32}^2 & 0 & d_{34}^2 \\ 1 & d_{41}^2 & d_{42}^2 & d_{43}^2 & 0 \end{vmatrix}$ where the eco-georefernced, geosampled potential super breeder, LULC, canopy edge between vertices and had length. Setting the left side equal to 0 (corresponding to a tetrahedron of volume 0) rendered a relationship between the tabulated Euclidean distances of the highly reflected, prolific, canopied, county abatement waste tire, Ae aegypti, geosampled capture points from the less reflective canopied reference points (i.e., vertices of a planar quadrilateral). This determinant in thereal-time UAV dashboard ArcGIS employed the Heron's formula which was equal to −16 times the square of the area of a triangle with side lengths d(AB), d(BC), and d(AC). If this determinant equaled zero in the model, our assumption was that the procedure was equivalent to checking whether the vertices A, B, and C had zero area. Thereafter, the vertices in the shade -canopied, explanatorial, potential super breeder, county abatement, seasonal, larval habitat, sub-meter resolution, RGB eco-endmember, geospectrally, temporally dependent, forecasting, explanatorial, risk model was diagnosed as collinear.

We employed a residual autocorrelation matrix in SAS/GIS to treat the larval habitat eco-endmember, spectral collinearity. It consisted of elements of the discrete autocorrelation function, arranged in the following manner: $R_x = E[xx^H] = \begin{bmatrix} R_x(0) & R_x^*(1) & R_x^*(2) & \cdots & R_x^*(N-1) \\ R_x(1) & R_x(0) & R_x^*(1) & \cdots & R_x^*(N-2) \\ R_x(2) & R_x(1) & R_x(0) & \cdots & R_x^*(N-3) \\ \vdots & \vdots & \vdots & \ddots & \vdots \\ R_x(N-1) & R_x(N-2) & R_x(N-3) & \cdots & R_x(0) \end{bmatrix}$. This was clearly a Hermitian matrix in the real-time dashboard ArcGIS. In mathematics, a Hermitian matrix (or self-adjoint matrix) is a square matrix with complex entries that is equal to its own conjugate transpose—that is, the element in the i-th row and j-th column is equal to the complex conjugate of the element in the j-th row and i-th column, for all indices i and j $a_{ij} = \bar{a}_{ji}$ or $A = \bar{A}^T$ or $A = \overline{A}^T$, in matrices that can be understood as the complex extension of real symmetric matrices.

A probabilistic estimation matrix was then employed in SAS consisting of n the dependent, discontinuously canopied, explanatorial, potential super breeder, eco-georeferenceable, larval habitat RGB eco-endmember, unmixed, sub-pixel, observations x1,..., xn and a p-dimensional random vector X ∈ Rp×1 (i..e, a p×1 column-vector) and an unbiased estimator of the (p×p) covariance matrix . The sample covariance matrix $Q = \frac{1}{n-1}\sum_{i=1}^{n}(x_i - \bar{x})(x_i - \bar{x})^T$ was generated in the real-time UAV platform where i was the i-th eco-endmember, explanatorial, waste tire, Ae aegypti, capture point, potential super breeder, larval habitat, county abatement, eco-georeferenced, signature observation of the p-dimensional random vector, where $\bar{x} = \begin{bmatrix} \bar{x}_1 \\ \vdots \\ \bar{x}_p \end{bmatrix} = \frac{1}{n}\sum_{i=1}^{n}x_i$ was the sample mean. The reason for the factor n − 1 being employed in spectral uncertainty habitat signature, prognosticative model rather than n was because a factor appeared in the biased estimates of the sample variances and sample covariances, which was interpreted as the mean being unknown. There fater a sample mean was generated in the real-time, drone dashboard, ArcGIS, epi-entomological model.

Next, an MLE of the potential super breeder, seasonal, waste tire, Ae aegypti, sub-meter resolution, real-time UAV, geosampled, unmixed, RGB, eco-endmember uncertainty, frequency, covariance matrix was constructed which rendered an unbiased estimate: $Q_n = \frac{1}{n}\sum_{i=1}^{n}(x_i - \bar{x})(x_i - \bar{x})^T$ in the ArcGIS module. The unbiased uncertainty estimate of the covariance matrix provides an acceptable estimate when the data vectors in the observed dataset are all complete: that is, they contain no missing elements. This approach for optimally estimating the shade-canopied, explanatorial, vector arthropod, seasonal, prolific, larval habitat, eco-endmember, Bayesian, ovariance matrix was to treat the estimation of each variance separately, and to use all the decomposable, krigable, LULC signature observations for which both variables had valid values.

Bayesian covariance matrix estimation arises in multivariate medical, vector, arthropod, signature entomological, problems including multivariate normal sampling models and regression models where random effects are jointly modeled, e.g. random-intercept, random-slope models (Jacob [107]). A Bayesian analysis of these problems requires a prior on the covariance matrix. In order to complete a non-frequenctistic, time series, vector arthropod, real-time, sub-meter resolution, LULC, capture point, larval habitat signature model and run a Bayesian analysis, an expeimneter needs to add priors to parameter estimators including the covariance matrix for optimally quantitating regression coefficients (e.g.,the inverse-Wishart distribution) Here we assess, through a simulation, epi-entomological, LULC signature, interpolation study of an oviposition geosampled, eco-georeferenceable, unmixed dataset of geo-spectro temporal, capture point, potential seasonal, super breeder, waste tire, Ae aegypti, larval habitat, county abatement, capture point, RGB eco-endmembers for establishing the posterior inference of the covariance matrix.

Inverse Wishart distribution is the natural choice for a covariance matrix prior because its conjugacy on normal model and simplicity, is usually available in Bayesian statistical software. Here we employed a scaled inverse Wishart distribution, for attaining more flexibility on the variance priors for conserving the conjugacy properties and for eliminating the prior relationship between variances and correlations in a real-time, UAV dashboard ArcGIS, Ae aegypti, waste tire, county abatement, frequency, signature model. We fit separate priors for individual correlations and standard deviations in the county abatement model. This strategy eliminated any prior relationship within the covariance matrix parameters, hence rendering real-time, unknown, eco-georeferenceable, super breeder, geolocations of seasonal, Ae aegypti, county abatement, capture points.

Assuming the missing data were missing at random resulted in an estimate for the covariance matrix which was unbiased. When estimating the cross-covariance of a pair of signals that are wide-sense stationary, missing samples in an epi-entomological, geo-spectro temporal, sub-meter resolution, LULC signature, unmixed, forecast-oriented, vulnerability model do not need be random (e.g., sub-sampling by an arbitrary factor is valid) [53]. Confidence intervals were generated corresponding to a given seasonal, super breeder, county abatement, endmember uncertainty, probability estimate in the real-time, ArcGIS, epi-entomological, sub-meter resolution, LULC signature model. For a normal distribution, the probability that a given, Ae aegypti larval habitat, unmixed, interpolative, RGB, eco-endmember, UAV, geosampled measurement fell within standard deviations $(n\sigma)$ of the mean μ (i.e., within the interval) was given by $P(\mu - n\sigma, \mu + n\sigma) = \frac{1}{\sigma\sqrt{2\pi}}\int_{\mu-n\sigma}^{\mu+n\sigma}e^{-(x-\mu)^2/(2\sigma^2)}dx = \frac{2}{\sigma}\frac{1}{\sqrt{2\pi}}\int_{\mu}^{\mu+n\sigma}e^{-(x-\mu)^2/(2\sigma^2)}dx$ We then let $u \equiv (x-\mu)/\sqrt{2}\sigma$, Then $P(\mu - n\sigma, \mu + n\sigma) = \frac{1}{\sigma\sqrt{2\pi}}\int_{0}^{\frac{n}{\sqrt{2}}}e^{2}/(2\sigma^2)dx = \frac{2}{\sqrt{\pi}}\int_{0}^{\frac{n}{\sqrt{2}}}e$ = where $\mathrm{erf}\,(x)$ was the so-called erf function. is the "error function" encountered in integrating the normal distribution (which is a normalized form of the Gaussian function). It is an entire function defined by $erf(z) = \frac{2}{\sqrt{\pi}}\int_{0}^{\frac{z}{2}}e$. Erf is implemented in the Wolfram Language as Erf[z] https://www.wolfram.com/language/. A two-argument form giving $\mathrm{erf}\,(z_1) - \mathrm{erf}\,(z_0)$ was also implemented as Erf [z0, z1]. The unmixed, eco-georeferenced, waste tire, capture point, Ae aegypti, larval habitat, eco-endmember erf satisfied the identities $\mathrm{erf}\,(z) = 1 - \mathrm{erfc}\,(z) = \frac{2}{\sqrt{\pi}}\int_{0}^{\frac{z}{2}}e$ = where $\mathrm{erfc}\,(z)$ was erfc, the complementary error function, and was a confluent hypergeometric function of the first kind. For, $z < 0$ where $\gamma(a,x)$ was the incomplete gamma function. In mathematics, the upper incomplete gamma function and lower incomplete gamma function are types of special functions, which arise as solutions to various mathematical problems such as certain integrals.

We also defined a potential, unmixed, capture point, LULC, signature, sub-meter resolution, potential, super breeder, Ae aegypti, predictive, larval habitat, RGB, eco-endmember erf in the real-time UAV, dashboard ArcGIS, vulnerability models as a Maclaurin series where $erf(z) = \frac{2}{\sqrt{\pi}}\sum_{n=0}^{\infty}\frac{(-1)^n z^{2n+1}}{n(2n+1)}$ $= \frac{2}{\sqrt{\pi}}\left(z - \frac{1}{3}z^3 + \frac{1}{42} + ...\right)$ Similarly, we noted that in the model outputs For $x << 1$, $erf(x)$ was computed from $erf(x) = erf(z) = \frac{2}{\sqrt{\pi}}\sum_{n=0}^{a}\frac{(2x)^{2n+1}}{n(2n+1)}$ For, $\mathrm{erf}\,(x)$ = Using integration the county abatment, capture point, forecasts rendered so $Q = \frac{1}{n-1}\sum_{i=1}^{n}(x_i - \bar{x})(x_i - \bar{x})^T$ Continuing the procedure rendered the asymptotic series had the values =0 and $erf(0)$ =The erf had an odd function [i.e. ,] and satisfied where H_n was an eco-georeferenceable, potential, seasonal, super breeder, LULC, waste tire, Ae aegypti, larval habitat, capture point. We expressed erf in terms of a hypergeometric

function of the first kind with a confluent Hermite polynomial for each capture point the first derivative was $\frac{2}{\sqrt{\pi}}\sum_{n=0}^{\alpha}\frac{(2x)^{2n1}}{n(2n+1)}$ and the intergral was in the sub-mter resolution, LULC, signature, county abatement, real-time, drone dashboard ArcGIS models

The multivariate normal distribution of a k-dimensional random vector x = [X1, X2, ..., Xk] was written in the following notation in ArcGIS where the drone real-time, geo-sampled, LULC, capture point, potential, seasonal, super breeder, eco-georefernced, Ae aegypti, waste tire, larval habitat, capture point and the foci's real-time, signature regressors were expressed employing In so doing it became explicitly known that X was k-dimensional , with k-dimensional mean vector $\mu=\left[E[X_1],E[X_2],....,E[X_k]\right]$ and $K\times K$ covariance matrix $\sum=\left[COV\left[X_i,X_j\right]\right], i=1,2,....,k; j=1,2,....k$ in the waste tire, Ae aegypti, capture point, real-time, ArcGIS, county abatement models. The multivariate normal distribution was "non-degenerative" since the symmetric covariance matrix was positive definite. The distribution of the geo-sampled, county, abatement, potential seasonal, super breeder, capture point, larval habitat, shade-canopied, time series, RGB eco-endmber, covariate coefficients was where X was a real k-dimensional column vector and $\sum$ was the determinant of $\sum$. Note the equation reduced the univariate normal distribution in the ArcGIS, real-time. epi-entomological, county abatement, LULC signature models $\sum$ if was a 1×1 matrix. A table was generated in the real-time drone dashboard. A random vector X ∈ Rp (i.e., a p×1 "column vector") multivariate normal distribution with a nonsingular covariance matrix Σ was then generated. We noted that Σ ∈ Rp × p was a positive-definite matrix and the probability density function of X was in the, ArcGIS, signature models when μ ∈ Rp×1 was the expected, sub-meter resolution, forecasted, LULC signature, unmixed frequency values of X The shade-canopied, larval habitat, capture point, eco-endmember, sub-pixel, decomposed, covariance matrix Σ was the multidimensional analog which here was expressed as the variance in the UAV, dashboard ArcGIS model, and which normalized the density $f(x)$ so that it was integrated to 1. We also noted that the unmixed dataset of the eco-georefenceable, potential super breeder, larval habitat, RGB eco-endmembers X1, ..., Xn were independent and identically distributed samples.

The likelihood function of the unmixed, seasonal, super breeder, Ae aegypti, larval habitat, county abatment, capture point, forecasting risk model was then calculated as . It was then readily shown thereafter that the MLE of the mean vector μ in the shade-canopied, larval habitat, eco-endmember, sub-pixel, covariance matrix in the real-time, UAV dashboard ArcGIS was "sample mean" vector: Since the estimate did not depend on Σ, we substituted it for μ in the likelihood function in the epi-entomological, waste tire, Ae aegypti, county abatement, LULC signature, RGB eco-endmember, forecast, vulnerability, eco-georefene cablw models which rendered in the real-time ArcGIS. Thereafter, the value of Σ that maximized the likelihood of the county abatement, signature paradigms.

We regarded the scalar as the trace of a 1×1 matrix in the real-time, potential, super breeder, ArcGIS, waste tire, seasonal, sub-meter resolution, LULC signature, forecast model. This made it possible to employ the identity tr(AB) = tr(BA) as A and B matrices. We then obtained where was the scatter matrix. Since it follows from the spectral theorem of linear algebra that a positive-definite symmetric matrix S has a unique positive-definite symmetric square root S1/2, we used the "cyclic property" of the trace in the real-time,UAV, dashboard ArcGIS to write for the canopied, explanatorial, LULC, Ae aegypti, larval habitat, capture point, LULC, signature RGB, eco-endmember, covariance matrix. We then let B = S1/2 Σ −1 S1/2. Then the expression became $\det(s)n/2$ The positive-definite matrix B can be diagonalized, and then the problem of finding the value of B maximizedusing $\det(B)^{\frac{n}{2}}\exp\left(-\frac{1}{2}tr(B)\right)$ [61].

Since the trace of a square matrix equaled the sum of the capture point, LULC dataset in the real-time, UAV, dashboard of eco-georeference able, oviposition, time series, county abatment, Ae aegypti, larval habitat, unmixed, eco-endmember, sub-pixel, ArcGIS, real-time eigenvalues ("trace and eigenvalues"), the equation reduced to the problem of finding the capture point, interpolative eigenvalues λ1, ..., λp specifically that which maximized When we solved the equation we obtained λi = n for all i for the capture point, LULC signature, potential, seasonal, super breeder, county abatement, larval, habitat foci.

Finally, we obtained [i.e., the p×p "sample, county abatement, potential super breeder, seasonal, waste tire, Ae aegypti, capture point, larval habitat, eco-endmember covariance, uncertainty matrix"(i.e., $\frac{s}{n}=\frac{n}{2}\sum_{i=1}^{n}\left[X_i,\bar{X}\right]\left[X_i,\bar{X}\right]^T$)] which was the MLE of the decomposed population covariance matrix" Σ. The random matrix S was shown to have a Wishart distribution with n – 1 degrees of freedom. The Wishart distribution is a member of the family of probability distributions defined over symmetric, nonnegative-definite matrix-valued random variables (i.e.,"random matrices").

Our results indicated that the cause of the azimuthal variation could be traced to solar flux illumination of the vertically-oriented hanging floating and dead, RGB, eco-endmember, canopy-vegetated, unmixed, capture point, LULC. larval habitat, signature, components. The variation of the sub-meter resolution reflectance in the real-time UAV, dashboard, ArcGIS model outputs of the potential super breeder, seasonal, Ae aegypti, eco-georefenecable, county abatement habitats was moderated by azimutually isotropic sources of flux from sky light and gridded, LULC, reflectance values unbiasedly. The spectral unmixing yielded abundance estimates for each canopied, eco-endmember, oviposition, LULC, signature dataset together summing-up to the 100% reflectance measured in the image. A scattergram representing the canopy RGB eco-endmember, reference points, in the canopied, signature, Ae aegypti larval habitat, capture points and its associated hanging and floating, vegetated, LULC sub-pixel, spectral, eco-endmember, reflectance values was then generated in the drone dashboard. The spectral signature found to be characteristic of a potential, seasonal, super breeder, waste tire, Ae aegypti, eco-georeceable, larval habitat, capture point, in the Hillsborough county abatement, epi-entomological, study site was red 134.67, 145.24 blue and 114.101 green. The images were analyzed to predict potential unknown larval habitats in the study site.

We used an Ordinary kriged-based algorithm in the uav, dashboard ArcGIS® for predicting unknown, potential, seasonal, super breeder, *Ae aegypti*, larval habitats in the study site employing the decomposed reference signatures.

For determining optimal, county abatement, potential, sub-meter resolution, seasonal, super breeder, waste tire, Ae aegypti, larval habitat, capture points, explanatorial, eco-georeferenecable LULC predictors, a semivariogram was constructed which expressed the variation in the unmixed, spectral, RGB, ecoend member covariates. The semivariogram was nonnegative. The semivariogram at distance 0 in the drone forecasted vulnerability, epi-entomological, county abatement, LULC, real-time map, since at zero the residual forecast in the capture point signature interpolations. A semivariogram if and only if it is a conditionally negative definite function, (i.e. for all weights $w_1, \ldots, w_N$ subject to $\sum_{i=1}^{n} x_\gamma^2 = 0$ and locations it holds:) $ss_{xy} = \sum_{i=1}^{n}(x_\gamma - \bar{x})(y_\gamma - \bar{y}) = \left(\sum_{i=1}^{n} x_\gamma y_\gamma\right) - n\bar{x}\bar{y},$

The geospectrally, iteratively interpolated, explanatorily decomposed, potential seasonal, super breeder, eco-georeferenceable, unmixed, LULC signature, Ae aegypti, waste tire, capture point, larval habitat RGB eco-endmembers in the real-time ArcGIS datasets corresponded to the variance of which was given by the negative of this double sum in the drone dashboard. Consequently, the interpolated, temporally dependent, capture point, larval habitat semivariogram wasnon-continuous only at the origin. The height of the jump at the origin is sometimes referred to as nugget or nugget effect [Matheron, G., "Principles of geostatistics", Economic Geology, 58, pp 1246–1266, 1963].The variogram [i.e., 2γ(x, y)] was a function describing the degree of dependence between the predicted, potential, super breeder,, discontinuously canopied, Ae aegypti, habitats [i.e., Z(x)]. This was defined as the expected squared increment of the forecasted values between the eco georeferenced, county abatement, capture point, LULC geolocations.

The geospectrally interpolated, operationizable, LULC signature, explanatorily decomposed, county abatement, larval habitat, RGB, eco-endmember, model output was nonnegative since it was the expectation of a square. The covariance function was related to semiovariogram by 2γ(x,y) = C(x,x) + C(y,y) − 2C(x,y). Interestingly, γ(x, y) = E(| Z(x) − Z(y) | 2) = γ(y,x) was a symmetric function in the real-time UAV, dashboard, ArcGIS models, consequently, γs(h) = γs(− h) was an even function. Coincidentally the function was also a semivariogram as it was a conditionally negative definite function, for all the forecasted, prolific sub-mter resolution, waste tire, Ae aegypti, capture point. signature LULC weights in the, habitat model,

Since the covariance function of the stationary process existed in the real-time, ArcGIS, LULC signature, county abatement, forecast model, we related it to a semiovariogram by $\sum = \left[COV\left[X_i, X_j\right]\right], i = 1, 2, \ldots, k; j = 1, 2, \ldots k$. But since the geosampled, stochastic, RGB eco-endmember, geospectrally interpolated, larval habitat, forecasting, epi-entomological, ArcGIS model reflected a non-stationary process the square of the difference between the expected values was quantitatable by . For quantitating a random field [i.e., stochastic process] Z(x) on the domain D employing a covariance function C(x, y), we used the covariance of the interpolated, RGB, eco-endmember frequencies of the decomposed, signature RGB values of the random field at model forecasted, prolific, geolocation, capture point, county abatement, LULC sites x and y as $COV\left[xy\right] = COV\left(Z(x), Z(y)\right)$

The following parameters described the discontinuously canopied, geospectrally interpolated, potential super breeder, seasonal, Ae aegypti, larval habitat, capture point LULC variograms: The nugget represented the height of the jump of the semivariogram at the discontinuity at the origin. The sill was the limit of the variogram tending to infinity lag distances. We also computed the range in the real-time, UAV, dashboard ArcGIS which was the distance in which the difference of the semiovariogram from the sill became negligible. In geospectrally/geospatially, RGB eco-endmember interpolative operationizable, vector entomological, seasonal, prognosticative LULC signature habitat eco-epidemiological, forecast, risk models with a fixed sill, it is the distance at which this is first reached; for models with an asymptotic sill, it is conventionally taken to be the distance when the semivariance first reaches 95% of the sill[Jacob BG, Gu W, Caamano EX, Novak RJ. Developing operational algorithms using linear and non-linear square estimation in Python for the identification of Culex pipiens and Culex restuans in a mosquito abatement district (Cook County, Illinois, USA) Geospatial]. Theoretically, at zero separation distance (lag = 0), in a waste tire, Ae aegypti, capture point, sub-meter resolution, LULC signature iterative interpolation, for optimally determining unknown, prolific, eco-georeferenceable, county abatament foci geolocations, the semivariogram value would be zero however, at an infinitesimally small sampled habitat distances, the semivariogram often exhibits a nugget effect (i.e., measurement errors or spatial sources of variation at distances smaller than the sampling interval), which is some value greater than zero [68]. In addition to the constant and the assumption of intrinsic stationarity, ergodicity was defined in the larval habitat, capture point, signature LULC models to estimate the empirical semivariance.

 Using the geosampled, eco-georefernced signature, decomposed, Ae aegypti waste tire, capture point, LULC, sub-meter resolution, larval habitat NDVI values of LAGDISTANCE=8 and MAXLAGS=10 was run in PROC VARIOGRAM without the NOVARIOGRAM option in order to compute the empirical semivariogram. We specifed the CL option in the COMPUTE statement to calculate the 95% confidence limits for the classical semivariance. The section COMPUTE Statement described how to use the ALPHA= option to specify a different confidence level in the signature model.

We rquested a robust version of the semivariance with the ROBUST option in the COMPUTE statement. PROC VARIOGRAM produced a plot of the iteratively interpolated, unmixed, waste tire, capture point, LULC,Ae aegypti, larval habitat, signature, RGB eco-endmembers and then revealed both the classical and the empirical semivariograms. In addition, the autocorrelation Moran's and Geary's statistics was tabulated

under the assumption of randomization employing binary LULC weights. The following statements implement all of the preceding requests:

```
proc variogram data=Ae aegypti outv=outv;

compute lagd=7 maxlag=10 cl robust

autocorr(assum=random);

coordinates xc=East yc=North;

var Ae aegypti;

run;

ods graphics off;
```

The VARIOGRAM procedure computed the empirical semivariogram from an unmixed RGB eco-endmember, sub-meter resolution, LULC signature dataset of Hillsborough county abatement capture point measurements. Semivariograms are used in the first steps of spatial prediction as tools that provide insight into the spatial continuity and structure of a random process. Naturally occurring randomness was accounted for by describing a process in terms of the spatial random field (SRF) which here was a collection of random RGB eco-endmember decomposed signature variables throughout a spatially prognosticatie LULC domain. Based on our sample frequency, sub-meter resolution, unmixed, signature dataset, spatial prediction of the prolific, unknown, eco-georferenceable, LULC, oviposition, county abatement geolocations were aimed to provide highly productive, larval habitat coordinate values of the SRF at un-geosampled foci geolocations where no measurements were available. Prediction of the SRF values at the un-geosampled, waste tire, potential super breeder, eco-georeferenceable, county abatement geolocations employing the real-time as ordinary kriging algorithm which required the usage of a covariance model in the UAV dashboard ArcGIS. Due to the randomness involved in quantitating the stochastic processes in the larval habitat, forecasting, eco-epidemiological, predictivem risk model, the theoretical semivariance could not be computed. Instead, we generated an empirical semivariance which provided an estimate of the signature semivariance, which was then used to characterize the spatial structure of the potential, super breeder, county abatement, Ae aegypti, waste tire, larval habitat, capture point, LULC signature desomposition processes. An Ordinary kriged-based algorithm for predicting the unmixed, discontinuously canopied, seasonally prolific, eco-georeferenceable, waste tire, Ae aegypti, larval habitat, RGB eco-endmembers was employed to identify the reference LULC signature interpolated variables generated from the extraction algorithms overlaid onto a 3-D DEM in the real-time UAV dashboard ArcGIS. Semivariogram plot of the logit scale model residuals confirmed a short-range spatial pattern up to approximately 0.5km from the predicted, productive, discontinuously canopied, larval, habitat sites. To carry out this process, residuals for all observed, geoclassified, county abatement, LULC, epi-entomological, signature capture points were calculated on the logit $(\ln(p/1 - p))$ scale of the model.

A krige map of deviance residuals was then calculated, which was added to the predicted values on the logit scale in the real-time, UAV dashboard ArcGIS. Spatial dependence displayed by these plots was analyzed using the semivariogram. The addition of kriged residuals allowed the *Ae. aegypti*, LULC, vulnerabiltiy map to deviate from the signature model and move closer to the original geosampled eco-georeferenced uncoalesced, wavelength, covariate coefficient indicator RGB, sub-mter resolution, measurement values of possible eco-georeferenceable prolific, canopy-shaded, county abatement foci. These smoothed values improved the final maps of the forecasted, waste tire habitats and its associated hanging, floating and dead vegetated LULC, signature, eco-endmember components.

An exponential model was fitted to the semivariogram employing a range of 72.3m, a nugget of 0.12 (variance), a lag size of 11.3m with 12 lags and a partial sill of 0.26 (variance). The coordinates of the alleged breeding sites were recorded, and the sites visited to ground truth the model predictions. Of the 125 sites predicted to be larval habitats by the model, (100%) were found tobe potenetial, super breeder, seasonal, eco-georeferenceable foci. We geosampled an additional 50 habitats not predicted by the model. Based on the number of prolific habitats predicted by the Ae aegypti, LULC, sub-meter resolution, capture point, signature and the randomly geosampled immature habitats, the specificity was 1.00. Subsequently we generated a dataset of Voroni tessellations from the iteratively interpolated, potential seasonal, sub-meter resolution, waste tire, super breeder, eco-georeferenecable, capture points.

Figure 9 reveals both the classical and robust empirical, Ae aegypit waste tire. larval habitat, Hillsborough county abatement study site semivariograms. In addition, the plot features the approximate 95% confidence limits for the classical semivariance. The figure exhibited a typical behavior of the computed semivariance uncertainty, where in general the variance increased with distance from the origin at Distance=0. The needle plot in the lower part of the Figure provides the number of pairs that were used in the computation of the empirical *Ae. aegypti,* larval habitat semivariance for each lag class shown. We noted that the number of pairs shown in the needle plot in the real-time, UAV, dashboard ArcGIS depended on the particular criteria specified in the COMPUTE statement of PROC VARIOGRAM. Importantly the Euclidean habitat distances shown for each lag on the Distance axis in the real-time ArcGIS platform were not the midpoints of the lag classes as in the pairwise distances plot, but rather the average distance from the origin Distance=0 of all predicted, shade, canopied, waste tire, potential, seasonal, super breeder, Ae aegypti, .larval habitat, capture points in a given lag class.

Figure 9: Tires at a commercial site near 3899 Whittier St., Tampa, Florida (Photo credit Jordan Moberg).

We assumed that for the SRF in the habitat signature model had measurements whose sample mean was estimatable by. The hypothesis of ergodicity dictated that in general, an SRF is characterized as ergodic if the statistical moments of its realizations coincide with the corresponding ones of the SRF. In spatial analysis you are often interested in the first two statistical moments, and consequently a more relaxed ergodicity assumption is made only for them.

The iterativelt interpolated, sub-meter resolution UAV interpolated real-time, signature, unmixed, LULC dataset of capture point, Ae aegypti, waste tire, habitat foci in the real-time ArcGIS was embedded in the dashboard. The practical assumptions for the application of simple kriging are wide sense stationarity of the field, the expectation is zero everywhere: and the known covariance function . In probability theory and statistics, covariance is a measure of how much two variables change together and the covariance function describes the variance of a random variable process or field. For a random field of eco-georferenecable, unmixed, stochastically iteratively, intrepreted, LULC, signature sub-meter resolution, RGB eco-endmembers, the drone dashboard ArcGIS was able to quantitate the gridded, capture point, epi-entomological, potential super breeder, seasonal, larval habitat, continuous process $Z(x)$ on a domain Din real-time. Subsequently a covariance function C (x, y) rendered the covariance of the prolific habitat values of the random field at two, potential seasonal, super breeder, capture points, geolocations x and employing. The same C (x, y) (i.e., autocovariance) in the time series was able to robustly delineate explicative, geo-classifiable, multivariate, LULC, geo-spectro temporal, oviposition, random fields of unknown county abatement, larval, habitat geolocations, [i.e., $Cov(Z(x1), Y(x2)]$.

The uncoalesced, kriged capture point, *Ae. aegypti,* waste tire, RGB, larval habitat, spectral weights employed in the geospatial algorithm in the real-time UAV, dashboard ArcGIS had no unbiasedness condition and were quantifiable in geospace by the equation system: $\begin{pmatrix} \omega \\ \vdots \\ \omega \end{pmatrix} = \begin{pmatrix} c(x_1,x_1) & \cdots & c(x_1,x_1) \\ \vdots & \ddots & \vdots \\ c(x_1,x_1) & \cdots & c(x_1,x_1) \end{pmatrix} \begin{pmatrix} c(x_1,x_1) \\ \vdots \\ c(xn,x_0) \end{pmatrix}$. This was analogous to a linear regression of on in the interpolation epi-entomological, real-time signature drone model. For devising optimal, unbiased, real-time, potential seasonal, super breeder, *Ae. aegypti,* capture point, waste, tire, sub-meter resolution, LULC estimators, the kriging algorithm in the real-time ArcGIS rendered : $Z(x_0)\begin{pmatrix} z1 \\ \vdots \\ zn \end{pmatrix} = \begin{pmatrix} c(x_1,x_1) & \cdots & c(x_1,x_1) \\ \vdots & \ddots & \vdots \\ c(x_1,x_1) & \cdots & c(x_1,x_1) \end{pmatrix} \begin{pmatrix} c(x_1,x_1) \\ \vdots \\ c(xn,x_0) \end{pmatrix}$ The signature interpolation kriging error was subsequently given by $\begin{pmatrix} c(x_1,x_1) \\ \vdots \\ c(xn,x_0) \end{pmatrix} = \begin{pmatrix} c(x_1,x_1) & \cdots & c(x_1,x_1) \\ \vdots & \ddots & \vdots \\ c(x_1,x_1) & \cdots & c(x_1,x_1) \end{pmatrix} \begin{pmatrix} c(x_1,x_1) \\ \vdots \\ c(xn,x_0) \end{pmatrix}$ which led to the generalized least squares version of the Gauss-Markov theorem whence The Gauss–Markov theorem, states that in a linear regression model in which the errors have expectation zero and are uncorrelated and have equal variances, the best linear unbiased estimator (BLUE) of the coefficients is given by the ordinary least squares estimator. In this research "best" meant robustly parsimoniously quantitating the lowest possible mean squared error of the regressed, time series, eco-georeferenecable, capture point, LULC, Ae aegypti, waste tire, larval, habitat, iteratively interpolative, frequency estimates.

The errors were not normal, nor independent and identically distributed (only uncorrelated and homoscedastic). Amongst the assumption of frequenctistic regression is common variance (i.e., homosckedascity). Non-Gaussian epi-entomological, vulnerability, forecast habitat, signature models may not optimally target prolific, seasonal, LULC, vector entomological, larval habitat, capture points in a county abatement, intervention, study site.

The oviposition, epi-entomological LULC, larval habitat, signature model, however, assumed the expectation of the random field generated by the time series, geosampled, clinical, field and remote, explanatively geosampled, unmixed, geo-spectro temporal, *Ae aegypti*, larval habitat, waste tire, capture point, predictive, regression coefficients to be known, and relied on a covariance function in the real-time drone dashboard ArcGIS. Commonly in autoregressive expositorial, LULC eco-endmember, time series, RGB analyses, neither the expectation nor the covariance are known beforehand [107].

A kriged map of deviance residuals was then calculated in the UAV real-time dashboard which was added to the predicted values on the logit scale. Spatial dependence displayed by these plots in the real-time, dashboard, ArcGIS frequency, county abatement LULC, signature, larval habitat, time series models was analyzed using the semivariogram. The addition of kriged residuals allowed the map to deviate from the model and move closer to the original geosampled eco georeferenced, covariate coefficient, unmixed, indicator, measurement values of possible prolific, canopy-shaded, seasonal, hyper productive habitats. These smoothed values improved the final maps of the forecasted habitats and its associated hanging, floating and dead vegetation LULC components.

We then generated a dataset of Voroni tessellations for the kriged decomposed Ae aegypti, potential, super breeder, larval habitat, stochastic interpolator in the UAV embedded ArcGIS in the realtime platform. The Voronoi decomposition produced a set of polygons Vi with area f i (i=1..., n). An approximation, based on the midpoints of the legs and center of the triangle were used to evaluate the area covered by each polygonized, Voronoi eco-endmember, waste tire, larval habitat eco-epidemiological, eco-georeferenceble, prolific, capture point, LULC. A new canopied, geosampled, county abatement, capture point was calculated using the importance metric (i.e., Gamma) for all the Voronoi polygons which were generated according to the emissivity estimates of the decomposed signature data. Gamma (u, v) was the importance metric of that sub-pixel geospectrally interpolated canopy spectra, and C(p) was the coordinates of the new polygon center (i.e., the predicted potential super breeder larval habitat). To do this calculation on each polygon we used a scan conversion in the drone dashboard real-time ArcGIS. We ran a scan conversion and examined the frame buffer for each polygon. The unknown global mean zD was estimated by a weighted mean of the predicted, waste tire, potenetial super breeder, shade-canopied, spectrally unmixed, geometrical values using: . The extension error of each polygon was subsequently calculated by employing a discrete version of . If the elementary error terms are uncorrelated, errors can be combined to an estimate of the global error: $Q_n = \frac{1}{n}\sum_{i=1}^{n}(x_i - \bar{x})(x_i - \bar{x})^T$ where the summation is over all polygons[17].

By convention we assumed a normal probability distribution for the global error zD - mg and achieved a 90% confidence limits for zD. The global estimation error decreased with an increasing number of predictive, county abatement, LULC geosamples but some local deviation from this tendency did occur due to large LULC polygons (i.e., the predicted productive, shade canopied, waste tire, potenetial super breeder, eco-georferenecable, LULC, larval habitats). We noted that as the number of predictive geosamples increased the global estimation error which converged to zero. The Voronoi diagram in the real-time UAV, dashboard ArcGIS provided a spatial trend analyses of the error in the spectral canopy RGB, eco-endmember decomposed, geospectrally interpolated, signature, reflectance model which revealed that all geosampled, photosynthetic and NPV, unmixed, explanatorial, covariate coefficients were within normal statistical limitations.

Discussion

Streamed infrared (IR) and RGB video of the potential, seasonal, eco-georeferenced, county abatement, LULC, waste tire, *Ae. aegypti,* larval habitat, super breeder foci imaged in the real-tike UAV was sent to ground stations where Hillsborough county mosquito control personnel viewed the live footage in real time. The compact, and weatherproof ground control station provided a high trans-reflective daylight readable screen with simple, intuitive on-screen information. The standard payload had three compact cameras - forward, angled, downward - for navigation, track, and optimal, geometric, drone dashboard, RGB eco-eco-endmember targeting, interpolative, LULC signature explorations and field epi-entomological, operations in the intervention, county abatement, study site.

When looking for the un-geosampled, capture point, waste tire, potential, seasonal, super breeder, *Ae. aegypti*, ground targets, the center crosshairs of the drone dashboard ArcGIS provided the precise GPS location of the LULC and the eco-georeferenced, larval, habitat foci. Since the multi-directional, real time, ArcGIS, platform streamed live footage to the ground station, the county abatement, mosquito, control personnel were able to identify additional capture points of interest (e.g., super breeder, backyard, birdbath, larval habitats on eco-georeferenceable LULC foci) during the missions as the researchers were able to dynamically alter the aircraft's surveillance mission on the fly.

The drone app wayward algorithms were of particular importance in densely wooded areas in the Hillsborough county abatement, intervention, epi-entomological, study site where the UAV initially flew above the trees, but then descended below the tree line in order to get to its destination (e.g., potential, super breeder, eco-georeferenced, *Ae. aegypti,* waste tire, larval habitat). The UAV visually discriminated between trees (i.e., discontinuous canopy gaps) and the ground to identify clearings (e.g., spaces between trees) so it could safely descend while navigating below the tree line. The UAV required real-time, obstacle, avoidance algorithms from the drone dashboard ArcGIS to safely negiotate obstacles such as branches and vines as it navigated towards an eco-georeferenced, potential, super breeder, LULC, county abatement, waste tire, sampling area. Since the UAV may have lost GPS signal as it navigated below the county tree line, we constructed multiple, real-time, predictive, LULC maps in the drone dashboard ArcGIS. UAVs or RPASs hardware and image processing techniques in the drone dashboard ArcGIS optimally iterately interpolated, the eco-georeferenceable, UAVs/RPASs, capture point, potential, seasonal, super breeder, waste tire, *Ae. aegypti,* larval habitat, unmixed, proxy and LULC signatures (e.g., sparse vegetation, NDVI NIR reflectance, 3-D, DEM, slope coefficients,] for

optimally detecting images of unknown, prolific, breeding site foci for all sorts of purposes including a wide range of county abatement, IVM, larval monitoring and management applications.

The potential for taller trees and shrubs to block the view of vegetation, LULC signature features associated to a potential, county abatement, seasonal, super breeder, Ae aegypti, eco-georeferenceable, waste tire, capture point, larval habitat within discontinuous (i.e., intermittently, shaded-canopied) gaps can be minimized by flying at an elevation that is at least three times the average height of the canopy at a county abatement intervention site. To assess which canopied LULC signature, interpolative parameters can be inferred and under what conditions, we constructed first a simple single-scattering (only one reflection or one transmission) canopy, Ae aegypti, waste tire, geo-spectro temporal, frequency, LULC signature, RGB eco-endmember, real-time model. Our canopy consisted of inclined leaves with the Lambertian reflectance property based on object based algorithmic classifiers (i.e., SAM and SID) in the platform. Diffuse leaf transmittance was assumed, independent of the direction of illumination and distributed according to the cosine law (that is, equivalent to the Lambertian reflectance). Orientation of a potential, seasonal, super breeder, eco-georenenecable, capture point, LULC canopy -leaf was specified by the zenith angle and the solar azimuth of the leaf normal. An all-leaves-alike model was developed, that is, for only one leaf category (a common zenith angle, leaf azimuth, leaf reflectance, and leaf transmittance). Summation over several leaf categories render a county abatement waste tire, Ae aegypti, larval habitat, LULC signature, unmixed model in which the leaf area distribution was nonuniform in azimuth. Noninferability was convenient to assume since characterize all leaves-alike canopy, (homogeneity) wavelengths was not possible (varying illumination levels.). Instead a priori was created in the UAV model where multiple leaf category frequencies was described in the real-time platform. For a complete ("infinitely" dense), LULC canopy, full characterization means determining the zenith angle and the azimuth of the leaf upper side normal, leaf reflectance and leaf transmittance{ Schowengerdt RA (1997) Remote Sensing, Models and Methods for Image Processing, 2nd ed. San Diego, United States: Academic Press).

When two canopied, *Ae aegypti*, waste tire, county abatement geosampled parameters appeared only as a product (e.g., r cos W, where W is the zenith angle of the capture point, geoclassified, LULC gridded, leaf upper side normal), these two parameters cannot be individually inferred (only their product). We use this argument to suggest that the leaf reflectance is not an inferable canopy parameter, in a potenetial, seasonal, eco-georeferenceble, super breeder, Ae aegypti, waste tire, larval habitat unless leaf inclination is determined at a county abatement. In the case of a sparse canopy, leaf area and leaf reflectance cannot be inferred, only their product (even when leaf inclination is known) for such a vector arthropod, LULC signature, capture point. This argument may be trivially simple to conceive since the limitations on an inversion imposed by them onto a real-time UAV, prognosticative, sub-meter resolution, county abtaement, forecast, vulnerability-oriented signature, interpolation model is readily apparent. A difficult question in connection with the argument may be at what geosampled, UAV, dashboard, real-time detected, canopy signature, LULC change value should the change in the reflectance with direction of viewing be regarded as very small. We do present some numerical examples, calculating the extent of the "Lambertian viewing," based on a somewhat arbitrary assumption that a very small change means a change by a fraction (e.g.<than 0.02.). The answer may depend on the signal-to-noise ratio of the radiometer, on the number of leaves viewed in the field of view, and on the accuracy of the real time, UAV, *Ae. aegypti,* real-time, signature, geometric-optical signature model. Properties of several leaf categories are more difficult to infer than those of an all-leaves-alike canopy. Nilson T (1992) Radiative transfer in nonhomogeneous plant canopies. Advances in Bioclimatology 1: 59-88. Multiple scattering (highly important in the reflective infrared) has, for a given structure [109].

While larger abatement areas at the Hillsborough County, abatement, study site were covered by LULC signature images as the elevation increased, there was also a slight loss of resolution of smaller habitat objects on the ground. We compensated the loss of acuity at higher elevations by capturing larval habitat, waste tire, LULC images within aggregated grid-stratified, site, pixel densities; the UAV, gridded image size was sufficient to eco- cartographically delineate, capture point, unmixed, signature characteristics based on the charge-coupled device (CCD) image sensor within the UAV camera. The epi-entomological, capture point, county abatement, study site, LULC, signature image did not require long time for processing and storage. The optimal flight elevation for the aerial surveys for optimally, remotely, targeting, unknown, potential, un-geosampled, seasonal, super breeder, eco-georeferenecable, county abatement, signature, capture points was deduced per breeding site by tabulating a compromise between maximum coverage, image acuity for the identification of vegetation and landform features, and the image overlap requirements for real-time ArcGIS processing. In doing so, we were able to generate orthomosaics of potential prolific eco-georefer-enceable, county abatement, capture point, foci in the real-time, UAV dashboard.

The combination of flight elevation, spacing between capture point, sub-meter resolution, grid-stratifiable, LULC, signatures acquired along the county abatement transects, need to be considered to determine optimal, UAV, real-time, sampling strategies for future research for optimally, remotely, targeting, eco-georeferenceable, capture point, potential, super breeder, seasonal, Ae aegypti, waste tire, larval habitats in an epi-entomological, intervention, county abatement, study site. In this research, the distance between the eco-georeferenced, UAV, real-time, geosampled, Hillsborough county images on the sampling grid were half the flight elevation or less, which was dependent on the complexity of the eco-geoclassified, vegetation, LULC, topography imaged. At certain county abatement, capture point, geolocations it was necessary to use higher densities of the LULC, grid-sampled, unmixed, signature data in the real-time, UAV dashboard, ArcGIS module.

Experimenters should consider the fact that UAV coverage may be lower at the edge of the sampling grid when targeting potential seasonal, eco-georeferenceable, super breeder, waste tire, Ae aegypti, larval habitat, capture points at an epi-entomological, intervention, county

abatement, study site. The geosampled LULC area should exceed the eco-geographic boundaries of an unknown, un-geosampled, eco-georef-erenceable, super breeder, seasonal, signature, sub-mter resolution, breeding site possible, county abatement geolocation of interest. Some of these factors may not need to be considered if low-resolution, UAV, geosampled, gridded, LULC images with rapid capture times are employed for the signature, vector, larval habitat acquisition and iterative, interpolation for prognosticatively simulating the unknown potential, seasonal, super breeder, larval habitat, county abatement, eco-georeferenceable, geolocations (i.e., differentially corrected GPS wayward markings of potential, seasonal, super breeder, waste tire, *Ae. aegypti,* larval habitats). The image capture and LULC data storage of the UAV real-tike signaturs should be tested before designing the sampling grid for discriminating seasonal, waste tire, *Ae. aegypti,* county abatment, potential, super breeder, eco-georeferenceable foci. Higher-density, real-time, UAV dashboard ArcGIS sampling grids, object-based classifiers and higher resolution images can ensure adequate coverage of and identification of vegetation and landform features within a county abatement, epi-en-tomological, intervention, study site, eco-geographic, region of interest (seasonal super breeder, waste tire, capture point).

For example, shadowing by the leaf area on a horizontal plane in the Ae aegypti, UAV real-time, capture point, signature model was propor-tional to the cosine of angle between the leaf normal and the solar beam, divided by the cosine of the beam zenith angle. The absolute value of illumination coefficient was geo-spectro temporally quantitable. This absolute signature value was regarded as the interception coefficient for the direct beam by a leaf layer of a potential, partially canopied seasonal, super breeder, waste tire, larval habitat, capture point with projection of leaf area on the horizontal plane. In parallel to the Lambert cosine law, we assumed that sunlight is diffusely transmitted at Hillsborough county with the transmittance dependent of the direction of illumination which emerges distributed (with respect to the leaf normal) accord-ing to the cosine law.

Aerial imaging, real time, grid designs for optimally remotely, geo-spectro temporally targeting, potential, eco-georeferenceable, season-al, super breeder, waste tire, Ae aegypti, larval habitat, capture points employing a sub-meter resolution, unmixed, iteratively interpolative, grid-stratifiable, LULC signature will depend on the topography of the terrain being geosampled in a county abatment, epi-entomological, intervention, study site. It may be easier to sample relatively flat areas where a single-elevation grid of a county abatement study site can be established. Conducting epi-entomological, aerial, LULC, sub-meter resolution, signature searches over flat terrain is relatively easy when employing UAVs since they have GPS positioning capabilities, which are capable of holding a relatively constant elevation above sea level. For sloping, county abatment, study site terrains, it may be necessary to conduct stratified sampling at different elevations along the slope for iden-tifying geolocations of *Ae. aegypti,* waste tires, seasonally, hyper productive, county abatement foci. Each sampling grid in the real-time, UAV, dashboard, ArcGIS module should have good overlap with others to facilitate orthomosaic image and digital surface model construction. In this research we kept the distance between the drone camera and the ground within a range that allowed adequate resolution of the capture point, vegetated, LULC features, so steeper slopes required more overlapping grids. More complicated terrains such as valleys and curved slopes at the Hillsborough county, intervention, epi-entomological, study site required larger numbers of sampling grids to be generated in the real-time ArcGIS drone dashboard to provide adequate coverage and resolution of partially shaded-canopied, potential super breeder, eco-georeference-able, LULC, immature habitat seasonal objects on the ground.

Unmixed, geo-spectro temporally real-time, eigendecomposable, visible and NIR, sub-meter resolution (i.e.,0.31m), RGB, eco-endmember, reference, capture point, eco-georeferenecable, LULC signature fractions of incident radiation reflected, transmitted and absorbed by seasonal, partially canopied, super breeder, capture points of *Ae. aegypti,* waste tires is crucial for implementing larval control strategies in county abate-ments. For any given, grid-stratifiable, time series, eco-georeferenceable, capture point, potential, seasonal, super breeder, LULC object the optical reflectance spectrum as devised in a real-time, drone dashboard, ENVI classification, can robustly eco-cartographically delineate a plot of grid-fractionalized, radiation, reflected as a function of the incident wavelength. In so doing, here, we were able to identify different partially, shade-canopied eco-georeferenceable, LULC signature substances (e.g., seasonal, super breeder, capture point anisotropic, soil reflectance) and classify them by their RGB, eco-endmember, spectral frequencies employing real-time, UAV, object-based, classification algorithms (SAM, SID). The dependence of uncoalesced, vegetation, LULC, refleectance on sensor geometry provided information on the eco-georeferenced, shade-canopied, capture point properties, but may have also been a source of unmodelled systematic propagational error especially in the multi-angle, UAV, real-time, captured signature measurements

Disturbances in the unmixed, empirically regressable, eco-georeferenecable, capture point, LULC, signature, reflectance, datasets of re-al-time intermittently canopied, sub-meter resolution, imaged, potential, super breeder, waste tire, *Ae. aegypti,* larval habitat, feature attributes can aid in optimally prognosticating signature, county abatement, eigenvector, eco-endmember emissivities (e.g., sub-meter resolution, plant constituent spectra refractive fraction of leaf weight at canopy level).Here we were able to determine spectral frequencies which altered the ra-diative interactions within the capture point, potential super breeder, county abatement foci based on LULC topography and, thus the amount of radiation-related, reflection received by the UAV real-time sensor. The ability to unambiguously interpret, unmixed, sub-meter resolution, RGB, eco-endmember, shade-vegetated, discontinuously canopied, LULC signature, derivative, spectra [e.g., canopy optical properties and ar-chitecture parameter rsuch as canopy bidirectional reflectance in the NIR region,] may hinge directly on the ability to resolve the multitude of seasonal, super breeder, breeding site, sub-meter resolution, LULC, sub-pixel view-angle dependence on seasonal vegetation metrics in real-time. Fractional covers of major scene components at the epi-entomological, intervention, county abatement, study site (e.g. green vegeta-tion, LULC), in each image pixel allowed inclusion of photometric shade. The uncoalesced, RGB eco-endmembers compensated for view angle

by modelling the portion of each capture point pixel that was blocked from direct sunlight. However, wavelength dependent multiple scattering in some county abatement, real-time geosampled, capture point, geoclassifiable LULC, vegetation canopies may have resulted in some unquantitated shade. Therefore, there may have been some variability to be expected in the UAV products due to viewing and solar geometry, although this may have been minuscule. Real-time drone dashboard object-based classifiers can eco-cartographically forecast unknown county abatement, waste tire, larval habitat potential, super breeder, waste tire, count *Ae. aegypti,* larval habitats, employing a sub-meter resolution, unmixed LULC signature as a dependent variable in a stochastic interpolator.

UAV real-time sensors can directly measure the distribution of eco-georeferenceable, potential, super breeder, waste tire, county, *Ae. aegypti,* capture point, LULC material along the vertical axis in an entomologically geoclassifiable county abatement, (urban residential), sub-meter resolution image which can be subsequently employed to provide volumetric characterizations of vegetation structure of unmixed, sub-meter resolution iteratively interpolative, potential seasonal, super breeder, *Ae. aegypti,* waste tires. The prospect of employing drones for vegetation, LULC, signature sampling for identifying potential, un-geosampled, prolific, *Ae. aegypti,* waste tire, larval habitats in an ArcGIS, real-time, stochastic interpolator, for a county abatement, is exciting because of the large amount of information that can be collected, managed and stored with minimal effort for any epi-entomological, intervention, study site.

On the other hand, there are many limitations to this approach that should be considered before investing in the equipment necessary to conduct micro-UAV, county abatment, sub-meter resolution, LULC signature surveys for predicting, seasonal, super breeder, capture point, waste tire, Ae aegypti, foci. Experimenters should begin by carefully considering whether their goals are a good match for the acquisition of grid-stratifiable, real-time, LULC signatures from aerial images obtained from drone sensors. Suitable applications include epi-entomological, signature, capture point surveys of the occurrence, distribution and abundance of individual, vector, arthropod, entomological species or vegetation types, and aerial sampling of sensitive habitats or terrain in partially shaded-canopied, agro-pastureland LULCs that may be difficult to access. These remote techniques are particularly suitable in cases where researchers wish to develop accurate forecastable, sub-meter resolution, signature, RGB eco-endmember, vegetation, real-time, LULC maps over moderately large areas (i.e., up to 40 ha). Conducting aerial surveys employing small UAVs greatly expands the size of the county abatement, epi-entomological, LULC study area that can be assessed with minimal disruption of sensitive plants and vegetation. By obtaining a high density of images, experimenters can construct real-time composite images (orthomosaic) and 3-D, models (DEMs) for optimally, remotely targeting unknown, potential, seasonal, eco-georeferenceable, potential, super breeder, waste tire, Ae aegypti, county abatement, capture point geolocations.

Before engaging in drone usage, researchers should be careful to obtain permission from land owners and managers. Regulations for drone use differ among nations and are constantly in flux in response to new technologies and applications. Researchers should check with local and federal agencies before engaging in research activities with UAVs.

DEMs of contour differences of the vegetation and landforms over a county abatement, eco-cartographically geoclassified LULC region may aid in constructing real-time, unmixed, 3-D, RGB eco-endmember, sub-meter resolution, larval habitat, county abatement, LULC, signature, forecast models for remotely targeting unknown prolificeco-eco-geoferenceable, capture point. Currently, in medical entomological GIS literature, epi-entomological vector arthropod, remotely sensed, LULC prognosticative, signature model applications have been restricted to 1 or 2-D indices to characterize canopy height for risk mapping potential, superbreeeder, county abatement, eco-georeferenceable, unknown foci. A novel 3-D, DEM real-time analysis in a drone dashboard ArcGIS constructed employing, capture point, frequency, unmixed, sub-meter resolution, signature, RGB, eco-endmember waveforms, may optrimally characterize the total volume and geospatial organization of vegetation LULC materials within discontinuously canopied county abatement geolocations for targeting potential, seasonal, super breeder, eco-georeferenceable, Ae aegypti, waste tire, larval habitat, capture points. Real-time acquired, sub-meter resolution, explanatory, biogeophysical explanatorial, eco-georeferenceable, uncoalesed, LULC structures (e.g., intermittently canopied, fractionalized, stomatal conductance) may be frequently seasonally measured, in a drone dashboard ArcGIS paradigm).

Leaf photosynthetic and stomatal conductance efficiencies may be investigated with the aid of 3-D, radiative transfer, real-time, decompsoition methods coupled to a semiempirical mechanistic model constructed in a UAV, real-time, dashboard ArcGIS module. Vegetation LULC signatures may be modeled as clumps of leaves randomly distributed on a bright dry soil with partial ground cover for an eco-georeferenced, drone forecasted, iteratively interpolated, potential seasonal, super breeder, *Ae aegypti*, waste tire, county abatement, capture point. For example, NDVI, canopy photosynthetic (Ep), and stomatal efficiencies (Es) may be calculated by quantitating various geometrical, optical, and illumination conditions in a real-time drone dashboard ArcGIS. A base case may be defined to investigate the dynamics of Ep and Es with respect to ground cover, clump, LAI, soil reflectance, and atmospheric conditions for optimally targeting potential, seasonal, eco- georeferenceable, super breeder, waste tire, Ae aegypti, LULC, county capture points in an epi-entomological, intervention study site. The contribution of various radiative fluxes to estimates of Ep may be evaluated and the magnitude of errors in bulk canopy formulations of problem parameters (e.g., non-Gaussian, frequency shifting, non-regressable, interactions in canopy LULC radiation sources) in an unmixed, signature, UAV geosampled, iterative, interpolative, geo-spectro temporal, RGB eco-endmember, sub-meter resolution, county abatement, LULC model.

In this research, the nature and sensitivity of the relationship between Ep and Es to NDVI was investigated and an algorithim in the real-time, UAV dashboard ENVI operationally unmixed, the drone, remotely sensed, LULC signature of the potential super breeder, waste

tire, *Ae. aegypti,* eco-georefereneced, artificial, breeding site, larval habitats. Each geosampled, epi-entomological, grid-stratifiable, study site, experimental plot had coincident, UAV, real-time, geosampled, unmixed, LULC signature, interpolative data and field measurements of stand structures of potential, waste tire, county abatement, capture points.

Employing the indices of canopy structure reterived from the real-time, UAV dashboard, ArcGIS, independent variables, in a real-time, stepwise, multiple regression rendered nonasymptotic predictions of biomass and LAI over a wide range, up to 1100 Mg ha−1 of biomass and a LAI of 11, with 80% of variance explained, respectively for the Hillsborough County epi-entomological, county abatement, intervention study site. Further, we were able to make accurate signature estimates of canopied, LULC, stand structure attributes at the study site employing foliar densities. The mean and standard deviation of diameters of simulated, artificial, capture point, potential super breeder, seasonal, eco-georeferenceable, waste tire, Ae aegypti, larval habitat, discontinuous canopy heights, (e.g., the number of stems greater than 31 cm in diameter). A sensitivity study of the flow to the morphology of the canopy, i.e. the density and vertical leaf-area (LAI) distribution, was then performed numerically over three types of county abatment canopies with five levels of leaf-area index, from 1 to 5. The model revealed that the typical features of canopy flow in a potential, super breeder, seasonal, Ae aegypti, waste tire, larval habitat, capture point became more pronounced as canopy density increased.

Differences in seasonal, canopy morphology may explain the experimental variability observed between capture point canopies. This variability in turbulent characteristics was mostly visible in the subcanopy space in the UAV, gridded image, and was dependent significantly on the density of the upper foliated layers. The mean longitudinal separation between adjacent coherent habitat structures at a potential seasonal, hyper productive LULC, breeding site was also computed for each capture point canopy employing the wavelet transform and approximating the convection velocity of coherent structures as 1.5 times the average wind velocity at canopy top Approaches to characterize chlorophyll/ nitrogen status of crop canopies. Analysis of Remote Sensing Data workshop, Hannover.). Except for the sparsest *Ae. aegypti,* waste tire, larval habitat canopies, the analogy between the atmospheric flow near the top of a vegetation canopy and a plane mixing layer was well verified: Λw ws directly related to the shear length scale Ls=U(h)/U′(h), where hwas canopy height, U mean velocity and U′ was the vertical gradient dU/dz, in a way close to the prediction Λw/h=8.1Ls/h. These real-time geosampled, drone, LULC, signature, eco-endmember measurements were directly related to unmixed indices of canopy, stand which was employable as an independent, explanatorial structural complexity regressors in the multivariate analysis for optimal identification of eco-georeferenceable, seasonal, potential, super breeder, waste tire, non-continuous, LULC signature, Ae aegypti, larval habitat, covariates.

Unmixed signature indices of canopy LULC structure developed using the novel, 3-D, DEM, real time, UAV dashboard analysis accounted for most of the terrain-related catchment, watershed variables employed in the real-time ArcGIS, stepwise, multiple regression, as geometric, orthogonal, signature, RGB ecoendmember prognosticators. The capture point, county abatement models were able to parsimoniously quantitate relationships between geomorphological 3-D processes in real time, while simultaneously eco-cartographically delineating, eco-georeferenceable, uncoalesced, signature, capture point, LULC distributions of potential, seasonal, super breeder, *Ae. aegypti,* larval habitats, within a UAV geosampled, real-time, sub-meter resolution, modelling framework. The real-time 3-D DEMs were obtained by digitizing scaled, topographic, UAV geosampled, real-time, RGB, eco-endmember, frequeny maps of the county abatement, epi-entomological, intervention, study site. The parameters were normally estimated on the basis of altitude matrices in the drone dashboard ArcGIS.

Extraction algorithmic techniques in ArcGIS quantitated flow directions, contributing (upslope) areas, and nested catchments from the sub-meter resolution DEMs which revealed eco-hydrologically dominated, eco-geoclassifible, topological, county abatement, eco-georefereenceable, geolocation, LULC, unmixed signature characteristics. For example, the real-time drone imagery of agro-pasturelands in the Hillsborough County abatement study site had multiple catchments with land use capability classes which varied in signatures derived fron the geosampled, slope coefficient values. Architecture and optics of the capture point, leaf canopy, and their parameterization was quantized in a UAV 3-D model. Regression analysis indicated that flow at any upstream potential, seasonal, super breeder, Ae aegypti, waste tire, eco-georferenecable, LULC, capture point can be estimated by multiplying the flow at a downstream reference geolocation (e.g., gage) by the watershed area ratio. This method accurately predicted upstream flows at area ratios as low as 0.005. We also observed a very strong relationship (R2 = 0.77) between area ratio and flow–flow slopes in non-nested, county abatement catchments. Our results indicate that a simple flow estimation method based on watershed area ratios in a real-time UAV dashboard AecGIS module is justifiable, for the estimation of daily streamflow in ungaged watersheds in the Hillsborough, County abatement, epi-entomological, study site. The DEM model outputs revealed a 0-6% difference in contour elevation at the intervention study site. Existing tools for acquiring descriptive, grid-stratifiable, LULC variables of potential, super breeder, Ae aegypti, waste tire, seasonal, larval habitat, eco-georeferenceble, capture points, in ArcGIS such as surface flow directions and contributing areas, may be developed in real-time, from moderate to steep county abatement, topographic, 3-D, drone imagery.

Errors in DEMs are usually classified as either sinks or peaks. A sink is an area surrounded by higher elevation values and is also referred to as a depression or pit. [17]. This is an area of internal drainage. Some of these may be natural, particularly in karst areas [62]. Quantitating ThreeDimensional Impervious Surface Fractions Employing Geo-Schematic Layout algorithms, Isarithmic Maps and Non-Contiguous Cartograms for Identifying Hydrodynamic Catchment Flood Vulnerable Basins of High-Priority Hurricane Evacuation Routes and Levee Construction Sites in Hillsborough County, Florida Journal of Remote Sensing & GIS 5(2):16-27.). Likewise, a spike or peak in an eco-georeferenced, county

abatement, UAV real time, geosampled, geoclassfied, grid-stratifiable, LULC area will be surrounded by cells of lower spectral frequency values (e.g., potential super breeder, eco-georeferenceable, waste tire, *Ae. aegypti*, seasonal, larval, habitat, capture point foci).

Common, county abatement, natural, landscape features may be less detrimental to the calculation of flow direction in a real-time, UAV dashboard, ArcGIS environment. Errors such as sinks, should be removed before attempting to derive any surface information of potential, eco-georeferenceable, prolific, capture point waste tire, larval habitats of Ae aegypti. Sinks can prevent downslope flow routing of water (www. esri.com).The number of sinks in a given DEM is normally higher for coarser resolution DEMs. A common cause of sinks in our unmixed, iteratively interpolative, eco-georeferenecable, waste tire, potential super breeder, Ae aegypti, waste tire, larval habitat 3-D model resulted from storing the LULC elevation data as an integer number in the real-time drone dashboard ArcGIS. This was particularly troublesome in areas of low vertical relief in the Hillsborough county, real-time, imaged, contour dataset. It is not uncommon to find 1 percent of the cells in a 30-meter-resolution DEM to be sinks in a vector epi-entomological, forecast-oriented, vulnerability, geo-spectro temporal model. Mapping Minimum and Maximum Standard Deviation 3- [15]. This can increase as much as 5 percent for a 3 arc–second epi-entomological DEM. Non-real-time generated DEMs may also contain noticeable horizontal striping, a result of systematic sampling errors when creating the DEM. In our submter resolution LULC signature datatset these disturbances were most noticeable on integer data in flat county abatement LULC images areas. [101]. Fortunately, the real-time UAV dashboard ArcGIS and object-based functions modelled the convergence of flow across natural terrain surfaces, in the Hillsborough county intervention, epi-entomological, study site for optimally remotely identifying eco-georeferenceable, seasonal, potential, county abatement, LULC, signature super breeder, *Ae aegypti*, larval habitat, capture points without integer data.

Real time cartographic software tools may be applied to gentle topography in county abatements owing to embedded nosie reduction algorithms in ArcGIS and ENVI for explicitly handling erroneous emittance in large, flat, county abatement, LULC areas. We addressed the problem of accurately representing general topographic features in a county abatement, sub-meter resolution, LULC waste tire, Ae aegypti, capture point, real-time, drone geosampled, signature paradigm by first identifying field-distinguishable grid-stratifiable, LULC features, such as county resevoirs in the gentle, county abatement, topography. Subsequently we employed these eco-georeferenced, landscape, feature attributes to guide the drone search employing differentially corrected, GPS, topographic, flow directions and catchment, wayard markings. Lakes are explicitly represented in the topology of a watershed for use in water routing [Gates DM (1980) Biophysical Ecology. New York, NY: Springer Advanced Texts in Life Sciences.]. Non-geohydrological flat LULC, unmixed, data, feature attributes also helped guide the search for topographic flow directions in multiple, potential super breeder, eco-georeferenecable, capture point, waste tire geolocations in the Hillsborough county abatement, (e.g., superfund land fill sites) which we were able to remotely discriminate employing low signal to noise in the real-time UAV dashboard ArcGIS. This combined signature feature-based and grid-based, real-time, drone search for potential, waste tire, Ae aegypti, capture point, topographic LULC features yielded watershed boundaries where large reservoirs, swamps lakes and other flat areas were remotely distinguishable at the study site. The real-time mapped, potential, super breeder, seasonal, waste tire, county abatment piles ("hot spots") were easily geo-classifiable from the real-time, UAV, sensed imagery. Automated representations of these grid-stratifiable, LULCs as subsystems within a watershed system were tractable employing the *Ae. aegypti*, capture point, UAV geosampled, decomposed, RGB eco-endmember, sbmter resolution, frequency datasets. The geohydrologic analysis was conducted in real-time, using ArcHydro module in the ArcGIS software in the drone dashboard.

Primary considerations for conducting, real-time, LULC signature surveys for remotely identifying eco-georeferenecable, seasonal, potential, super breeder, waste tire, Ae aegypti, larval habitat, capture points in a county abatement with UAVs, is the density and elevation of images over the region of interest at the county abatement, intervention, epi-entomological, study site. Reconstruction of orthomosaics and digital surface, 3-D, larval habitat, vector, entomological, grid-stratifiable, LULC signatures requires a high density of seasonal, sub-meter resolution images that provide overlapping views of landscape features from multiple angles. The typical sampling strategy in a real-time UAV dashboard ArcGIS may establish a grid of aerial transects. The UAV then may be either flown at a constant speed along county abatement transects in automatic image LULC, signature capture mode, or may be flown manually between imaging grid points of potential, seasonal, eco-georeferenceble, super breeder, waste tire, Ae aegypti, waste tire, larval habitats. The former strategy can be facilitated by real-time ArcGIS software that allows programming flights based on multiple wayard GPS coordinates. Manual flights may be necessary if the time required to store large, epi-entomological, real-time, unmixed, LULC, signatures and images is greater than a few seconds. Here we noted that this was particularly true of raw image formats of the capture point, waste tire, LULC signatures geosampled required approximately 5seconds to process. JPEG images in the UAV dashboard ArcGIS module employed real-time averaging unmixing algorithms to reduce capture point LULC image size which consequently lowered resolution. Whether lower-resolution, LULC signature, capture point,RGB eco-endmember image formats such as JPEGs can be used for predictive RGB eco-endmember 3-D mapping unknown, un-geosampled, potential, county abatement super breeder seasonal, waste tire, Ae aegypti, LULC sites will depend on the flight elevation and the level of detail needed to identify potential, capture points from real-time UAV imagery at an intervention, county abatement. Some small UAVs may not allow the association of the metadata needed for orthomosaic construction (i.e., GPS coordinates and flight elevation) for all *Ae aegypti*, waste tire, larval habitat image formats so it may be necessary to use raw, capture point, LULC signature images.

Based on our experimental evidence, stochastically kriging, unmixed, sub-meter resolution, imaged, *Ae. aegypti*, larval habitat, RGB eco-endmember, LULC reflectance, in a UAV dashboard, real-time ArcGIS can predict multiple, unmixed, shade-canopied, data feature attri-

butes especially those based primarily as a function of tissue (i.e. foliage clumping leaf, orientation) and viewing geometry for identifying potential seasonal, super breeder, eco-georeferenceable, county abatement, unknown, un-geosampled foci. By eigende composing geosampled, prolific, seasonal, eco-georeferenceable, waste tire, larval habitats and their, partially canopied, uncoalesced, radiomeric properties with their respective, county abatement, geo-classifiable, grid-stratifiable, real-time, sub-meter resolution, LULC scenes, the capture point's wavelength proportions were partioned and proportionally determined within an object-based classifier (e.g., ENVI) in the real-time drone dashboard.

Object – based image analysis (OBIA), a technique employed to analyze digital imagery, was developed relatively recently compared to traditional pixel-based image analysis (http://wiki.landscapetoolbox.org/doku). Optical remote sensing has expanded from the use of panchromatic and multispectral sensors to off-nadir looking instruments and object-based LULC classifications which are remotely imposable into real-real-time drone technology. While pixel-based, real-time, image analysis is based on the information in each pixel, object-based image, real-time signature analysis is based on information from a set of similar pixels called objects or image objects. More specifically, in OBIA geospatially processing solutions, image LULC objects (e.g., unmixed, county abatement, potential, super breeder, *Ae. aegypti*, seasonal foci) are groups of pixels] that are similar to one another based on a measure of spectral properties (i.e., color), size, shape, and texture, as well as context from a neighborhood surrounding the pixels may be highlighted. OBIA builds on older segmentation, edge-detection, feature extraction and classification concepts that have been employed in remote sensing [Jensen 2005]. Image segmentation in OBIA, from an algorithmic perspective, is generally divided into four categories: (a) point-based, (b) edge-based, (c) region-based and (d) combined. (http://www.exelisvis.com/docs). Segments have additional spectral information compared to single pixels (e.g. mean values per band, and also median values, minimum and maximum values, mean ratios, variance etc). The primary advantage of OBIA for hyper productive, seasonal, UAVreal-time, identification of unknown, eco-georeferenceable, potential, seasonal, super breeder, *Ae. aegypti*, waste tire, habitats for implementing county abatement larval control, (e.g., IVM) other than the diversification of spectral, RGB eco-endmember, capture point, LULC descriptions of drone objects in Cloud technology, is the additional band information for objects such as, prolific, seasonal, capture point, foci, eco-georeferenceable, sub-meter resolution, signatures in real-time.

Imaging object based, drone spectrometry is a unique type of optical real-time, remote sensing as the surface, fractionalized, LULC, canopy radiance is geo-spectro temporally quantifiable in contiguous, narrow, expositiorial, spectral bands. Narrow spectral bands can measure many individual, LULC absorption features of interest. Here unmixed, seasonal, sub-meter resolution, imaged, Ae.aegypti, capture point, eco-georeferenecable, reference, waste tire, seasonally infrequently, canopied, RGB eco-endmembers, such as pigment composition water content, and dry plant litter (i.e., senesced leaves and stems of an intermittently canopy-shaded, super breeder, county abatement foci), or wood and other aspects of foliar chemistry was inlcuded in the real-time signature analyses. For example, narrow-band, canopy, spectral reflectance within 400 to 1100 nm was used here for imaging different LULC grass species and cultivars under drought stress at multiple, eco-geoeferenced, waste tire, potential, super breeder, county abatement, Ae aegypti, larval habitat, capture points. The peak correlations occurred at 678 to 691 nm and 645 to 617nm for turf quality and leaf firing in the grassland, county abatement, LULC siganatures, respectively. All tall fescues had the strongest correlation at 671 nm for both turf quality and leaf firing. The highest correlations in the NIR was at 750, 775, or 870 nm which were found in three, potential, super breeder, waste tire, Ae aegypti, capture point, larval habitat, eco-georeferenced, county abatement, LULC sites. Although all grasses exhibited some correlations between canopy reflectance and turf quality or leaf firing in the county abatement, intervention, epi-entomological study site, significant capture point, RGB eco-endmember, correlation coefficients were only observed in some grasses associated to the waste tires.

Wavelengths in the photosynthetic region at 645 to 720nm or/and NIR from 707 to 804nm predominated in the sub-meter resolution, *Ae. aegypti*, larval habitat, super breeder, capture point, LULC signatures, that was imaged in the county abatement grasslands. This experiment proved that turf quality and leaf firing could be well forecasted in county abatement tall fescue by employing iteratively interpolative, UAV, real-time geosampled, discontinuously canopied, sub-meter resolution, RGB eco-endmembers evidenced by a coefficient of determination (R2) above 0.50. The results indicate that correlations of unmixed, LULC, canopy reflectance versus turf quality and leaf firing varied with Hillsborough county abatement, LULC, grass species and cultivars. The photosynthetic regions specifically from 661 to 679 nm was relatively important in determining turf quality and leaf firing LULCs in selected, potential super breeder, waste tire, seasonal, Ae aegypti, capture point, eco-georeferenceable geolocations. These leaf morphological LULCs contained tall fescue, under drought stress which was present in agro-pastureland, county abatement, eco-georeferenced, geolocations associated with foci of the arboviral, entomological vector arthropod.

Foliage and nonphotosynthetic vegetation (NPV) standing litter, etc.) may disproportionately affect UAV sampling of eco-georeferenceable, geosampled, potential, super breeder, waste tire, capture point, LULC, Ae aegypti, county abatement, larval habitat, bidirectional, canopy, radiation fields in a real-time dashboard ArcGIS platform through their seasonal reflectance and transmittance. Plant material lacking chlorophyll is referred to as NPV which includes materials such as dry leaf matter (e.g., dry grass and litter), bark, wood, and stems [110] Here, the absorbing and scattering properties of a geosampled, grid-stratifiable, LULC, signature, capture point, eco-georeferenecable, super breeder, seasonal, Ae aegypti, larval, habitat, partially shaded, canopied capture point, optical, prognosticator was defined by the chemical bond frequencies of NPVs and by analyzing the unmixed, 3-D, modelled, RGB, eco-endmember frequency LULC dataset in the drone dashboard ArcGIS . Quantitative estimation of eco-endmember, LULC, fractional cover of photosynthetic vegetation, NPV and bare soil was critical for stochastically modeling the *Ae. aegypti*, sub-meter resolution, county abatement, unmixed signature frequencies. Kriging geo-spectro temporal, eco-georeferenceable,

eigendecomposable, spectroscopic, sub-meter resolution, LULC signatures of woody encroachment, capture point, waste tire, *Ae. aegypti*, seasonal, super breeder, canopy reflectance, in a real-time drone dashboard ArcGIS dis determine seasonal explantorial variables and immature seasonal productivity of unknown, super breeder, larval habitat foci in the Hillsborough county abatement, epi-entomological, intervention, study site.

The presence of NPV, and nonlinear spectral mixing associated with NIR transmission and scattering county abatement, green vegetation, LULCs maycomplicate seasonal interpretation of eco-georeferenceble, geo-spectro temporal UAV real-time, geosampled, capture point, potential, suprebreeder, waste tire, *Ae. aegypti*, larval habitat, capture point, partially canopied, unmixed RGB eco-endmembers. Spectral mixtures that include green vegetation LULCs have the potential of being nonlinear due to transmission and scattering of NIR light by green leaves and the high spectral contrast between red and NIR of leaves (Huete AR [18]) Soil influences in remotely sensed vegetation-canopy spectra in Theory and Applications of Optical Remote Sensing. New York, NY: John Wiley and Sons [Linear mixing occurs when light interacts only with one material. Hence, drone real-time, geosampled, transmissions of seasonal, eco-georeferenceable, gridded, seasonal, waste tire, canopy leaves may lead to multiple scattering and nonlinear mixing in an optimizable, capture point, *Ae. aegypti*, sub-meter resolution, LULC, signature model for real-time detection of un-geosampled, unknown, county abatement, super breeder, waste tire foci. For example, a linear, *Ae. aegypti*, waste tire, sub-meter resolution, LULC, drone geosampled, real-time, ArcGIS, frequency model applied to spectral mixtures of vegetation,soils and shade may overestimate the fraction of green vegetation LULC in an eco-georeferenceable, super breeder, capture point, seasonal, waste tire, county abatement,geo-spectro temporally geosampled, larval habitat thus inducing propogagtional, residual, error probabilities while under estimating, canopy shade in the regression estimate of soil or other habitat properties (e.g., structural traits affecting light scattering "over scales ranging from plant cells to canopies) .The eco-entomological, prognosticative, sub-meter resolution, LULC, larval habitat, RGB eco-endmember, county abatement, risk model erroneous regression coefficients may be smaller, depending on the spectral shape of the county abatement sample (e.g., soil substrate, leaf morphology). The degree of nonlinearity would vary, however, within an intervention, county abatement, epi-entomological, intervention, study site depending on capture point, LULC radiance (e.g., soil LULC reflectance leaf transmittance), and RGB reflectance which may be geosampled in real time and subsequently refined in a drone real-time dashboard ArcGIS module during iterative interpolation of the larval habitat, *Ae. aegypti*, sub-meter resolution, unmixed signatures.

 Unmixed, iteratively fractionalized, LULC, canopy radiance, sub-meter resolution, wavelength spectra can be geo-spectro temporally regressively quantified in geospace (e.g., latent autocorrelation) to determine clustering of non-linearly dependent, transmission-related, hyper-endemic, explanatorial, canopy-related, RGB, eco-endmember, estimator interactions (e.g., lower hanging, immersed vegetation and immature, super breeder, seasonal,waste tire, eco-georeferenceable, LULC, Ae aegypti, larval habitat production) during specific seasonal sample frames (e.g., county flooding) in an abatement ecosystem. While the horizontal extent of real-time, county abatement, drone geosampled, LULCs can be adequately determined from a linear mixing perspective, the interaction of photons with vegetation geoclassified, RGB components in vertical space is known to be highly nonlinear (see Jacob [76]). Nonlinearity in volumetric (e.g., county abatement, LULC canopies with increasing leaf area) makes it extremely difficult to study the role of tissue and structural unmixed, RGB eco-endmember, LULC signature krigable, capture point feature attributes that could determine canopy and landscape radiative characteristics of eco-georeferenceable, potential, super breeder, seasonal, waste tire, unknown *Ae. aegypti*, capture point, county abatement, larval habitat, explanatory foci using drone, real-time, reterived geosampled, known habitat measurements based on illumination conditions, and viewing geometry alone. Nonlinearity in, real-time, imaged uncoalesced, seasonal, LULC, sub-meter resolution, signature datasets increases with an increase in leaf transmittance and/or an increase in background. Conversely, a geosampled, UAV real-time, epi-entomological, LULC signature, in an unmixed, RGB, eco-endmember, time series, vulnerability, predictive analyses based solely on linearizable, *Ae. aegypti*, capture point LULC models without direct connection to field-measurable, 3-D, non-frequentistic quantities can lead to erroneous conclusions if the realistic range of the model parameter estimator values is not known. In contrast to multispectral satellite sensors, real-time, drone imaging spectroscopy can robustly render quantitative LULC estimates related to seasonal, canopy absorption which can be employable to parsimoniously prognosticate, non-linear, seasonal relationships (i.e., hierachical Bayesianisms) of, immature, Ae aegypti, larval, habitat seasonal immature production of specific, geosampled, intermittently canopied, iteratively interpolatable, uncoalesced, RGB eco-endmember surfaces (e.g.,fractionalized, floating vegetation LULCs).

The terrestrial component of unmixed geo-spectro temporal, sub-meter resolution larval habitat seasonal datasets of capture point, signature, potential, super breeder, waste tire, *Ae. aegypti*, larval habitat, partially canopied, geosampled, RGB eco-endmember, vulnerability, real-time, parameterizable estimators may address the physics of energy and water exchanges at the land surface in a epi-entomological, intervention, eco-georeferenceable, county abatement, study site. Here an unmixing SPA extracted an LULC dataset of geosampled, sub-pixel, sparsely canopied, sub-meter resolution RGB, eco-endmembers from UAV real-time imaged, data (i.e., 0.31cm visible and NIRwavelengths) of a prolific, eco-georeferenced, waste tire, *Ae. aegypti* larval habitat, capture point, county abatement LULC scene, SPA builds on the convex geometry endmember search algorithms by including a constraint on the spatial adjacency of candidate pixels, whereby reduction of the susceptibility to outlier pixels occurs when generating realistic endmembers [Jensen 2005]. The task of geolocating decomposable, partially shade-canopied, LULC, orthogonal, spatial filter eigenvectors from the sub-meter resolution imaged, RGB eco-endmembers was associated in geospace with the identification of the simplex vertices in the UAV real-time dashboard ArcGIS. In linear algebra, an eigenvector or characteristic vector of a linear transformation is a non-zero vector that only changes by a scalar factor when that linear transformation is applied to it.

Our assumption was that inconspicuous propogagtional erroneous spatial autocorelation coefficients may render pseudo-replicated LULC, orthogonal, synthetic, spatial filter, eigenvector, sub-meter resolution, epi-entomological data (iteratively interpolative RGB,capture point, waste tire, eco-endmembers) which could denoise spatially non-Guassisms (heteroskedascticy and or multicollinearity), hence rendering more robust interpolatable signatures. The spatial autocorrelation index in the geosampled epi-entomological, time series, capture point, sub-meter resolution, oviposition, LULC dataset was optimally semi-paramterically quantitated on the basis of eigenvector spatial filter parameterizable signature, sub-mter resolution, habitat estimators.

Moran eigenvector spatial filtering (MESF) is a novel methodology in the spatially varying coefficients traditionally promoted in spatial statistics, quantitative geography, and statistical ecology that deals with spatial autocorrelation in eco-georeferenceable data. Moran Coefficient based estimators exhibit statistical properties of unbiasedness, efficiency, and consistency (Jacob [76]). Evidence is accumulating that it also exhibits robustness, or good performance with eco-georeferenceable sub-meter resolution, grid-stratfiable LULC data drawn from not only normal, but also at least Poissonian and binomial, epi-entomological, LULC signature probability distributions construtced from geosampled, time series, vector arthropod oviposition, county abatement, capture points, imaged by sub-meter resolution. Here we explored the performance of an eigenvector eigendecomposition of a dataset of UAV real-time, sub-mter resolution, images waste tire, Ae aegypti, LULC, capture points geosampled in Hillsborough county abatement. The authors addressed the sensitivity of ESF results to changing oviposition. LULC, seasonal characteristics of the eco-georeferenceable. larval habitats. The authors employed a spatial weights matrix specification for constructing MESF synthetic variates, in space–time, employing capture point, flows network structures in a real-time ArcGIS UAV platform.

The Global Moran I, ArcGIS tool computed the mean and variance for the geosampled, eco-georeferenced, capture point, LULC, seasonal, Ae aegypti waste tire, ovitrap attributes being evaluated. Then, for each uncoalesced, eco-geographic, county abatement, geosampled, attribute, feature, (RGB eco-endmember, capture point, discrete, wavelength, integer value), the model subtracted the mean, by creating a deviation from the mean. Deviation values for all neighboring, eco-georeferenceable, capture point, LULC, non-continuous, features (i.e., shaded canopy phenology), within a specified 3icm resolution visble or NIR waveband, were multiplied together to create a cross-product. The numerator for the Global Moran's I statistic in the epi-entomological, seasonal, LULC, vector arthropod, capture point, sub-meter resolution, eco-georeferenceable, vulnerability, RGB eco-endmember real-time signature UAV model included summed cross-products in the eco-georeferenced, geosampled, Ae aegypti ovitraps. Spatial filter algorithms established means, variances, distributional functions, and pairwise correlations for the geosampled, oviposition, seasonal, eigendecomposed signature, predictor variables. In doing so, the eigenfunction spatial filters optimally quantitated the latent autocorrelation explanatory coefficients in the mean response term of the epi-entomological real-time habitat siganture, county abatement model as a linear combination of various, distinct, eco-georeferenceable, oviposition, *Ae. aegypti* capture point, larval habitat, potential super breeder, seasonal, grid-stratifiable, Hillsborough, county, abatement, LULC, map patterns. We restricted their attention to the simultaneous autoregressive Gaussian spatial process and the autoregressive Gaussian response model (also called the spatial lag model). The real-time UAV specified dashboard specified, an autoregressive component in the LULC, *Ae. aegypti* risk model. A stochastic equation for an autoregressive component was generated. This statement included an autoregressive component in the signature, larval habitat, county abatement, frequency drone geosampled, risk model. The damping factor and the disturbance variance were estimated from the geosampled, waste tire, Ae aegypti, capture point, signature, oviposition, frequency, sub-meter resolution, grid-stratifiable, unmixed, LULC signature dataset. The analyses revealed pseudo-spatially replicated information in the eigenvector eigendecomposed LULC signature eco-endmember RGB dataset which was subsequently removed. This misspecification perspective for spatial autocorrelation was not directly comparable with the spatial process LULC signature, capture point models which was based on relationships of random signature frequency components. This research proved that eco-georeferenceable, seasonal, county abatement, super breeder, capture point, larval habitat, foci of *Ae. aegypti* waste tire habitats can be accurately, remotely targeted based on iteratively interpolative, sub-meter resolution grid-stratifiable, sub-mter resolution, visible and NIR frequencies and gesampled grid-stratifiable, immature, epi-entomological, seasonal larval count data of *Ae. aegypti* waste tire potenetial seasonal, super breeder, eco-georfernecable, county abatement LULC foci employing.non-homogeneous, negative binomial, gamma distributed estimates and space-time eigenfunctions.

The eigenfunction spatial filter eigenevector procedure was the foundation for the geometric optical interpretation for teasingout the clustering propensities in the potential, super breeder, eco-georefereneceable, waste tire, LULC, *Ae. aegypti*, larval habitat, sub-pixel, eco-epidemiological, time series imposed into the real-time, drone dashboard ArcGIS algebraic extraction algorithm. In so doing, the real-time, county abatement, waste tire, unmixed, LULC data, RGB eco-endmember, attributes were analyzed based on convex rectilinear or curvilinear data in the drone dashboard. A spatial constraint was introduced employing the spatial-spectral extraction algorithm (SSEE) in the UAV object-based classifier that subsequently made use of the, larval habitat, capture point LULC image mixes during searchs for optimal, non-homogenous, capture point, *Ae. aegypti,* county abatement, drone real-time, geosampled predictors to regress. A non-linear real time framework was constructed employing the unmixed, explanatorial, geosampled, absorption-related, elucidative, eigendecomposable, geoclassifiable real-time, LULC, partially shade-canopied, coefficient values.In the LULC signature model, immersed, hanging vegetation, reflectance was found to be an important field-operationizable RGB, eco-endmember wavelength estimator as it played an intricate role in quantitating the photosynthetic, reflection response of the capture point, *Ae. aegypti,* geosampled, LULC signature, sub-mter resolution model for optimally targeting unknown, potential seasonal, super breeder, eco-georeferenecable, county abatement foci. The SSEE operates differently from SPA using a roving endmember search window that covers the entire input image as it was designed to find similar but distinct endmembers [www.esri.com].

Here the SPA employed the spectral angle and the spatial adjacency of the sub-pixel, super breeder, eco-georeferenced, capture point, unmixed, larval habitat, RGB eco-endmember, *Ae. aegypti,* explanatorial, LULC, signatures which did not constrain the selection of candidate, geospectral absorption, shade-canopied, geometric-optical prognosticators for representing any extractable, photosynthetic or NPV, capture point, regressable frequencies. The SPA model in the real-time UAV dashboard ArcGIS module was designed employing empirical, time series dependent, waste tire, unmixed, eco-georeferenceable, larval habitat, incident, discontinuously canopied, unmixed, LULC radiation, capture point observations based on the assumption that many targets had spatial continuity (e.g. county abatement farmlands). We assumed a spatial constraint would be beneficial in the RGB eco-endmember LULC search. We also assumed that the regressable, larval habitat, unmixed, canopy, photosynthetic and NPV, drone derived, real-time, analyzed, caprture point LULC coefficient values were geospatially adjacent and thus were more likely to have similar spectral absorption, eco-endmember properties thereby, representing one super breeder, county abatement, waste tire, *Ae. aegypti,* capture point, larval habitat, representive, seasonal predictor. Importantly, the fractionialized, canopied, RGB eco-endmember, radiance, explanatorial, eco-georeferenecable, residual forecasts rendered from the unmixed, eco-epidemiological, immature, waste tire, larval habitat, risk model revealed the probability that two adjacent eco-georeferenceable, county abatement, geosampled, eigendecomposable, *Ae. aegypti,* sub-meter resolution, geoclassifiable, LULC, pixels both being spurious was low. Experiments on the non-continuous, LULC canopy, absorption rates demonstrated that SPA can have high efficiency in pure, eco-endmember extractability, UAV-related, unmixing algorithms in a real-time ArcGIS platform due to minimal user interaction. In particular, this component calculated the balance between net radiative turbulent fluxes in the Hillsborough county abatement, geosampled, ento-epidemiological, study site, potential super breeder, waste tire capture points for quantitating inhomogeneously distributed epi-centers of isotropic partially shade- canopied scattering in the seasonal, eco-georeference-able, LULC, forecaseted waste tire immature habitat dataset. In so doing, realistic 3D effects of photosynthetically and NPV, larval habitat. canopy radiation was efficiently calculated which was useful for constructing the waste tire, *Ae. aegypti*, capture point, stochastic LULC, signature, iterative interpolator in the real-time, drone dashboard object-based classifier. This was done so by employing robust, regressable, radiatiative, sub-meter, resolution, directional, RGB, information eco-endmembers for optimally geolocating unknown super breeder foci pixels in the county abatement study site.

In the iterative, stochastic interpolator in the real-time, UAV dashboard ArcGIS module, the RGB, eco-endmember signature, was optimally conducted by dividing the county abatement, LULC image into grid cells, for detecting traces of rescaling and rotation of the habitat signals in each grid. In the mathematical field of numerical analysis, interpolation is a method of constructing new data points within the range of a discrete set of known data points. Interpolation algorithms have been employed in multiple disciplines. For example, Gallagher [111], he developed an image, rotation angle, residual, target, RGB eco-endmember, parameterizable, unmixed estimator based on quantized relations between the rotation angle and the frequencies at which peaks occurred due to interpolation in the spectrum of the image's edge map. He then employed rescaling/rotation detection to detect maliciously adjusted objects inserted into images in geospace.

Interestingly, Popescu & Farid [112] presented their early method to find rescaling traces hidden in any portion of an image without resorting to a reference image by employing expectation maximization (EM) (see Appendix) iterations. An EM algorithm is a method for finding maximum likelihood or maximum a posteriori (MAP) estimates from an operational, empirical, unmixed, geo-spectro temporal, signature, RGB, eco-endmember dataset of optimizable, time series dependent, explanators (e.g., eco-georeferenceable empirically real-time, UAV geo-sampled eigende composable seasonal, intermittently canopied, super breeder, seasonal, *Ae. aegypti*, larval habitat, RGB eco-endmember, eco-system functioning LULC, capture point endoegenous regressors), especially when the model depends on unobserved, latent, eco-geographic, predictor variables [see Jacob [76]]. A MAP estimate is a mode of the posterior distribution which may be parsimoniously utilized to obtain an eco-georeferenceble, explanatorial, LULC signature,capture point estimate of an unobserved quantity (e.g., unknown, potential super breeder, Ae aegypti, waste tire, county abatement, larval habitat) on the basis of a empirically regressable, geo-spectro temporally dependent, eco-georeferenceable, unmixed, capture point, data feature attribute [113].

In Madihan & Saic S [114] the authors employed noise inconsistency to aid in the detection of image rescaling for image eco-endmember splicing detection. Kirchner (2008) [Kitchner M. (2008) in Proc. 10th ACM Workshop Multimedia and Security11–20] applied reliable resampling detection by spectral unmixed, RGB, eco-endmember, frequency analysis of fixed linear residuals. He constructed a rescaling detector based on periodic artifacts in the residue of a local, extrapolated, non-linearizable, geo-spectral, explanatorial, eco-endmember, LULC parameter estimator. Subsequently, he analytically derived the expected position of characteristic rescaling peaks and formed an optimal eco-endmember abrorption detector. Meanwhile Prasad & Ramakrishman [115] localized tampered areas by labeling a mixed pixel as 1 where the second derivative changed sign, otherwise labeling it as 0. If multiple, geometrically dependent, binary operations are involved in a real-time UAV dashboard, ArcGIS or object-based algorithmic sequences, different geospectral, unmixing processing, absorption, it may be usefuto regressively quantitate different peaks in an iteratable, interpolative, qualitatively geosampled, sub-meter resolution, eco-endmember, eco-georeferenceable, LULC optimizable unmixed, signature, dataset of explanatorial, waste tire, Ae aegypti, larval habitat, capture point frequencies . In so doing the county abatement model may reveal optimal imaging photosynthetic and NPV, reflectance, sub-meter resolution, coefficient values associated to potential, eco-georeferenecable, seasonal, super breeder, county abatement, capture points.

Unfortunately, extensively heterogeneous, horizontal, geospectrally extractable, temporally interpolative, shade-canopied, terrestrial biome-related, unmixed, LULC, signature, predictor variables may obscure accurately quantizing real-time, stochastic or deterministic, relation-

ships between sub-meter resolution, RGB eco-endmember UAV response-related, photosynsthetic and or NPV *Ae. aegypti,* waste tire, capture point, real-time, LULC signatures due to canopy multiscattering. As such, capture point, LULC signature, biomass uncertainties in incident, mean, solar radiation calculations at the leaf and canopy scale may be amply propagated in non-linear, quantitative,uncertainty, probabilistic estimates of regressed soil biochemistry,or other canopy structural unmixed information in a drone dashboard real-time, ENVI platform, Remotely retrieved eigendecomposed drone, real-time geosampled, Ae aegypti, larval habitat, photosynthetic and NPV, semi-canopied, seasonal, geoclassifiable LULC sigantures may target hypeproductive, waste tire, seasonal, Ae aegypti, county abatement,eco-georeferenceble, larval habitats. Time series, real-time, sub-meter resolution, grid-stratifiable, UAV geosampled LULC risk maps of explanatorily eigendecomposable, canopy-vegetated landscapes may contain significant classification errors (e.g., inconspicious, heteroskedastic, wavelength estimators), since current understanding of how to scale mixed, photosynthetic and NPV, intermittently canopied, sub-meter resolution, explanatorial, real-time, captured, LULC variables as stand age, and density classes from local regressed estimates are limited in literature.

 A UAV real-time sensor with a cosine response [i.e., follows Lambert's cosine law] may allow real-time dashboard measurements of flux densities in an unknown, waste tire,super breeder, seasonal, LULC, Ae aegypti, eco-georeferenecable, county abatement, larval habitat, capture point, photosynthetic and NPV covariates, through a given plane, (i.e. flux densities per habitat, canopied, unit area). In optics, Lambert's cosine law states that the radiant intensity or luminous intensity observed from an ideal diffusely reflecting surface (e.g., an individual, super breeder, Ae aegypti, LULC, capture point, larval habitat, canopy plant leaf), or ideal diffuse radiator, may be directly proportional to the cosine of the angle(i.e., θ) remotely, geo-spectotemporally, eco-georeferenceable quantizable between the direction of the incident light and the surface normal. Surface incidence is governed by the Lambert cosine law which states that the relative intensity of radiation or light on a surface is equal to the cosine of the angle of incidence, and that the relative area over which it is distributed is the inverse of this value [116,117]. Hence, when a parallel beam emitted from an eco-georeferenceable, real-time, UAV captured, seasonal, super breeder, waste tire, *Ae. aegypti,* larval habitat canopy radiation, image dataset retrieved from a given cross-sectional, county abatement stusy site geolocation spreads over a relatively flat surface capture point, (e.g., agro-pastureland LULC), the area that it covers would be inversely proportional to the cosine of the angle between the beam and a plane normal to the surface in the real time drone dashboard.

Hence, probabilistic spectral uncertainties in canopy irradiance emitted from the sub-meter resolution, imaged, eco-georeferenceble, seasonally, partially shaded, *Ae. aegypti,* geosampled, super breeder, seasonal, waste tire, larval habitat was qualitatively regressively quantitated employing an unmixed capture point datatset of photosynthetic and NPV and RGB eco-endmember, signature-oriented, coefficients values associated to beam disproportionality based on the cosine of the LULC sub-pixel, angles tabulated in the drone dashboard. These non-linear, discrete, integer values, remotely described fluctuating elevations of eco-georeferenceable, gridded, flooded county abatement landscapes in which clustered aggregations of prolific, eco-georeferenceble, intermittently, seasonally canopied, super breeder, *Ae. aegypti,* immature habitats, (i.e., possible high density, hyperendemic, transmission, capture point, LULC, county abatement foci) was forecasted. In radiometry, irradiance is the radiant flux received by a surface per unit area, and spectral irradiance is the irradiance of a surface per unit frequency or wavelength, depending on whether the spectrum is taken as a function of frequency or of wavelength.

The SI unit of irradiance is the watt per square metre (W/m^2), while that of spectral irradiance is the watt per square metre per hertz (W·m^{-2}·Hz^{-1}) or the watt per square metre per metre (W·m^{-3})-commonly the watt per square meter per nanometer (W·m^{-2}·nm^{-1}) [118]. Differences of real-time, drone modeled surface upward and downward longwave and shortwave irradiances may be optimally calculable for partially canopied, geo-spectro temporally geosampled, super breeder, seasonal, partially canopy-shaded, *Ae. aegypti,* waste tire, capture point, LULC, larval habitat, eco-georeferenceable images using real-time unmixed irradiance computed with active derived cloud and aerosol properties. The irradiance differences may be then optimally tabulated for various temporal and spatio-temporal drone scales of monthly gridded, monthly zonal, monthly global, and annual, global, meterological, LULC signature, sub-meter resolution, breeding site foci, county abatement, sub-pixel estimators of unknown, seasonal, super breeder, Ae aegypti, waste tire, larval habitat, capture points.

Parameterizations in a global canopy, model (GCM) in a drone real-time dashboard ArcGIS may be designed to describe the 'collective effects' of seasonal LULC, processes that occur at scales smaller than grid-stratifiable GCM sizes of county abatement, capture point, super breeder, eco-georeferenceable, *Ae. aegypti* larval habitats. Radiation exchange within the canopy plays a crucial role in the canopy microclimate. Parameterizations of many processes such as radiation transfer and autoconversion employ the assumption of independent column approximation (ICA), [i.e., there is no interaction between sub-columns and the grid-averaged LULC effects] which subsequently may depend only on the probability distribution function (PDF) of relevant waste tire, *Ae. aegypti,* UAV captured, signature, sub-meter resolution, grid-stratifiable, eco-georeferenceable, orthogonal predictors. In probability theory, a PDF, or density of a continuous random variable, is a function, whose value at any given sample (or capture point) in the sample space (i.e., the set of possible uncoalesced, RGB eco-endmember values taken by the vector, epi- entomological, larval habitat, potential, superbreeeder, frequency-related, random variables) can be interpreted as providing a relative likelihood that the value of the random variable would equal that sample. In other words, while the absolute likelihood for a continuous UAV real-time, geosampled, geo-spectro temporal, real-time reterived, seasonal, super breeder, eco-georeferenceable, unmixed, LULC, signature random variable to take on any particular specified value is 0 (since there are an infinite set of possible irradiance capture point, values), the value of the PDF at two different, county abatement, hyper productive, breeding waste tire, seasonal samples can be employed to infer, how much more likely it is that the random variable would equal one sample compared to the other sample.

The propagation of radiation through a medium (i. e, waste tire, capture point, super breeder, seasonal, larval habitat, Ae aegypti LULC, vegetation canopy) in a GCM may be affected by absorption, emission, and scattering processes. Hence accurate simulation of canopy microclimate may be contingent on successful pixel decomposition and simulation of the surface radiation balance in an LULC, Ae aegypti, sub-meter resolution, capture point, larval habitat, capture point, real-time, UAV, geo-spectro temporal,eco-endmember signature, wavelength paradigm. Independent column approximation approaches employ one-point statistical information (e.g., PDF), called sub-grid variability and structural information (e.g., geospatial organization and arrangement) that can be remotely characterized by multi-point statistics (Jacob [54,67]). However, coherent, unmixed, LULC, eco-endmember structures have been found at scales ranging from droplet clusters to organized cloud, and have complex interactions with canopied radiation, dynamical processes (e.g., bi-directional, LULC reflectance of floating vegetation around a super breeder, eco-georidenceble, *Ae. aegypti,* waste tire, larval habitat) in mesoscale county, abatement ecosystem. Failure to include sub-grid cloud and convection structures in a radiative transfer equation in a real-time drone dashboard ArcGIS platform for targeting unknown, county abatement, prolific foci may thus lead to inadequate simulations of large-scale, capture point, *Ae. aegypti,* partially shade-canopied, eco-georefernced, larval habitats, and their remotely sensed, partially shaded photosynthetic and NPV–oriented, LULC-related signature, regressable, unmixed, biophysical seasonally explanatorial RGB, constituents. It may be found that ignoring cloud spatial organization in epi-entomological, real-time, signature, vector, epi-entomological, county abatmnt sub-meter resolution, LULC models tends to non-linearly underestimate or overestimate the domain-average radiation fluxes which may be dependent on many factors, (e.g., solar angle and cloud geometry).

The terrestrial component of GCMs may require computationally efficient unmixing algorithms in a UAV real-time, dashboard, object-based classifier for determining real-time, multi-scattered, canopied, LULC radiation contributing to its heating from solar radiation at a county abatement, intervention, epi-entomological, study site. Much of the canopy vegetated, LULCs, geoclassified geosampled, potential, hyper productive, eco-georeferenceable, capture point, *Ae. aegypti,* waste tire, county abatement, larval habitats had strong 3-D controls on its radiation. The scattering from a 3-D object of isotropic scatters may be formulated abstractly and an approach to solution may be described for robustly, parsimoniously, geospectrally, interpolating, decomposed, partially, shade-canopied, eco-georeferenceable, Ae aegypti, waste tire, larval habitats, bio-geochemical, –oriented, LULC products (e.g., photosynthetic and NPV covariates). The resulting approximate description of multi-scattered radiation may correspond to replacing the 3D scattering, capture point, wayward paths with a drone swath with attenuation amplified by a diffusivity factor. This description may provide analytic solutions for single scattered radiation in the capture point LULC while providing an efficient representation of the bidirectional scattering from the 3 dimmesionalized eco-georeferenced, super breeder, eco-georeferenced, seasonal larval habitat.

Seasonal variation in LAI may be estimated for *Ae. aegypti,* waste tire, larval habitat by determining a mid-season maximum value and then reducing this in proportion to the amount of leaf litterfall collected periodically throughout the year. The most common method of estimating seasonal variation in LAI is from measurements of the fraction of visible light transmitted through the canopy to the ground. In more open canopies where county abatement, *Ae. aegypti,* larval habitat, waste tires may occur, the vertical and horizontal distribution of the within canopied leaves becomes important because certain LULC configurations may alter the normal exponential decrease in the net radiation and wind speed from the top of a canopy downward. Roughness length is a term related to boundary-layer conductance that describes how height and other structural features of vegetation LULC modify the generally logarithmic wind profile through canopies and defines the height above the ground surface where wind speeds extrapolate to zero. Roughness length and related expressions of how LULC vegetation affects momentum transfer may be important in radiometric or geometric turbulence created by variations in eco-endmember, LULC, vegetation and topographic conditions across county abatement landscapes when optimally, remotely targeting, seasonal, potential, super breeder, Ae aegypti, larval habitat, capture points.

The Laplace transform is related to the Fourier transform but whereas the Fourier transform expresses a function or signal as a superposition of sinusoids, the Laplace transform expresses a function, more generally, as a superposition of moments. Fourier transform of a function of time itself is a complex-valued function of frequency, whose absolute value represents the amount of that frequency present in the original function, and whose complex argument is the phase offset of the basic sinusoid in that frequency. Given a simple mathematical or functional description of an input or output to an eco-georeferencable, canopied, Ae aegypti, capture point LULC larval habitat decomposable, prognosticative signature, sub-meter resolution, real-time drone dashboard ArcGIS modelling system, the Laplace transform may provide an alternative functional description that may algebracially simplify the process of geospectrally analyzing the behavior of the vector habitat. By optimally synthesizing seasonal, unmixed, canopy, signaturem LULC specifications, Laplace transformation from the time domain to the frequency domain may transform differential equations into algebraic equations and convolution into multiplication in the real-time ArcGIS.Such discretization can provide the solution in terms of solutions to 3-D Helmholtz equations. In mathematics, the Helmholtz equation is the partial differential equation $\nabla^2 A + k^2 A = 0$ where ∇2 is the Laplacian, k is the wavenumber and A is the amplitude [4].

An elliptic partial differential, unmixed,iterative, interpolative, sub-meter resolution, LULC waste tire, capture point,Ae aegypti, larval habitat, RGB eco-endmember signature equation may be given by ∇^2 in a real-time, UAV dashboard ArcGIS where φ is a scalar function and ∇^2 is the scalar Laplacian, or where $\mathbf{F}$ is a vector function and ∇^2 is the vector Laplacian .When $k = 0$, the Helmholtz differential equation reduces to Laplace's equation. the equation becomes the space part of the diffusion equation [119]. The Helmholtz differential equation may be solved in real-time by separation of sub-meter resolution, LULC signaure, RGB eco-endmembers of seasonal, super breeder, waste tire, Ae aegypti,

larval habitat, county abatement, capture point, forecastable variables in a UAV dashboard coordinate system. With the exception of confocal paraboloidal coordinates from the confocal ellipsoidal system: Cartesian, confocal ellipsoidal, confocal paraboloidal, conical, cylindrical, elliptic cylindrical, oblate spheroidal, paraboloidal, parabolic cylindrical, prolate spheroidal, and spherical coordinates may be input into Laplace's equation (i.e., the Helmholtz differential equation with $k=0$ Glantz SA, Slinker BK [64] Primer of Applied Regression and Analysis of Variance. McGraw-Hill Professional Publishing.which may be optimally separable employing sub-meter resolution, grid-stratifiable, eco-georeferenceable, LULC signatures of potential super breeder, county abatement, seasonal, Ae aegypti, waste tire, UAV geosampled, bispherical and toroidal coordinates.If Helmholtz's equation is separable in a 3-D coordinate system in a UAV dashboard real-time ArcGIS platform, then an Ae aegypti, capture point,epi-entomological, LULC habitat signature, model for identifiying real-time seasonally prolific,unknown, un-geosampled, breeding site, eco-endmember, waste tire foci may show that $\frac{h_1 h_2 h_3}{h_n^2}$ where. The Laplacian of the capture point, signature, real-time, Ae aegypti, waste tire, LULC model therefore could be of the form where could simply be decomposed to . Further, such a coordinate system may obey the Robertson condition, which means that the Stäckel determinant would be of the form $S = \frac{h_1 h_2 h_3}{h_n^2}$ in the capture point, drone geosampled county abatement, vulnerability, forecast-oriented, real-time, UAV model outputs. For the Helmholtz differential equation to be separable in a coordinate system, the scale factors in the Laplacian and the functions and may be defined by which can bemust be of the form of a Stäckel determinant [120] In so doing, an Laplace integral representation of the 3-D integral equation for radiative transfer may be discretized for a super breeder, eco-georerenecable, LULC, sub-meter resolution, signature,capture point, LULC, county abatement, forecast-oriented, Ae aegypti, larval habitat vulnerability-oriented model in a real-time, UAV dashboard ArcGIS. Such discretization may provide the solution in terms of solutions to 3D capture point, Helmholtz equations in ArcGIS for identifying potential, super breeder, eco-georerenecable, waste tire, Ae aegypti, larval habitat, county abatement, capture points based on an iteratively interpolated, sub-meter resolution, grid-stratifiable, unmixed, LULC signaturedataset of breeding site. RGB eco-endmember frequencies.

An elliptic partial differential equation given by $\nabla^2 \varphi + k^2 \varphi = 0$ where φ is a scalar function and ∇^2 is the scalar Laplacian, or F where is a vector function and is the vector Laplacian [119]. When k=0, the Helmholtz differential equation derived for a capture point, eco-georeferenceable, real-time. forecast-oriented, signature, UAV model may reduce to Laplace's equation in a real-time ArcGIS module. When (i.e., for an eco-georferenced, drone geosampled, capture point, sub-meter resolution. grid-stratified, LULC image k, the equation may become the space part of the diffusion equation. An arbitrary function f (x) on that domain may be subsequently the solution to an in homogeneous, differential, LULC, sub-meter resolution, signature, Ae aegypti, larval habitat, real-time drone geosampled, RGB eco-endmember equation for f (x). In other words, a county abatement vector control experimenter may optimally quantitate eco-georeferenceable, unmixed, geo-spectro temporally interpolated capture point, signature wavelengths for realizing geolocations of unknown, potential, super breeder, county abatement, waste tire, *Ae. aegypti,* larval habitats. A stochastically or deterministically interpolated sub-meter resolution, LULC signature may be a sum of delta functions in a linear ordinary differential equation (ODE), source. In mathematics, an ordinary differential equation (ODE) is a differential equation containing one or more functions of one independent variable and its derivatives.

Green's function approximate solution (see Apendix) along the paths of entering and exiting, inhomogenously, seasonally geosampled, waste tire, super breeder, *Ae. aegypti,* larval habitat, canopy radiation may also be integrated over an empirically operationizable, field-geosampled, sub-mter resolution LULC dataset of geo-spectro temporally eigendecomposed, canopy, radiation absorption, sub-meter resolution, RGB eco-endmember, signature, regressable covariates. In so doing seasonal regressable qualitatively quantized paths may be assumed to coincide for direction in a GCM. In mathematics, a Green's function is the impulse response of an inhomogeneous differential equation defined on a domain, with specified initial conditions or boundary conditions [64]. Via the superposition principle, the convolution of a Green's function with an arbitrary function f(x) on that domain is the solution to an inhomogeneous differential equation for f(x). The resulting approximate description of a heuristically optimizable empirical explanatorial, uncoalesced dataset of multi-scattered, super breeder, seasonal, immature habitat, canopy radiation may correspond to replacing the 3D scattering paths with a 1D path with attenuation in the waste tire, *Ae. aegypti,* larval habitat, eco-epidemiological, risk, forecasting, LULC signature, county abatement, GCM amplified by a diffusivity factor. This description may be combined with previously derived analytic solutions for qualitatively regressively quantitating single scattered, canopy radiation for parsimoniously providing an efficient seasonal representation of the bidirectional scattering from a 3-D-interpolated, waste tire, super breeder, *Ae. aegypti* larval habitat, geo-spectro temporal, eco-georeferenceable, LULC signature, intermittently canopied object, intended for use in the GCM.

Given the detailed, waste tire, super breeder, county abatement, eco-georeferenecable, *Ae. aegypti,* larval, habitat, capture point, cloud field, the canopy radiation field can be found by numerically solving the 3-D transport equation in UAV dashboard ArcGIS in real-time. However, in many county abatement, vector epi-entomological, capture point, prognosticative, real-time LULC, signature, model applications, the knowledge of 3-D drone geosampled, cloud fields have not been thoroughly understood. Hence drone observations provide the only practical means to obtain a synoptic view of seasonal, immature habitat ecosystems, for optimally remotely determining the geospatial distribution, extent, and temporal dynamics of eco-georeferenceable, seasonal, potential super breeder, capture point, larval habitats of important entomological vectors such as Ae aegypti waste tire breeding foci.It would be difficult to draw any theorectical conclusions based on non-LULC signature iterative, interpolative, time series configurations from a nonreal-time, geosampled,3-D waste tire, capture point, county abatement, cloud field. Further, numerically solving the 3-D problem in a UAV real-time dashboard may be cost effective for precisely, mapping seasonal, eco-geor-

ferenecable, sub-meter resolution, decomposable, potenetial, super breeder, *Ae. aegypti,* larval, habitat, capture point, LULC signature, RGB eco-endmember frequencies in a real-time UAV dashboard ArcGIS or object-based classifier. Traditional field-based geo-sampling methods are prohibitively expensive and time-consuming at large spatial scales, and such methods are inadequate for today's needs.

Previous efforts on parameterization of 3-D cloud-radiation interaction terms in large-scale canopy-related, black fly vector of onchocerciasis, S. damnosum s.l., agro-village, riverine, tributary, larval habitat, capture point, sub-meter resolution, unmixed, LULC signature GCMs have focused on binary medium or oversimplified closure assumptions. Interestingly, a statistical physics-like simulation approach that makes a direct connection between the statistical characterization of cloud structure and the geostatistical moments of the radiation field, in a real-time UAV dashboard, ArcGIS platform, may reduce probability uncertainties in a radiative transfer equation. In so doing, specifications for precisely, remotely targeting, prolific, unknown, intermittently canopied, eco-georeferenceable, capture point, immature habitats may be faciliatated by optimally employing decomposed, iteratively interpolative, LULC signature, sub-meter resolution, RGB eco-endmember-related, photosynthetic and NPV explanatorial, empirically geosampled, waet tire, potential super breeder, Ae aegypti, larval habitat canopied, predictive variables. The unknowns of the resultant statistical radiative transport (SRT) equations may also be calculated and, by so doing, the statistical moments of the radiation field, and the capture point, waste tire, Ae aegypti, larval habitat, frequency model, geo-spectro temporal frequency inputs could be optimally rendered as some statistical moments of the 3-D, partially shade-canopied, medium structure. It may be shown that a spatial correlation function can serve as the key to statisticlle optimally, eco-geographically describing cloud–radiation interactions in an empirically interpolated real-time, UAV geosampled, ArcGIS dataset of clustered, unknown, un-geosampled, potential super breeder, eco-georefernced, shade, canopied, Ae aegypti larval habitats in a epi-entmological, county abatement, intervention, study site.

Further, employing the 3-D medium irradiance differences as quantitated in a UAV, dashboard ArcGIS may be employed for estimating the propagational noise emitted from regressed, surface, prolific, shade-canopied, real-time geosampled, Ae aegypti, waste tire, county abatement, capture point, potential, seasonal, super breeder, larval habitats, grid-stratifiable, LULC, signature irradiances. The uncertainty (e.g., 1r) of the annual global surface downward longwave and shortwave may be seasonally respectively, 5 W m^{-2} (out of 345 W m^{-2}) and 4 W m^{-2} (out of 200 W m^{-2}), for example, after known bias errors are removed. Similarly, the uncertainty of the real-time UAV geosampled, annual, global, LULC surface upward longwave and shortwave for regressable eco-georeferenceable, infrequently canopied, uncoalesced, waste tire, potential seasonal, super breeder, Ae aegypti, larval habitat, phostosynthetic and NPV, explanatorial, time series, predictor variables may be tabulated respectively as 3 W m^{-2} (out of 400 W m^{-2}) and 3 W m^{-2} (out of 25 W m^{-2}). The uncertainty residual probabilistic, estimates may model canopy irradiances of unknown capture point, super breeder, county abatement foci employing cloud properties derived from imagers on a sun-synchronous orbit that covers high-resolution maging spectrometers of UAV, real-time, frequency, sub-meter resolution LULC modeled, signature irradiances computed from nadir view on active sensors If the assumption is that longwave and shortwave eco-georeferenceable, larval habitat, partially canopied, reflectance wavelength probabilities rendered from a potential seasonal, super breeder, Ae aegypti, waste tire, capture point, eco-epidemiological, regression-related forecasting, LULC risk model are independent of each other, but up- and downward components are correlated with each other, the remotely tabulated probabilistic error in global annual mean net surface irradiance may be low for the forecasted, county abatement, capture point (e.g., 15 W m-2). Net surface irradiance may be approximated with low W m-2 measures for optimally remotely targeting potential, seasonal, super breeder, waste tire, *Ae. aegypti,* larval habitats in an epi-entomological, county abatement capture point geolocation, employing iteratively interpolative, unmixed sub-meter resolution datasets of partially canopied, eco-georeferenceable, leaf optical properties. Leaf optical properties have been successfully included for inhomogeneous canopies at the computational level in GCMs Schowengerdt RA (2007) Optical radiation models in Remote Sensing: models and methods for image processing, 45-88. Amsterdam]. multi-scattered, isotropic, seasonal, potential, seasonal, super breeder, waste tire, eco-georeferenecable, Ae aegpyti, larval habitat, canopy radiation may be conceptualized as consisting of discrete streams of non-opaque exiting radiation. Canopy radiation interacting at multiple scales of the county abatement capture point habitats can then be addressed in a real-time drone dashboard ArcGIS or object-based classifier. Each capture point, habitat canopy level may be summarized by its "input–output" values as previously mentioned. That is, since the incident radiation is of external origin, it would arrive at the outside of the geosampled, inhomogeneously canopied, waste tire, potential, seasonal, super breeder, eco-georeferenceable, county abatement, larval habitat, then would enter in and some fraction again would exit in various directions. The description of this exiting radiation may be then qualitatively captured as an unmixed, potential super breeder, *Ae. aegypti,* waste tire, LULC signature, log-transformed, non-linear, explicatory regressor in a GCM in a UAV real-time, county abatment LULC signature, sub-meter resolution model. The optical properties of a plant cell (i.e., photosynthetic capability) may then be employed to construct the optical properties of a waste tire, habitat canopy leaf and the latter can be used to construct optical properties at higher levels of organization up to that of the canopy in a real-time UAV dashboard ArcGIS model.

Alternatively, the geosampled, eco-georeferenceble, potential, super breeder, waste tire, capture point, *Ae. aegypti* larval habitat, seasonal, canopy radiation may be represented by precisely tabulating polynomials in the cosine of their angle made by the direction of the radiative flux relative to the same reference direction, (e.g. the vertical). These approaches may optimally regressively quantitate low order numerical discretizations of the continuous directionality of UAV real-time geosampled, potential super breeder, seasonal, waste tire, county abatement, larval habitats scattered isotropic radiation. The photosynthstic and NPV geospectrally interpolated, orthogonally eigendecomposable, LULC signature RGB eco-endmembers may subsequently describe the canopy scattering from other terrestrial LULC, vegetation surrounding the

habitat in the drone dashboard. Further, employing robust seasonal explanators in the regression equation in the drone dashboard real-time ArcGIS may create computational simplicity when constructing a waste tire Ae aegypti, real-time, seasonal GCM for remotely targeting, eco-geoerferenecable, seasonal, super breeder, county abatement foci with acceptable discretization error. Unfortunately, currently experimenters are not able to explicity remotely address the complexities in any geometeric analytical module in any UAV ArcGIS or ENVI real-time cyberenvironment for parsimoniously regressively robustly capturing ellipsoidal,,within-canopy, eco-georeferencable geo-spectrotemrpoal,,geoclassifiable, LULC objects (e.g., hanging, trailing vegetation) in a geo-spatiotemporally, geosampled, hyper productive, partially shae-canopied, waste tire, county abatement, Ae aegypti, larval habitat, capture points.

Importantly, real-time UAV geosampled, sensor data without an accurate cosine correction can render a severe error under diffuse radiation conditions within any potential, seasonal, super breeder, Ae aegypti, waste tire, capture point, partially canopied. LULC predictively modeled, county abatement epi-entomological, study site geolocation at low solar elevation angles. The cosine error at angle 0 is the percent difference of the ratio of the measured output at angle 0 and normal incidence as compared to the cosine of angle 0, which may be repeatable for various azimuth angles when accurately qualitatively, regressively unmixed datasets of eco-georeferenceable, seasonal, canopy-shaded, potential, seasonal, super breeder, *Ae. aegypti,* capture point, county abatement, geosampled, larval habitat, canopy, emittance values. Total diffuse radiation introduced a cosine error of approximately 2.5% in a, geo-spetrotemporally-dependent, geosampled, unmixed dataset of eco-georeferenecable, Precambrian rock, trailing vegetation, seasonal super breeder, *S. damnosum s.l.*, partially canopied, riverine, larval habitat, sub-pixel, sub-meter resolution, RGB eco-endmember capture points based on sn ArcGIS stochastic, iterative interpolator employing an LULC signature as a dependent /respose variable [Jacob [76]].

Commonly explanatorial, time series dependent, geospectro temporal, probabilitic errorroneous photosynthetic and NPV covariates in regressed, canopy vegetation, LULC, radiance-related calculations consist of the cosine error (or the angular error) and azimuth error[121, 122]. Angular error in an eco-georeferenced, seasonally, sub-meter resolution, UAV, real-time imaged, potential, hyper productive, shade-canopied, waste tire, Ae aegypti, county abatemen.t caprture points may be measured by directing a collimated source at normal incidence and rotating the sensor 360oabout an axis directly through the center of the sphere at 90o from normal incidence in the UAV dashboard. This may be repeatable for optimally calculating various azimuth angles as necessary to remotely seasonally characterize the capture point fron the data retrieved from the drone sensor in the real-time ArcGIS platform. The solar azimuth angle is the azimuth angle of the sun which may be determined by defining sun direction, whereas the solar zenith angle or its complementary angle solar elevation can define how high the sun is [29].

There are conventions for the solar azimuth, however it is traditionally defined as the angle between a line due south and the shadow cast by a vertical rod on Earth. Angular error is due to variations in density in the diffusion sphere and the sphere area lost because of the sensor base. Here angular error was less than 10% for the sub-meter resolution, drone sensed, county abatement, potential seasonal, super breeder, eco-georeferenecable, waste tire, discontinuously shade-canopied, Ae aegypti, larval habitat, capture point based on unmixed real-time geo-spectro temporal, field geosampled, count data as the upwelling radiation was much smaller than the downwelling radiation in most of the Hillsborough epi-entomological, county abatement, intervention study site,

The mathematical theories of regressively quantitaing canopy radiative multi-scattering LULCs have already been extensively developed in literature especially in the context of astrophysics and neutron diffusion where the system-properties differ significantly from seasonally geosampled, partially canopied, potential, super breeder, waste tire, Ae aegypti, county abatement, larval habitat, capture point, unmixed, phostsynthetic and NPV, time series, explanatorial LULC signature, diagnostic regressors. In particular, the astrophysical scattering systems may be very deep and appropriately approximated as semi-infinite, whereas the study of neutron scattering may be focused on the issue of "criticality" Spectro temporally-dependent, geosampled, intermittently shade-canopied, potential seasonal, super breeder, real-time UAV geosampled, waste tire, Ae aegypti, larval habitat canopies, on the other hand, may be optically relatively thin and at most wavelengths their leaves absorb a substantial fraction of the radiation they attenuate. Thus, a different analytic approach for optimal, spectral determination of real-time geosampled, county abatement datasets of uncoalesced explanatorily, iteratively, quantitatively interpolatable, seasonally geosampled, waste tire, Ae aegypti, capture point, LULC signature, sub-meter resolution RGB eco-endmember, canopy scattered radiation may be required in the UAV drone dashboard object-based classified [e.g., Atmospherically Resistant Vegetation Index (ARVI)]

In this research quantitated interactions of solar radiation emitted from a geosampled, shade-canopied, potential seasonal, super breeder, capture point, waste tire, Ae aegypti, larval habitat geosampled in an epi-entomological, intervention, county abatement, study site was described by the 3-D radiative transfer equation in a drone dashboard ArcGIS module. Solar radiation scattered from the vegetation –related, partially shade-canopied LULC signatures was measured by the real-time drone sensors which resulted from interaction of photons traversing through the foliage medium, bounded at the bottom by a radiatively participating capture point, LULC surface. Solar radiation after passing through the atmosphere arrives either in the form of direct beam or diffuse, that is after molecular (Rayleigh) or particulate scattering from cloud or aerosol droplets{Ben-Dor E, Irons JR, Epema G (1999) Soil reflectance 111-188 in Rencz An, ed. Remote Sensing for the Earth Sciences. New York, NY: John Wiley and Sons.].

Rayleigh scattering is the dominantly elastic scattering of light or other electromagnetic radiation by particles much smaller than the wavelength of the radiation [89]. The Rayleigh scattering does not change the state of material hence it is a parametric process. The particles

may be individual atoms or molecules. It can occur when light travels through transparent solids and liquids but is most prominently seen in gases. Rayleigh scattering results from the electric polarizability of the particles. The oscillating electric field of a light wave acts on the charges within a particle, causing them to move at the same frequency. The particle therefore becomes a small radiating dipole whose radiation we see as scattered light. Rayleigh scattering of sunlight in the atmosphere causes diffuse sky radiation, which is the reason for the blue color of the sky and the yellow tone of the sun itself [19].

Here, rayleigh radiation passed through the unmixed, geo-spetrotemporal, geosampled, county abatement, waste tire, Ae aegypti, potential, super breeder, larval habitat, LULC, signature vegetation canopies to reach the surface and was either absorbed by the canopy or surface or was reflected back to the atmosphere. The treatment of the radiation passing through vegetation canopies is complicated by the presence of multiple levels of organization, from that of the chloroplast cells to that of the arrangement of individual plants within the landscape [47, 123]. Thus, a comprehensive treatment of all the radiative details within a gridded ArcGIS, 1 km2 plot of county abatement geoclassifiable sub-mter resolution LULCs where the centroid is the geosampled, county abatementm capture point immature habitat, for example could easily reduce the computation of terrestrial radiation while adequately generating realistic, regressively quantifiable, canopy particulate, scattering mesurements in a real-time UAV dashboard object-based classfier.

Radiation interacting at multiple scales of organization can be addressed with an adding principle [89] The scattering waste tire, Ae aegypti, potential super breeder, capture point, LULC signature iteratively interpolative, unmixed sub-meter resolution, shade-canopied, eco-georenceable, larval habitat objects in an epi-entomological, county abatement may be considered when treating radiation within the habitat canopy which may not be opaque. Radiation both reflects from a leaf surface and is transmitted diffusely through it [89]. However, this scattering at leaf level is commonly asymmetric, (i.e., the fraction of incident light reflected from the habitat canopy surface of a thick leaf differs from that transmitted). Scattering from leaves in a real-time UAV geosampled, sub-meter resolution waste tire, Ae aegypti, capture point, LULC signature model signature outputs (i.e., eco-georeferenceable of potential, seasonal, super breeder geolocations) may be further complicated by the geometry of leaf orientation of the breeding site foci which may be characterized by a statistical distribution.

The equation of radiative transfer describes scattering interactions mathematically. Equations of radiative transfer have application in a wide variety of subjects including optics, astrophysics, atmospheric science, and remote sensing [124]. Analytic solutions to the radiative transfer equation (RTE) exist for simple cases but for more realistic media, with complex multiple scattering effects, such as those for determing UAV real-time geosampled, fractional, iteratively interpolatable, canopy radiance, unmixed, LULC signature estimates emitted from a geo-spectro temporally, geosampled, potential, seasonal, super breeder, Ae aegypti, larval habitat, capture point invasive, optimal resolution, numerical remote methods would be required. The interaction cross-section that appears in a drone geosampled, sub-meter resolution, LULC signature in a real-time ArcGIS or ENVI regression equation may be be treated as an individual wavelength for independently considering the size of the scattering elements (e.g., canopy leaves, branches, twigs, etc.) relative to the wavelength of solar radiation of canopy leaf structures in the eco-georefernced,county abatement, larval habitat.Radiation incident on the top of the atmosphere is a monodirectional solar beam while the vegetation canopies are illuminated both by a monodirectional beam attenuated by atmospheric radiation [125].

Although spherical coordinates (Appendix) might appear to be the most obvious choice, a local system with a Cartesian metric along a real-time UAV geosampled, county abatement path in real time may quantitate entering canopy radiation in a geo-spectro temporally, geo-sampled, capture point, ecogeorefernced, potential super breeder, waste tire, Ae aegypti, larval habitat. The explanatory irradiance covariates may be shown to be analytically integrable in an Ae aegypti, forecast, LULC signature, RGB eco-endmember model. The dependence of these solutions may be addressed by introducing a numerical integration into the UAV dashboard real-time ENVI platform. The integration can be written in terms of another transform variable, [eg., $q = 1/(sp)$] which would be put it in the form most familiar for plane parallel system in the drone dashboard object-based classifier with q interpreted as the cosine of the angle of the direction of the canopy radiation and the larval habitat radiation as p. It has been established over the history of radiative transfer research with such systems that a few integration capture, e co-georferenecable, unmixed, LULC points, even one (e.g. the classical 2-stream and Eddington approximations) provides useful accuracy for integration of regressive expressions).

In the study of stellar atmospheres, it has been found that the plane - parallel approximation had led to many useful and simplifying expressions such as the Eddington approximation, in which the radiation field has two components : a component outward along the z axis that I out and a component inward that being Iin. These approximations may be coupled with definitions of intensity, flux and radiation pressure, for robustly expressing the Iout and Iin for a prolific, geo-spectro temporal, geosampled, potential seasonally hyper productive shade canopied, waste tire, Ae aegypti, larval habitat in a county abatment, epi-entomological, intervention, stusy site. An analytical approximation method may be presented to calculate the radiation flux in the larval habitats employing the Eddington approximation when the upwelling radiation from the capture point emittance is negligibly small. Numerical experiments may be carried out to investigate the feasibility of the method in flooded and droughted seasonal scenarios. The results may show good consistency for discontinuous canopy reflectivity at the top of atmosphere and transmissivity just above the canopy surface, in comparison with the exact values calculated by radiative transfer UAV, real-time geosampled, models in each case .Moreover, an obvious error might be introduced for the calculation of radiation flux at larger solar zenith angles when the roughness of the canopy surface is neglected.

The radiative transfer equation for leaf canopies, in 3-D geometries as constructed in a UAV dashboard real-time ArcGIS platform, has certain unique features (e.g., the extinction coefficient is a function of the direction of photon travel). Also, the differential scattering cross-section is not, as a rule, rotationally invariant for unmixing geosampled, vector entomological, eco-georeferenecable, larval habitat capture points, (e.g., potential super breeder, waste tire, Ae aegypti larval habitats) LULC signature,(i.e., it may depend on the absolute directions of photon travel and 0, and not just the scattering angle arc cos ^{2} 0.) as Jacob [75] reports. Further, the single scattering albedo may be a function of spatial and directional capture point, sub-meter resolution, imaged, shade-canopied, unmixed, LULC variables. These properties may make solving the radiative transfer equation for a productive, shade-canopied, geo-spectro temporally, geosampled, prolific, eco-georeferenceable, waste tire, Ae aegypti, county abatement, capture point, LULC, larval habitat more complicated; for example, the expansion of the differential scattering cross-section in spherical harmonics cannot be used.

In mathematics, spherical harmonics are a series of special functions defined on the surface of a sphere employed to solve some kinds of differential equations. As Fourier series are a series of functions used to represent functions on a circle, spherical harmonics are a series of functions that are used to represent functions defined on the surface of a sphere [126]. Spherical harmonics are important in many theoretical and practical applications, particularly in the computation of atomic orbital electron configurations, representation of gravitational fields, geoids, and magnetic fields of planetary bodies afor characterization of the cosmic microwave background radiation. Spherical harmonics are functions definable in terms of spherical coordinates which may be organized by angular frequency, as seen in the rows of functions which may in turn be parsimoniosly employable for optimally quantitating multi-scattered, canopy radiance from 3-D computer graphics of a seasonally geosampled, hyper productive, Ae aegypti, county abatement, larval habitat. Spherical harmonics play a role in a wide variety of topics including indirect lighting (ambient occlusion, global illumination, precomputed radiance transfer, etc.) and modelling of 3-D shapes [17]. Further, spherical harmonics of a differentially modelled potenetial, super breeder, county abatement, eco-georferenecable, Ae aegypti, waset tire, larval habitat may be defined as the angular portion of a set of solutions to Laplace's equation in three dimensions. Represented in a system of spherical coordinates, Laplace's spherical harmonics () are a specific set of spherical harmonics that forms an orthogonal system [127].

In contrast to radiative transfer in clouds, the extinction coefficient in vegetation canopies is wavelength independent, considering the size of scattering elements (leaves, branches, twigs, etc.) relative to the wavelength of solar radiation [128, 129]For our radiative transfer habitat signature models, the time series dependent, regressable explanatorial, unmixed RGB coeffcients corresponded respectively to canopy micro-(e.g., distribution of canopy -type geometry) structures, leaf optical properties and boundary illumination conditions of the capture point, potenetial super breeder, Ae aegypti, waste tire, county abatement, larval habitats. The scattering and absorption LULC processes were different in the spectral datasets as the optical distance between arbitrary eco-georefernced, shade-canopied, potential super breeder, capture point, Ae aegypti, waste tire, larval habitat was dependent on the uncoalesced sub-meter resolution wavelengths. Spectral invariance results in the necessity to quantitate various unique relationships when geo-spectrally explanatorily interpolating, eigendecomposable, partially shaded-canopied, sub-pixel, signature-related, RGB eco-endmember, time series predictor variables [130]. By so doing, compensation mechanisms may be revealed for resolving difficulties in a radiative transfer equation due to the features of the extinction and the differential canopy scattering cross-sections of these habitats.

With the recovery of surface sub-meter resolution, RGB eco-endmember, eco-georeferenceable, waste tire, potential super breeder, Ae aegypti, laval habitat capture point, parameters based on BRDFs, first order directional LULC signature iteratively interpolative properties was determined for the Hillsborough county, epi-entomological, intervention, study site.Often critical to inversion processes and their success are the second order directional properties, or the bidirectional reflectance functions as defined by Jupp and Woodcock [1992]Jupp, D.L.B. and Woodcock, C.E., Variance in directional radiance of open canopies, Proceedings of the IGARSS'92 Symposium: International Space Year: Space Remote Sensing, 1490-1492, 1992]. The definition or use of second order directional LULC properties for iteratively interpolating geo-spectro temporally extracted, signatures, requires a higher level of organization in images above individual pixels (Jacob [75]). Individual, vector arthropod, larval habitat, capture point, grid-stratifiable, LULC, decomposed pixels must be viewed as samples from larger entities (e.g., eco-georeferecd, superbreeeder, waste tire, seasonal *Ae. aegypti* larval habitats). For naturally vegetated landscapes these entities are usually patches or stands. Vegetation LULC classes for real-time sub-mter resolution, real-time, drone tracking a potential super breeder, county abatement, eco-georeferenecd, *Ae. aegypti* capture point can also serve as a higher-level entity. For such multipixel objects the bidirectional reflectance variance function (BRVF0 may be thought of as the pixel to pixel variability in the BRDF. Little is known about the properties of the BRVF or the influence of variance on inversion processes based on directional properties of images. Jupp and Woodcock [1992] and Jupp [131] studied the BRVF of a woodland in Australia using digitized aerial photographs and a simple two-component, model of bidirectional directiona, variance factors (BRVFs). Beyond those efforts little is known about how variance changes as a function of viewing and illumination directions, or its causes. Exploring BRVFs over county abatement, UAV real-time, geosampled canopy stands employing dashboard ArcGIS platform may : 1) identify their basic spectral characteristics of an eco-georeferenceable, potential seasonal, super breeder, waste tire, Ae aegypti, larval habitat, 2) determine if the prolific capture point can be related to LULC sub-meter resolution signature iterative interpolative unmixed properties of partially canopy-shaded, seasonal vegetation canopies; and, 3) evaluate the validity of Jupp's simple two-component model of the BRVF. The result may be a modification of Jupp's model to incorporate the effect of more capture point, unmixed, geosampled, county abatement, super breeder, waste tire, *Ae aegypti*, LULC scene components in the real-time drone geosampled eco-entomological, signatures.

Our exploratory study on the the spatial variance of the unmixed, bidirectional reflectance over the discontinuous, plant, shade, canopied, waste tire, Ae aegypti, seasonal, super breeder, county abatement, foci indicated that the spatial variance of the bidirectional reflectance calculated from UAV images has peak values at the hotspot and near nadir. This behavior can be explained by the geometric effect of discontinuous crowns and the regularization effect of the epi-entomological, county abatement study sites. Validation of Jupp and Woodcock's two component geometric optical (GO) model may also reveal the basic features of the spatial variance of the bidirectional reflectance over discontinuous plant canopies of eco-georeferenceable. capture point, potential, super breeder, Ae aegypti, waste tire,larval habitat, real-time, UAV geosampled, county abatement, breeding site in a A two-component GO, capture point, Ae aegypti, geo-spectro temporal, county abatement, unmixed, LULC, signature, sub-meter resolution, grid-stratifiable, UAV real-time model for identifying unknown, eco-georeferenceable, potential, seasonal, super breeder foci in an epi-entomological, county abatement, intervention,study site which may be modified to account for the spatial interactions of four scene components simuataneously in the dashboard ENVI platform. Validation may reveal that the modified UAV real-time, GO model improves the capture point, larval habitat, county abatement model predictions of potenetial hypeproductive seasonal, county abatment, breeding site foci. Such an exploratory, signature, interpolation study may help lay the foundation for future retrieval of surface statistical information from UAV sensed, real-time, grid-stratifiable, LULC data (e.g., variance in bidirectional reflectance over discontinuous geosampled potential, seasonal, super breeder, county abatement, waste tire, Ae aegypti, larval habiatats).

The components of each eigendecomposed orthogonal super breeder, eco-georeferenceable, seasonal, capture point, LULC, county abatement, waste tire, larval habitat, sub-meter resolution, UAV, real-time signature, eigenvectors when mapped onto an underlying spatial tessellation, in the dashboard ArcGIS, exhibited a distinctive spatial pattern ranging from positive spatial autocorrelation to negative spatial autocorrelation. d. The associated Moran's I autocorrelation coefficient of each eigendecomposed, capture point, eco-georefered, county abatement, waste tire, potential, super breeder, larval habitat frequency, LULc signature, parameter estimator was equal to its associated eigenvalue (i.e., the Rayleigh quotient). In the epi-entomological models. The spatial pattern in the capture point, LULC orthogonal, signature eigenvectors was, however, somewhat synthetic: for positive global autocorrelation all local county abatement, LULC signature, study site patterns exhibited only positive local autocorrelation but not negative local autocorrelation (and vice versa for negative global autocorrelation). For empirical spatial patterns we would expect a few local patterns that indicate spatial local autocorrelation opposite to that for the overall global autocorrelation.

A general problem which holds both for finding a minimum of an expensive objective function or a solution to the QS equation is to efficiently explore the parameter search space when only a limited computational budget is available for simulation. A suitable approach for this kind of problem for potential, seasonal, super breeder, time series, vector, eco-entomological, LULC, signature, iterative interpolative, eco-endmember, prognosticative, signature models (e.g., county abatement, *Ae. aegypti*, waste tire larval habitats), may rely on the usage of drone response surface models in place of the original black box function for optimization. This could include first-degree and second-degree (multivariate) polynomial approximations of real-time. UAV response functions which may be employable for determining unknown, seasonal, eco-georeferenceable, super breeder, waste tire, capture point, *Ae. aegypti,* seasonal, larval habitat geolocations, based on derivates rendered from response surface models Another approach for optimally identifying potenetial, seasonal, super breeder, waste tire, Ae aegypti, larval habitats include the kriging signature LULCs (see, e.g., Sacks, Stiller, and Welch 1989a) who treat the response of an objective function as a realization of a stochastic process. The main idea in this type of habitat, signature interpolation is to start by evaluating the expensive function at a geosampled, super breeder, seasonal, Ae aegypti. capture point, for example, within an eco-georeferenced, grid-stratified, geolocation (i.e., LULC) with the intent for implementing an experimental design over the whole, county abatement, parameter space. Then a real-time UAV, ArcGIS, global response surface, habitat, signature interpolation, model may be constructed in a real-time dashboard platform and fitted based on the initially evaluated county abatement, eco-georeferenceable, field-verifiable dataset of, vulnerability, unmixed, signature, LULC markers which may be subsequently employed to identify promising unknown, county abatement, capture points (e.g., seasonal, super breeder, *Ae. aegypti,* waste tire, larval habitats) in a real-time UAV platform. This process may be repeated, including the evaluated points, for sequential updates of the response, surface LULC, vector entomological, county abatement signature models. In order to improve the model within subsequent iterations the aim would be to select new, geosampled, grid-stratifiable county abatement, geoclassifiable, LULC capture points, (e.g., GPS geolocations of county, abatement, super breeder, seasonal, waste tire, *Ae. aegypti,* larval habitats) geolocations to estimate the geolocation of the optimum, that is, the unknown, sub-meter resolution, unmixed, RGB eco-endmember, signature parameters in a seasonal setting, while, simultaneously, identifying sparsely, shade-canopy sampled abatement regions of the parameter search space in the UAV dashboard where little information about the criterion function may be available. In this context, two outcome possibilities exist: first, this procedure allows the UAV to exploit the spectral data-inherent smoothness LULC properties in the *Ae aegypti,* sub-meter resolution geosampled, real-time, signature dataset by specifically tuned covariance RGB models which may measure the spatial dependency of the response variable (unmixed potential, seasonal, super breeder, ccounty abatement capture point) and, second, it provides an indication of the overall achievable prediction or estimation accuracy of the unknown foci. Almost all global optimization methods, such as the well-known Efficient Global Optimization algorithm by Jones, Schonlau, and Welch (1998), are based on the evaluation of prediction variances in one way or another. Although these models have been widely used in the community of global optimization of expensive black box functions with applications to engineering and economic sciences these is no current literature in the context of simulation estimation of prolific seasonal, eco-georerenecable, epi-entomological, vector, arthropod,larval habitat such as county abatement, waste tire, Ae aegypti, larval habitat, signature, super breeder, LULC, capture points. The drone simulation results may indicate that the proposed RGB estimators perform well in terms of biases and efficiencies for optimally targeting, seasonal, super

breeder, *Ae. aegypti*, county abatement, eco-georeneceable, capture points. It may be that the combined signature estimators significantly reduce the mean bias of the RGB estimators which may be more efficient than existing estimators for real-time, UAV, targeting of these vector habitats. The relative efficiencies of all the combined estimators may increase as the sample size increase as well.

We kriged the unmixed, LULC signature geosampled, dataset of the eco-georferenecable capture point, Ae aegypti, waste tire, larval habitat foci in the real-time ArcGIS embedded in the drone dashboard. The practical assumptions for the application of simple kriging are wide sense stationarity of the field, the expectation is zero everywhere: and the known covariance function. In probability theory and statistics, covariance is a measure of how much two variables change together and the covariance function $c(x,y) = Cov(Z(x), Z(y))$ describes the variance of a random variable process or field. For a random field of stochastic, LULC, sub-meter resolution, uncoalesced, RGB, eco-endmember, frequencies of grid-stratifiable, capture points, continuous process Z(x) on a domain D {i.e., epi-entomological, intervention, county abatement, study site],a potenetial super breederm capture point covariance function C(x, y) rendered the covariance of the immature breeding site values of the random field at multiple, county abatement geolocations x and y employing $c(x,y) = Cov(Z(x), Z(y))$ in the real-time UAV interpolator. The same C(x, y) is called autocovariance in two instances: in time series (to denote exactly the same concept, where x is time), and in, multivariate, random fields (to refer to the covariance of a variable with itself(Griffth 2003) as opposed to the cross covariance between two different capture point, seasonal, vector arthropod optimizable, iterative, interpolative LULC, geo-spectro temporal, decomposed, explanative variables at different larval, habitat, county abatement, eco-georenceable, unknown, potential, seasonal super breeder foci geolocations,[i.e., Cov(Z(x1), Y(x2)].

The waste tire, larval habitat, *Ae. aegypti,* geoclassified, LULC, signature, kriging estimator was parsimoniously rendered by a linear combination $\hat{Z}(x_0) = \sum_{i=1}^{n} \omega_i(x_0) Z(x_i)$ based on the observed, eco-georeferenced, seasonal, super breeder, capture point, larval habitat, geosampled, unmixed, LULC, signature values with sub-meter resolution, RGB weights $\omega_i(x_0), i = 1, ..., n$ which were chosen such that the variance (i.e, kriging error): was equal to which was then minimized further due to the the the unbiasedness condition : For instance, the so-called simple kriging assumption in prognosticative, sub-meter resolution, unmixed, LULC signature, stochastic, eco-endmember, frequency, signature modelling is the mean and the covariance of which is known and as such the kriging predictor is the variable that minimizes the variance of the prediction error (Jacob [62]).

The first step in the iterative stochastic interpolation of the unmixed dataset of sub-meter resolution, waste tire, Ae aegypti, potential, seasonal, super breeder, eco-georeferenced, capture point, larval habitat, LULC signatures, was to construct a variogram from the unmixed, scatter points in the UAV dashboard ArcGIS. Our capture point, variogram consisted of two parts: an experimental variogram and a model variogram. Here, the signature values to be interpolated (e.g., unmixed, seasonal, county abatement, *Ae. aegypti* super breeder, foci, RGB, eco-endmember frequencies) was referred to as f. The experimental variogram was found by calculating the variance (g) of each eco-georeferenced, capture point, LULC in the real-time, UAV geosampled dataset with respect to each of the other county abatement, eco-georeferenced capture points, and subsequently plotting the variances versus distance (h) between the points. We computed the capture point, eco-endmember, *Ae. aegypti,* model variance as half the difference in the f squared county abatement, waste tire, RGB, spectral signature, larval habitat model output.

Once the experimental variogram was constructed in the real-time ArcGIS, the next step was to define a waste tire, *Ae. aegypti,* capture point, larval habitat variogram. A model variogram is a simple mathematical function that models the trend in the experimental variogram. The shape of the, super breeder, waste tire, LULC signature, *Ae. aegypti,* larval habitat, county abatement variogram indicated that at small predicted, separation in capture point distances, the variance in f was insignificant. In other words, sub-meter resolution, RGB, eco-endmember, eco-georeferenceable, *Ae. aegypti* LULC, capture points that were close together in geospace had similar f values in the waste tire, larval habitat UAV, county abatement, real-time dataset. After a certain level of separation, the variance in the f values became somewhat random and the LULC model variogram flattened out to an explanatory value corresponding to the average variance.

An important feature of our kriging was that the variogram was employable to tabulate the expected error of estimation at each interpolated *Ae. aegypti,* capture point, LULC, waste tire, super breeder, breeding site, foci in the real-time, drone dashboard ArcGIS since the estimation error was a function of the larval habitat distance to the surrounding scatter points in the epi-entomological, county abatement, intervention, study site. The estimation variance was calculated as: $s_z^2 = W_1 S(d_{1p}) + W_2 S(d_{2p}) + W_3 S(d_{3p}) + \lambda$ Traditionally, ordinary kriging estimates the unknown value using a weighted linear combinations of the available sample: .The error of i-th estimate, ri, then was the difference of estimated value and true value at that same county abatement, potential, seasonal, super breeder, waste tire, eco-georeferenecable, larval habitat geolocation: The average error of a set of k estimates was .Here the geo-spectro temporal, eco-endmember, frequency error variance was calculated as . The unmixed kriged, LULC capture point, *Ae. aegypti,* waste tire, RGB, larval habitat, spectral weights employed in the geospatial algorithm, in the real-time UAV model, had no unbiasedness condition and were quantifiable in geospace by the equation system:
$\begin{pmatrix} \omega_1 \\ \vdots \\ \omega_n \end{pmatrix} = \begin{pmatrix} c(x_1,x_1) & \cdots & c(x_1,x_1) \\ \vdots & \ddots & \vdots \\ c(x_1,x_1) & \cdots & c(x_1,x_1) \end{pmatrix} \begin{pmatrix} c(x_1,x_1) \\ \vdots \\ c(xn,x_0) \end{pmatrix}$. This was analogous to a linear regression of on which we employed for estimating unbiased, *Ae. aegypti,* capture point, waste, tire, UAV captured, county abatement, time series, paramterizable, LULC, eco-georeferenceable, signature, RGB, eco-endmember estimators. The interpolation by the kriging algorithm rendered: in the real-time UAV model output. For the interpolated, eco-georefenecd, super breeder, waste tire, *Ae. aegypti,* larval habitat, capture point, unmixed, sub-meter resolution, LULC signatures, the kriging error was given by
$\begin{pmatrix} c(x_1,x_1) \\ \vdots \\ c(xn,x_0) \end{pmatrix} \begin{pmatrix} \omega_1 \\ \vdots \\ \omega_n \end{pmatrix} = \begin{pmatrix} c(x_1,x_1) & \cdots & c(x_1,x_1) \\ \vdots & \ddots & \vdots \\ c(x_1,x_1) & \cdots & c(x_1,x_1) \end{pmatrix} \begin{pmatrix} c(x_1,x_1) \\ \vdots \\ c(xn,x_0) \end{pmatrix}$ which led to application of the generalized least squares version of the Gauss-Markov theorem.

The Gauss–Markov theorem, states that in a linear regression model in which the errors have expectation zero and are uncorrelated and have equal variances, the best linear unbiased estimator (BLUE) of the coefficients is given by the ordinary least square's estimator. In this research "best" meant quantitating the lowest possible mean squared error of the real-time geosampled, UAV, imaged, capture point, super breeder, LULC, waste tire, Ae aegypti, larval, habitat, unmixed, seasonal, frequencies. The errors were not normal, nor independent and identically distributed (only uncorrelated and homoscedastic). This, county abatement ento-eepidemiological, LULC, larval habitat real-time, waset tire, ArcGIS model, however, assumed the expectation of the random field generated by the geosampled, eco-georferenecd, field and remote, time series, predictive, Ae aegypti, larval habitat, eigendecomposable, capture point, regression coefficients to be known, and relied on a co-variance function. Commonly in autoregressive, epi-entomolgical, unmixed, LULC, capture point, RGB eco-endmember, geo-spectro temporal, vector entomological, arthropod time series, signature analyses, neither the expectation nor the covariance are known beforehand (Jacob [59]).

The basic equation employed in the ordinary kriging of the sub-meter resolution, UAV, real-time, captured, grid-stratifiable, Ae aegypti, LULC, waste tire, RGB eco-endmember, larval habitat, county abatement, signatures were as follows: where n was the number of scatter points in the set, fi were the extracted, signature values of the geosampled, eco-georferenecd, potenetial seasonal, super breeder, capture point, and wi were the foci frequency weights assigned to each county abatement LULC. Our format was essentially the same as the equation employed for inverse distance weighted interpolation in ArcGIS, except that rather than employing sampled weights based on an arbitrary function of distances,(ei.e., Euclidean measurements between, waste tire, hyper productive, *Ae. aegypti,* larval habitat to a human habitation) the RGB, capture point, siganture weights used modelled variogram coefficients. For example, to iteratively interpolate a capture point, urban, residential, eco-georeferenced, LULC,waste tire, *Ae. aegypti,* larval habitat, signature, unmixed RGB eco-endmember, sub-meter resolution, frequency P based on the surrounding county abatement, real-time, geosampled, capture points P1, P2, and P3, the weights w1, w2, and w3 had to be remotely UAV discernable. The unknown LULC weights in the real-time UAV dashboard ArcGIS module were henceforth found through the solution of the simultaneous equations:

$$W_1 S(d_{11}) + W_2 S(d_{12}) + W_3 S(d_{13}) = S(d_{1p})$$
$$W_1 S(d_{12}) + W_2 S(d_{22}) + W_3 S(d_{23}) = S(d_{2p})$$
$$W_1 S(d_{13}) + W_2 S(d_{23}) + W_3 S(d_{33}) = S(d_{3p})$$

where S(dij) was the eco-endmember, LULC, waste tire, potential, seasonal, super beeder, eco-georeferenceable, *Ae. aegypti,* larval habitat, frequency variogram evaluated at a geosampled, larval habitat distance which here was equal to the distance between the capture points i and j. For example, S(d1p) was the model variogram evaluated at a capture point, county abatement, LULC distance which was equal to the separation of the forecasted *Ae. aegypti,* larval habitat, unknown, super beeder, capture points P1 and P. Since it was necessary that the frequency weights summed to unity (see Griffith 2003), a fourth equation: was added to the sub-meter resolution, real-time, epi-entomological, seasonal, signature model employing time series real-time ArcGIS archived shapefiles. Since there were now four equations and multiple unknowns, in the UAV, spectral library a slack frequency, larval habitat, geosampled, *Ae. aegypti,* LULC variable was added to the equation set. Subsequently, the final set of equations in the dashboard platform were as follows:

$$W_1 S(d_{12}) + W_2 S(d_{22}) + W_3 S(d_{23}) + \lambda = S(d_{2p})$$
$$W_1 S(d_{12}) + W_2 S(d_{22}) + W_3 S(d_{23}) + \lambda = S(d_{2p})$$
$$W_1 S(d_{13}) + W_2 S(d_{23}) + W_3 S(d_{33}) + \lambda = S(d_{3p})$$
$$W_1 + W_2 + W_3 + 0 = 1.0$$

The equations were solved for the capture point, LULC waste tire, larval habitat, frequency weights w1, w2, and w3 in the UAV real-time dashboard. The f value of the iteratively interpolated, capture point, larval habitat,county abatement, potential, seasonal, super breeder, LULC signatures were calculated as: . By employing the variogram in this fashion to compute the frequency weights in the, RGB ecoendmember model, the expected estimation error was minimized in a least squares sense.Hence, kriging unmixed, geo-spectro temporal, grid-stratifiable, LULC, sub-meter resolution, *Ae. aegypti* aquatic, larval habitat, explanatory coefficients in a real-time UAV ArcGIS platform can produce optimal, linear, unbiased, elucidative estimates of unknown, un-geosampled, eco-georeferenceable, potenetial, seasonal, super breeder, county abatement, breeding site foci.

Iteratively interpolating an eco-georeferenceable, poitenetial capture point, vector arthropod, larval habitat, sub-meter resolution, spectral signatures such as a super breeder, seasonal, waste tire, *Ae. aegypti,* capture point can aid in optimally remotely targeting unknown, eco-georeferenceable, county abatement,hyper productive, foci in a real-time LULC map in a UAV dashboard ArcGIS. In geostatistics, kriging or Gaussian process regression is a method of interpolation for which LULC signature values (e.g., capture point, LULC, sub-meter resolution, geo-spectro temporal, RGB eco-endmembers) of a waste tire, Ae aegypti, aquatic, larval habitat) are modeled by a Gaussian process governed by prior covariances, as opposed to a piecewise-polynomial spline chosen to optimize smoothness of the fitted values (e.g., geosampled, habitat, frequency, larval density counts). Under suitable assumptions on the priors, kriging renders the best, linear, unbiased prediction of the intermediate sub-pixel frequencies for precise, sub-meter resolution, vector arthropod, larval habitat, breeding site, super breeder, seasonal foci, LULC, signature mapping (Jacob [76]). The basic idea of kriging in a real-time UAV dashboard ArcGIS is to optimally predict geolocations of unknown larval habitats, and their density, frequency, immature, count values employing a function at a given eco-georeferneceable, hyper

productive, capture point by computing a weighted average of the known capture point, LULC, values in the neighborhood of the seasonal, hyper productive county abatement foci. The method is mathematically closely related to regression analysis. Both theories derive an unbiased linear estimator (e.g., geolocation of a seasonal, super breeder, eco-georeferenced, *Ae. aegypti,* waste tire, larval, habitat, county abatement foci) based on assumptions on covariances, which makes use of Gauss–Markov theorem to prove independence of the estimate and error.

The Gauss–Markov theorem states that in a linear regression model in which the errors have expectation zero and are uncorrelated and have equal variances, the best linear unbiased estimator of the coefficients is given by the ordinary least squares (OLS) estimator, provided it exists [63].. In this research, "best" meant giving the lowest variance of the real-time,UAV geosampled, eco-georeferenecable, super breeder, seasonal, Ae aegypti, capture point, LULC, sub-meter resolution, RGB eco-endmember estimates, as compared to other unbiased, linear estimators. The errors did were not normal, nor were they independent and identically distributed (only uncorrelated with mean zero and homoscedastic with finite variance).

Using geosampled, drone based, geo-spectro temporal, LULC, signature, empirical data for super breeder, seasonal, capture point, *Ae. aegypti* larval habitat, detection provided explanatory results with a 92.7% success rate for the Hillsborough County abatment, epi-entomological LULC site. The real-time method effectively captured RGB spectral signatures that fed into the kriging interpolation to predict eco-georeferenceable, prolific un-geosampled, waste tire county abatement geolocations. Further, this real-time ArcGIS and object based, real-time modeling, LULC signature approach was useful for optimally, remotely, identifying, geoclassifiable UAV captured partially, shade-canopied, landscapes and waste tire habitats in urban residential and agro-pastureland environments where the vector foci could exist.

UAV real-time LULC imagery can capture large swaths of land, which can help develop detailed and accurate predictive, sub-meter resolution, signature,RGB eco-endmember, county abatement, vulnerability maps of potential, seasonal, super breeder, *Ae. aegypti* and other vector /nuisance county abatement mosquito larval habitats in real time. A drone can survey a 30-hectacre geolocation in 20 minutes, for example, whose imagery may then be processed and analyzed in real-time to scope out water bodies potentially harboring vector mosquito larvae. Our research process was highly accurate and efficient for remotely targeting seasonal, hyper productive, eco-georeferenceable, unknown, seasonal, larval habitat, capture point, foci .We employed one of the most popular off-the-shelf drone models- the Phantom 3 (developed by DJI). This particular model is roughly the size of a shoebox, weighs about 1.2 kg, and is used across the globe for leisure and commercial purposes.

With hopes of further exploring how real-time,UAV technology can be incorporated into operational, *Ae. aegypti,* potential, eco-georeferenceable, super breeder, county abatement, seasonal eliminating activities, we integrated UAV imagery into smartphone and iphone technology for guiding larvicide spraying teams to water bodies (on foot), while tracking their progress and coverage. Multiple, un-geosampled, *Ae. aegypti*, waste tire, potential, seasonal, super breeder, capture points may be spectro temporally defined and subsequently kriged in a stochastic iterative interpolator embedded in the drone dashboard ArcGIS in real time. In so doing, multiple unknown, seasonal, eco-georeferenceable, super breeder site foci may be identified in a county abatement epi-entomological, intervention, study site.

Importantly the UAV imagery was able to identify a large number of potential super breeder, Ae aegypti, larval habitats not identified by the field team; in most instances, almost half the waste tires in the county abatement identified in the real-time orthomosaics were missed by the field survey. These habitats were not identified on the ground largely because they were obscured from immediate view (i.e. within/behind dense vegetation LULC canopies, behind housing and other structures, too small to be detectable at a distance from the ground), highlighting the need to undertake synoptic surveys of waste tires,using drones, to generate real-time inventories of potential, seasonal, super breeder, *Ae. aegypti* and other vector/nuisance mosquito, county abatement, larval habitats.

At each potential super breeder, seasonal, eco-georeferenced, waste tire, *Ae. aegypti,* larval, habitat site in Hillsborough County the drone was flown to an altitude of approximately 60m. This altitude provided images with an approximate ground footprint of 270 m × 270 m with a spatial resolution of 31 cm. Alongside the drone survey an entomological survey was conducted at each site to determine the presence of Ae aegypti larvae and pupae in a waste tire eco-georeferenced, county abatement, LULC capture point as well as environmental characteristics of the foci,such as evidence of predators, presence of aquatic vegetation, including algae, degree of turbidity and shade, and water body dimensions.

Semi-autonomous, unmanned drone aircraft systems are a powerful tool due to their ability to quickly fly over large regions as well as access hard to reach areas where sometime seasonal, eco-georeferenecable, super breeder*, Ae. aegypti* foci may reside in a county abatement geolocation. They can be employed in real time and do not have cloud cover issues associated with satellite system images.Very-high resolution imagery (<5 m pixels) from satellite systems such as IKONOS, QuickBird, WorldView, GeoEye and Pleiades has been used for the detection of individual water bodies (potential vector mosquito aquatic habitats) at a community scale (e.g., see Mutuku et al. 2009). Sub-meter resolution, geo-classifiable, grid-stratified, LULC data may reveal great potential for use in targeting and prioritizing county abatement control initiatives; however, optical satellite imagery relies on clear-sky conditions that occur infrequently for many regions burdened by vector/nuisance arthropod diseases.Coupled with infrequent revisit periods, as well as the relatively high cost, this limits the operational use of satellite, optical, remote sensing in a real-time ArcGIS. Abatement survey teams would need to wait until clear-sky conditions occurred, coinciding with the timing of the satellite overpass, meaning that field teams (that disseminate larvicide and/or undertake environmental management) would need to remain on standby and, in fact, whole seasons may pass without a useable image being available. For instance, a review of the Sentinel-2 archives demonstrates that out of the 81 scenes that were centered over Unguja, Zanzibar for malaria, aquatic, larval, habitat, risk mapping, since

December 2015, no images were completely cloud free; just two images had less than 5% cloud cover and could have been considered useable for habitat targeting. Radar systems are not reliant on clear-sky conditions, offering an exciting alternative to optical imagery but this approach is limited by a coarser spatial resolution and the lack of contextual information that is provided by visual analysis of optical habitat imagery.

Unlike, high, spatial, resolution imagery from manned aircraft and satellites that tends to be expensive to acquire as well as being less flexible to operate, drone technology offers the potential to obtain very high resolution imagery at a relatively low cost. Drones are less expensive than purchasing high resolution satellite imagery and also have the added benefit of carrying and distributing items to sites. Hardy et al. (2016) employed drones to map water bodies and rice paddies in Zanzibar for malaria larviciding, and conducting entomological surveys and environmental management activities, and found it to be a low cost option. As well as the ability to identify water bodies and potential,seasonal, super breeder, Ae aegypti, waste tire,larvl habitats and other vector /nuisance capture points,, drone-based, ArcGIS real-time imagery also has the potential to provide ancillary information for planning of logistics: (i.e. geolocations and nature of homes, access points/routes to eco-georeferenceable, real-time DEM mapped potential hyper productive, county abatement foci) to direct, field larvicidal, teams. Additionally, real-time, grid-stratifiable, sub-meter resolutionUAV, geosampled, county abatement imagery can be employed to establish and monitor links between environmental factors and disease transmission, such as changes in land cover and the emergence of new vector habitats (Anopheline gambiae s.l. for malaria, Culex quiquefasciatus for filarsis, Culex erraticus for Eastern Equine Encephilitis, Aedes triceteratus for LaCross Encephilitis ect.).

The resulting real-time, UAV geosampled, capture point, Ae aegypti, waste tire, larval habitat potential, county abatement, seasonal, super breeder, eco-georeferenceable, grid-stratifiable, breeding site foci imagery was imported into AgisSoft Photoscan Pro (https://www.agisoft.com) and processed to extract an orthomosaic (an eco-georeferenced mosaic of overlapping photographs and sub-meter resolution LULC images) which included correction for topographic distortions. For each county abatement, LULC signature, site the UAV real-time dashboard followed a standard procedure: (i) precision remote alignment of capture points; (ii) built dense point cloud for high quality depth filtering: (iii) built a DEM of 31cm pixel resolution size employing multiple, potential, seasonal, super breeder, waste tire, *Ae. aegypti*, capture point, LULC classes to conduct a digital surface analyses; and, (iv) built real-time orthomosaics employing input surface values extracted from the 3-D, county abatement geosampled, unmixed frequency, signature dataset. The position of the UAV at the time of image capture for each LULC acquisition was recorded automatically by the on-board GPS; as such, the orthomosaic was eco-georeferenced automatically by the real-time, UAV, object-based platform without the need for reference images, maps or ground control points (GCP). An accurately surveyed reference, waste tire, capture point or larval habitat, LULC feature is employable in an epi-entomological, county abatement, intervention, study site model to georeference real-time UAV images or improve its locational accuracy.

Robust, real time, UAV, signature mapping and monitoring of urban residential and agro-pastureland, discontinuously canopied, forest carbon stocks across large areas in a county abatement epi-entomological, intervention, study site may depend on field estimates of biomass for calibration and validation purposes. Here, we used gridded, field plot data collected in Hillsborough County Fl, to gain a better understanding of the uncertainty associated with interpolating, waste tire, Ae aegypti, potential, seasonal, super breeder, larval habitat-level sub-meter resolution, capture point,unmixed, signature estimates obtained specifically for the calibration of real-time UAV sensed,discontinuously canopied measurements. In addition to accounting for sources of error that would be normally expected in conventional biomass estimates (e.g., measurement and allometric capture poit LULC, signature errors), we examined sources of uncertainty that were specific to the calibration process of the *Ae. aegypti,* geosampled, potenetial, seasonal, super breeder, eco-georeferenecable data. We found that in the real-time, time series, UAV waste tire, signature model the error resulting from spatial disagreement between field and UAV sensed measurements (i.e., co-location error), and the error introduced when accounting for temporal differences in real-time data acquisition were the most common. We found that the overall uncertainty in the field biomass in the Hillsborough county epi-entomological, intervention, study site was typically <4% for urban LULCs, but ranged from 1 to 3% in agrocommercial, pasturelands based on Kappa statistics. Co-location and temporal errors accounted for a large fraction of the total variance (>65%) and were identified as important targets for reducing uncertainty in studies relating potential, seasonal, super breeder, waste tire, Ae aegypti, larval habitat, county abatement, LULC signature, capture points, to remotely sensed data.

 Although measurement and allometric errors were relatively unimportant when considered alone, combined they accounted for roughly 11% of the total variance on average in the capture point paradigms. Our results suggest that a thorough understanding of the sources of error associated with field-measured, waste tire, larval habitat–level, sub-meter resolution, unmixed, LULC signature, RGB eco-endmember frequency estimates geo-spectro temporally retrieved in a real-time dashboard is critical to determine confidence in UAV sensed estimates of fluxes, and to develop strategies for reducing the overall uncertainty of signature interpolation approaches for optimally targeting unknown, potential, seasonal, super breeder, county abatment, eco-georeferenceable foci.

One of the greatest advantages of real-time UAV systems is their flexibility. Although drones cannot be flown in the rain, they are not reliant on clear sky conditions (as they are flown at low altitudes, below clouds, unlike optical satellites) and the timing of satellite overpasses and they can therefore be flown at times convenient for county abatement, survey field teams, making them an ideal tool for supporting waste tire, Ae aegypti, seasonal, larval control initiatives at the abatement level.

This researched revealed that demographics such as income and education impacted the quantity of waste tires improperly disposed on a county aabatement property. Further, anthropogenic population density was not correlated to the amount of tires in the Hillsborough County

epi-entomological, intervention study site since the highest populated zip codes did not equate to occurrence abundance and distribution of waste tires. There was not a strong correlation between zip codes with higher number of tire sites and higher proportion of an ethnicity such as Black/African American or Hispanic. However, 60% of these races were more likely to live in a zip code with a waste tire site than White.

Limitations, however, existed as a result of atmospheric influences and soft substrate differences during the UAV signature acquisition process. Atmospheric turbidity generally inhibits reliable measures of vegetation LULC and may delay the detection of an onset of stress in canopies (Slater and Jackson, 1982; Jackson et al., 1983). Uncorrected atmospheric effects are also a problem in multitemporal studies where atmosphere-induced variations on canopy spectra exceed those due to vegetation development. Soil background conditions exert considerable influence on partial canopy spectra and the calculated vegetation indices(Tucker 1991). Soft brightness influences have been noted in numerous studies where, for a given amount of vegetation, darker soil substrates resulted in higher vegetation index values when the ratio vegetation index (RVI = MR/red) or the normalized difference vegetation index [NDVI --(NIR - red)/(NIR + red) = (RVI - 1)/(RVI+I)] were used as vegetation measures (Colwell, 1974; Elvidge and Lyon, 1985). Huete et al. (1985) found an opposite soil brightness influence on the perpendicular vegetation index (PVI) such that brighter soils resulted in higher index values for a given quantity of incomplete vegetation cover. Thus, in areas where there are considerable soil brightness variations in an intervention, epi-entomological, study site, potenetial seasonal, superbrreder, Ae aegypti, waste tire, larval habitats may be defferentiaed based on real-time UAV geosampled moisture differences.

Limitations to this research also included the inherent bias associated within the ordinary kriging interpolation algorithm in the real-teme, UAV dashboard. The eco-georeferenceable, measurement, waste, tire, Ae aegypti, larval habitat, error model was $Z(s) = \mu(s) + \varepsilon(s) + \delta(s)$, in the real-time ArcGISwhere $\delta(s)$ was measurement error and $\mu(s)$ and $\varepsilon(s)$ were the mean and random variation in the geosampled LULC unmixed, sub-meter resolution, time series, signature, .parameter, estimators geosampled in the Hillsborough county abatement dataset. In this model, the nugget effect (i.e.,sum of eco-geographic canopy microstructure and measurement error) was composed of the variance of $\varepsilon(s)$ (called microscale variation) plus the variance of $\delta(s)$. In ArcGIS Geostatistical Analyst, we specified a proportion of the real-time UAV dashboard estimated nugget effect as microscale variation and measurement variation. When there is no measurement error, kriging is an exact interpolator, meaning that if you predict at a location where data has been collected, the predicted value is the same as the measured value. However, measurement errors did exist in the sub-meter resolution, super breeder, seasonal, waste tire, *Ae. aegypti,* LULC signatures, so we employed a filtered value, $\mu(s0) + \varepsilon(s0)$, which did not have a measurement error term. At various, county abatement, larval habitat, capture points, the filtered value (i.e., predicted LULC county abatement potential hyper productive, breeding site geolocations) was not the same as the measured value. The effect of choosing measurement error models is that a final map can be smoother and have smaller standard errors than the exact kriging version .

Further, LULC signature Items might have been added, shifted or removed between the time of the UAV real-time image acquisition and the date of field verification. Due to reflectivity, items can have multiple RGB spectral values and therefore obtaining the optimal range is critical[Jensen 2005]. The field verification team also did not perform a thorough search to locate tires that were not detected by this process; therefore, some habitats were not included. Future studies will include testing for other diseases or items, employing a UAV for real time land capture and analysis as well as potentially incorporating weather (i.e. during wet precipitation season) and temperature (summer), time series variables to create an even more robust, LULC, signature, sub-meter resolution, unmixed, RGB eco-endmember, capture point, waste tire, county abatement, real-time, signature model that can optimally geolocate unknown, hyperendemic, immature. Ae aegypti, ovipsoition sites and continue to isolate significant LULC, iteratively interpolative variables. Additionally, experimenter might include sampling of waste tire or other active county abatement geolocations to identify seasonal trends in super breeder, eco-georferenceable foci of this mosquito vector species for implementing even more refined, targeted, urban and agro-pastureland, county abatement LULC larval, control strategies(targeted IVM).

Conclusion

This research provides a srong proof of concept for the use of a low-cost (< U.S.\$1000) drone (DJI Phantom) for real-time, sub-mter resolution, LULC signature mapping water bodies including natural water bodies, irrigated and non-irrigated,peri-urban and urban, county abatement, various inhomogenously shade-canopied, seasonal geolocations. The objective of this research was to employ sub-meter resolution RGB signature of a super breeder, *Ae. aegypti* vector mosquito, aquatic, larval habitat, endemic, eco-georeferenceable, capture point waste tire,LULC foci) to identify other unknown breeding site foci at the county abatement geolocations. The drone data remotely identified a sub-sample dataset with 92.7 % accuracy based on predicted, potential, seasonal, super breeder, capture point, county abatement, GPS coordinates.

 Based on the LULC properties (such as its terrain, elevation, size, and arrangement of obstacles), the DJI Phantom 3. drone dashboard ArcGIS algorithm generated county abatement, surveillance flight plans (which included takeoff and landing locations and differentially corrected GPS waypoints t) for the small, fixed-wing UAV. S mall, fixed-wing UAVs are useful for surveillance because they are typically faster and have a higher durance compared to multicopter systems(www.esri.com). Compared to fixed-wing aircraft, quadcopter UAVs may be better suited for localized, very low altitude flights in complex county abatement environments (which may contain tress) and for visually detecting the presence of waste tire, super breeder, eco-georferenecable, *Ae. aegypti* larval habitats as they are more maneuverable and, unlike fixed-wing aircraft, can also hover (like a helicopter) over a particular, geolocation. Since localized, very low altitude flights in the Hillsborough county

abatement study site put the UAV in close proximity to obstacles such as trees, we developed intelligent ArcGIS (IoS app) and other spectral signature algorithms that safely navigated the quadcopter to and from potential eco-georeferenced, geoclassified, LULC, geolocations of potential, unknown, grid-stratfiable, super breeder, waste tire *Ae. aegypti,* aquatic, larval habitats.

With flying times of less than 30 min for each site, high-resolution (31 cm), eco georeferenced, real-time,UAV images wmay be successfully generated for multiple artificial, capture point, sites on various grid-stratefiable,, LULC geoclassifications (e.g., urban- residential, agro-pasturelands). Water bodies were readily identifiable in the imagery, as well as ancillary information for planning integrated, county abatement, vector, larval, mosquito management activities (access routes to water bodies by road and foot) and public health management (e.g. identification of drinking water sources, mapping individual households and the nature of their construction). The drone-dashboard cartographic signature surveys provide a low-cost and flexible solution to real-time, mapping water bodies for operational dissemination of control initiatives for any epi-entomological, county abatement intervention, study site employing wayard differentially corrected GPS points. The UAV scale and resolution is sufficient for operational eco-georeferenceable surveying of Ae aegypti waste habitats at the community scale regardless of geographic location (e.g., agricultural paddies, culverts, transporation networks, river channels, streams etc). Here, Natural water bodies such as springs and smaller pools of water were associated with borrow pits at the side of roads All of the habitats identified by the field entomological team were correctly identified in the relevant drone orthomosaic.

Acknowledgment

Appendix 1

works to improve $Q\left(\theta/\theta^{(t)}\right)$ rather than directly improving $\log p\left(X/\theta\right)$ Here we show that improvements to the former imply improvements to the latter for any with non-zero probability we can write $\log p\left(X/0\right)=\log\left(X,Z/0\right)-\log p\left(Z/X,0\right)$ We take the expectation over values of by multiplying both sides by and summing (or integrating) over. The left-hand side is the expectation of a constant, so we get: $\log p\left(X/0\right)\sum p\left(X,Z/0\right)-\log p\left(X,Z/0\right)$ where is defined by the negated sum it is replacing. This last equation holds for any value of including $Q\left(\theta/\theta^{(t)}\right)\log p\left(X/\theta\right)$ and subtracting this last equation from the previous equation renders $\log p\left(X/0\right)\sum p\left(X,Z/0\right)-\log p\left(X,Z/0\right)$ However, Gibbs' inequality tells us that so we can conclude that $\log p\left(X/0\right)=\log\left(X,Z/0\right)-\log p\left(Z/X,0\right)$ Suppose that $P=\{p_1,...,p_n\}$ is a probability distribution. Then for any other probability distribution $Q=\{q_1,...,q_n\}$ the following inequality between positive quantities (since the pi and qi are positive numbers less than one) holds $ss_{yy}=\sum_{i=1}^{n}\left(y_r-\bar{y}\right)^2=\left(\sum_{i=1}^{n}y_r^2\right)-n\bar{y}^2$, with equality if and only if $p_i=q_i$ for all i. Put in words, the information entropy of a distribution P is less than or equal to its cross entropy with any other distribution The difference between the two quantities is the Fullback–Libeler divergence or relative entropy, so the inequality can also be written: For discrete probability distributions P and Q, the Fullback–Libeler divergence of Q from P is defined to be In words, it is the expectation of the logarithmic difference between the probabilities P and Q, where the expectation is taken using the probabilities P. The Fullback–Libeler divergence is defined only if Q(i)=0 implies P(i)=0, for all I (absolute continuity). Whenever P(i) is zero the contribution of the itch term is interpreted as zero because $\lim x In\left(x\right)=0$ For distributions P and Q of a continuous random variable, the Fullback–Libeler divergence is defined to be the integral: [5] $DK\left(P/Q\right)=\int_{a}^{-\alpha}p\left(x\right)In\frac{p\left(x\right)}{q\left(x\right)}dx$ where p and q denote the densities of P and Q.More generally, if P and Q are probability measures over a set X, and P is absolutely continuous with respect to Q, then the Kullback–Leibler divergence from P to Q is defined as $DK\left(P/Q\right)=\int_{x}In\frac{p\left(x\right)}{q\left(x\right)}dp$ where is the Radon–Nikodym derivative of P with respect to Q, and provided the expression on the right-hand side exists. In mathematics, the Radon–Nikodym theorem is a result in measure theory which states that, given a measurable space $\left(X,\Sigma\right)$ if a σ-finite measure V on $\left(X,\Sigma\right)$ is absolutely continuous with respect to a σ-finite measure μ on $\left(X,\Sigma\right)$ then there is a measurable function such that for any measurable subset $v\left(A\right)=\int_{A}f d\mu$ Equivalently, this can be written as which we recognize as the entropy of P relative to Q. Continuing in this case, if is any measure on X for which $p=\frac{dp}{d\mu}andq=\frac{dq}{d\mu}$. The logarithms in these formulae are taken to base 2 if information is measured in units of bits, or to base e if information is measured in nets. Most formulas involving the Fullback–Libeler divergence hold regardless of the base of the logarithm.

Various conventions exist for referring to DKL(P‖Q) in words. Often it is referred to as the divergence between P and Q; however, this fails to convey the fundamental asymmetry in the relation. Sometimes it may be found described as the divergence of P from, or with respect to Q (often in the context of relative entropy, or information gain). However, in the present article the divergence of Q from P will be the language used, as this best relates to the idea that it is P that is considered the underlying "true" or "best guess" S. damnum sold larval habitat distribution, that expectations will be calculated with reference to, while Q is some divergent, less good, approximate distribution. Note that the use of base-2 logarithms is optional and allows one to refer to the quantity on each side of the inequality as an "average surprisal" measured in bits. Thus, choosing to improve beyond will improve $\log p\left(X/\theta\right)$ beyond $\log p\left(X/\theta\right)$ at least as much. Under some circumstances, it is convenient to view the EM algorithm as two alternating maximization steps. Consider the function: where q is an arbitrary probability distribution over the unobserved data z, pZ|X(· |x;θ) is the conditional distribution of the unobserved data given the observed data x, H is the entropy and DKL is the Kullback–Leibler divergence.Then the steps in the EM algorithm may be viewed as:Expectation step: Choose q to maximize F: $q^t=\arg\max F\left(q,\theta\right)$ Maximization step: Choose θ to maximize F: $\theta^{(t+1)}=\arg\max F\left(q,\theta\right)$

Appendix 2.

In spherical coordinates, the scale factors are and the separation functions are $f_1(r) = r^2 f_2(\theta) = 1$ $f_3(\theta) = \sin\theta$ giving a Steckel determinant of The Laplacian is $\frac{\partial R_\perp^2}{\partial_{a_n}} = \frac{2}{1+b^2}\sum_{i=1}^{n}[y_\gamma - (a+bx_\gamma)](-1) = 0$ To solve Laplace's equation in spherical coordinates, attempt separation of variables by writing $f_1(r,\theta,\phi)$ Then the Helmholtz differential equation becomes $\frac{\partial R_\perp^2}{\partial_a} = \frac{2}{1+b^2}\sum_{i=1}^{n}[y_\gamma - (a+bx_\gamma)](-x_\gamma) + \sum_{i=1}^{n}\frac{[y_\gamma - (a+bx_\gamma)](-1)(2b)}{(1+b^2)^2} = 0$ Now divide by $R\Phi$ The solution to the second part of (5) must be sinusoidal in a S. damnum sold larval habitat risk model so the differential equation is which has solutions which may be defined either as a complex function with $m = -\infty$ or as a sum of real sine and cosine functions with $m = -\infty$ By so doing,, the equation created would be The radial part must be equal to a constant $\frac{r^2}{R}\frac{d^2R}{dr^2} + \frac{2r}{R}$ But this is the Euler differential equation, so we try a series solution of the form $R = \sum_{n=0}^{\infty} a_n$ .Then $r = \sum_{n=0}^{\infty}(n+c)(n+c-1)a_n + 2r\sum_{n=0}^{\infty}(n+c)a_n r^{n+c-1}$ and thereafter $-1(l+1)\sum_{n=0}^{\infty} a_n r^{n+c} = 0$ and $r = \sum_{n=0}^{\infty}(n+c)(n+c-1)a_n + 2r\sum_{n=0}^{\infty}(n+c)a_n r^{n+c-1(l+1)}\sum_{n=0}^{\infty} a_n = 0$ $r = \sum_{n=0}^{\infty}(n+c)(n+c-1) - l(l-r) = 0$.

The general nonhomogeneous differential equation is given by $x^2\frac{d^2}{dx^2} + \alpha x$ and the homogeneous equation is $x^2 y'' + \alpha x y' + \beta y = 0$ $y'' + \frac{\alpha}{x}y' = 0$. Now attempt to convert the equation from to one with constant coefficients $\frac{d^2}{dx^2} + A\frac{dy}{dx^2} + B = 0$ by using the standard transformation for linear second-order ordinary differential equations. Comparing the equation functions $p(x)$ and $q(x)$ are Let $B = 0$ and define Then is given by which is a constant. Therefore, the equation becomes a second-order ordinary differential equation with constant coefficients $\frac{d^2 y}{dz^2} + (\alpha-1)\frac{dy}{dx} + \beta y = 0$ Define $\Gamma^m = r1\frac{1}{2}(-A + \sqrt{A^2 - 4D})$, $r2\frac{1}{2}(-A - \sqrt{A^2 - 4D})$ and $\frac{1}{2}(\alpha-1)$ The solutions are $y = \begin{cases} c1e^{r1z} + c2e^{r2z} & (\alpha-1)^2 > 4\beta \\ (c1+C2z)e^{r1z} & (\alpha-1)^2 = 4\beta \\ e^{az}[c1\cos(bz) + c2\sin(bz)] & (\alpha-1)^2 < 4\beta \end{cases}$ In terms of the original variable x,

Zwillinger [119] gives two other types of equations known as Euler differential equations, $y' = \pm\sqrt{\frac{ay^4 + by^3 + cy^2 + dy + e}{ax^4 + bx^3 + cx^2 + dx + e}}$ and $y' + y^2 = \alpha x^m$ For the rc term (with n=0), which is true only if c=l-1 and all other terms vanish. So $a_n = 0$ for $n \notin l, -1-1,$. Therefore, the solution of the R component must be given by Plugging the output back into ($\diamond$) renders and which is the associated Legendre differential equation for and The general $y = \begin{cases} c1|x|^{r1} + c2|x|^{r2} & (\alpha-1)^2 > 4\beta \\ (c1+C2\ln|x|) & (\alpha-1)^2 = 4\beta \\ |x|^a[c1\cos(bz) + c2\sin(bz)] & (\alpha-1)^2 < 4\beta \end{cases}$ complex solution is therefore where are the (complex) spherical harmonics.

The generalized real solution would be $r = \sum_{n=0}^{\infty}(n+c)(n+c-1)a_n + 2r\sum_{n=0}^{\infty}(n+c)a_n r^{n+c-1}$. Some of the normalization constants of p_i^m can be absorbed by S_m and C_m, so this equation may appear in the form $r = \sum_{n=0}^{\infty}(n+c)(n+c-1)a_n + 2r\sum_{n=0}^{\infty}(n+c)a_n r^{n+c-1(l+1)}\sum_{n=0}^{\infty} a_n = 0$ wher $y_1^{m(0)}(\theta,\phi) = P^m(\cos\phi)(\sin m\theta)$ are the even and odd (real) spherical harmonics. If azimuthal symmetry is present, then is constant and the solution of the component is a Legendre polynomial.

The general solution would then be then $-1(l+1)\sum_{n=0}^{\infty} a_n r^{n+c} = 0$.

Appendix 3

Generally speaking, a Green's function is an integral kernel that can be used to solve differential equations from many families including simpler examples such as ordinary differential equations with initial or boundary value conditions, as well as more difficult examples such as inhomogeneous partial differential equations (PDE) with boundary conditions.

A second order, linear nonhomogeneous differential equation is $y' + p(t)y' + q(t)y = g(t)$ $y' + p(t)y' + q(t)y = g(t)$ where g(t) is a non-zero function. Note that we did not employ constant coefficients in the geo-spatiotemporally, geosampled, S. damnsoum s.l. riverine larval habitat eco-epidemiological, risk model here because everything that we're going to do in this section doesn't require it. Also, we're using a coefficient of 1 on the second derivative just to make some of the work a little easier to write down. It is not required to be a 1. Thus, the final model would be $y' + p(t)y' + q(t)y = 0$ $y' + p(t)y' + q(t)y = 0$.

Important for several reasons, Green's functions allow for visual interpretations of the actions associated to a source of force or to a charge concentrated at a point (Qin 2014), thus making them particularly useful in areas of applied mathematics. Green's function methods are widely used in, (e.g., physics, and engineering). More precisely, given a linear differential operator acting on the collection of distributions over a subset of some Euclidean space , a Green's function at the point corresponding to is any solution of where denotes the delta function. The motivation for defining such a function is widespread, but by multiplying the above identity by a function and integrating with respect to yields $\int \iota G(x,s)f(s)ds = \int \delta(x-s)f(s)ds$. The right side reduces merely to f(x) due to properties of the delta function, and because l is a linearizable operator acting only on x and on s.

In the forecasting, *S. damnosum* s.l. riverine larval habitat eco-epidemiological, risk model. The right-hand side reduces merely to due to properties of the delta function, and because is a linear operator acting only on *x* and not on *s*, the left-hand side was rewritten as $G(x,s)f(s)ds$. This reduction was particularly useful for solving $u = u(x)$ in differential equations of the form $\iota u(x) = f(x)$ where the arithmetic confirmed that $\int G(x,s)f(s)ds$ and whereby it followed that has the specific integral form $u(x)\int G(x,s)f(s)ds$ The intuitive physical interpretation of a Green's function was associated to our S. damnosum s.l. –related differential equation. In particular, these functions revealed a length t suspended between two walls, held into place by an identical horizontal force applied on each of its ends, and a lateral load placed at some interior point on a line of integers.

Let x' be the point corresponding to on the deflected tangent, and then suppose the downward force is rope. Corresponding to this physical system would then be the differential equation $-Hu''(x) = F(x)$ for $0 < x < \ell$ with $u(0) = u(\ell) = 0$, a system whose simplicity allows both its solution $u(x)$ and its Green's function $G(x,y)$ to which we wrote explicitly: $u(x) = \frac{F}{2H}(\ell x - x^2)$ and $G(x,y) = \frac{1}{H\ell}\begin{cases} y(\ell - x) & \text{for } y < x \\ x(\ell - x) & \text{for } x < y \end{cases}$ respectively. The displaced rope then had the piecewise linear format given by $G = G(x,y)$ above, thus confirming the claim that the Green's function associated to this system represents the action of the horizontal rope corresponding to the application of a force F.

A Green's function taking a pair of arguments (x,s) is sometimes referred to as a two-point Green's function [25]. This is in contrast to multi-point Green's functions which are of particular importance in the area of many-body theory. As an elementary example of a two-point function we considered the problem of determining the potential generated by a interrogatable distribution whose density was $p(r)$, whereby applications of Poisson's equation had the potential at r_1 produced by each element $p(r_2)d^3r_2$ which yielded a solution which held, over the entire riverine region where $p(r_2) = 0$ Because the right-hand side can be viewed as an integral operator converting p into φ we re-wrote this solution in terms of a Green's function $G = G(r_1, r_2)$ having the form $G = G(r_1, r_2) = \frac{1}{4\pi\varepsilon_0}$ whereby the solution can be rewritten: $\varphi(r_1) = \int d^3r_2 G(r_1, r_2)\rho(r_2)$ The above figure shows the Green's function associated to the solution of the $\varphi - \rho$ equation discussed above where $\varepsilon_0 = 4$ and r_1, respectively r_2, is plotted on the x-, respectively y - axis. A somewhat comprehensive list of Green's functions corresponding to various differential equations was then generated.

Due to the multitude of literature written on Green's functions, several different notations and definitions may emerge, some of which may be topically different than the above but which in general do not affect the important properties of our results. In our model output we denoted the empirically regressed S. damnsoum s.l.-related variables x and s in terms of vectors r_1 and r_2.

Appendix 4

The situation for a Lambertian surface may be classified as emitting or scattering. For conceptual clarity we thought in terms of photons rather than energy or luminous energy. The wedges in the circle each represented an equal angle $d\Omega$, and for a Lambertian surface, the number of photons per second emitted into each wedge is proportional to the area of the wedge It was seen that the length of each wedge is the product of the diameter of the circle and $\cos(\theta)$. It can also be seen that the maximum rate of photon emission per unit solid angle is along the normal and diminishes to zero for $\theta = 90°$. In mathematical terms, the radiance along the normal is I photons/(s·cm2·sr) and the number of photons per second emitted into the vertical wedge is I $d\Omega$ dA. The number of photons per second emitted into the wedge at angle θ was in the S. damnsoum s.l. larval habitat forecasting, risk, eco-epidemiological, model was I $\cos(\theta)$ $d\Omega$ dA.

The observer directly above the area element sees a scene through an aperture of area dA0 and the area element dA will subtend a (solid) angle of $d\Omega0$. We can assume thus without loss of generality that the aperture happens to subtend solid angle $d\Omega$ when "viewed" from the emitting area element. This normal observer will then be recording I $d\Omega$ dA photons per second and so will be measuring a radiance of $I_0 = \frac{Id\Omega dA}{d\Omega_0 dA_0}$ photons/(s·cm2·sr). The observer at angle θ to the normal will be seeing the scene through the same aperture of area dA0 and the area element dA will subtend a (solid) angle of $d\Omega0 \cos(\theta)$. This observer will be recording I $\cos(\theta)$ $d\Omega$ dA photons per second, and so will be measuring a radiance of $I_0 = \frac{I\cos(\theta)d\Omega dA}{d\Omega_0 \cos(\theta)d_0 A} = \frac{Id\Omega dA}{d\Omega_0 dA_0}$ photons/(s·cm2·sr), which is the same as the normal observer.

In general, the luminous intensity of a point on a surface varies by direction; for a Lambertian surface, that distribution is defined by the cosine law, with peak luminous intensity in the normal direction. Thus, when the Lambertian assumption held, we calculated the total habitat canopy luminous flux, F from the peak luminous intensity, I_{max} by integrating the cosine law: $F_{tot} = \int_0^{\pi/2}\int_0^{2\pi}\cos(\theta)I_{max}\sin(\theta)d\theta = 2\pi.I_{max}\int^{\pi/2}\cos(\theta)\sin(\theta)d\theta = 2\pi.I_{max}\int^{\pi/2}\frac{\sin(2\theta)}{2}d\theta$ and so $F_{tot} = \pi Sr$ where $\sin(\theta)$ was the determinant of the Jacobian matrix for the unit sphere and realizing that is luminous flux per steradian.

Appendix 5

The Digma function is special function which is given by the logarithmic derivative of the gamma function (or, depending on the definition, the logarithmic derivative of the factorial). Because of this ambiguity, two different notations are sometimes (but not always) used, with $\psi(z) \equiv \frac{d}{dz} ln\Gamma(z) = \frac{\Gamma'(z)}{\Gamma(z)}$ defined as the logarithmic derivative of the gamma function $\Gamma(z)$ and $F(z) \equiv \frac{d}{z} lnz$ defined as the logarithmic derivative of the factorial function. The two are connected by the relationship $F(z) = \Psi(z+1)$ The n th derivative of $\psi(z)$ is called the polygamma function, denoted $\psi_n(z)$. The notation $\psi_0(z) \equiv \Psi(z)$ is therefore frequently used for the digamma function itself, and Erdélyi et al. (1981) use the notation $\psi(z)$ for $\psi(z)$. The digamma function $\psi_0(z)$ is returned by the function PolyGamma[z] or PolyGamma [0, z] in the Wolfram Language, and typeset using the notation $\psi^{(0)}$ The digamma function arises in simple sums such as9] $\sum_{k=0}^{\infty}\frac{(-1)}{k+1} = \frac{\phi(-1,1,z^{-1})}{z}$ = where $\Phi(z,s,a)$ is a Lerch transcendent.

The Lerch transcendent is generalization of the Hurwitz zeta function and polylogarithm function. Many sums of reciprocal powers can be expressed in terms of it. It is classically defined by $\Phi(z,s,a) = \sum_{k=0}^{\infty}\frac{z^k}{(a+k)} = \frac{\phi(-1,1,z^{-1})}{z}$ for and It is implemented in this form as Hurwitz LerchPhi [z, s, a] in the Wolfram Language. The slightly different form $\Phi(z,s,a) = \sum_{k=0}^{\infty}\frac{(-1)}{k+1} = \frac{\phi(-1,1,z^{-1})}{z}$ sometimes also denoted $\Phi(z,s,a)$ is implemented in the Wolfram Language as LerchPhi [z, s, a]. Note that the two are identical only for $R(a) > 0$.

Refences

1. Joan-Pau Millet, Tomàs Montalvo, Ruben Bueno-Marí, Arancha Romero-Tamarit, Albert Prats-Uribe, et al. (2017) Imported Zika Virus in a European City: How to Prevent Local Transmission. 8: 1319.

2. Muturi Ephantus J, Benjamin G Jacob, Chang-Hyun Kim, Charles M Mbogo, Robert Novak (2007) Are co-infections of malaria and filariasis of any epidemiological significance? Parasitol Res 102(2): 175-181.

3. Luke Alphey, Mark Benedict, Romeo Bellini, Gary G Clark, David ADame, et al. (2010) Sterile Insect Methods for Control of Mosquito-Borne Diseases: An Analysis. Vector Borne Zoonotic Dis10(3): 295-311.

4. Peter RJ, Van den Bossche p, Penzhorn BL, Sharp B (2005) Tick, fly, and mosquito control--lessons from the past, solutions for the future. Vet Parasitol 132(3-4): 205-215.

5. Barnard DR, Xue RD (2004) Laboratory evaluation of mosquito repellents against Aedes albopictus, Culex nigripalpus, and Ochierotatus triseriatus (Diptera: Culicidae). J Med Entomol 41(4): 726-730.

6. Rowland M, Downey G, Rab A, Freeman T, Mohammad N (2004) DEET mosquito repellent provides personal protection against Supposedly repellants are useful when employed where human activity coincides with the diurnal activity patterns of mosquitoes, (e.g., outdoor activities that take place at dusk and dawn, e.g., hunting and fishing).

7. Taylor RW, Romaine IM, Liu C, Murthi P, Jones PL (2012) Structure-activity relationship of a broad-spectrum insect odorant receptor agonist. ACS Chem Biol 7(10): 1647-1652.

8. Suh E, Bohbot JD, Zwiebel LJ (2014) Peripheral olfactory signaling in insects. Curr Opin Insect Sci 6: 86-92.

9. Chadee DD, Ward RA, Novak RJ (1998) Natural habitats of Aedes aegypti in the Caribbean--a review. J Am Mosq Control Assoc 14(1): 5-11.

10. Soumyajit Banerjee, Gautam Aditya, Goutam K Saha (2015) Household Wastes as Larval Habitats of Dengue Vectors: Comparison between Urban and Rural Areas of Kolkata, India. PLoS One 10(10): e0138082.

11. Jacob BG. Mwangangi JM Mbogo CB, Novak RJ (2011) A Taxonomy of Unmixing Algorithms Using Li- Strahler Geometric- Optical Model and other Spectral Endmember Extraction Techniques for Decomposing a QuickBird Visible and Near Infra-red Pixel of an Anopheles arabiensis Habitat Open Remote Sensing. 17(3): 11-24.

12. Sota, Mogi (1992) Interspecific variation in desiccation survival time of Aedes (Stegomyia) mosquito eggs is correlated with habitat and egg size. Oecologia 90(3): 353-358.

13. Diniz DF, De Melo-Santos MA, Santos EM, Beserra EB, Helvecio E (2015) Parasit Vectors 8: 662.

14. John C Beyer, Joseph Keating, John I Githure, Michael B Macdonald, Daniel E Impoinvil, et al. (2008) Integrated vector management for malaria control. 7 (Suppl 1): S1- S4.

15. Pinching S, Samuel Aloo, Benjamin Jacob Ricardo Azurite (2016) Mapping Minimum and Maximum Standard Deviation 3-Dimensionsional Slope Coefficients for Geo-Spectro temporally Iteratively Quantitatively Interpolating an End-member Proxy Signature of Cyanobacteria (Bluegreen Algae) for Eco-cartographically Delineating Cholera Risk in a Riverine Tributary Ecosystem in Ecuador Journal of Remote Sensing & GIS 6(7): 13-19.

16. Darvish Zadeh R, Skidmore A, Schlerf M, Atzberger C, Corsi F, et al. (2008) LAI and chlorophyll estimation for a heterogeneous grassland using hyperspectral measurements. Isprs Journal of Photogrammetry and Remote Sensing 63(4): 409-426.

17. McCoy RM (2005) Field methods in remote sensing. The Guilford Press, New York, USA.

18. Huete AR (1989) Soil influences in remotely sensed vegetation-canopy spectra in Theory and Applications of Optical Remote Sensing. John Wiley and Sons, New York, USA.

19. Ben Door E, Irons JR, Edema G (1999) Soil reflectance 111-188 in Renzo An, ed. Remote Sensing for the Earth Sciences. John Wiley and Sons, New York, USA.

20. Hopkinson, LE Chaser (2007) Modelling Canopy Gap Fraction from Lidar Intensity.

21. Fidela I, Penuelas J (1994) The red edge position and shape as indicators of plant chlorophyll content, biomass and hydric status. International Journal of Remote Sensing 15(7): 1459-1470

22. Jacob BG, Lampman RL, Ward MP, Muturi E, Funs J, et al. (2010) Geospatial variability of Culex pippins and Culex returns aquatic habitats in urban Champaign, Illinois. International Journal Remote Sensing 30(8): 5-19.

23. Pimstein A, Eitel JUH, Long DS, Mufradi I, Karnieli A, et al. (2009) A spectral index to monitor the head-emergence of wheat in semi-arid conditions. Field Crops Research 111(3): 218-225.

24. Darvishzadeh R, Skidmore A, Schlerf M, Atzberger C, Corsi F, et al. (2008) LAI and chlorophyll estimation for a heterogeneous grassland using hyperspectral measurements. Isprs Journal of Photogrammetry and Remote Sensing 63(4): 409-426.

25. Choi S, Kim T, Yu W (2009) Performance Evaluation of RANSAC Family. Proceedings of the British Machine Vision Conference, pp. 81.

26. Herout A, Dubska M, Havel J (2013) Real-Time Detection of Lines and Grids. 1: 3-16.

27. Salisbury FB, Ross C (1969) Plant Physiology. Wadsworth Press, Belmont California, USA.

28. Homolova L, Malenovsky Z, Clevers JG, Garcia Santos G, Schaepman ME (2013) Review of optical-based remote sensing for plant trait mapping.

a. (2007) Optical radiation models in Remote Sensing: models and methods for image processing. Amsterdam, Netherlands, pp. 45-88.

29. Duggin M J, (1977) Likely effects of solar elevation on the quantification of changes in vegetation with maturity using sequential Landsat imagery. Appl Optics 16(3): 521-523.

30. ETN D, Jacob B (2016) A Negative Binomial with a Non-Homogenous Gamma Distributed Mean for Robustifying Pseudo R2 Regression Values of Immature Vector and Nuisance Mosquito Count Data for Optimally Discerning Un-Geosampled Waste Tires in a Subtropical Oviposition Site in SAS®/GIS employing Worldview-3 Visible and Near Infra-Red Data in Hillsborough County, Florida. J Remote Sensing & GIS, 5(3).

31. Warner TA, Xianfeng C (2001) Normalization of Landsat thermal imagery for the effects of solar heating and topography. International Journal of Remote Sensing 22(5).

32. Jackson RD, Pinter PJ (1986) Spectral response of architecturally different wheat canopies. Remote Sensing Environ 20(1): 43-56.

33. Chandrasekhar S, (1950) Radiative Transfer. Dover, New York, USA.

34. E P Shettle, JA Weinman (1970) The Transfer of Solar Irradiance Through Inhomogeneous Turbid Atmospheres Evaluated by Eddington's Approximation.

35. Samuelson RE, (1970) Non-Local Thermodynamic Equilibrium in Cloudy Planetary Atmospheres.

36. Liou KN, (1973) Numerical Experiments with Chandrasekhar's Discrete-Ordinate Method. J Atmos Sci 30 (1303).

37. Dave JV (1974) A Direct Solution of the Spherical-Harmonics Approximation to the Transfer Equation for a Plane-Parallel, Nonhomogeneous Atmosphere 13(1): 21-39.

38. W J Wiscombe (1976) On Initialization Errors and Flux Conservation in the Doubling Method 16(8): 637-658.

39. Hansen JE, Travis LD (1974) Light Scattering in Planetary Atmospheres. Space Sci Rev 16(4): 527-610.

40. Jiang Z, Huete A, Chen J, Chen Y, Li J, et al. (2006) Analysis of NDVI and scaled difference vegetation index retrievals of vegetation fraction. 101(3): 366-378.

41. Huete AR, Jackson RD (1988) Soil and atmosphere influences on the spectra of partial canopies. Remote Sensing of the Environment 25(1): 89-105.

42. Rundquist BC (2002) The influence of canopy green vegetation fraction on spectral measurements over native tallgrass prairie. Remote Sensing of the Environment 81(1): 129-135

43. Sjoberg RW, Horn BKP (1983) Atmospheric effects in satellite imaging of mountainous terrain. Applied Optics 22: 1702-1716.

44. Pinty B, Szejwach G, Stum J (1985) Surface albedo over the Sahel from Meteosat radiances. Journal of Climate and Applied Meteorology 24: 108-113.

45. Nagler PL, Daughtry CST, Goward SN (2000) Plant litter and soil reflectance. Remote Sensing of Environment 71: 207-215.

46. Jacob BG, Novak RJ (2014) Integrating a Trimble Recon X 400 MHz Intel PXA255 Xscale CPU®Mobile Field Data Collection System Using Differentially Corrected Global Positioning System Technology and a Real Time Bidirectional Actionable Platform within an ArcGIS Cyberenvironment for Implementing Mosquito Control. Advances in Remote Sensing 3(3): 141-196.

47. Baumgardner MF, Silva LF, Biehl LL, Stoner ER (1985) Reflectance properties of soils. Advances in Agronomy 38: 1-44.

48. Price JC (1990) On the information content of soil reflectance spectra. Remote Sensing of Environment 33(2): 113-121.

49. Qi J, Chehbouni A, Huete AR, Kerr YH, Sorooshian S (1994) A modified soil adjusted vegetation index. Remote Sensing of Environment 48(2): 119-126.

50. Chaiken S, Kleitman D (1978) Matrix Tree Theorems. Journal of Combinatorial Theory Series A 24(3): 377-381.

51. Doyle PG, Snell L (1984) Random Walks and Electric Networks.

52. Jacob BJ, Novak LT, Sanfo S Caliskan, Unnasch T (2014) Denoising a model employing automated bandwidth selection procedures and pre-whitened Euclidean-based quadratic surrogates in PROC ARIMA for optimizing asymptotic expansions and simulations of onchocerciasis endemic transmission zones in Burkina Faso Journal of Public Health and Epidemiology 6(11): 347-389.

53. Jacob BG, Ranjit de Alwiss, Semiha Caliskan, Daniel A Griffith, Dissanayake Gunawardena (2013) A Random-effects Regression Specification Using a Local Intercept Term and a Global Mean for Forecasting Malarial Prevalence. American Journal of Computational and Applied Mathematics 3(2): 49-67.

54. Huete AR, Didan K, van Leeuwen WJD, Vermote EF (1999) Global-scale analysis of vegetation indices for moderate resolution monitoring of terrestrial vegetation. Proceedings of SPIE 1: 141-151.

55. Jacob BG, Novak RJ (2016) Pernicious quasi-normal non-monotonic Poissionian non-negativity constraints for optimally rectifying incompatibilistic endeogeneity in sub-meter resolution pseudo-Euclidean regression space employing analogs of the Pythagorean theorem and parallelogram laws for semi-parametrically demarcating non-trivial land cover wavelength filters and time series impulse-response metrological functions in an invertible Hermitian transjugate matrix while consolidating synergistic semi-logarithmic non- ordinate axis-scaled covariances in C++ for forecasting episodical yellow fever sylvatic, case distributions in an eco-geo referenceable irrigated riceland complex in Gulu, Uganda Journal of Applied Mathematics and Statistics 3(4): 42-366.

56. Jacob BG, Shafer S, Alinda P, Loun D, Mc Kinnon A, et al. (2017) Lexicographically, cartesian-ordered, differential calculi in canonically extractable in-situ near infra-red fluorescence quantum spectroscopic sub-surface continuous geodesic fluxions for metaheuristic chlorophyll- a translucent emissivty mapping intermittently canopied immature narrow riverine tributary Simulism damnosum sl oviposition sites for bio-optically delineating multivariate normalized Gaussian processes elucidative administrated by prior covariances and a spline within a reproducing non-frequentist simultaneous diagonalization of amalgamized positive definite kernels in Hilbert space: Implementation of a 'Slash and Clear' control intervention in two eco-georeferenceable agro-village complexes in northern Uganda Uganda Journal of Geophysics and Remote sensing 4(5): 26-221.

57. Jeesen Chen, Herman Rubin, bounds for the difference between median and mean of gamma and Poisson distributions. Statistics & Probability Letters 4(6): 281-283.

58. Van Noortwijk JM (2009) A survey of the application of gamma processes in maintenance. Reliab Eng Syst Safety 94(1): 2-21.

59. Jacob BG, Toe LSMS, Afriyie A, Ibrahim MI, Griffith DA (2012) Quasi- likelihood techniques in a logistic regression equation and probability density functions from an inverse Wishart-distributed matrix for identifying intra-cluster covariate coefficients of Simulium damnosum sl riverine habitats in Togo Geospatial Information Science 15(2): 117-133.

60. Li X, Strahler AH (1992) Geometric-optical bidirectional reflectance modeling of the discrete crown vegetation canopy: effect of crown shape and mutual shadowing. IEEE Transactions on Geoscience and Remote Sensing 30(2): 276-292.

61. Jacob, Zachariah N Brown, Samuel S Alao, Sarah E Schaffer, Benjamin G Jacob et al. (2016) Quantitating Three-Dimensional Impervious Surface Fractions Employing Geo-Schematic Layout algorithms, Isarithmic Maps and Non-Contiguous Cartograms for Identifying Hydrodynamic Catchment Flood Vulnerable Basins of High-Priority Hurricane Evacuation Routes and Levee Construction Sites in Hillsborough County, Florida Journal of Remote Sensing & GIS 5(2): 16-27.

62. Jacob BG, Griffith DA, Mwangangi JM, Gathings DG, Mbogo CB, et al. (2011) A cartographic analyses using spatial filter logistic model specifications for implementing mosquito control in Kenya Urban Geography 32: 363-337.

63. Glantz SA, Slinker BK (1990) Primer of Applied Regression and Analysis of Variance. Mc Graw-Hill Professional Publishing.

64. Novak RJ (2011) Adjusting second moment bias in eigenspace using Bayesian empirical estimators, Dirichlet tessellations and Worldview 1 data for predicting Culex quinquefasciatus in Trinidad Journal of Geographic Information Systems 14(2): 244-274.

65. Hoffman K, Kunze R "Characteristic Values." §6.2 in Linear Algebra, 2nd ed. Englewood Cliffs, NJ: Prentice Hall, Marcus M, Minc H (1971) Introduction to Linear Algebra. Dover, New York, USA, pp. 145.

66. Jacob B, Novak RJ, Toe L, Sanfo MS, Cali Lampman RL skhan S, et al. (2013) Unbiasing a Stochastic Endmember Interpolator Using ENVI Object-Based Classifiers and Boolean Statistics for Forecasting Canopied Simulium damnosum s.l. Larval Habitats in Burkina Faso. J Geophys Remote Sensing 2(7): 6-73.

67. Jacob BG, Morris JA, Caamano EX, Griffith DA, Novak RJ (2011) Geomapping generalized eigenvalue frequency distributions for predicting prolific Aedes albopictus and Culex quinquefasciatus habitats based on spatiotemporal field-sampled count data Acta Tropica 2: 61-68.

68. Jacob BG, Burkett N, Luvall J, Parcak S, McClure CJW, et al. 2010 Developing GIS-Based Eastern Equine Encephalitis Vector-host Models in Tuskegee, Alabama. International Journal of Health Geographics 9: 12-21.

69. Jacob BG, Lampman RL, Ward MP, Muturi E, Funes J, et al. (2010) Geospatial variability of Culex pipiens and Culex restuans aquatic habitats in urban Champaign, Illinois. International Journal Remote Sensing 30(8): 5-19.

70. Hastings WK (1970) Monte Carlo Sampling Methods Using Markov Chains and Their Applications. Biometrika 57(1): 97-109.

71. Glantz SA, Slinker BK (1990) Primer of Applied Regression and Analysis of Variance. McGraw-Hill Professional Publishing.

72. Rthur G, Griffith A (2010) in Regression Analysis, Geographical Analysis 34(2): 130-140.

73. Griffith AD, Wong WD, (2007) Modeling population density across major US cities: a polycentric spatial regression approach, Journal of Geographical Systems 9(1):53.

74. DA Griffith (2009) Spatial Autocorrelation, International Encyclopedia of Human Geography. 308-316.

75. Jacob BG, Novak RJ, Toe LD, Sanfo MS, Lassane K, et al. (2015). Ecogeographically and Non-Ecogeographically Forecasting Discontinuous Canopied Simulium damnosum s.l. Habitats by Interpolating Metrizable Sub-Mixel Mean Solar Exoatmospheric Quantum Scalar Irradiance. Journal of Remote Sensing & GIS 4: 152.

76. Chonggang Xu, Mathieu Legros, Fred Gould, Alun L Lloyd, Scott O'Neill, (2010) Understanding Uncertainties in Model-Based Predictions of Aedes aegypti Population Dynamics, PLoS Neglected Tropical Diseases 4(9): e830.

77. Fox J (1997) Applied Regression Analysis. Linear Models and Related Methods. Sage.

78. Jacob BG, Nelson PG, Lampman R, Morris J, Raim A, et al. (2006) Comparing GPS technology for identifying spatial ecological variation for urban mosquito management. Wing Beats. Journal of Mosquito Control Association 16: 30-33.

79. Kamiński B, Jakubczyk M, Szufel P (2017) A framework for sensitivity analysis of decision trees. Central European Journal of Operations Research.

80. Kenney JF, Keeping ES (1951) Linear Regression, Simple Correlation, and Contingency. Mathematics of Statistics, Chapter 8, 2nd edition, Princeton, Van Nostrand, New York, USA, pp. 199-237.

81. S Lipschutz, M Lipson (2009) Linear Algebra. (4th edn), Schaum's Outlines, McGraw Hill, New York, USA.

82. Borisenko AI, Taparov EI, Silverman RA, (1968) Vector and tensor analysis with applications. Translated by Richard Silverman. Dover, USA, p 14.

83. Jacob BJ, Novak LT, Caliskan S, Unnasch T (2013) Finite –Difference derivatives of a fist-order integral approximation quantized with a default Quasi-Newton Optimizer and a Pseudo-Lipschitzian property for predictive mapping spatially inhomogenous Similium damnosum s.l. explanatory covariates. Journal of Statistics: Advances in Theory and Applications 10(10): 1-250.

84. Hannan NP, Prince SU, Begue A (1997) Modelling vegetation primary production during HAPEX-Sahel using production efficiency and canopy conductance model formulations. 3: 651-675.

85. Gu W (1994) TriDyn: A simulation model of the dynamics of Culex tritaeniorhynchus populations. Jap J Sanit Zool 45: 319-326.

86. Wentzell PD, Andrews DT, Kowalski BR, (1997) Maximum likelihood multivariate calibration. Anal Chem 69: 2299–2311.

87. Tyler AN, Sanderson DCW, Scott EM, Allyson JD (1996) Accounting for spatial variability and fields of view in environmental gamma ray spectrometry. Journal of Environmental Radioactivity 33: 213-235.

88. Penndorf R (1957) Tables of the refractive index for standard air and the Rayleigh scattering coefficient for the spectral region between 0.2 and 20.0 µ and their application to atmospheric optics. J Opt Soc Amer47: 176-182.

89. Schowengerdt RA (1997) Remote Sensing, Models and Methods for Image Processing. (2nd edn), San Diego, Academic Press, USA.

90. Gates DM (1980) Biophysical Ecology. NY: Springer Advanced Texts in Life Sciences, New York.

91. Baret F, Jacquemoud S, Guyot G, Leprieur C (1992) Modeled analysis of the biophysical nature of spectral shifts and comparison with information-content of broad bands. Remote Sensing of Environment 41: 133-142.

92. Hosmer DW, Lemeshow S (2000) Applied logistic regression. John Wiley and Sons, New York, USA.

93. Fletcher, Roger (1987) Practical methods of optimization. (2nd edn), New York, USA.

94. Bateson CA, Curtiss B (1996) A method for manual endmember selection and spectral unmixing. Remote Sensing of the Environment 55: 229-243.

95. Blackburn GA, Steele CM (1999) Towards the remote sensing of matorral vegetation physiology: relationships between spectral reflectance, pigment, and biophysical characteristics of semiarid bushland canopies. Remote Sensing of the Environment 70: 278-292.

96. Roberts DA, Green RO, Adams JB (1997) Temporal and spatial patterns in vegetation and atmospheric properties from AVIRIS. Remote Sensing of Environment 62: 223-240.

97. Myneni R, Hall F, Seller P, Marshak A (1995) The interpretation of spectral vegetation indexes. IEEE Transactions on Geoscience and Remote Sensing 33: 481.

98. Jackson RD, PN Slater, PJ Pinter Jr (1983) Discrimination of growth and water stress in wheat by various vegetation indices through clear and turbid atmospheres: Remote Sens, Environ 13: 187-208.

99. Tucker CJ, CL Vanpraet, MJ Sharman, G Van Ittersum 1985. Satellite remote sensing of total herbaceous biomass production in the Senegalese Sahel: 1980-1984. Remote Sens Environ 17: 233-249.

100. Recio JA, Helmholz P, Müller S (2011) Potential evaluation of different types of images and their combination for the classification of GIS objects cropland and grassland. The Internat Archives of the Photogramm, Remote Sens, And Spatial Info Sc 38: 19-25.

101. Schuster G, Förster M, Kleinschmit B (2012) Testing the red edge channel for improving land-use classifications based on high-resolution multi-spectral satellite data. International Journal of Remote Sensing 33: 5583-5599.

102. Liu J, Pattey E, Jégo G (2012) Assessment of vegetation indices for regional crop green LAI estimation from Landsat images over multiple growing seasons. Remote Sensing of Environment 123: 347-358.

103. Nilson T (1992) Radiative transfer in nonhomogeneous plant canopies. Advances in Bioclimatology 1: 59-88.

104. Li X, Strahler AH (1985) Geometric-optical modeling of a conifer forest. IEEE Trans Geosci, Remote Sensing 23: 705-721.

105. Jacob, BG, Gunter JT, Muturi EJ, Caamano EX, Githure JI, Regens JL, Novak RJ. 2010. Quantifying Stochastic Error Propagation in Bayesian Parametric Estimates of Anopheles gambiae s.l. aquatic habitats. International Journal of Remote Sensing 11: 67-78.

106. Jacob Benjamin G, Daniel Griffith, James Gunter, Ephantus J Muturi, Erick Caamano, et al. (2009) A spatial filtering specification for an auto- negative binomial model of Anopheles arabiensis aquatic habitats. Transactions in GIS 12: 515-539.

107. AFF (2017) 2011-2015 American Community Survey 5-Year Estimates.

108. Addink EA, de Jong SM, Pebesma EJ (2007) The importance of scale in object-based mapping of vegetation parameters with hyperspectral imagery. Photogrammetric Engineering and Remote Sensing 73: 905-912.

109. Delegido J, Fernandez G, Gandia S, Moreno J (2008) Retrieval of chlorophyll content and LAI of crops using hyperspectral techniques: application to PROBA/CHRIS data. International Journal of Remote Sensing 29: 7107-7127.

110. Gallagher AC (2005) Detection of linear and cubic interpolation in JPEG compressed images in Proc 2nd Canadian Conf.Computer and Robot Vision, Washinghton, DC, USA, pp. 65-72.

111. Popescu A. and Farid H, (2005). Exposing digital forgeries by detecting traces of resampling IEEE Trans. Inf. Forensics Security 53: 758-767.

112. Mahidan B, Saic S (2008) Blind authentication using periodic properties of interpolation, IEEE Trans Inf Forensics Security, 3: 529-538.

113. Madihan (2007) Detection of copy-move forgery using a method based on blur moment invariants Forsenic Sci Int 2: 180-189.

114. Prasad and Ramakrishman (2006). [On resampling detetction and its application to detect image tampering in P Proc IEEE Int. Conf. Multimedia and EXPO, 2006, pp. 1325–1328.

115. Inada K (1976) Action spectra for photosynthesis in higher plants. Plant Cell Physiology 17: 355-365.

116. Mathews S (2006) Phytocrome-mediated development in land plants: red light sensing evolves to meet the challenges of changing light environments. Molecular Energy 15: 3483-3503.

117. KnyazikhinY Martonchik JV, Myneni RB, Diner DJ, Running SW (1998) Synergistic algorithm for estimating vegetation canopy leafarea index and fraction of absorbed photosynthetically active radiation from MODIS and MISR data Journal of Geophysical Research, 103(32): 257-276.

118. Moon P, Spencer D E (1988) Eleven Coordinate Systems and The Vector Helmholtz Equation. §1 and 5 in Field Theory Handbook, Including Coordinate Systems, Differential Equations, and Their Solutions, 2nd edition Springer-Verlag, New York, pp. 1-48 and 136-143.

119. Zwillinger D (1997) Handbook of Differential Equations. (3rd edn), Boston, MA: Academic Press, USA.

120. Suits GH (1972) The calculation of the directional reflectance of a vegetative canopy. Remote Sensing of Environment 2: 117-125.

121. Addink EA, de Jong SM, Pebesma EJ (2007) The importance of scale in object-based mapping of vegetation parameters with hyperspectral imagery. Photogrammetric Engineering and Remote Sensing 73: 905-912.

122. Aguirre Obando O, Pietrobon A, Bona A, Navarro Silva M (2016) Contrasting patterns of insecticide resistance and knockdown resistance (kdr) in Aedes aegypti populations from Jacarezinho (Brazil) after a Dengue Outbreak. M and V Entomology 60(1): 94-100.

123. Fourty T, Baret F (1998) On spectral estimates of fresh leaf biochemistry. International Journal of Remote Sensing 19: 1283-1297.

124. Treuhaft RN, Law BE, Asner GP (2004) Forest attributes from radar interferometric structure and its fusion with optical remote sensing. BioScience 54: 561-571.

125. Wulder MA, Hall RJ, Coops NC, Franklin SE (2004) High-resolution remotely sensed data for ecosystem characterization. Bio Science 54: 511-521.

126. Schowengerdt RA (2007) Optical radiation models in Remote Sensing: models and methods for image processing, Amsterdam pp. 45-88.

127. Jensen JR (1983) Biophysical remote sensing – Review article. Annals of the Associations of American Geographers 73: 111-132.

128. Asner GP (1998) Biophysical and biochemical sources of variability in canopy reflectance. Remote Sensing of Environment 64: 234-253.

129. Turner DP, Ollinger SV, Kimball JS (2004) Integrating remote sensing and ecosystem process models for landscape-to-regional-scale analysis of the carbon cycle. BioScience 54: 573-584.

130. Lambin EF (1996) Change detection at multiple temporal scales: seasonal and annual variations in landscape variables. American Society for Photogrammetry and Remote Sensing 62: 931-938.

131. Jupp DLB (1997) Modeling directional variance and variograms using Geo-Optical models, Journal of Remote Sensing, 1:101-107.

132. Van der Meer F (1999) Iterative spectral unmixing (ISU). International Journal of Remote Sensing 20: 3431-3436.

133. Bouwmeester H, Heuvelink G, Stoorvogel J (2016) Mapping crop diseases using survey data: The case of bacterial wilt in bananas in the East African highlands. E J Agronomy 74: 173-184.

134. Center for Disease Control and Prevention CDC (2018) Microcephaly & Other Birth Defects.

135. Center for Disease Control and Prevention (2018) Zika Virus, Pregnancy.

136. Chen R, Crawford K, Davis C, Ehsani R, Vougioukas S, et al. (2015) The Drones are Coming Unmanned Aerial Vehicles for Agriculture. Citrograph 6(4): 18-23.

137. Conklin KA, Panaou T, Jacob BG (2017). Accounting for first-order differential flux extinction through dimensionless, radiation-based discontinuous vegetated canopies employing near infra-red and red wavelength proxy spectral irradiance for approximating unobserved isoline convergence and soil-perturbed responses in capture point endmember signatures positively autocorrelated to endemic Naegleria fowleri sample sites. J Geographic Information System 4(3): 1-31.

138. Florida Department of Health FDOH (2018) Zika Free Florida.

139. Florida Department of Health (2017) Hillsborough County Disease Surveillance Newsletter.

140. Freire IL, Torrisi M, (2014) Similarity solutions for systems arising from an Aedes aegypti model. Communications in Nonlinear Science and Numerical Simulation 19(4): 872-879.

141. Gringeri C (2001) The poverty of hard work: multiple jobs and low wages in family economies of rural Utah households. Journal of Sociology & Social Welfare 28(4): 3.

142. Hamid PH, Prastowo J, Ghiffari A, Taubert A, Hermosilla C (2017) Aedes aegypti resistance development to commonly used insecticides in Jakarta, Indonesia. Plos One 12(12): 1-11.

143. Hares S (2018) Mosquito-packed drones could give extra bite to Zika fight. Reuters.

144. Hardy A, Makame M, Cross D, Majambere S, Msellem M (2016) Using low-cost drones to map malaria vector habitats. Parasites & Vectors.

145. Lana RM, Morais MM, Lima, TD, Carneiro, (2018) Assessment of a trap based Aedes aegypti surveillance program using mathematical modeling. Plos ONE 13(1): 1-16.

146. Landau K, Leeuwen W (2012) Fine Scale Spatial Urban Land Cover Factors Associated with Adult Mosquito Abundance and Risk in Tucson, Arizona. Journal of Vector Ecology 37(2): 407-418.

147. Li X, Ren Z, Wang L, Zhang H, Jiang S, et al. (2016) Co-endemicity of Pulmonary Tuberculosis and Intestinal Helminth Infection in the People's Republic of China. PLoS Negl Trop Dis 10(3):1-23.

148. Maneerat S, Daude E (2018) A spatial agent-based simulation model of the dengue vector Aedes aegypti to explore its population dynamics in urban areas. Ecological Modelling, 333: 66-78.

149. Montagner FRG, Silva OS, Jahnke SM (2018) Mosquito species occurrence in association with landscape composition in green urban areas. Braz J Biol 78(2): 233-239.

150. Multi-Resolution Land Characteristics Consortium MRLC (2011) National Land Cover Database.

151. Ndenga BA, Mutuku FM, Ngugi HN, Mbakaya JO, Aswani P, (2017) Characteristics of Aedes aegypti adult mosquitoes in rural and urban areas of western and coastal Kenya. Plos One 12(12): 1-14.

152. Nicolaci da Costa P (2017) More Americans need a 2nd job to make ends meet-and it's sending a troubling message about the economy. Businness Insider.

153. Panaou T, Alao S, Jacob B (2016) Hypothetically quantifying flood vulnerability in a reservoir tributary employing 3-dimensional geomorphological terrain related covariants, a stochastic iterative quantitative interpolator and a space-time global circulation model paradigm. J Remote Sensing & GIS 5(4): 183.

154. Pérez D, Van Der Stuyft P, Toledo M, Ceballos E, Fabré F, et al. (2018) Insecticide treated curtains and residual insecticide treatment to control Aedes aegypti: An acceptability study in Santiago de Cuba. PLoS Negl Trop Dis 12(1): 1-20.

155. Qing Y, Ning X, Shi-jie Y, Shuai H (2017) Deworming of stray dogs and wild canines with praziquantel-laced baits delivered by an unmanned aerial vehicle in areas highly endemic for echinococcosis in China. Infectious Diseases of Poverty, p. 61.

156. Seixas G, Grigoraki L, Weetman D, Vicente JL, Silva AC, et al. (2017) Insecticide resistance is mediated by multiple mechanisms in recently introduced Aedes aegypti from Madeira Island (Portugal). PLoS Negl Trop Dis 11(7): 1-16.

157. Ryu J, Kim M, Cha K, Lee T, Choi D (2002) Kriging interpolation methods in geostatistics and DACE model. KSME International J 16(5): 619-632.

158. U.S. Census (2011) US Gazetteer files: 2010, 2000, and 1990.

159. U.S. Census. (2015) Tiger.

160. Vazquez-Prokopec G, Medina-Barreiro A, Che-Mendoza A, Dzul-Manzanilla F, Correa-Morales F, et al. (2017) Deltamethrin resistance in Aedes aegypti results in treatment failure in Merida, Mexico. PLoS Negl Trop Dis 11(6):1-14.